Preparation of multicomponent systems as a means of controlling the properties of peptide-based low molecular weight hydrogels

Libby Jane Marshall

Submitted in fulfilment of the requirements for the Degree of Doctor of Philosophy

School of Chemistry

College of Science and Engineering

University of Glasgow

Month and Year of Deposit to Library

Abstract

Multicomponent systems can be used to achieve different properties and behaviors from low molecular weight gelators (LMWGs) that cannot be accessed from single component systems. In this thesis, we exemplify a number of interesting multicomponent systems. We cover many possible systems, mixing two gelators, mixing a gelator and a non-gelator and mixing a gelator and a cross-linking agent, all of which give different possibilities.

In Chapter 2, we use a two-component system, showing that a non-gelling component modifies the assembly of the gelling component, allowing access to co-assembled structures that cannot be formed from the gelling component alone. We characterised the systems across multiple length scales, from the molecular level by NMR and CD spectroscopy, to the microstructure level by SANS and finally to the material level using nanoindentation and rheology. By exploiting the enhanced mechanical properties achieved through addition of the second component, we formed multicomponent noodles with superior mechanical properties to those formed by the single component system. Furthermore, the non-gelling component can be triggered to crystallise within the multicomponent noodles, allowing us to prepare new types of hierarchical composite noodles.

In Chapter 3, we prepared a variety of multicomponent systems where both components are *N*-functionalised dipeptide-based LMWGs that may either co-assemble or self-sort. We exemplify how varying the concentration ratio of the two components can be used to tune the properties of the multicomponent system. We also investigated the effect of changing the chirality of a single component on the assembly of the systems. While predicting the outcome of multigelator assembly is a challenge, the preparation of a variety of systems allows us to probe the factors affecting their design.

In Chapter 4, we show that preparing multicomponent systems from a lysine- (K)-containing peptide-based LMWG and the cross-linking agent glutaraldehyde (GTA) allows tuning of the mechanical properties of the final gel depending on the position of the K residue in the peptide chain, whether the cross-linking agent is added to the system before or after gelation and whether gelation is triggered by a reduction in pH or by physical cross-linking with Ca^{2+} ions

Contents

Acknowledgments

First, I would like to thank my supervisor, Professor Dave Adams for his constant support from my undergraduate Masters project to now. I could not have asked for a better supervisor and am so fortunate to have spent the start of my career working in his lab. Thank you for always encouraging me and reminding me to relax when I was getting stressed or overthinking and for all the opportunities working in your group has provided me.

Thank you to the Adams group who have been with me to the end. Courtenay, you have been a constant force driving me forward and keeping me grounded. I don't know where I'd be without you. Chloe, you have been one of us from the very beginning and now I can't imagine life without you. Keep going, you are so much more amazing than you know. Simona, what would I do without you? You are brilliant in every way and so ready to give up your time to help others. I am going to miss seeing you all every day so much.

Thank you to past members of the Adams group: Dr Kate McAulay, Dr Emily Cross, Dr Ana María Fuentes Caparrós, Dr Santanu Panja, Dr Daniel McDowall and Dr Lisa Thomson for your kindness and support and for being amazing role models whose work ethic and quality of research output I have continued to strive toward throughout my studies. A special thanks to Lisa for keeping me sane throughout alternating weeks in the lab due to COVID. I would not have got through without you. You are such an amazing researcher and friend and I owe so much of my knowledge to you.

Thank you to the Draper Group (past and present) for so many fond memories both inside and out of the lab. Thank you to Bart for all your help, from synthesis to general lab queries. You have the patience of a saint putting up with all of our questions and I know your supervision during my Masters project helped lead me to where I am today. To Becky for your strength and Jakki for your friendship. Neither of you take any bullshit and I have so much respect for you. Rebecca (my SANS partner in crime and fellow gym girl), you are so wonderful in everything you do. I am so proud to have worked with you and to call you a friend. Nick, you have brought so much life and a wonderful energy to the lab, keep working hard.

Thank you to my second supervisor, Dr Emily Draper, for your guidance and advice throughout my PhD. Having young women researchers like you (and many others in the School of Chemistry and beyond) to look up to during my PhD has been invaluable.

Thank you to my fiancé, Daniel, for always looking after me and supporting me. Knowing I had you by my side has helped me through the toughest times. You have seen me at my worst and at my best. I am so grateful for everything that you do for me, and I can’t wait to spend the rest of my life with you.

Thank you to my family, in particular my Dad, Richard, my brother, Martin, and Daniel’s parents, Christine and William. You have been my cheerleaders throughout my career. Finally, thank you to my mum, Linda. I wish you were still here to see where I am and who I have become. I hope I have made you proud and will continue to do so.

Declaration of authorship

I declare that, except where explicit reference is made to the contribution of others, that this thesis is the result of my own work and has not been submitted for any other degree at the University of Glasgow or any other institution.

Libby Jane Marshall

List of publications arising from this PhD

(In order of publication)

Giuri, D., Adams, D., **Marshall, L.J.**, Schweins, R., Dietrich, B., McDowall, D., Thomson, L., Newton, J.Y. and Wilson, C., 2021. Exploiting and Controlling Gel-to-Crystal Transitions in Multicomponent Supramolecular Gels. *Chemical Science*, 12, 9720-9725.

Giuri, D., **Marshall, L.J.**, Wilson, C., Seddon, A. and Adams, D.J., 2021. Understanding gel-to-crystal transitions in supramolecular gels. *Soft Matter*, 17, 7221-7226.

Marshall, L.J., Matsarskaia, O., Schweins, R. and Adams, D.J., 2021. Enhancement of the mechanical properties of lysine-containing peptide-based supramolecular hydrogels by chemical cross-linking. *Soft Matter*, 17, 8459-8464.

Thomson, L., McDowall, D., **Marshall, L. J.**, Marshall, O., Ng, H., Homer, W.J.A., Ghosh, D., Liu, W., Squires, A.M., Theodosiou, E. and Topham, P.D., 2022. Transferring micellar changes to bulk properties via tunable self-assembly and hierarchical ordering. *ACS nano*, *16*, 20497-20509.

Marshall, L. J., Wallace, M., Mahmoudi, N., Ciccone, G., Wilson, C., Vassalli, M., & Adams, D. J., 2023. Hierarchical Composite Self-Sorted Supramolecular Gel Noodles. *Advanced Materials*, 2211277.

Ghosh, D., **Marshall L. J.**, Ciccone, G., Liu, W., Squires A., Seddon, A., Vassalli, M., Adams D. J., 2023. Fine-tuning Supramolecular Assemblies by Controlling Micellar Aggregates, *Macromolecular Materials and Engineering*, 2300082.

List of abbreviations

1Nap, 1-naphthyloxyl;

2Nap, 2-napthyloxyl;

2Nap-OH, 2-Naphthoxyacetic acid;

A, alanine;

AFM, atomic force microscopy;

Boc, tert-butyloxy carbonyl;

Cbz, carboxybenzyl;

CCM, Centre for the Cellular Microenvironment;

CD, circular dichroism;

Cha, cyclohexylalanine;

CTAT, cetyltrimethylammonium tosylate;

D, aspartic acid;

DCM, dichloromethane;

DMSO, dimethyl sulfoxide;

E, glutamic acid;

EtOAc, ethyl acetate

EtOH, ethanol;

F, phenylalanine (see also Phe);

Fmoc, fluorenylmethyloxycarbonyl;

G, glycine;

G′, storage modulus;

G″, loss modulus;

GdL, glucono-δ-lactone;

GTA, glutaraldehyde;

HT, high tension;

I, isoleucine;

IBCF, iso-butyl chloroformate;

ILL, Institut Laue-Langevin,

K, lysine;

LVR, linear viscoelastic region;

LMWG, low-molecular weight gelator;

L, leucine;

MeOH, methanol;

NMM, *N*-methyl morpholine;

NMR, nuclear magnetic resonance;

NOE, nuclear Overhauser effect;

OMe, methyl ester;

OBzl, benzyl ester;

Phe, phenylalanine (see also F);

PXRD, powder X-ray diffraction;

R, arginine;

rpm, revolutions per minute;

RQC, residual quadrupolar coupling;

S, serine;

SANS, small angle neutron scattering;

SAXS, small angle X-ray scattering;

SEM, scanning electron microscopy;

SLD, scattering length density;

tanδ, loss factor;

TFA, trifluoroacetic acid;

TEM, transmission electron microscopy;

THF, tetrahydrofuran;

TLC, thin layer chromatography;

Tyrosine, Y;

UEA, University of East Anglia;

UofG, University of Glasgow;

V, valine;

WAXS, wide angle X-ray scattering.

Chapter 1

Introduction

1.1 Low molecular weight hydrogels

Supramolecular gels are attractive alternatives to polymeric gels due to their reversible nature allowing them to respond to external stimuli.[1-4] Polymeric gels are formed by the physical entanglement or chemical cross-linking of pre-formed, covalently linked polymeric chains. Supramolecular gels are formed by the hierarchical self-assembly of small molecules, so-called low molecular weight gelators (LMWGs). These LMWGs assemble into one-dimensional fibres that further interact to form a three-dimensional network capable of trapping the solvent (Figure 1.1).[5-7] In the case of hydrogels, the solvent is water. Despite being composed of mostly liquid (the solvent), gels display solid-like properties. The properties of hydrogels are controlled by the microstructure underlying the three-dimensional gel network.[8, 9] The morphology and mechanical properties of the self-assembled structures, the propensity for the structures to entangle and laterally associate as well as the type and number of interactions between neighbouring structures all affect gel properties.[10] The dynamic nature of the interactions that drive supramolecular assembly makes it difficult to predict the gelation ability and properties of any resulting gels.[11]

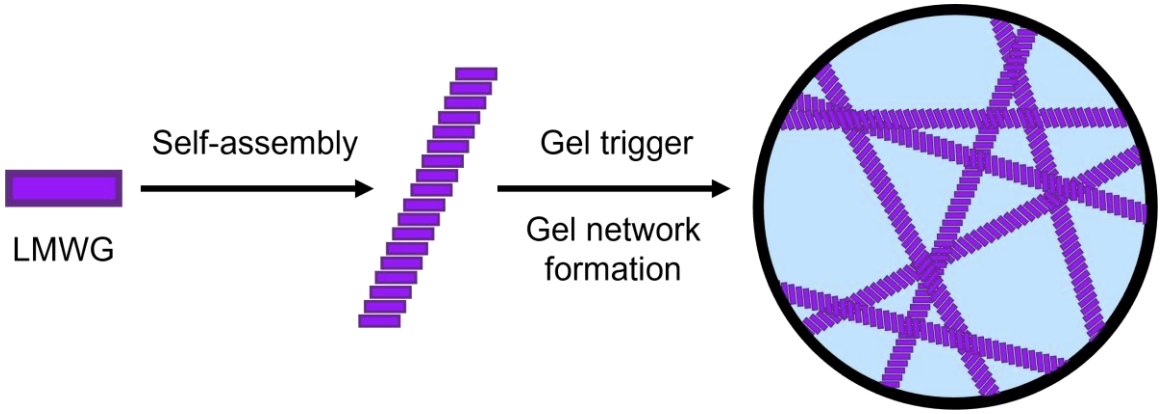

Figure 1.1. Simplified schematic showing self-assembly of a LMWG. On application of a trigger, the structures formed by the LMWG interact to form a three-dimensional network capable of trapping the solvent.

The self-assembly of LMWGs is driven by the formation of physical interactions, such as hydrogen bonds, electrostatic forces, van der Waals forces, π-π stacking and the hydrophobic effect.[12, 13] Being held together by physical interactions offers many advantages over conventional polymeric hydrogels such as, reversibility of gelation,[14] the opportunity for self-healing,[15] and biocompatibilty.[16] This makes supramolecular hydrogels attractive for use in many applications including as antimicrobial agents,[17] scaffolds for cell culture,[13] drug delivery systems[18] and for environmental remediation.[19] Each application requires the gels to have specific properties. It is therefore of great importance that we can finely control the

properties of gels to maximise their use for any given application. This is particularly important owing to the difficulties faced when designing new LMWGs.

LMWGs have been designed based on a wide range of functional moieties including ureas,[20] nucleobases,[21] dendritic systems,[22] sugars,[23] metallogels,[24] and peptides.[25] Here we will focus on peptide-based LMWGs. Peptide-based LMWGs form directional hydrogen bonds during self-assembly, driving formation of the one-dimensional structures required for gel formation.[26] Peptide-based supramolecular hydrogels have many advantages over other types of hydrogel, including easy synthesis, potential for chemical modification, responsiveness to external stimuli, bioactivity and biocompatibility.[27, 28] However, peptide-based supramolecular hydrogels often lack the mechanical strength required for certain applications owing to the non-covalent nature of the interactions holding the gel network together.[28-30] Examples of such applications include: scaffolds for cell and tissue engineering, where the mechanical properties of the scaffold need to mimic the cells' native environment and are essential in determining the outcome of cellular differentiation;[31] 3D printing, where the gel must have sufficient strength to be extruded through a needle;[32] and as drug delivery vehicles where sufficient stiffness ensures sustainable release of drug molecules.[33] Supramolecular hydrogels can be formed from short oligopeptides.[27] However, here the discussion will mainly focus on short peptides functionalised with a large aromatic group at the *N*-terminus.

Bing Xu's group first reported LMWGs based on dipeptides conjugated to 2-naphthoxyacetic acid (2Nap) in 2007.[34] Since then this has become a common template for dipeptide-based LMWGs (Figure 1.2).[34-38] The naphthalene ring can be replaced with other large aromatic groups such as fluorene[39-42] or pyrene.[43-45] However, such polyaromatic compounds are carcinogenic,[46, 47] making them unsuitable for biomedical applications. The Xu group selected the naphthyl group as a potential replacement for fluorene and pyrene as it is a fragment commonly found in drug molecules. Cell cytotoxicity studies indicate that the hydrogelators designed by Xu's group are biocompatible.[34] The naphthalene ring has further advantages in that it can be functionalised *via* ring substitutions. This allows further tuning of the properties of systems composed of naphthalene-functionalised peptides.[48]

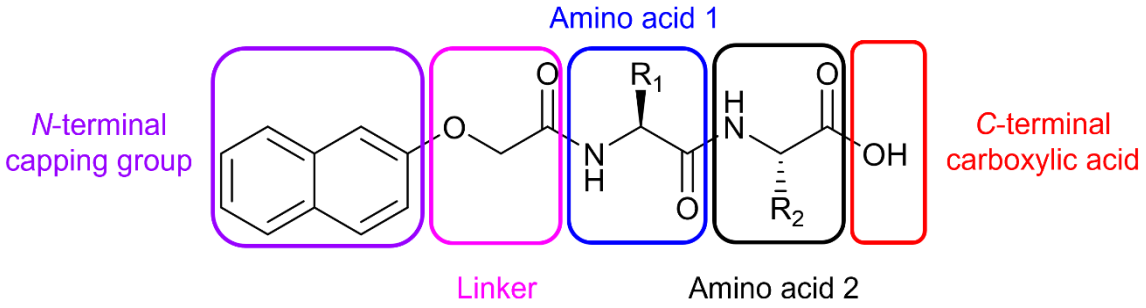

Figure 1.2. *N*-Functionalised dipeptide using a naphthalene ring as an example aromatic *N*-terminal capping group.

Various studies have investigated the importance of π-π stacking and hydrophobic interactions in the self-assembly of peptide-based LMWGs. Wide angle X-ray scattering (WAXS) and molecular dynamics experiments suggest that peptide-based LMWGs functionalised with a fluorenylmethyloxycarbonyl (Fmoc) group at the *N*-terminus stack together with distances less than 4 Å between Fmoc rings which strongly supports π-π stacking as the driving force behind assembly.[49, 50] However, when the π-π stacking of the LMWG 2NapAA (where a dialanine is conjugated to a naphthalene ring via a linker; note throughout we will use the one letter amino acid codes, Figure 1.3) was disrupted by addition of a bromo substituent to the 6-position of the naphthalene ring, the modified molecule was still able to form hydrogels.[50] This suggests that the hydrophobicity supplied by the aromatic group at the *N*-terminus is also important for gel formation.[51]

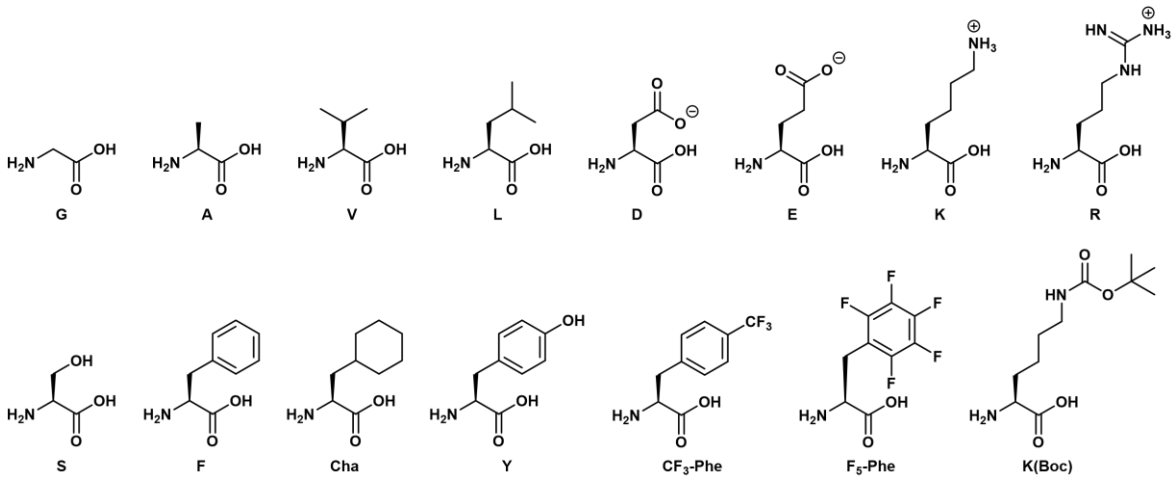

Figure 1.3. Chemical structures of the amino acid residues discussed in Chapter 1. The single letter code of the natural amino acids and abbreviated names of the non-natural amino acids are shown below the structures. The amino acids with charged side chains are shown with the side chains in their charged states.

Aromatic groups in the peptide chain also contribute to self-assembly through π-π stacking and hydrophobic effects. Yang *et al*. found that multicomponent gels composed of Fmoc-F

and N^{ε}-Fmoc-K were stronger and more elastic than multicomponent gels composed of Fmoc-L and N^{ε}-Fmoc-K.[52] The authors postulate that this increased strength and elasticity results from the additional phenyl group in Fmoc-F increasing the π-π stacking of the system compared to the Fmoc-L system.[52]

Replacing F with cyclohexylalanine (Cha) removes aromatic interactions but increases the hydrophobicity of the system. Cha-containing peptide-based LMWGs were shown to be more efficient hydrogelators than their F-containing equivalents, highlighting the importance of hydrophobic interactions.[53] This work shows that aromatic interactions are not essential for peptide self-assembly. However, the unique behaviour of the F-containing variants compared to non-aromatic variants of varying hydrophobicity show that aromatic interactions play a distinct role in self-assembly and thereby can be used to control the properties of the resulting assemblies.[53]

1.2 Methods for triggering gelation

Supramolecular gel formation results from changing the environment of LMWGs from one in which they are relatively soluble to one in which they are insoluble.[54] Many different methods can be used to form supramolecular hydrogels. Some of the most common gelation triggers include a heat-cool cycle,[55, 56] enzymatic reaction,[38, 57, 58] irradiation with light,[59] solvent switch,[60, 61] change in pH[56, 62, 63] or addition of metal salts. [26, 64] The work in this thesis uses two methods: reduction in pH and physical cross-linking using Ca^{2+} ions.

Supramolecular hydrogels usually exist in a kinetically trapped state.[65-67] The structures they adopt, and hence their properties, depend on the process by which they are formed.[8, 54] Adams *et al*. highlighted the possibility of accessing gels with different network types, and thereby different mechanical properties, from a single LMWG by forming gels using different methods.[68] Gel properties can be related to the structure of the gel network.[69] While gels prepared using a reduction in pH contained many thin fibres resulting in an entangled network, salt-triggered gels were composed of networks containing a significant number of fibres with the tendency to align.[68]

Before hydrogel formation, the LMWG must first be suspended in water. For pH-sensitive peptide-based LMWGs, the pH of the solution must be raised sufficiently so that the *C*-terminal carboxylic acid is deprotonated. Deprotonation creates a negative charge, increasing the polarity of the gelator molecules and allowing them to dissolve (Figure 1.4).[37] Gelation can then be triggered by decreasing the pH to below the apparent pK_a value of the peptide so that the carboxylate group is reprotonated.[70-72] At this point the molecule is no longer soluble in water and would prefer to self-assemble.[70, 73]

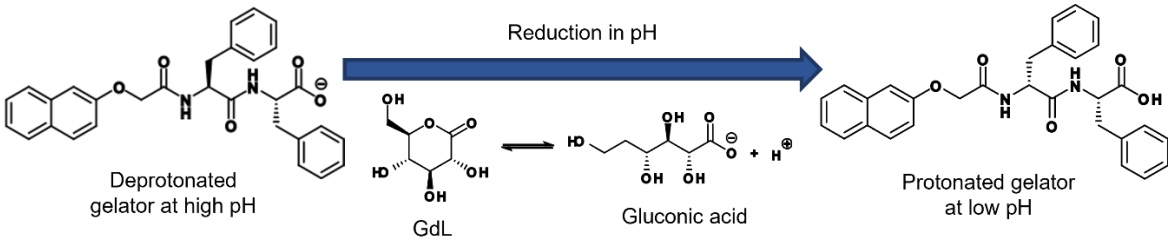

Figure 1.4. The gelation process using GdL as a trigger.

N-Functionalised peptides have considerably higher pK_a values when incorporated within self-assembled structures compared to when they are free in solution.[37, 72] This is important to take into consideration when designing a system for applications that require a specific pH value. Previous work investigating the dipeptide-based LMWG FmocFF showed two apparent pK_a shifts.[72] These transitions were associated with two different types of self-assembled structures that FmocFF molecules form depending on the pH of their environment.

In this thesis, pH-triggered gels were prepared using glucono-δ-lactone (GdL).[71] The use of GdL as a pH trigger is advantageous as the rate of dissolution of GdL is greater than the rate of its hydrolysis.[37] This allows uniform release of protons throughout the sample and formation of homogenous gels.[70] The slow hydrolysis of GdL to gluconic acid (Figure 1.4) allows gradual self-assembly with the potential for re-arrangement in order to achieve a thermodynamic minimum rather than a kinetically trapped state.[8, 74, 75] This allows preparation of stable gels with reproducible properties as well as allowing the assembly process to be investigated using techniques such as nuclear magnetic resonance (NMR) spectroscopy, rheology and small angle X-ray and neutron scattering (SAXS and SANS respectively).

While triggering gelation of peptide-based LMWGs using a reduction in pH is effective, it restricts the pH of the gels to values below the apparent pK_a of the LMWG, which tends to be below pH 6.[7, 76] Work by the Adams group has shown that LMWGs with the ability to form worm-like micelles at high pH can form rigid, self-supporting gels on the addition of

divalent cations.[26] Solutions of 2NapFF-based LMWGs at high pH exhibit shear-thinning behaviour. Such behaviour suggests alignment of long, one-dimensional aggregates under flow when the rate of deformation is greater than the time required for the network structure to reform equilibrium.[26] Chen *et al*. used SAXS experiments to demonstrate strong orientation under shear, proving the presence of anisotropic species. The presence of long, worm-like micelles was further confirmed using transmission electron microscopy (TEM).[26] It is expected that gel formation occurs via the formation of salt bridges between carboxylate groups on different worm-like micelles, creating cross-links and thereby a 3D network capable of trapping the solvent.[26]

The kinetics of gel formation will also play a role in determining the final properties of the gel. Increasing the concentration of GdL used to trigger gelation will increase the rate of gel formation and decrease the final pH of the resulting gel. The concentration of GdL used to form gels from the dipeptide-based LMWG 2NapAV was shown to alter the strength of the final gels.[37] The gels formed using lower GdL concentrations were less resistant to strain, as shown by lower critical strain values recorded during strain sweeps of these gels. However, the crossover point of these gels was increased, showing higher strain is required to completely break down the gel network and cause the sample to undergo a transition from a gel to a liquid.[37] This behaviour suggests that the fibres within gel networks formed at lower pH values are more rigid than those formed at higher pH values. The fibres are therefore less able to withstand large deformations.[37]

A more extreme example compares gels formed by the slow hydrolysis of GdL to gels formed by direct addition of HCl.[77] The gels formed *via* a fast reduction in pH using HCl had far lower moduli values than those formed more slowly using GdL. When HCl was added to the pre-gel solution in an uncontrolled manner or a large excess of GdL was used, precipitation occurred rather than gelation. Meanwhile, addition of HCl in a slow and controlled manner resulted in formation of hydrogels with similar mechanical properties to hydrogels formed using an optimal amount of GdL.[77] This work highlights that the rate of acidification is the determining factor in the properties of the gels formed by a reduction in pH.

The gels discussed thus far are bulk gels where the container in which they are prepared dictates the size and shape of the gel. Supramolecular gel noodles (Figure 1.5), a relatively recent form of supramolecular gel, have become of interest for specific applications where elongated structures are required, such as formation of cellular wires and as scaffolds for neural and muscle cell growth. This type of gel is formed by extruding a pre-gel solution into a trigger medium, usually a salt bath.[78, 79] For a given LMWG to form supramolecular gel noodles, it must assemble in water to form long one-dimensional structures in solution prior to gelation.[78] As with bulk gels formed using a salt trigger, the noodles are formed by physical cross-linking of the pre-gel structures *via* ions present in the trigger medium.

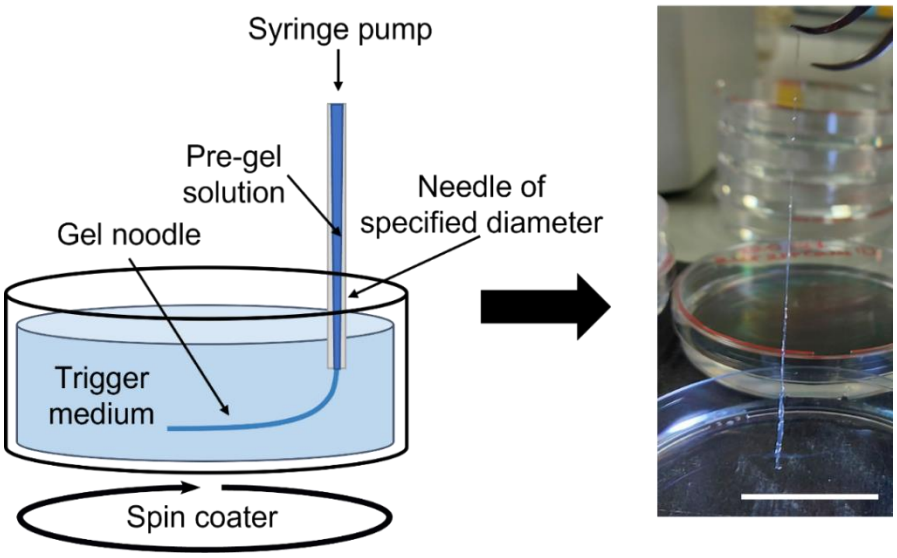

Figure 1.5. Schematic showing gel noodle formation using the syringe pump-spin coater set up.

Extrusion of the pre-gel solution results in the formation of a long, thin gel. This can be done by simply pipetting the pre-gel solution into the trigger medium.[79] However, considerably longer and more homogenous gel noodles can be formed using a syringe pump-spin coater setup (Figure 1.5).[78, 79] The syringe pump allows uniform and controlled force to be applied when extruding the pre-gel solution. Spinning the trigger medium also aids in formation of long homogenous noodles and minimises entanglements and blockages during extrusion. This setup allows precise control over flow rate and rotation speed, both of which can affect the morphology of the resulting gel noodles.[78]

1.3 Effect of structure on gel properties

Altering the identity and order of the amino acid residues as well as the identity of the *N*-terminal capping group provides an easy method for changing the properties of *N*-

functionalised peptide-based systems. Hydrophobicity, flexibility, types of intermolecular interaction available and steric effects will all play a role in the ability of a molecule to form hydrogels as well as the properties of any resulting gel phases. The structures and one-letter codes of the amino acid residues discussed in Chapter 1 are shown in Figure 1.3.

Yang *et al*. studied a series of dipeptides with a naphthalene ring at the *N*-terminus. They found that the increased steric hinderance resulting from the introduction of bulky groups, such as hydroxymethyl group in serine (S), disfavours intermolecular interactions and results in less stable hydrogels.[34] More subtle changes can improve a molecules ability to form gels. For example, replacing a glycine (G) residue with an alanine (A) residue decreased the flexibility of the peptide chain, reducing the conformational entropy and resulting in formation of more stable hydrogels.[34]

Changes to the order of amino acids in the peptide chain can also have considerable effects. For example, swapping Fmoc-VLK(Boc) to Fmoc-K(Boc)LV results in gels with dramatically different properties.[49] CD spectroscopy showed lower chiral ordering of Fmoc-K(Boc)LV compared to Fmoc-VLK(Boc). Fmoc-VLK(Boc) formed highly aligned fibrils while Fmoc-K(Boc)LV formed dense clusters of branched fibrils amongst a small number of straight fibrils. The gels formed by Fmoc-K(Boc)LV had significantly higher moduli than the gels formed by Fmoc-VLK(Boc). Hence a small change to the ordering of the amino acid sequence led to drastically different properties.[49]

F is commonly included in peptide-based hydrogelators due to its hydrophobicity and potential to contribute to π-π interactions. FF alone can self-assemble in water to form hydrogels, highlighting the power of the FF motif in driving self-assembly of peptide-based LMWGs.[80] Saiani *et al*. investigated a set of four octa-peptide gelators. The F-containing peptides formed β-sheets in solution. When the F residues were replaced with A residues, the peptides formed α-helices or did not self-assemble in water at all.[81] This further shows the importance of aromatic interactions in driving self-assembly.

A study conducted by Orbach *et al*. using a library of Fmoc-peptides shows that inclusion of specific peptide sequences allows gels to be designed for enhanced biocompatibility.[82] Their work highlights the importance of aromatic interactions in predicting the types of structures formed during self-assembly. For example, Fmoc-FRGD and Fmoc-RGDF self-assembled to form a fibrous network while Fmoc-RGD (which does not contain an aromatic group in addition to the Fmoc group) forms a small number of nanotubes.[82] Fmoc-FG which contains two adjacent aromatic groups also forms a network while Fmoc-GF forms large

tubes. The number and location of aromatic groups therefore have a direct impact on the structures formed.[82]

Aromatic side chains clearly play an important role in the properties of gels formed from peptide-based systems. Gels formed from multicomponent systems where one component contained a F residue were stronger and more elastic than gels formed from systems where the F residue was replaced with a L residue.[49] The improved mechanical properties in the F-containing gels was attributed to increased π-π interactions. Inclusion of F residues can therefore be utilised during gelator design to improve the mechanical properties of the resulting gels.

Further aromatic interactions can be introduced by addition of a large aromatic group, such as a naphthalene, fluorene or pyrene ring (Figure 1.6). A systematic study using a variety of aromatic groups conjugated with a single F residue revealed that rotational freedom of the *N*-terminal aromatic group is essential for self-assembly to take place.[35] The results from this work led to the conclusion that the cinnamoyl group (Figure 1.6) is the smallest structure capable of providing sufficient aromatic-aromatic interactions to allow hydrogel formation when conjugated to a single F residue.

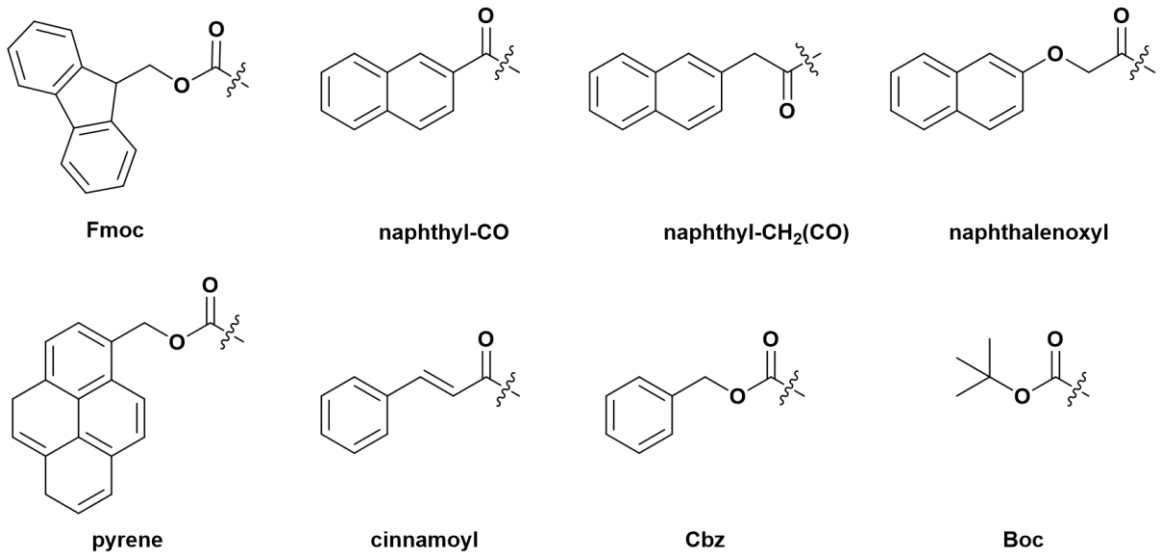

Figure 1.6: Chemical structures of the *N*-terminal groups discussed here. The zig-zag line shows where these groups would be linked to the *N*-terminus of the peptide *via* an amide bond.

A similar study prepared a series of *N*-functionalised F derivatives in order to investigate the effect of hydrophobicity and electronics on self-assembly.[83] Replacing Fmoc with the much smaller carboxybenzyl group (Cbz, Figure 1.6) prevented hydrogelation of all the F derivatives under study. No fibrillar structures were observed on microscopic analysis of

these samples. Replacing the Fmoc group with the tert-butyloxy carbonyl group (Boc, Figure 1.6) removed the ability of the *N*-terminus to form π-π interactions and prevented fibril formation.[83] These results highlight the importance of the *N*-terminal capping group in self-assembly.

Many studies illustrate the importance of π-π stacking in hydrogel formation.[49, 50, 81, 83] However, the expected disruption of π-π stacking by addition of a bromo substituent to the naphthalene ring of the dipeptide-based LMWG 2NapAV does not prevent gel formation. It is therefore proposed that the additional hydrophobicity imparted by aromatic groups, such as naphthalene rings, is also important for gelation. The Adams group previously conducted a study on a series of Fmoc-functionalised dipeptides.[71] The ability of the dipeptides studied to form strong hydrogels was related to their hydrophobicity. We can therefore use the calculated hydrophobicity of a compound to predict the properties of any resulting gels. Alternatively, hydrophobicity can be used to aid in the design of new gelators.

Hydrogen bonding interactions also contribute to the self-assembly of peptide-based LMWGs. Each amino acid provides a hydrogen bonding acceptor and a hydrogen bonding donor *via* the amide bond formed between amino acid residues. Carbonyl amide is commonly used as a linker between the *N*-terminal capping group and the peptide chain since it contributes two further hydrogen bonding sites.[84] Use of a carbonyl amide linker also means that the *N*-terminal groups can easily be appended to the peptide chain using a peptide coupling reaction. Linker length and flexibility are important factors to consider. If the linker is too rigid, there won't be enough flexibility within the molecule for aromatic groups to favourably arrange themselves for formation of aromatic interactions such as π-π stacking. Yang *et al*. found that dipeptides functionalised with a naphthalene ring at the *N*-terminus that lacked an OCH_2 linker between the naphthalene ring and the first peptide residues were unable to form hydrogels (naphthyl groups, Figure 1.6).[34] They proposed that, as well as acting as a potential acceptor for a hydrogen bond, the OCH_2 linker in the naphthalenoxyl group (Figure 1.6) may allow favourable conformations to form and direct intermolecular hydrophobic interactions and hydrogen bonds.[34]

Yang *et al*. found that the angles between the backbones of the dipeptides and the planes of the naphthalene rings are important in determining hydrogel formation.[34] An angle of ~169° in 2NapGG allows GG and 2Nap to extend out for optimal intermolecular interactions. Removal of the O atom in the linker between the naphthalene ring and the amide bond connecting the ring to GG reduces the angle to 147°. This change in angle prevents gel

formation. Removal of the OCH_2 linker entirely further reduced the angle to 93°. Again, no hydrogels were formed by these molecules, showing that the increased curvature of the molecules reduces the intermolecular interactions, preventing hydrogel formation.[34]

Fleming *et al*. studied the assembly of Fmoc-YL with a series of linkers between Fmoc and YL (Figure 1.7).[85] They note an increased rotational energy barrier in **3** compared to **4** owing to the carbamate group in **3**. The methoxy oxygen in **3** also has the potential to act as a hydrogen bond acceptor which may act to further stabilise self-assembly.[85] All compounds studied were able to form hydrogels under the conditions tested. Fluorescence emission spectroscopy suggest that the linker in **1** is too short to allow orientation of the Fmoc rings for effective aromatic stacking interactions.[85] **3** was shown to exhibit the most extensive π-π-stacking arrangement. Results from circular dichroism (CD) spectroscopy show that the length of the alkyl chain in the linker has a direct impact on Fmoc conformation and the supramolecular chirality adopted by the self-assembled structures.[85] Atomic force microscopy (AFM) showed that **3** had the greatest propensity for fibre formation while **1** appeared to form amorphous structures.[85] These results highlight the significance of the linker segment in the self-assembly of these systems. π-π stacking was clearly affected by the choice of linker, with short linkers restricting favourable orientations.[85]

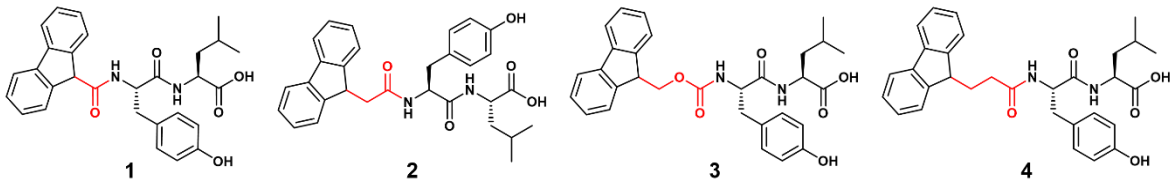

Figure 1.7. Fmoc-YL dipeptides with different linkers studied by Fleming *et al*. The linker segments are highlighted in red.

1.4 Effect of chirality on gel properties

The chirality of peptide-based LMWGs can be easily altered by changing the chirality of one or more amino acid residues. Most studies focus on the (*S*) conformation due to its relevance in biological systems.[86, 87] However, the ability to change the chirality of peptide-based systems in one or more positions within the peptide chain provides a further level to which we can control the self-assembled structures formed by these systems. In some cases, a change in chirality at even one position in the peptide chain may completely remove the ability of the system to form supramolecular hydrogels.[88] Changing chirality may also have more subtle effects on the outcome of self-assembly. The perhaps most obvious effect of

changing chirality is the handedness of any chiral structures formed.[34, 89] Control over the helicity of the nanofibers formed by a hydrogelator provides the potential for preparation of optically active materials by transcribing the helicity of supramolecular nanofibers to other materials.[90-92]

Alterations in the chirality of peptide-based self-assembling systems can change a multitude of properties. For example, Marchesan *et al*.[93] prepared the eight stereoisomers of VFF and found that the positions of (*S*)- and (*R*)-amino acids in the tripeptides with the ability to form gels determined the rheological and thermal behaviours of the resulting gels. This in turn determined their utility for cell culture applications.[93] The handedness of the secondary structures formed was determined by the chirality of the central amino acid, even when the central amino acid had the opposite chirality to the other two residues.[93, 94] The systems with F residues of opposing chirality were unable to form the continuous networks of amyloid structures observed in the systems containing two F residues with the same chirality.[93] X-ray diffraction analysis showed that the antiparallel β-sheets formed by the systems with homochiral F residues were more tightly packed and had higher supramolecular order. The systems with heterochiral F residues formed disordered β sheets.[93, 94] We can therefore use the chirality to change the primary and secondary structures formed by self-assembling peptide-based systems. This in turn will affect the gelling ability and rheological properties of these systems.[93, 94]

Introduction of (*R*)-amino acids at the *N*-terminus of *N*-functionalised peptide-based LMWGs that contain the FF motif removes steric clashes between amino acid side chains. This allows formation of tripeptide zippers.[95] However, preparation of multicomponent systems from homologous (*S*) and (*R*) amphiphilic peptides has been shown to both prevent co-assembly and disrupt self-assembly of either component. Thus, resulting in formation of amorphous or globular aggregates rather than well-defined fibres.[96]

Systems composed of individual enantiomers tend to have superior mechanical properties compared to racemates, or racemates simply precipitate.[34] However, hydrogels prepared from enantiomeric mixtures have also been shown to exhibit non-additive, synergistic increases in mechanical rigidity with the racemic hydrogel showing the greatest effect.[97] This study also highlights the importance of the ratio of components in multicomponent systems. Alone, the two gelling components formed hydrogels with nearly identical mechanical properties.[97] A multicomponent system composed of an equimolar mixture of the two enantiomers (MAX1 and DMAX1) formed a hydrogel with a storage modulus (G′)

value four times greater than that of the single component gels.[97] The use of different enantiomers of the same gelator can result in the formation of self-sorted gel networks with favourable interactions on the hydrogel network level.[97] This increase in cross-linking density will result in enhanced mechanical properties compared to single component systems of the same total gelator concentration. The observed increase in stiffness can be controlled by varying the concentration ratio of the two components, with an equimolar mixture showing the greatest enhancement in rheological properties.[97]

Results from spectroscopy, rheology and microscopy experiments suggest that the enhanced mechanical properties observed in the multicomponent systems arise from energetically favourable interactions between the two enantiomers.[97] Such interactions can occur at the molecular level and/or the hydrogel network level. Favourable interactions at the molecular level will result in the formation a hydrogel network composed of heterogenous fibrils that contain both enantiomers. Favourable interactions at the gel network level will result in a greater number of interactions between fibres within the gel network, which would explain the enhanced stiffness of the multicomponent gel.[97] Synergistic effects have also been reported for homochiral mixtures of two structurally similar LMWGs.[98] Consideration of all these studies together suggests the effect of the chirality of the two components in LMWG-LMWG systems cannot easily be predicted.

Similarly, while some studies highlight that enantiomeric discrimination leads to self-sorting,[99] others show that enantiomeric peptides undergo co-assembly to form hybrid fibres containing both (*S*) and (*R*) forms of the peptide.[97, 100] Bera *et al*. found that the self-assembly kinetics and morphology of pure enantiomers can be completely altered by co-assembly with one another.[101] The new nanostructures formed by co-assembly of the two enantiomers were more mechanically robust than the enantiomerically pure systems.[101] In a different study, Basak *et al*. found that homochiral assemblies formed stronger and more stable gels than heterochiral assemblies. [102] It appears that cooperative interactions between components can be just as important as chirality in determining the packing of gelator molecules in a multicomponent system.

1.5 Methods for investigating the properties of low molecular weight hydrogels

To fully understand supramolecular systems, we need to characterise their properties across multiple length scales using a wide variety of techniques. The molecular packing of gelators within a system can be investigated using techniques such as UV-Vis and CD spectroscopy.[103-106] However, the utility of these techniques for the study of multicomponent systems depends on the individual components being significantly different or on multicomponent assembly resulting in formation of structures very different to the two components alone.

Conceptually, UV-Vis spectroscopy can be used to determine whether co-assembly or self-sorting is taking place. If self-sorting is taking place, the spectrum obtained from the multicomponent system should be an overlay of the spectra obtained from the individual components.[103, 104] In contrast, if co-assembly is taking place, the spectrum obtained from the multicomponent system should show new features as the energy levels resulting from aggregation would be different compared to the single component systems.[107] Proof of self-sorting at the molecular level does not rule out interactions at the network level.

The signals observed in CD spectra arise from chiral arrangement of the supramolecular structures formed. As with UV-Vis spectroscopy, the CD spectrum obtained from self-sorted systems should be the sum of the spectra obtained from the single component systems.[105, 106] For co-assembled systems, the spectrum obtained from the multicomponent system will not be the sum if the spectra obtained from the individual components.[108] Further information can be obtained from CD spectra. For example, the sign of any Cotton effects tells us the handedness of any chiral structures formed and the intensity of peaks indicate the strength of interactions between molecules.[34]

NMR spectroscopy can be used to follow the gelation process owing to the small molecules used to form supramolecular gels becoming NMR invisible on assembly into solid-like fibres. This is due to the large correlation time associated with assembled aggregates resulting in a very short transversal relaxation time and thereby unobservable signals.[109] This can be of particular use when studying the kinetics of multicomponent systems as can provide clear evidence for self-sorting as well as to aid in optimisation of the gelation process. For example, Cornwell *et al*. used NMR spectroscopy to monitor the assembly of a

two-component system. By increasing the concentration of GdL used to trigger gelation, they were able to maximise the percentage assembly of each component.[110]

Hence, NMR spectroscopy can be used to monitor the self-assembly process of each individual component in a supramolecular system. This can give an indication as to whether the two components have sufficiently distinct gelation kinetics for self-sorting to take place. Sequential disappearance of the peaks corresponding to each component indicates self-sorting as one component self-assembles before the other.[63, 108]

Despite the inability to gain structural information on supramolecular assemblies from NMR spectroscopy, NMR techniques such as nuclear Overhauser effect (NOE) NMR experiments can be used to gain insight into how multiple components interact within assemblies[109] as well as prove if a given molecule is forming persistent structures in solution.[62] NOE NMR spectroscopy can be used to characterise the spatial relationship between nuclei.[111] The NOE arises from dipolar interactions between nuclear spins (Figure 1.8).[112] The main requirement for observation of the NOE between two molecules within an aggregated structure is that there is a sufficient number of each molecule in the structure and that there is a significant probability of a cross-relaxation event occurring between the nuclei of interest.[112] This is because the NOE is a relatively small effect.

During a NOE NMR experiment, changes to the signal intensity of the observed nucleus (*I*) are recorded during selective irradiation of a second nucleus (*S*).[112] Irradiation of the w_{1s} transitions causes rapid multiple flips of the *S* spins, causing equalisation of the population states caused by that transition (Figure 1.8a). At equilibrium, the population difference across the w_2 transition is 2δ and 0 across the w_0 transition. Saturation of the w_{1s} transitions changes the population differences across both w_2 and w_0 to δ. The system wants to return to the larger equilibrium population difference. To do so, the w_2 transition increases the population difference across the w_{1s} transitions while the w_0 transition decreases the population difference across the w_{1s} transitions resulting in a decrease in the signal intensity of spin *I*. Hence, the sign and intensity of the NOE depends on whether w_0 or w_2 predominates. If w_0 is more efficient, the NOE will be negative (Figure 1.8b). If w_2 is more efficient the NOE will be positive (Figure 1.8c). w_0 will be more efficient if the two nuclei are close in space.[112]

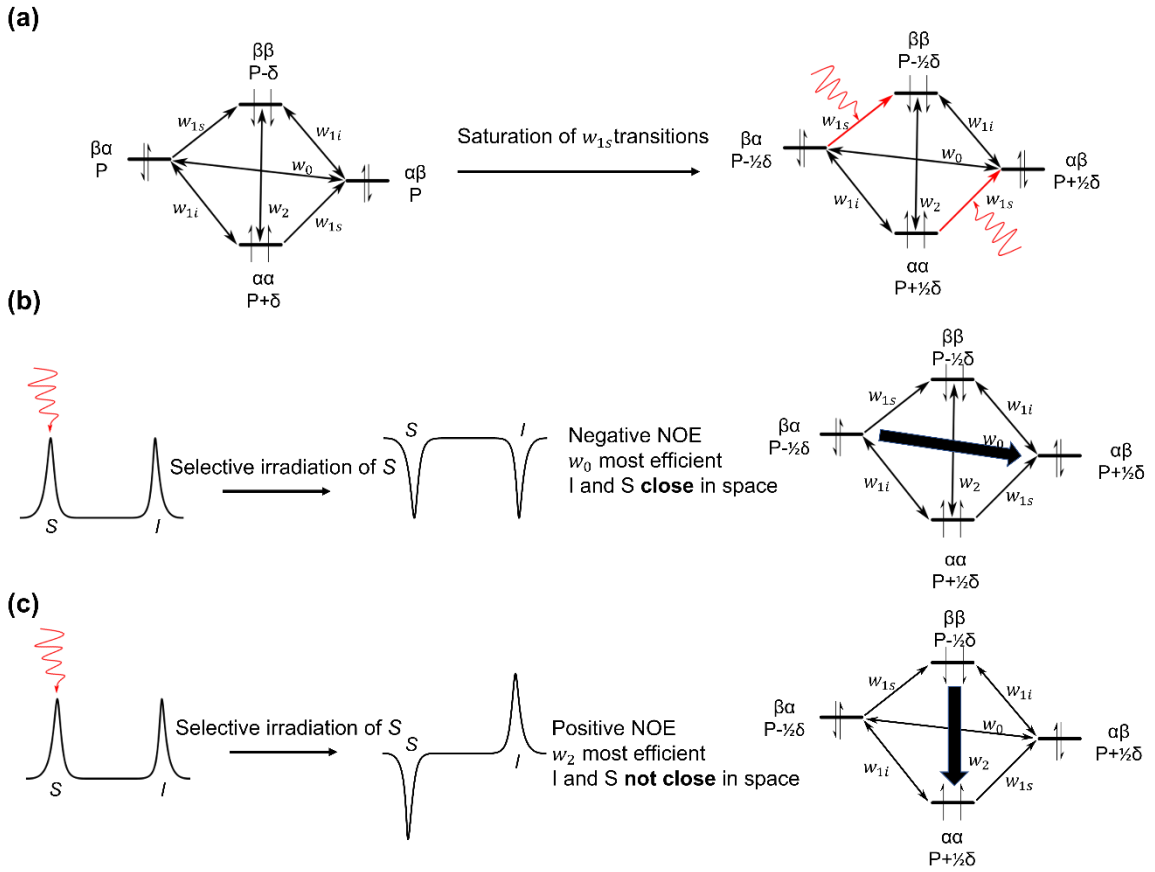

Figure 1.8. (a) Schematic showing energy diagrams of a two-spin (spin = ½) system. The new spin functions resulting from the linear combination of the spin functions of two nuclear spins *I* and *S* are abbreviated as αα, αβ, βα and ββ. The spin state of *I* is represented by the left-hand symbol and the spin state of *S* is represented by the right-hand symbol. w_0, w_1 and w_2 are zero-, single- and double-quantum numbers respectively. The αα state has a population of P+δ where δ is the small number representing the Boltzmann excess due to the slightly lower energy of the αβ state compared to the βα state. For the same reason the ββ state has a slightly smaller population of P-δ. (b) Schematic showing the result of selective irradiation of *S* when *S* and *I* are close in space, causing the w_0 transition to dominate. (c) Schematic showing the result of selective irradiation of *S* when *S* and *I* are not close in space, causing the w_2 transition to dominate.

Hence, if selective excitation results in a signal from a neighbouring proton reducing or becoming negative (a negative NOE effect) then the molecule has low mobility and is most likely involved in large scale aggregation.[62] If two molecules are co-assembled within the same structures, the energy from irradiation of nuclei from the first molecule will be passed to nuclei from the second molecule via relaxation pathways, resulting in a negative NOE difference being observed in the resulting NMR spectrum (Figure 1.8b). If the two nuclei are not close in space, no energy transfer will occur and a positive NOE difference will be

observed (Figure 1.8c), indicating self-sorting and/or the absence of persistent aggregates. NOE experiments can therefore also be used to determine if co-assembly is taking place.

The techniques discussed above are highly concentration dependent. It is therefore of great importance that samples are prepared at the same concentrations as those under study in the gel state. Even more so since LMWGs show concentration-dependent assembly. This can make techniques such as UV-Vis and CD spectroscopy challenging, as it is not possible to use dilution as a means of reducing intensity of signals and scattering artefacts. Use of cuvettes with a shorter path length is a possible method of circumventing these issues.[107]

Imaging techniques such as scanning electron microscopy (SEM), TEM and AFM are commonly used to investigate the fibre-level assembly of LMWG-based systems.[113, 114] This can be useful in identifying whether self-sorting, where structures reminiscent of each individual component will be present,[114] or co-assembly, where a single and potentially new morphology may be present, [115] is taking place. However, the methods used to prepare samples for these techniques can result in drying artefacts.[10, 116] It is possible to use cryo-TEM, which allows images of structures while still in a hydrated environment. However, the low thickness of the films used for cryo-TEM makes it difficult to capture the 3D gel network.[107]

SAXS or SANS are therefore preferable techniques for investigating the fibre-level assembly of LMWGs as they are non-destructive and allow characterisation of structures in the fully hydrated state.[107, 117] The scattering data (Figure 1.9) is fit to a model, with the choice of model depending on which model provides the best fit to the data. Data from LMWGs tend fit best to cylinder-based models. The parameters obtained from the fits provide information about the length, radius and flexibility of the secondary structures formed during self-assembly.[118]

During a small angle scattering experiment, a beam of X-rays or neutrons is fired at the sample (Figure 1.9a).[118] The majority of the radiation is transmitted through the sample and blocked from hitting the detector by a beam stop. However, a small proportion of the radiation interacts with the sample and is elastically scattered. This scattering is measured by the detector. The angle of scattering (θ) is inversely related to the size of the object. Hence, larger objects scatter to smaller angles. Small angle scattering probes structures of the order of 1-100 nm in size.[118]

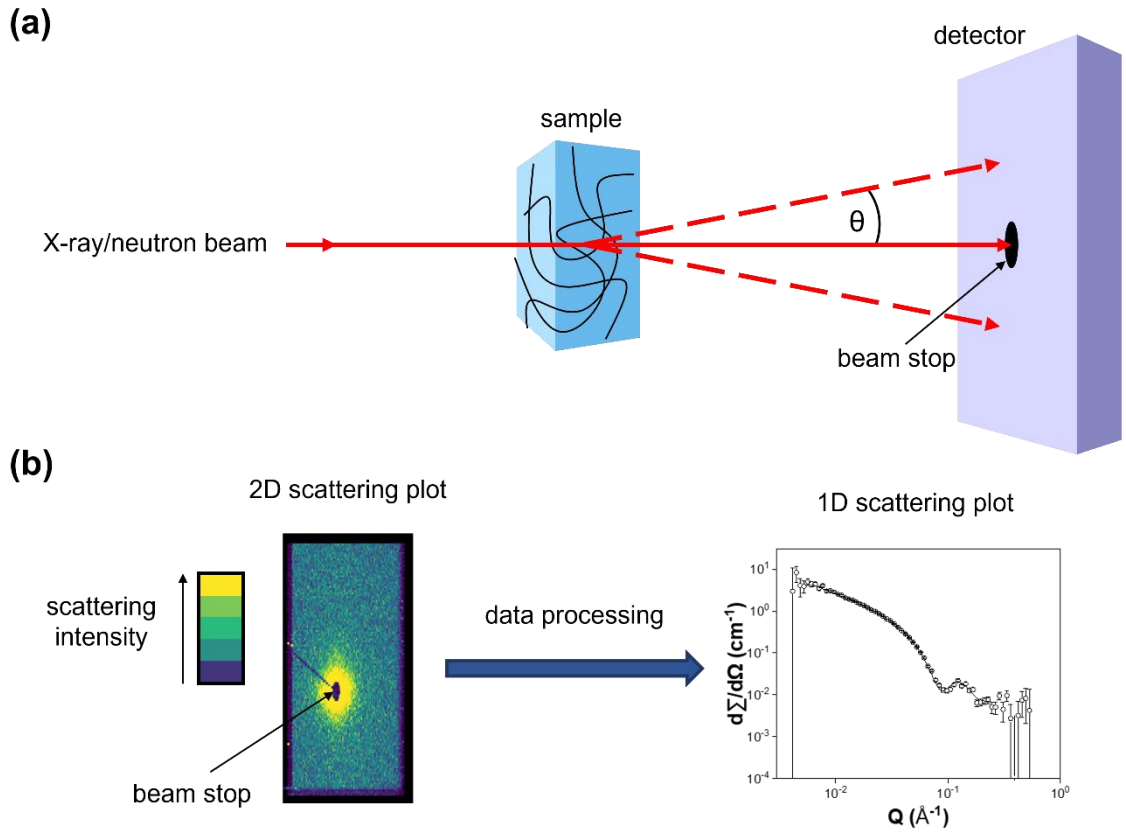

Figure 1.9. (a) Schematic showing the basic design of a small angle scattering experiment. (b) Schematic showing an example the two-dimensional scattering plot obtained from a small angle scattering experiment and the resulting one-dimensional plot. The one-dimensional plot is used to fit the data to standard models.

The scattering intensity of X-rays or neutrons scattered by the sample is measured as a function of the scattering vector, Q.[118] Scattering intensity is related to the difference in the scattering length density (SLD) between the scattering object and its solvent. For effective scattering to occur, there must be sufficient contrast between the scattering object and its solvent. For neutron scattering, contrast comes from differences in SLD. Samples for SANS are prepared in deuterated solvents in order to exploit the difference between the SLDs of hydrogen and deuterium to achieve good contrast and thereby high-quality scattering data.[118]

The scattering obtained is an average representation of the sample, meaning that the scattering profile will be a combination of the individual scattering patterns of the components within the sample.[118] The raw scattering pattern comprises the scattering from the self-assembled structures in the sample, solvent, sample holder and air. Background subtractions must first be performed to remove all scattering that does not originate from the sample. Data is first obtained as a two-dimensional scattering pattern which is then reduced to a one-dimensional plot of scattering intensity vs Q, the scattering vector (Figure 1.9b). The one-dimensional plot can then be fitted to a model in order to obtain information about

the structures present in the sample.[119, 120] Information can also be obtained from the two-dimensional scattering pattern e.g., anisotropy within the scattering patterns obtained from rheoSANS or rheoSAXS experiments (where small angle scattering is combined with rheology) shows that the sample is composed of long one-dimensional structures that can be aligned under shear.[121]

Small angle scattering experiments can be used to investigate whether self-sorting or co-assembly is taking place. If the system is self-sorting, structures that resemble each individual component will be captured from the scattering data.[63] If the system is undergoing co-assembly, the new structures may be different from those formed by either component alone.[122] It is also possible that one of the components will guide the assembly of the other, resulting in the formation of a single type of structure that resembles the dominant component.[63, 108]

Selectively deuterated scattering experiments, in which the deuterated form of one component is used, can confirm whether a system is undergoing self-sorting or co-assembly.[63] Use of the deuterated form of one of the components removes the contrast between the deuterated component and the deuterated solvent, making scattering from the deuterated component indistinguishable from the scattering from the solvent (Figure 1.10).[123] This renders the deuterated component effectively invisible, removing any scattering contribution from that component. It is therefore possible to image structures formed from each component individually. If self-sorting is taking place, the scattering data would resemble the non-deuterated component alone (Figure 1.10a). If co-assembly is taking place, the scattering data from the selectively deuterated sample will still resemble the original sample (Figure 1.10b). It should be noted that the overall scattering from selectively deuterated samples will be reduced as the scattering from one of the components has been silenced.

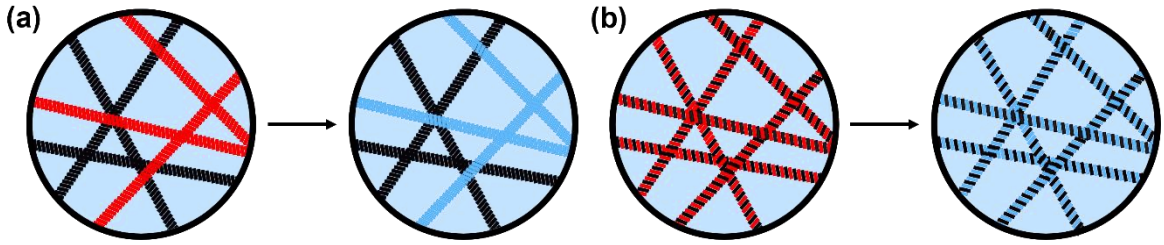

Figure 1.10. Schematic showing the effect of selective deuteration (indicated by the arrow) of the red component in a (a) self-sorted or (b) co-assembled multicomponent system.

The bulk mechanical properties of gels are measured using rheology.[124] The rheological properties of supramolecular gels are determined by the morphology of the primary fibres in

the gel network, the flexibility and mechanical strength of the primary fibres, the type and number of cross-links between primary fibres and the distribution of primary fibres in space.[8, 107] Rheological properties are often dependent on gelator concentration. Generally, as gelator concentration increases, mechanical strength also increases as more gelator means more primary fibres and thereby more solid-like behaviour.

It is usual to compare the behaviour of multicomponent systems to the behaviour of the components individually as single component systems as a means to determine whether self-sorting or co-assembly is taking place. It is important to consider the concentration of the single component systems to which the multicomponent system is going to be compared. If a multicomponent system contains two gelators of the same concentration, the total gelator concentration within the multicomponent system is double that of each individual component. It can therefore be misleading to compare multicomponent systems to single component systems composed of each component at the same concentration at which they are found in the multicomponent system. Instead, it may be beneficial to compare the multicomponent system to single component systems of the same total gelator concentration.

Gels are considered viscoelastic materials as they exhibit both flow and elastic behaviour.[126] During rheological measurements, the response of the gel to oscillatory stress is measured. The data output from these measurements are storage modulus (G′) and loss modulus (G″, Figure 1.11). G′ is a measure of the material's elastic response and represents the solid-like behaviour of the gel. G″ is a measure of the ability of the material to flow under stress and represents the liquid-like behaviour of the gel. For a material to be viscoelastic, G′ must be greater than G″: the energy stored by the material must be greater than the energy dissipated. The point at which G′ = G″ (sometimes referred to as the crossover point) is the point at which the material transitions from a viscoelastic solid to a liquid. The loss factor (tanδ) is defined as G″/G′ and is used as a measure of the elasticity of a gel.[125] For a gel to be considered a "true gel", tanδ should be less than 0.1. However, it is common for the tanδ value of supramolecular gels to be slightly greater than 0.1 owing to the non-covalent nature of the interactions that hold the gel network together.

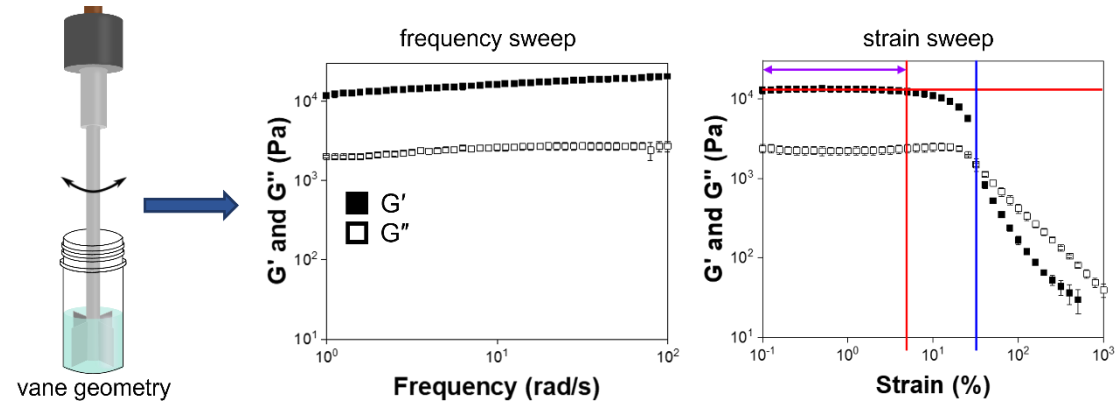

Figure 1.11. Schematic showing the vane geometry used to perform oscillatory rheology measurements and examples of the data obtained from frequency and strain sweeps. G′ is higher than G″ with nearly an order of magnitude between the two values. The frequency sweep shows the sample is relatively frequency independent, proving the sample is a gel. The strain sweep shows the critical strain (red) where the G′ value begins to deviate from linear and thereby the length of the LVR (purple). Strain sweeps also show the crossover point (blue) where G″ crosses over G′, signifying the sample has transitioned from a gel to a liquid.

Both self-sorting and co-assembly have been shown to increase the mechanical strength of supramolecular hydrogels. As previously discussed, preparation of a self-sorted system composed of enantiomeric mixtures resulted in increased mechanical properties compared to the corresponding single component systems owing to energetically favourable interactions between enantiomers at the gel network level.[97] Alternatively, by incorporating a component that increases the number of cross-links in the system, it is possible to enhance the properties of a co-assembled system by exploiting network level interactions.[126]

It is also possible that preparation of a multicomponent system will result in a reduction in the mechanical properties of the resulting gel compared to single component systems composed of the components individually. The new fibres formed on co-assembly may result in fewer or weaker entanglements in the gel network or the presence of a second component may disrupt the assembly of the first.[108, 127]

Strain sweeps are a rheological experiment commonly used to probe the mechanical properties of gels (Figure 1.11). These experiments measure G′ and G″ as the strain applied to the system is increased. While this allows us to measure the moduli values within the linear viscoelastic region (LVR), as with frequency sweeps, strain sweeps also allow us to probe the behaviour of the gel network as it breaks down.[107] The point at which the G′ value begins to deviate from linear signifies the end of the LVR and is sometimes referred to as

the critical strain value of the gel. It may be possible to observe the two individual networks present in self-sorted systems break down sequentially, as long as one network is sufficiently stronger than the other. If co-assembly has taken place, a new breakdown behaviour distinct to either component alone may be observed. For example, Che *et al*. showed that their multicomponent gel had G′ value almost 100 kPa greater than the sum of the G′ values recorded from gels formed from the individual components and a longer LVR than gels formed from each component individually.[128] This shows that the system is not self-sorting as the rheological behaviour of the multicomponent system is not simply a combination of the behaviour observed from the single component gels.

Nanoindentation is commonly used to test the mechanical properties of soft biological materials. Rather than measuring the bulk mechanical properties, as is the case with rheology, nanoindentation probes very small, specific areas of the sample.[129] During nanoindentation experiments, a probe of the desired geometry (e.g. spherical) is lowered onto the sample surface at a constant speed. The force required to indent the surface is measured, giving the data output as a force-distance curve. By fitting to an appropriate mathematical model, the Young's modulus of the hydrogel can be calculated.[129] Nanoindentation is used to probe the mechanical properties of gels with irregular shapes, such as supramolecular gel noodles.[78]

1.6 Multicomponent systems as a means for controlling the mechanical properties of low molecular weight hydrogels

It is difficult to design a LMWG with a particular application in mind as the ability of a given molecule to form a hydrogel and the properties of any resulting gels are hard to predict.[130] It is therefore important to design new methods for tuning the mechanical properties of well-studied LMWGs. Preparation of multicomponent systems is one such method.

Multicomponent systems with the ability to form supramolecular gels can be subdivided into different groups: gelator-gelator multicomponent systems, where both components have the ability to form gels independently; gelator-non gelator systems, where the non-gelling component is used to change some aspect of the resulting gel's properties and finally, systems where neither component can form a gel when alone, but together they self-assemble to form a gel (Figure 1.12). We will not discuss the final type of multicomponent system. In all cases, the two components may or may not be structurally similar. This thesis aims to

analyse specific examples of different types of multicomponent system. All the systems studied are based on a single well-known *N*-functionalised dipeptide-based LMWG: 2NapFF.

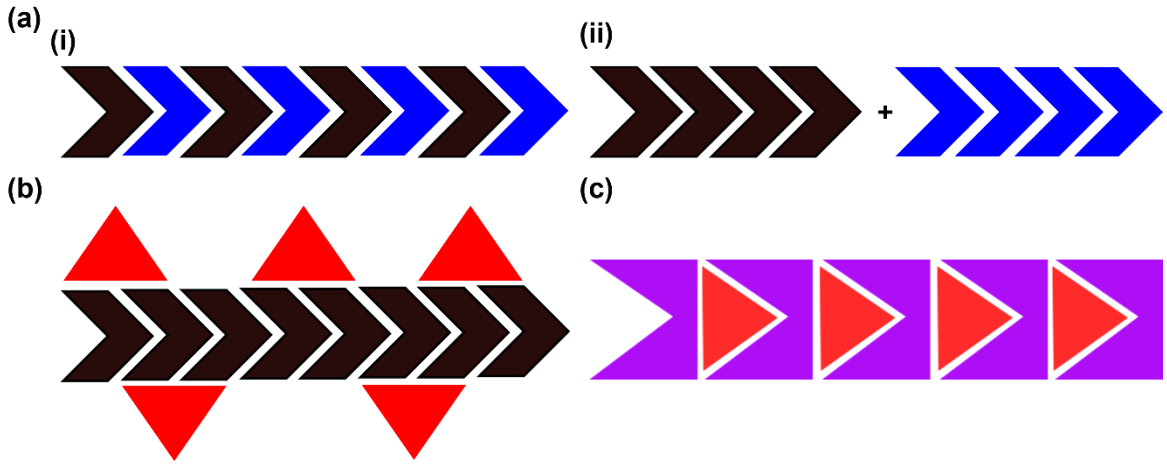

Figure 1.12. Schematic representations of the different types of multicomponent supramolecular systems. (a) Both components are gelators. Such systems can (i) co-assemble or (ii) self-sort. (b) Only one component is a gelator. (c) Neither component alone behaves as a gelator.

1.6.1 Gelator-non-gelator multicomponent systems

Non-gelling additives can be used to control the mechanical properties of supramolecular hydrogels and can be used to impart useful behaviours on the final gel. For example, a multicomponent system composed of pyrene-AA (Figure 1.13), a peptide-based LMWG, and Vancomycin, a glycopeptide antibiotic, resulted in the formation of hydrogels with a 106-fold increase in G′ value.[43] Here, Vancomycin acts as a cross-linker *via* its host-guest interactions with pyrene-AA and dimerisation with itself (Figure 1.13). CD data shows that the interaction between Vancomycin and pyrene-AA promotes π-π stacking of the pyrene groups of pyrene-AA. It was found that the binding of Vancomycin to 2NapAA cooperatively enhanced the self-association of Vancomycin.[43] This work shows that molecular recognition can be used to regulate the self-assembly of LMWGs and thereby control the material properties of the resulting gels. The authors suggest that an effective physical cross-linker for LMWGs must have high affinity for the LMWG and a high tendency for self-association.[43] The use of a physical cross-linker is desirable over a chemical cross-linker as it conserves the non-covalent interactions between the molecules in the gel network. This preserves the biocompatibility and biodegradability associated with supramolecular hydrogels that makes them attractive for biological applications.[43]

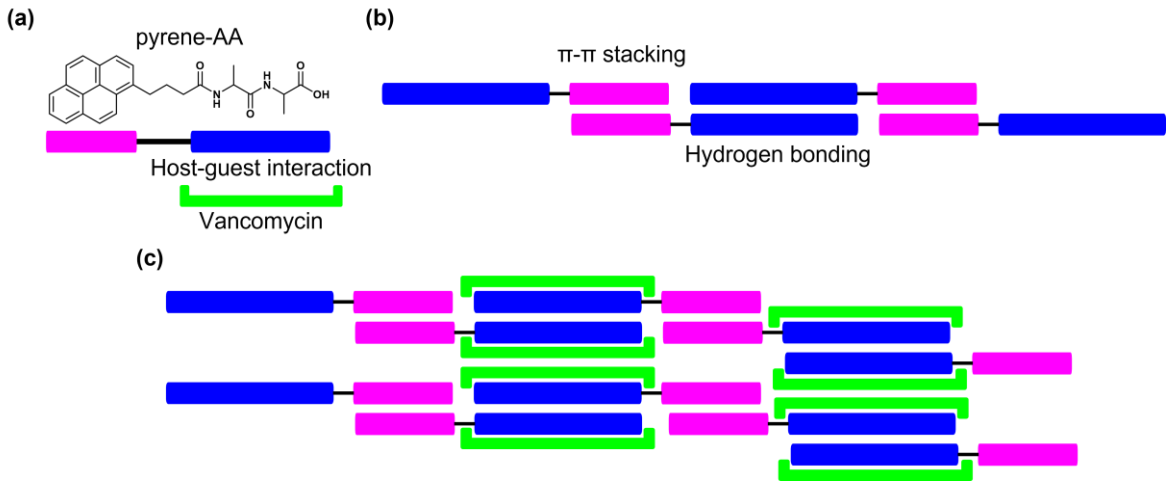

Figure 1.13. Schematics showing (a) the structure of LMWG pyrene-AA exemplifying its host-guest interaction with antibiotic Vancomycin, (b) the self-assembly of pyrene-AA *via* π-π stacking and hydrogen bonding interactions and (c) how physical cross-linking between Vancomycin molecules cooperatively enhances self-assembly of the system.

Non-gelling additives can be used to control a variety of gel properties, e.g. thermal and mechanical properties, stability and functionality. It is also possible to use the ratio of components to tailor the mechanical properties of these systems.[131, 132] Many studies have investigated the effect of surfactants on the assembly of LMWGs.[133-136] Co-assembly with surfactants can allow surface functionalisation of the fibres formed during self-assembly, without disrupting the self-assembled structures formed. Such co-assembly avoids covalent modification of LMWGs which can completely change the structure and properties of the resulting gels.

Abul-Haija *et al*. studied gelator/surfactant peptide-assembly systems composed of the phosphatase responsive Fmoc-FY*p* pre-gelator and a variety of surfactant-like peptide derivatives also functionalised with an Fmoc group at the *N*-terminus.[133] Gelation was triggered by enzymatic dephosphorylation of Fmoc-FY*p* to Fmoc-FY which then self-assembles to form a 3D gel network.[137] The authors found that the Fmoc-FY*p*/Fmoc-X multicomponent systems transform from micellar structures to fibres on dephosphorylation of Fmoc-FY*p*, with the X groups functionalised on the surface of the fibres.[133] Use of Fmoc as the *N*-terminal capping group in both components allowed stacking of the Fmoc rings from both components while the carboxylate groups at the *C*-terminus are displayed on the surface. Such *N*-terminal group directed co-assembly has been reported previously.[138] Use of an acetyl group in place of the Fmoc group of the surfactants significantly reduced the degree of co-assembly.[133] Further analysis highlighted the importance of the chemical nature of the two components in controlling co-assembly. The Fmoc-FY/Fmoc-S gelator/surfactant

system formed a core-shell structure with the S head group of the surfactant exposed on the surface. The Fmoc-FY/Fmoc-T and Fmoc-FY/Fmoc-RGD systems showed evidence of intercalation of the surfactants into the Fmoc-FY self-assembled fibres, suggesting a more disruptive form of co-assembly occurred in these systems.[133]

The Ulijn group continued this study by preparing a further series of *N*-functionalised dipeptide/*N*-functionalised surfactant systems using both Fmoc and pyrene as *N*-terminal groups.[136] Through these systems they were able to exemplify cooperative, disruptive, and orthogonal co-assembly modes. They were also able to postulate a set of design rules for determining the mode of assembly likely to be adopted by a particular multicomponent system. How two components assemble in the presence of one another is thought to primarily be determined by how similar both the *N*-terminal group and the peptide chain are to each other and thereby how effectively they can form favourable interactions with each other.[136] The systems studied contained either both LMWGs (Fmoc-YL and pyrene-YL), both surfactants (Fmoc-S and pyrene-S) or one of the two LMWGs and one of two surfactants. The authors used a wide variety of techniques to characterise these systems.

They found that when the *N*-terminal group of the surfactant did not match the *N*-terminal group of the LMWG, the system underwent orthogonal co-assembly.[136] The LMWGs formed the same supramolecular structures as when alone and the surfactants coated the surfaces of these structures. This was evidenced by relatively unchanged CD spectra when comparing the multicomponent systems to the LMWGs alone. FTIR analysis further proved that the pyrene and fluorene rings are not stacking in a cooperative manner. The systems composed of either the two LMWGs or the two surfactants underwent cooperative co-assembly. Such co-assembly resulted in enhancement of CD signals, confirming that two interpenetrating networks are not being formed by these systems. This was most likely due to fact that the amino acid residues present in both components matched each other, resulting in formation of β-sheets that complement one another.[136] Fluorescence emission data suggest extensive intercalation of the Fmoc and pyrene groups which further proves formation of a mixed cooperative structure over two self-sorted, interpenetrating networks. Interestingly, the pyrene-YL/pyrene-S and Fmoc-YL/Fmoc-S systems underwent disruptive co-assembly. This was observed by reduction in intensity of CD signals. This suggests that the presence of a surfactant bearing the same *N*-terminal group as the gelator disrupts self-assembly.[136]

The resulting self-assembled structures were imaged using AFM.[136] Cooperative co-assembly resulted in formation of a dense fibrous network, showing that when there is

sufficient commonality between two components such that they follow similar modes of assembly, the two components are able to accommodate the presence of each other in any resulting supramolecular structures. Orthogonal co-assembly also resulted in the formation of dense fibrous networks.[136] The fibres formed by the Fmoc-YL/pyrene-S system were thinner than those formed by the Fmoc-YL single component system, showing that the surfactant has an effect on the macroscale level of assembly. The pyrene-YL/Fmoc-S system did not show any changes in fibre morphology compared to pyrene-YL alone.[136] Disruptive co-assembly of the pyrene-YL/pyrene-S system resulted in formation of intermittent fibres amongst disordered regions reminiscent of pyrene-S assembly. The Fmoc-YL/Fmoc-S system formed fibres with a tendency to arrange into spiral structures, suggesting that Fmoc-S disrupts the one-dimensional structures formed by Fmoc-YL. Intercalation of the surfactants *via* the common *N*-terminal group is therefore inhibiting the self-assembly of these systems.[136]

Finally, the authors investigated the gelation ability and mechanical properties of the systems using rheology.[136] Fmoc-YL and pyrene-YL both form hydrogels at physiological pH. Orthogonal co-assembly between pyrene-YL and Fmoc-S did not significantly alter the rheological properties of the gel formed. Co-assembly between Fmoc-YL and pyrene-S enhanced the mechanical properties of the multicomponent gel compared to the Fmoc-YL single component gel. This reflects the apparent changes to the morphology of the structures seen by AFM. The authors suggest that robust co-assembly is facilitated when both *N*-terminal and peptide chain components are sufficiently different such that segregation between components can occur.[136] This prevents mismatch occurring between β-sheet type hydrogen bonding and between π-π stacking interactions.[136] This mismatch is likely the cause of disruptive co-assembly in the LMWG/surfactant systems that share the same *N*-terminal capping group.

The presence of pyrene-S in the pyrene-YL/pyrene-S system inhibited the ability of pyrene-YL to form hydrogels. The requirement for a lower pH to form a hydrogel implies that a greater degree of protonation and consequently increase connectivity between fibres is needed for gelation to occur. Intercalation of pyrene-S, which is unable to form β-sheets, into the pyrene-YL structures inhibits assembly. The presence of Fmoc-S significantly reduced the mechanical properties of the Fmoc-YL/Fmoc-S gels. As with the pyrene-YL/pyrene-S system, stacking between the fluorene rings of each component will result in YL β-sheet structure being distorted by the presence of S residues.[136] The authors concluded that cooperative co-assembly occurs between molecules that share the propensity to adopt a

β-sheet type mode of hydrogen bonding. Disruptive co-assembly occurred between components that share the same *N*-terminal aromatic group due to substantial intercalation of the surfactant disrupting β-sheet formation. Hence, both the *N*-terminal group and the peptide chain must be sufficiently different for orthogonal co-assembly to occur.[136]

Gelator-surfactant systems have also been observed to undergo self-sorting. Self-sorting of LMWGs and micelle-forming surfactants or phospholipids leads to the formation of gel networks with micelles or vesicles entrapped within the gel network.[134, 139] Interpenetrating networks are desirable as they allow mixing of two or more otherwise incompatible properties or functions.[114] It is also possible that synergistic effects might arise from the simultaneous assembly of two networks.

Hydrogels formed from the 1,3,5-triamide *cis*,*cis*-cyclohexane-based LMWG HG1 (Figure 1.14a) consist of an entangled network of long, thin, stiff fibres stabilised by mechanical contacts between fibres.[114] The surfactant cetyltrimethylammonium tosylate (CTAT) forms spherical micelles at concentrations above its critical micelle concentration (Figure 1.14b). As CTAT concentration increases, the spheres transform into cylindrical micelles which entangle to from a highly viscous solution (Figure 1.14). Cylindrical micellar networks are known to be highly dynamic and are stabilised by specific interactions or junction zones between the cylindrical micelles.[114]

To prepare homogenous LMWG/surfactant gels, HG1 and CTAT were dissolved together in water by heating the sample to temperatures greater than the gel-sol transition temperature of HG1, then cooled back down to room temperature.[114] CryoTEM of the gels clearly shows the presence of fibres reminiscent of those formed by both HG1 and CTAT alone. Both types of fibre were homogenously distributed throughout the sample, each forming their own network. These observations suggest that HG1 and CTAT undergo independent self-assembly.[114] Further analyses showed that the presence of self-assembled HG1 fibres did not significantly affect CTAT assembly. However, the presence of CTAT at low concentrations led to significant destabilisation of the HG1 gel network, which was observed as a reduction in gel-sol transition temperature. Increasing CTAT concentration resulted in the gel-sol transition temperature returning to its original value. The authors suggest that the presence of CTAT at low concentrations favours end-capping of HG1 fibres, reducing HG1 fibre length and preventing formation of a strong, entangled gel network (Figure 1.14c). As more entangled micelles are formed at higher CTAT concentrations, these may act to mechanically

support the HG1 network, resulting in an increase in gel-sol transition temperature as CTAT concentration continues to increase (Figure 1.14c).[114]

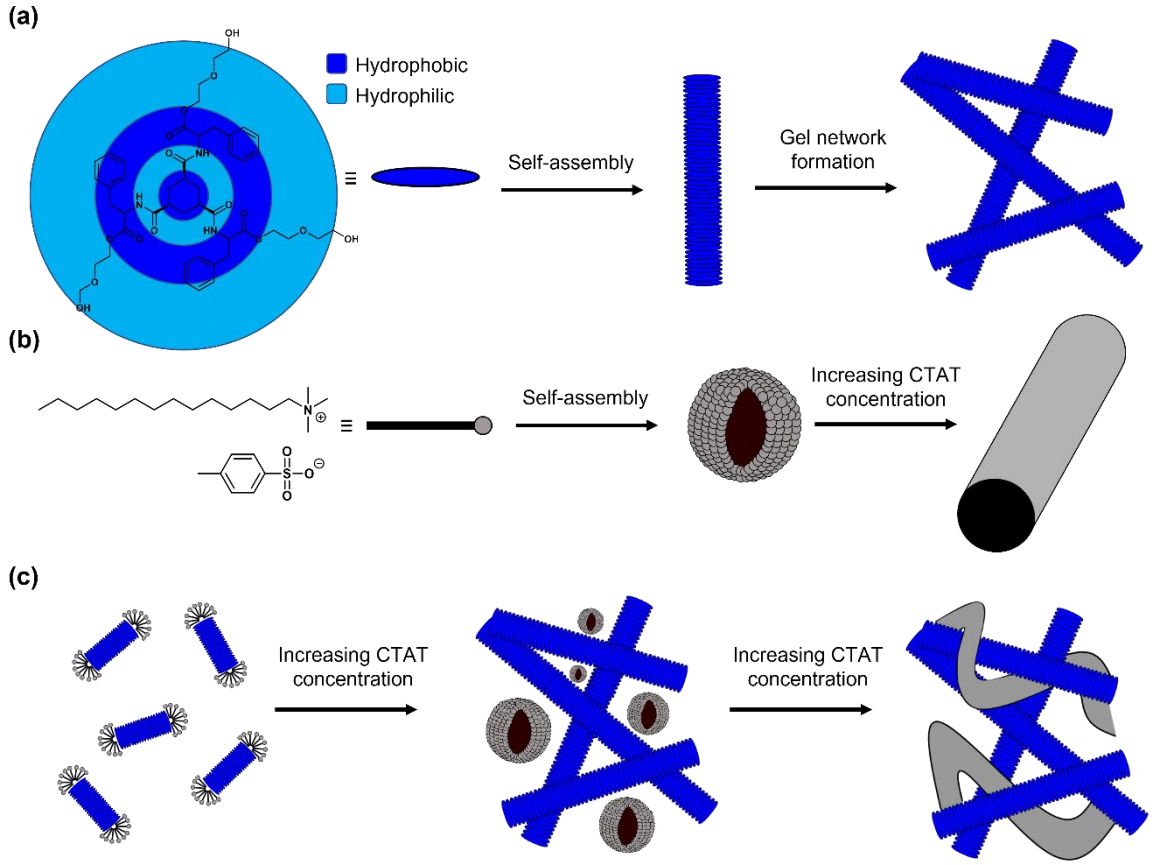

Figure 1.14 (a) The chemical structure of the LMWG HG1 and a schematic showing its hierarchical self-assembly in water, (b) the chemical structure of the surfactant CTAT and a schematic showing its self-assembly pathway in water with increasing CTAT concentration and (c) a schematic showing the self-sorted assembly of HG1 and CTAT with increasing CTAT concentration.

Additives other than surfactants e.g., polymers can be used to stabilise gels.[131, 140] The Adams group have investigated the effect of dextran, a highly water-soluble polysaccharide, on the properties of hydrogels composed of the peptide-based LMWGs Br2NapAV and FmocFF.[141, 142] Preparation of multicomponent hydrogels composed of a peptide-based LMWG mixed with large concentrations of a non-gelling, biocompatible biopolymer allows controllable modification of the material properties of the resulting hydrogels.[141] To allow modification of gel properties, dextran was added to micellar dispersions of the dipeptides pre-gelation. Previous work has shown that incorporation of gelling biopolymers, such as agarose, greatly improves the hydrogels response to fracture stress.[143] Unlike agarose which spontaneously forms hydrogels, dextran requires chemical cross-linking in order to behave as a hydrogelator. The presence of dextran resulted in a decreased rate of pH reduction, and

thereby a significantly shorter gelation time. This could be tuned by changing either the molecular weight of or the mass of dextran used.[141]

The rheological properties of the hydrogels could also be tuned by varying the dextran concentration. As dextran concentration increased, G′ decreased and G″ increased, showing that the gels become more viscous in nature with increasing dextran concentration. While dextran reduced the elasticity of the hydrogels, the crossover point of the gels remained the same, showing that the presence of dextran does not affect the gels resistance to strain, regardless of the molecular weight of the dextran added.[141] The authors suggest that the dextran does not interact specifically with the LMWG. Instead, the increase in viscosity caused by the presence of dextran, as well as the dextran molecules acting as a physical barrier, reduces the diffusion rates of LMWG molecules and the self-assembled fibres that they form. The fibres are thinner in the presence of dextran, suggesting that there is less lateral association between fibres, perhaps owing to lower diffusion rates. The authors also note that many dextrans have high radii of gyration, which will physically force the self-assembled gel network to have larger pores which will reduce the mechanical properties of the gels.[141]

The LMWG/dextran multicomponent hydrogels also showed interesting thermal behaviours compared to the LMWG single component hydrogels. When the LMWG hydrogels are heated to 50 °C, both G′ and G″ decrease. On cooling, G′ and G″ increase again but do not reach their original values. As the gels are subjected to further heat-cool cycles, the moduli values continue to decrease and increase in a reproducible manner. When the LMWG/dextran multicomponent hydrogels are heated to 50 °C, both G′ and G″ increased. Cooling the hydrogels back to room temperature results in a further increase in both moduli.[141] This provides a further method of tuning the properties of these hydrogels.

The He group performed a similar study where they combined FmocFF (a peptide-based LMWG) with konjac glucomannan (another water-soluble polysaccharide).[144] They found that the multicomponent hydrogels had higher stability and mechanical strength than single component hydrogels composed of the FmocFF alone. CD and Fourier transform infrared spectroscopy showed that the presence of konjac glucomannan did not significantly alter the molecular arrangement of self-assembled FmocFF. The authors propose that the large size of konjac glucomannan prevents it from being able to participate in the molecular self-assembly of FmocFF, thereby preventing co-assembly.

SEM analysis showed that FmocFF and konjac glucomannan self-sort to form two independent interpenetrating gel networks. The authors compare this structure to reinforced concrete (Figure 1.15), where steel wires (the konjac glucomannan fibres) are embedded in cement (the LMWG network).[144] The authors also noticed helical bundles formed from fibres twisted around each other. Further analysis led to the conclusions that the presence of konjac glucomannan during FmocFF self-assembly results in more crowded environments around FmocFF assembly sites as well as a large decrease in FmocFF diffusion rate due to the high viscosity of the environment. These conditions may lead to the reduced FmocFF assembly rate and decreased diameters of the FmocFF nanofibers compared to single component assembly.[144] The abundance of OH groups in konjac glucomannan may also increase the stability of the multicomponent gel by enhancing the hydrogen bonding in the gel network. These properties were shown to be useful for controlled release of the hydrophobic drug docetaxel from the multicomponent gel by varying the concentration and molecular weight of the konjac glucomannan or the aging time of the gel.[144]

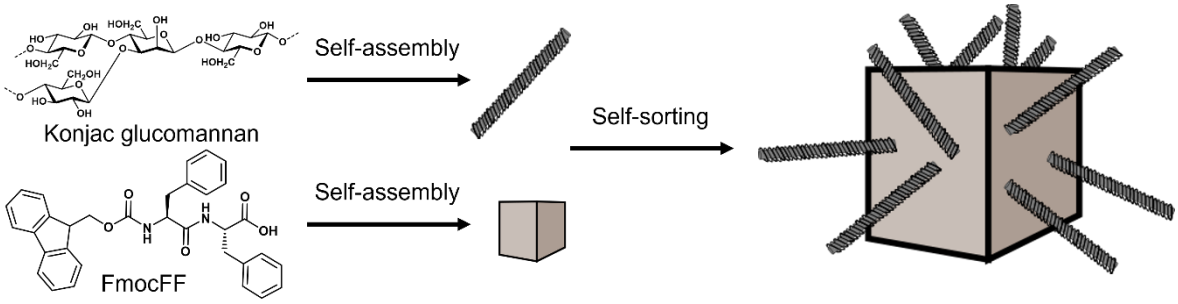

Figure 1.15. Schematic showing the chemical structures of the polysaccharide konjac glucomannan and the LMWG FmocFF and how they self-sort to form a structurally reinforced material.

The inclusion of cross-linking agents during preparation of supramolecular systems can also be considered a form of multicomponent system. Many studies have shown the possibility of changing the mechanical properties of supramolecular hydrogels *via* chemical cross-linking.[29, 30, 145-147] Chemical cross-linking between or within fibres in the gel network results in increased stiffness and sometimes strength of the bulk gel. Inclusion of cross-linkable groups, such as the amine group on K and the phenol group on Y, during gelator design can allow controlled enhancement of mechanical properties.[29, 30] The concentration of cross-linking agent included in the system can be used to modulate the increase in mechanical properties.[147]

Incorporation of a suitable cross-linking agent into a gelator-gelator multicomponent system can be used to form covalent interactions between two different components bearing

different cross-linkable groups.[146, 147] Panja *et al*. have shown that such post-gelation cross-linking increases the solid-like behaviour of the systems without changing the microstructures formed by self-assembly of the components.[147] This type of cross-linking relies on intimate co-assembly of the two different components. Panja *et al*. have also shown that it is possible to perform selective cross-linking between molecules of a single component as well as between molecules of the two different components within a multicomponent system by careful choice of cross-linking agents.[146] This allows access to different mechanical properties depending on the route of chemical cross-linking selected.

1.6.2 Gelator-gelator multicomponent systems

Multigelator systems can be prepared using two or more gelators with similar or different chemical structures. Each component in a multigelator system has the potential to bestow different properties on the resulting gel. For example, inclusion of a polymeric gelator in a supramolecular system allows formation of gels with soft, deformable regions composed mainly of the LMWG and more mechanically robust regions composed of the cross-linked polymer.[140, 149, 150] Such materials can be thought of as multidomain gels.[110] The Smith group designed a multicomponent system composed of a pH responsive LMWG and a photoinducible polymer gelator.[151] Use of a mask during photoirradiation allowed spatial control over formation of different domains in the resulting gel: one domain consisted of the LMWG while the photopatterned domain contained both the LMWG and the polymer gelator.[151] Diffusion rates of small molecules varied in the two different domains, making this system useful for controlled drug release.[151]

Hybrid hydrogels composed of the polymeric gelator agarose and a LMWG have significantly greater mechanical strength than hydrogels formed from the same LMWG alone.[143] Compared to the LMWG, the hybrid hydrogels were better suited for long-term, controlled drug release. The mechanical properties of these gels could be tuned by changing the LMWG chosen to form the hybrid hydrogel.[143]

Mixing of two LMWGs provides a system with multiple levels of assembly. Each level can be used to tune the properties of the system, providing a vast range of avenues for controlling the outcome of assembly. However, this also means there are multiple levels that must be considered when designing these systems. This includes how the components pack at the molecular level, characterisation of the resulting secondary structures, and the interactions between the secondary structures within the final gel network. Arguably the most important

question is how do all these factors influence the mechanical properties of the final gel formed?

Two-gelator systems are often described as either self-sorted or co-assembled. Self-sorting is where the two gelators do not interact during molecular assembly and form secondary structures entirely independently of one another (Figure 1.16a). Co-assembly is where the two gelators assemble together into the same secondary structures. While rarely discussed, it is likely that most systems exhibit behaviour somewhere in between these two extremes. Co-assembly can be further categorised as being co-operative, orthogonal or disruptive. Cooperative co-assembly results in secondary structures composed of an intimate mixture of the two components (Figure 1.16bi). Such co-assembly can be ordered, usually through specific design of the components, or random. Orthogonal co-assembly is used to describe components that assemble within the same secondary structures but form distinct structural components within the structures and only interact through specific groups (Figure 1.16bii). Disruptive co-assembly occurs when interaction between the two components inhibits their ability to form supramolecular structures (Figure 1.16biii).[108]

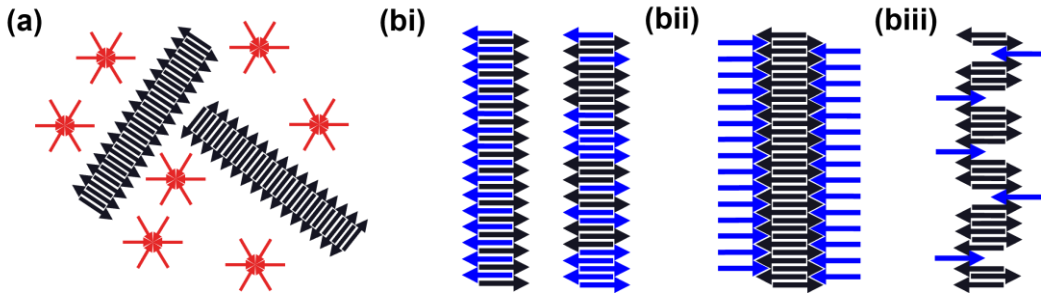

Figure 1.16. Schematic representations of (a) self-sorting and (b) co-assembly. Co-assembly can be further categorised as being (i) cooperative, (ii) orthogonal, or (iii) disruptive.

Self-sorting can be favoured over co-assembly through the preparation of systems composed of structurally dissimilar gelators. The differences in interaction modes between the two gelators can then be exploited to allow one-pot self-sorting.[105, 139, 152] Self-sorting of two LMWGs that form different types of nanofibers allows the properties from each component to be imparted upon the system individually with minimal interference. For example, Shigemitsu *et al*. prepared a self-sorted double network hydrogel composed of a peptide-based LMWG and a lipid-based LMWG.[105] Formation of two distinct supramolecular nanofibers allowed bidirectional control over the rheological properties of the system as well as the release rate of molecules encapsulated in the gel network by using external stimuli specific to each component.[105] The use of two different types of gelator with very different interaction modes allows facile formation of entirely segregated, self-sorted networks. The

formation of self-sorted systems becomes more complicated when using two LMWGs of the same type. For example, two peptide-based LMWGs that by default utilise the same non-covalent interactions that can only be varied slightly through structural design.

Okesola *et al*. designed a two-gelator system from a peptide amphiphile (PA-E3) and a sugar-based gelator (DBS-COOH, Figure 1.17). They used a range of techniques, including CD spectroscopy, TEM, AFM and SANS to confirm the two components were undergoing self-sorting.[113] AFM imaging showed that despite undergoing self-sorted assembly, the structures formed in the multicomponent system were different to those observed in the single component systems. The density of the nanofiber network also appeared to increase with increasing sugar-based LMWG concentration. The authors expect that this is due to entanglements between the structures formed by the two components.[113] SANS data showed that the peptide amphiphile formed the same secondary structures in the multicomponent system as it did alone, with some slight perturbation from the presence of the sugar-based component.[113]

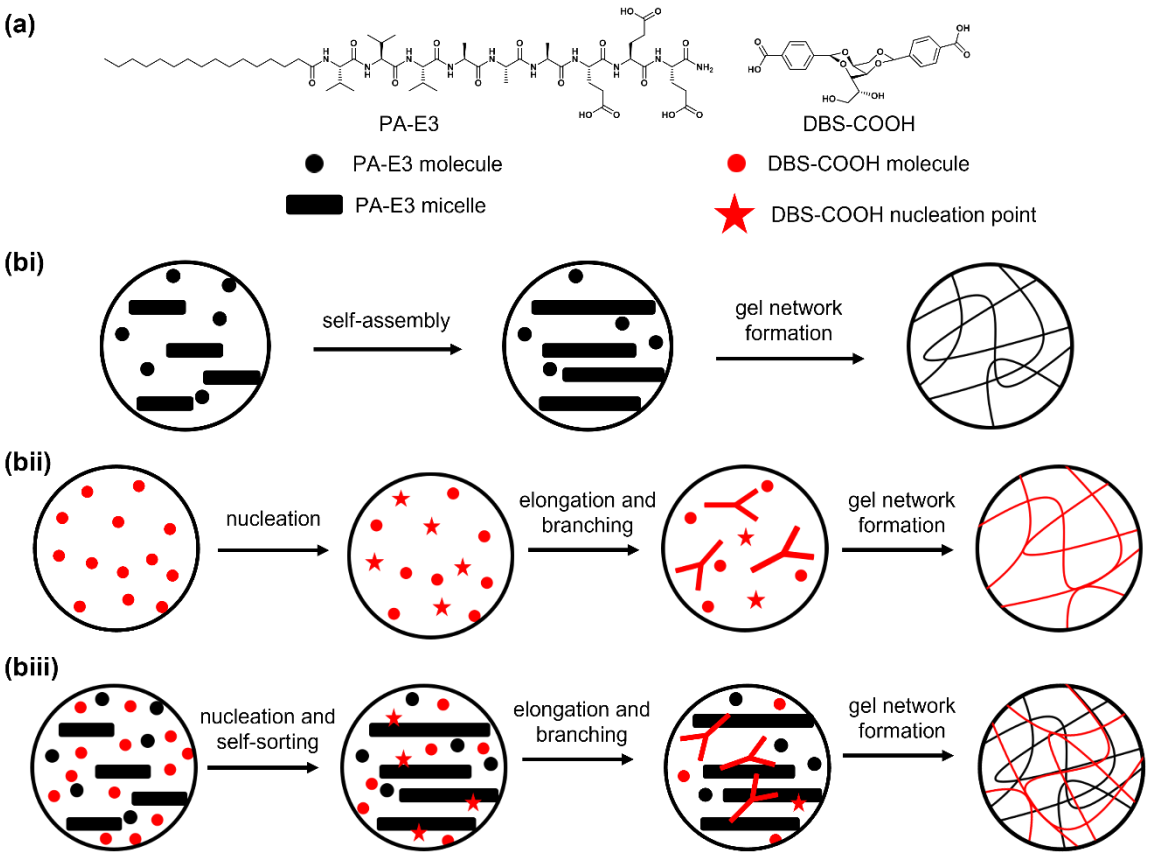

Figure 1.17. (a) Chemical structures of the peptide amphiphile-based LMWG PA-E3 and the sugar-based LMWG DBS-COOH in their uncharged states. (b) Schematics showing the sequential assembly of (i) PA-E3 and (ii) DBS-COOH alone and (iii) together, resulting in a self-sorted system.

The authors highlight the importance of assembly kinetics on the properties of the final system. Since the peptide amphiphile assembles first, it is assembling in the presence of the sugar-based component, allowing the sugar-based component to affect its assembly.[113] Dynamic oscillatory rheology experiments used to monitor self-assembly with time showed that the sugar-based component followed a different self-assembly mechanism when in multicomponent system. Since the peptide amphiphile assembles first, the structures formed by the peptide amphiphile are expected to act as nucleation sites (Figure 1.17). This is based on non-classical nucleation theory, where nucleation and growth are much faster in a heterogenous system that contains nuclei than in the system's homogenous equivalent.[153, 154] The sugar-based component therefore undergoes faster self-assembly in the multicomponent system than when alone due to the presence of peptide amphiphile structures which act as nucleation sites for both the sugar-based component and further peptide amphiphile assembly.[154]

The G′ values recorded for the multicomponent systems increased linearly with increasing percentage of the sugar-based component. This indicates that multicomponent assembly has a synergistic effect on gel properties.[154] Results from dynamic time-sweep experiments showed that the multicomponent gels exhibited both enhanced stiffness due to the sugar-based component and self-healing behaviour comparable to the peptide amphiphile alone. This demonstrates how two distinct gelators can cooperate to form a multicomponent gel with desirable properties that originate from each component.[154]

As previously discussed, techniques such as CD spectroscopy can be used to confirm self-sorting on the molecular level. In such cases, the CD spectrum obtained from the multicomponent system will be the sum of the spectra from the individual gelators.[106] However, it is important to note that this does not provide any information regarding interactions at longer length scales. It is of great importance that multicomponent assembly is assessed using a range of techniques that probe assembly at every stage of hierarchical assembly.

The Smith group have shown it is possible to confidently prove that self-sorting is taking place.[155, 156] They used NMR spectroscopy to probe the mobility of each component on the molecular scale, SEM to visualise the nanoscale structures formed during assembly and differential scanning calorimetry to show that each gelator provides its own thermal fingerprint to the thermal response of the bulk gel, thus showing that each self-sorted network breaks down at a different temperature.[155]

The Adams group have also shown it is possible to confirm self-sorting by employing a range of techniques that probe the system at a range of hierarchical levels.[63] Again, NMR spectroscopy can be used to show the sequential assembly of each component *via* the disappearance of peaks in the NMR spectra corresponding to each component over time. TEM and SANS were used to show the presence of two distinct populations of self-assembled fibres with morphologies resembling one of each of the two components. Finally, fibre X-ray diffraction was used to definitively prove self-sorting. The fibre X-ray diffraction pattern of the two-component system matched an overlay of the scattering patterns expected from the single component gels of each component.[63]

Challenges in the spatial control of these systems can be overcome by including a photoresponsive component which can be selectively irradiated using a mask.[59, 157] There is potential for electrochemical methods to provide spatial control over the properties of multicomponent systems.[158] Electrochemistry can also be used to induce self-sorting rather than co-assembly in structurally similar multigelator systems.[158] Similarly, a slow pH change afforded by use of GdL as a trigger allows sequential assembly of gelators with sufficiently different pK_a values.[63] Gelation temperature can also be used to promote self-sorting.[156]

As previously noted, hydrogen bonding plays an important role in the self-assembly of peptide-based LMWGs.[156, 158] Work by the Smith group suggests that differences in hydrogen bonding functionality can be exploited to promote self-sorting.[156] When two LMWGs bear the same hydrogen bonding motifs, e.g. both have amide bonds between the *N*-terminal capping group and the peptide chain, the two gelators will interact equally well with each other as they do with themselves, resulting in co-assembly.[156] When the two gelators have different hydrogen bonding motifs, e.g. a carbamate and an amide, amide-amide interactions are more favourable than carbamate-amide interactions,[160] creating a driving force for self-sorting. While hydrogen bonding interactions will undoubtedly play a role in determining the mode of multicomponent assembly, electronic and steric effects controlled by the peptide side chains will also affect whether self-sorting or co-assembly is more favourable.[156]

While self-recognition motifs appear to be an effective design rule, systems based on other design rules have been developed. Addition of a halogen to a benzyl group of one of the gelators affects π-π stacking interactions between the assembled gelators.[161] Choice and position of halogen can affect the mechanical properties of the resulting multicomponent gel. Co-assembly was favoured due to offset π-π interactions between halogenated

substituents on the benzyl ring of one gelator and the non-substituted benzyl of the second gelator.[161] Further work showed interactions dictating co-assembly are selective and complimentary. Hydrophobic interactions are not sufficient to promote co-assembly. Based on this work, complimentary π-π interactions via substitution on one of the benzyl rings is a design rule.[161]

It is possible to specifically design systems composed of two structurally similar gelators so that they undergo co-assembly. For example, the Nilsson group prepared a two-component system comprise of Fmoc-Phe and Fmoc-F_5-Phe.[161] They expected that since the side chains of these two components contain complimentary quadrupole electronics, they would prefer to co-assemble than to self-sort. However, molecular modelling showed that more subtle complimentary π-π interactions were responsible for driving co-assembly, rather than face-to-face stacking of complimentary quadrupoles.[161]

The co-assembly of two LMWGs can also result in the formation of new structures. Li *et al*. showed that mixing two short peptide-based LMWGs with different aromatic capping groups resulted in formation of hydrogels with significantly enhanced mechanical properties compared to the single component systems.[162] Both phenothiazine-GFFY and naphthalene-GFFY independently form hydrogels. Preparation of a two-component system (0.5 wt%:0.5 wt%) of both of these LMWGs resulted in a hydrogel with G′ value at least ten times greater than either of the single component hydrogels.[162] Such enhanced stiffness can originate from the formation of a double network due to self-sorting of the two LMWGs or from the formation of a more rigid network due to co-assembly of the two LMWGs. As only one population of fibres with different morphology to either component alone was observed, the authors expect that co-assembly is taking place between the two components. This conclusion was further confirmed by fluorescence emission and CD spectroscopy.[162]

Co-assembly can be designed to occur in a specific manner. For example, when one LMWG in the system acts as a donor while the second acts as an acceptor will result in alternating co-assembly of the two components within the same one-dimension structures.[163, 164]

External variables, such as temperature, component concentration and stoichiometry and pH can all effect the outcome of multigelator assembly.[165] The assembly of multigelator systems is further complicated by behaviour pre-gelation. Not all systems will start as two fully dissolved gelator molecules in solution. In most of the cases studied in this thesis, one if not both of the components start off as micellar aggregates suspended in water before gelation. We expect that the structures formed before gelation will play a role in the gelation process.

It is therefore important to characterise these assemblies in addition to the final structures formed within the gel network.

1.7 Gels as a medium for crystallisation

Gels can be used to control the nucleation and growth of crystals. Polymeric gels such as gelatin, agarose and silica are regularly used as media for crystal formation.[166-170] However, supramolecular gels can also be used. For example, Hartgerink *et al*. used a peptide amphiphile based LMWG to direct the crystallisation of hydroxyapatite such that they are aligned along the axes of the self-assembled fibres.[171] To be suitable as a medium for crystal formation, the self-assembled fibres formed by the peptide amphiphile must be robust and must contain functionalities that promote nucleation of the chosen crystal.[171] To meet these criteria, the authors designed the peptide sequence to contain four consecutive cysteine residues to allow covalent capture *via* the formation of disulfide bonds between adjacent molecules upon oxidation.[172] The reversible nature of disulfide bonds allows for self-correction.[171] In addition, the authors incorporated a phosphoserine residue into the peptide sequence.[171] This allows the self-assembled fibres to display a highly phosphorylated surface since phosphorylated proteins are known to play an important role in hydroxyapatite crystallisation. Growth of the hydroxyapatite crystals with their *c* axes oriented along the long axes of the nanofibers could be of interest in the design of materials for use in mineralised tissue repair.[171]

The preparation of crystals within a gel can therefore be an effective method of modifying crystal morphology that cannot be achieved using conventional solution phase crystal growth.[166] The increased viscosity of the gel medium is thought to minimise random collisions between crystallising small molecules which in turn reduced nucleation rates.[166, 167, 173] Suppression of convection currents also ensures that the crystallising compound is only supplied to the crystal surface *via* diffusion.[166] These attributes reduce crystal growth rate, resulting in the formation of large crystals with minimal internal defects.[167, 173, 174] For example, the use of silica gel as medium for protein crystal formation increases size and stability of crystals.[170]

Jayabhaven *et al*. used a series of bisurea-based LMWGs with complimentary functional groups similar to the antibiotic Metronidazole to investigate the effect of mimetic supramolecular gels on the crystallisation of the drug molecules.[175] The urea motif was selected as it is known to form α-tapes that further assemble into fibrils.[176] These fibrils can

align the drug-derived functional groups as a locally ordered array on the surface of the gel fibres (Figure 1.18a). This arrangement results in a fibrous surface that chemically matches the crystallisation substrate, creating the possibility for epitaxial crystal growth.[177, 178] This epitaxial growth resulting from favourable interactions between the crystallisation substrate, Metronidazole, and the gel fibres results in crystals with a needle-shape morphology were obtained from the mimetic gels (Figure 1.18b).[175] In comparison, crystals formed from non-mimetic gels resulted in plate-shaped crystals that clumped together in a herringbone pattern (Figure 1.18b), similar to that observed in crystals formed in the solution phase.[175] This work highlights the potential to achieve new crystal morphologies on crystallisation in specifically designed gels. This study builds on previous work by the Steed group showing that structural similarity between the crystallisation substrate and the LMWG plays a role in gel-phase crystallisation.[179, 180] Gels prepared from drug-mimicking LMWGs have also been used to prevent concomitant crystallisation, thus preventing crystallisation of non-active or dangerous forms of a drug.[181]

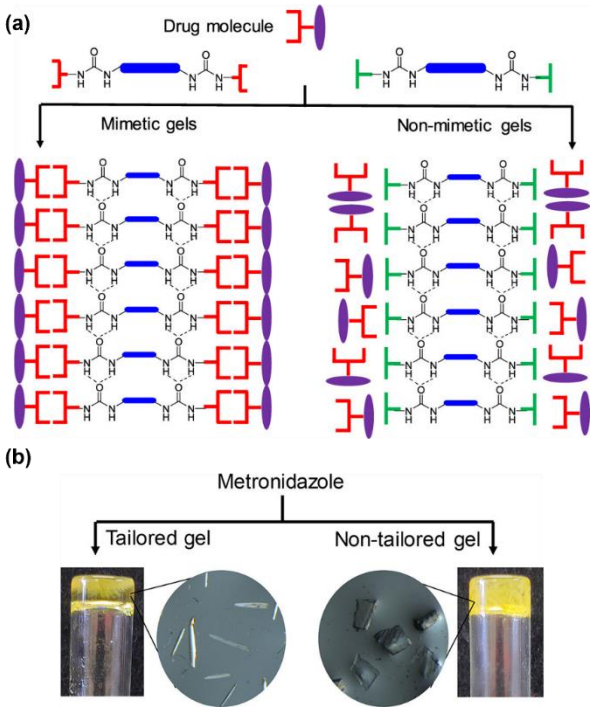

Figure 1.18. (a) Scheme showing gel phase crystallization in drug-mimetic and non-mimetic gels. Red lines represent drug-mimicking functional groups, and green lines represent random functional groups. Specific interactions between gel fibres and the drug in the mimetic case can give rise to changes in morphology and polymorphic form. (b) Photographs and microscope images showing Metronidazole crystals prepared in tailored and non-tailored gels. Adapted with permission from Sreejith Sudhakaran Jayabhavan, Jonathan W. Steed, and Krishna K. Damodaran, **2021**, *21* (9), 5383–5393, DOI: 10.1021/acs.cgd.1c00659. Copyright 2021 American Chemical Society.

The reversible nature of supramolecular gels makes them attractive for use as a crystal growth medium as it allows easy recovery of crystals without the need for acid hydrolysis or heating, both of which can dissolve the crystals.[182] The structure of LMWGs can be changed during synthesis to tune their solubility as well as to allow them to provide a nucleation surface by matching their chemical structure with the crystal-forming compound. It is also possible to use gelator concentration to control crystal morphology.[183, 184] It should be noted that changes in morphology do not always equate to polymorphism.

Hence, we can use the supramolecular gel formed by the gelling component in a supramolecular multicomponent system as a medium for the crystallisation of the non-gelling component. Concurrent formation of crystals and a gel network can be thought of as self-sorting.[177] Gelation and crystallisation are closely related: both occur under supersaturation conditions and have distinct nucleation and growth phases.[177] Gelation is a non-equilibrium self-assembly process that results in the formation of metastable structures. Such kinetically trapped systems exist due to the lack of sufficient thermal energy to overcome the energy barrier leading to the most thermodynamically stable state.[177] Crystallisation is also a non-equilibrium self-assembly driven by a supersaturation gradient. These processes are controlled by both kinetic and thermodynamic factors.[177]

In some cases, crystallisation and gelation may occur on different timescales, resulting in segregation of the two processes. Although the gel- and crystal-forming components self-sort, the gel network can influence crystal formation.[166] The presence of the non-gelling, crystal-forming component may also affect the properties of the resulting gel.[182, 185]

Some gelators may undergo a transition from a kinetically trapped gel state to a more thermodynamically favourable crystal state over time.[186-188] It is important to note that the packing in the crystal state will not necessarily be related to molecular packing in the gel state.[189-191] During collaboration with D. Guiri, we grew crystals of one gelator from a two-gelator multicomponent system.[192] This work was not included in this thesis. The crystal-forming component, 2NapAA (Figure 1.19), forms a self-sorted supramolecular hydrogel when mixed in a 1:1 ratio with the LMWG 2NapFF (Figure 1.19). Over time, the 2NapAA molecules transition from the gel state to the crystal state, resulting in a system where 2NapAA crystals are suspended within the 2NapFF gel. The resulting composite gel has enhanced mechanical rigidity compared to a single component 2NapFF gel.[192]

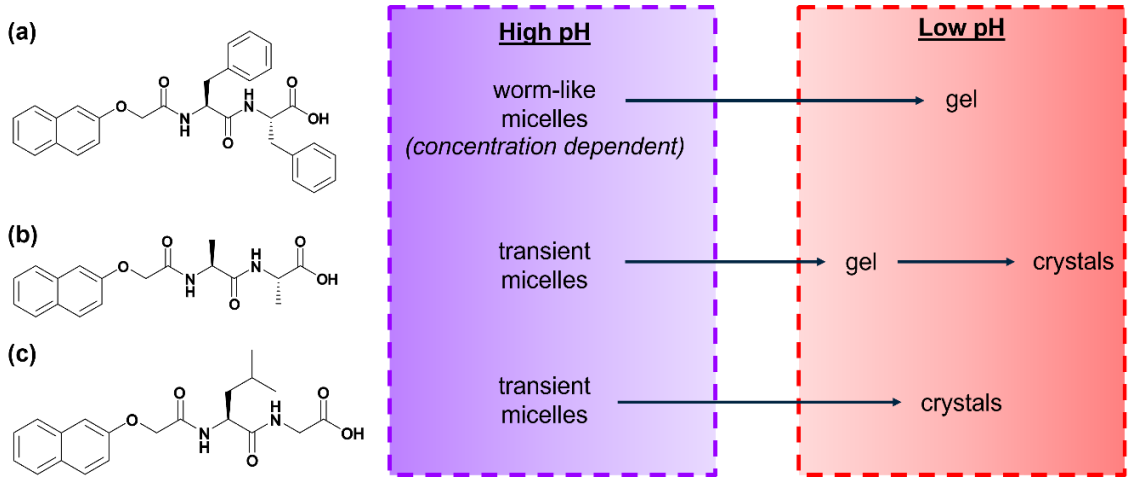

Figure 1.19. Summary of the transitions in self-assembly observed in (a) 2NapFF, (b) 2NapAA and (c) 2NapLG going from micellar dispersions at high pH to solid-like systems at low pH.

We were then able to exploit the time delay between gel formation and 2NapAA crystal formation to change crystal morphology *via* application of a magnetic field.[192] The anisotropic nature of the fibres formed by 2NapFF pre-gelation allows them to be aligned in a magnetic field (Figure 1.20). This alignment persists in the 2NapFF gel network when gelation is triggered within the magnetic field. Formation of 2NapAA crystals within an aligned gel network caused an increase in the length of the crystals in the same plane as the applied magnetic field (Figure 1.20).

Different outcomes are achieved depending on the crystal-forming second component 2NapFF is mixed with. Assembly of 2NapFF and 2NapAA in the same system gives a self-sorted gel that overtime becomes a 2NapFF gel with 2NapAA crystals suspended in the gel. While 2NapLG (Figure 1.19), another *N*-functionalised dipeptide that forms crystals at low pH, and 2NapFF co-assemble at high pH, reducing the pH results in a transition from co-assembly to self-sorting as 2NapLG forms crystals. While the formation of 2NapAA crystals in the 2NapFF gel results in increased mechanical properties of the gel, 2NapLG crystal formation results in collapse of the gel. This suggests that either the crystal-forming component must first form a gel, or that the two components must first self-sort before crystal formation in order to form stable gels.

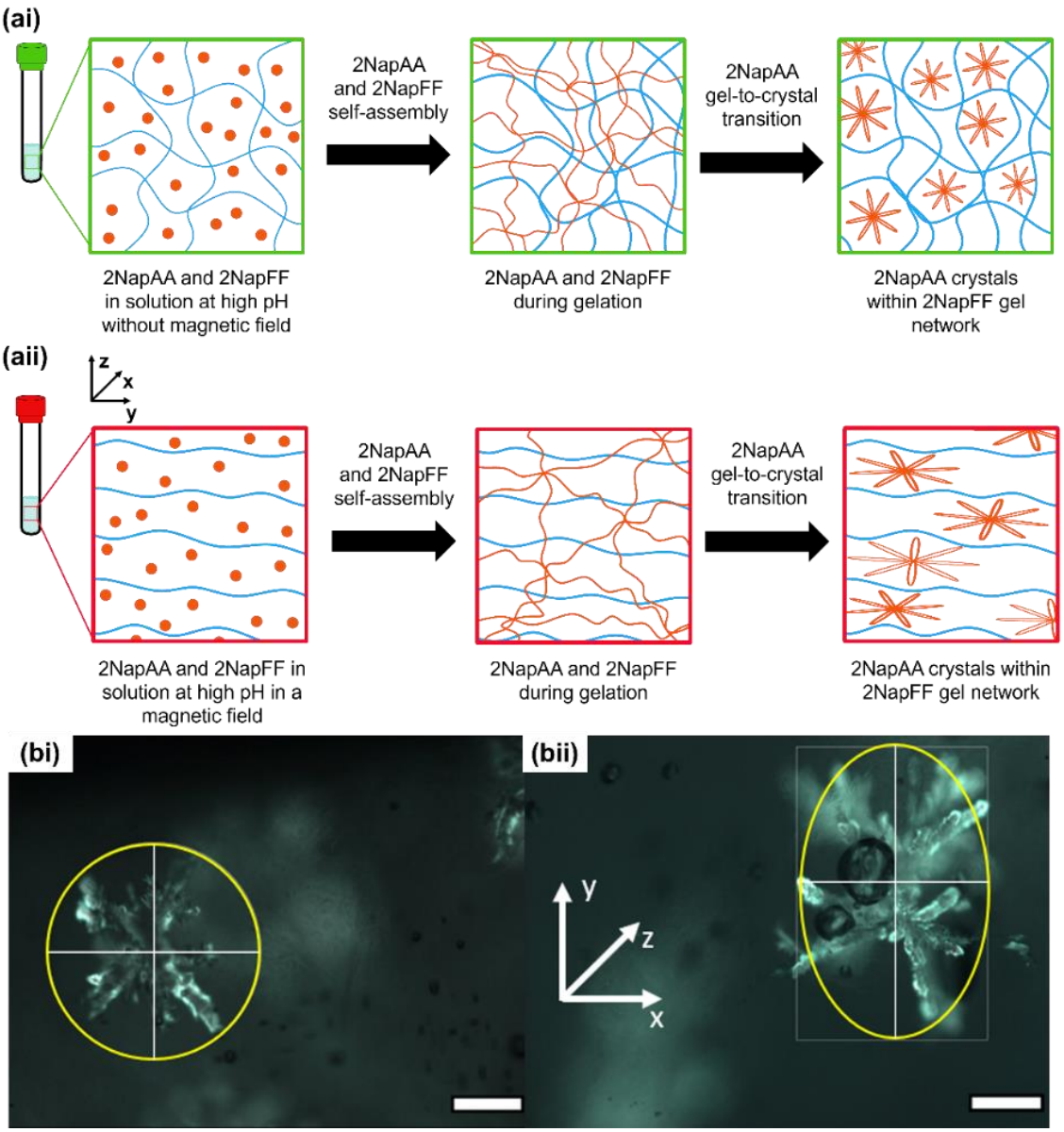

Figure 1.20. (a) Schematic showing the 2NapAA (orange) sol-to-gel transition in the presence of 2NapFF (blue) in the (i) absence and (ii) presence of a magnetic field. (b) Optical microscope images of 2NapAA crystals grown from a 2NapAA:2NapFF multicomponent gel in the (i) absence and (ii) presence of a magnetic field. The magnetic field lies along the *x*-axis, elongating the crystals in the *y*-direction. Images were collected under polarised light. The scale bars represent 300 μm.

1.8 Applications for multicomponent systems

As previously discussed, supramolecular gels are an attractive medium for crystal formation. The versatile and reversible nature of LMWGs makes them ideal for the crystallisation of drug substances.[182] Tuning of crystallisation conditions as well as the chosen LMWG can allow preparation of high quality, stable crystals as well as different polymorphs of the same

compound.[182] The Steed group highlighted the general applicability of supramolecular gels as mediums for crystal formation owing to evidence of effective phase separation between the rapidly forming gel phase and the slower growth of the crystal phase.[182] In the same study, they achieved crystallisation of compounds within a gel medium that could not be obtained from solution as well as preparation of different polymorphs to those observed in the solution phase.[182]

Preparation of multicomponent systems greatly expands the applications available to LMWGs. Control over the outcome of multicomponent assembly is essential for determining the utility of a system for the chosen application. Preparation of multicomponent systems allows specific behaviours and properties to be supplied by each individual component. For example, in gels composed of a polymeric and a LMWG component, the polymer can supply increased stiffness and stability against degradation while the LMWG provides enhanced self-healing properties.[113]

Similarly, two LMWGs can assemble together, each providing different properties. For example, co-assembly of Fmoc-FF and Fmoc-RGD results in formation of a stable hydrogel at physiological pH with structural and mechanical properties similar those of Fmoc-FF alone but with the RGD sequence exposed on the surface of the self-assembled nanostructures within the gel network, functionalising the gel for cell culture applications.[193]

Such multicomponent assembly can also be applied to gelator-non-gelator systems. In order to tailor hydrogels of varying stiffness suitable for stem cell culture and differentiation, Alakpa *et al*. prepared two-component systems comprised of a peptide-based LMWG (structural component) and a surfactant-like molecule (functional component).[194] The stiffness of the hydrogels could be tuned by varying the concentrations of the two components. Altering the stiffness of the hydrogels allowed them to mimic the mechanical properties of different tissues. The properties of the environment surrounding the stem cells results in their differentiation to form different types of cell.[195]

Self-sorting is essential for certain applications. For example, for the formation of self-sorted n-type and p-type supramolecular nanofibers for electronic applications.[106, 196] Heterojunctions occur when n- and p-type fibres are close enough in space to allow electron transfer. Network level assembly will therefore also play a role in determining the utility of a given system as a bulk heterojunction.[196] Increasing the number of entanglements between fibres of each type will increase the number of heterojunctions and thereby increase electron transfer (Figure 1.21).

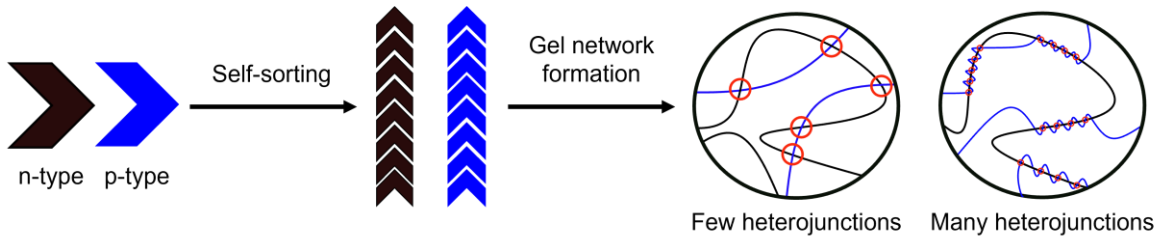

Figure 1.21 Schematic showing the self-sorting of n- and p-type LMWGs. Increasing the number of entanglements in the gel network will increase the number heterojunctions (highlighted by red circles) thereby increasing electron transfer, making the material more suitable as a bulk heterojunction.

Self-sorted systems can also be useful for stimuli-responsive materials. It is possible to prepare systems from components that respond individually to two different stimuli, creating an intelligent material with the ability to respond to a diverse range of environmental changes, such as those seen in living cells.[197] Self-sorting is desirable as it allows combination of two components with different functionalities with minimal perturbation of the structures formed by each component.[197] Tunaka *et al*. were able to create an AND logic gate for the presence of two distinct biomolecules: ATP and sarcosine. The presence of both ATP and sarcosine resulted in a transition from the gel state to the sol state.[197] The authors showed that the two biomolecule-responsive systems work independently by adding the two stimuli either successively or concurrently.[197] Such a response would not be possible in a single component system. Their logic gate was extended to allow the controlled release of an antibody embedded in the multicomponent network.[197]

A second component can also be used to protect peptide-based components from proteolysis.[154] As previously discussed, preparation of a self-sorted peptide-based LMWG/sugar-based LMWG multicomponent system provided gels with tuneable mechanical properties and self-healing behaviour.[154] The authors used liquid chromatography-mass spectrometry to show the sugar-based component forms a protective corona around the peptide-based nanofibers, preventing a proteolytic enzyme from accessing the peptide bonds.[154] These enhanced properties made the multicomponent gels suitable for cell culture applications. Further, the molecular composition and mechanical properties of the multicomponent gels could be tuned to control the morphology of the cells, opening new opportunities for multicomponent hydrogels in regenerative medicine.[154]

While self-sorting is essential for some applications, co-assembly is essential for others. For example, co-assembly of a component with the ability to form stable hydrogels that mimic the mechanical properties of the extracellular matrix with a structurally related bioactive

compound allows inclusion of groups required for cell adhesion for cell culture applications.[193] Co-assembly of peptides functionalised with different aromatic groups allows incorporation of a variety of aromatic groups into a single system. Such co-assembly can help stabilise π-π stacking *via* complementary interactions. It is by this method that intermolecular energy transfer mechanisms can be observed between fluorophores.[163] For example, co-assembly of the peptide-based LMWG 2NapFF with a dansyl or anthracene chromophore allows energy transfer between the naphthalene donor and the chromophore acceptor which intercalate into the fibres formed by 2NapFF (Figure 1.22).[198]

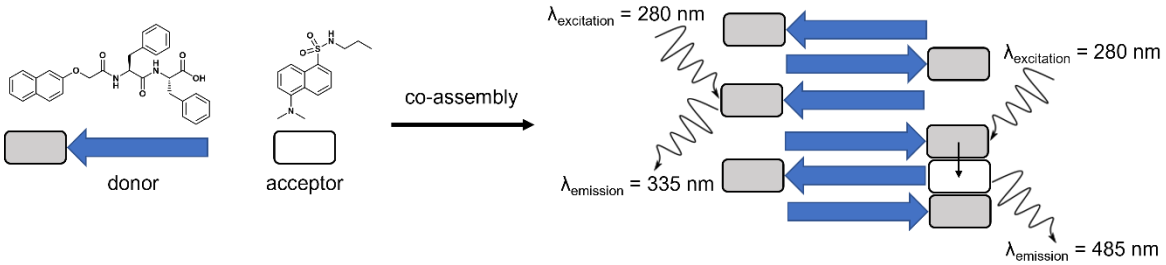

Figure 1.22. Schematic showing the chemical structures of the donor molecule, the LMWG 2NapFF, and the chromophore acceptor. Intercalation of the acceptor into the fibres formed by 2NapFF during co-assembly allows energy transfer between the donor and acceptor leading to emission at 485 nm in addition to emission at 355 nm from the donor alone.

As previously discussed, multicomponent systems composed of a polymeric and a supramolecular gelator can also be used for controlled drug release.[143, 151] It is possible to spatially control the type of gel network formed using photopatterned irradiation, resulting in different material behaviours and diffusion rates.[151] As such, drug-delivery gels that exhibit differential drug release kinetics from different regions of the gel can be prepared. This allows both burst and sustained release from a single system.[151] The same principles can be applied to achieve differential cell growth with significant spatial definition using laser irradiation.[151]

1.9 Aims of this thesis

Supramolecular hydrogels are an interesting material with properties making them of use in a vast range of applications. However, the difficulties faced in designing LMWGs with a particular application in mind provides an undeniable challenge. The preparation of multicomponent systems provides a method for controlling the properties of already established LMWGs, creating an opportunity to surpass this challenge. As such, this thesis

aims to exemplify some of the new properties and behaviours attainable through the preparation of multicomponent systems based on LMWGs.

In Chapter 2, we prepare two-component systems from a peptide-based LMWG and structurally similar crystal-forming components. We investigate the effect of the crystal-forming components on the properties of the system pre-gelation using SANS, viscosity measurements and NMR spectroscopy. We also investigated the effect of different temperature changes on the properties of the pre-gelation systems. We then use the single and multicomponent systems to prepare supramolecular gel noodles. Finally, we exploit the crystal-forming behaviour of the non-gelling component to prepare composite gel noodles.

In Chapter 3, we investigate a range of LMWG-LMWG multicomponent systems, identify their mode of multicomponent assembly and discuss how this might relate to the mechanical properties of the system. We use a wide variety of techniques to investigate the properties of these systems at each stage of self-assembly, in the sol state pre-gelation, during gel formation and in the gel state. We also investigate the effect of the concentration ratio of the two components on the systems, as well as the effect of altering the chirality of a single component on the properties of the systems.

Finally, in Chapter 4 we investigate how specific gelator design and inclusion of a cross-linking agent can allow control of gel mechanical properties. We further modulate the effect of chemical cross-linking by using different methods of triggering gelation.

1.10 References

1. J. Hoque, N. Sangaj and S. Varghese, *Macromol. Biosci.*, 2019, **19**, 1800259.
2. A. Shome, S. Debnath and P. K. Das, *Langmuir*, 2008, **24**, 4280-4288.
3. Z. Sun, Z. Li, Y. He, R. Shen, L. Deng, M. Yang, Y. Liang and Y. Zhang, *J. Am. Chem. Soc.*, 2013, **135**, 13379-13386.
4. C. D. Jones and J. W. Steed, *Chem. Soc. Rev.*, 2016, **45**, 6546-6596.
5. A. Z. Cardoso, L. E. Mears, B. N. Cattoz, P. C. Griffiths, R. Schweins and D. J. Adams, *Soft Matter*, 2016, **12**, 3612-3621.
6. L. A. Estroff and A. D. Hamilton, *Chem. Rev.*, 2004, **104**, 1201-1218.
7. M. de Loos, B. L. Feringa and J. H. van Esch, *Eur. J. Org. Chem.*, 2005, **17**, 3615-3631.

8. J. Raeburn, A. Z. Cardoso and D. J. Adams, *Chem. Soc. Rev.*, 2013, **42**, 5143-5156.
9. J. Raeburn, C. Mendoza-Cuenca, B. N. Cattoz, M. A. Little, A. E. Terry, A. Z. Cardoso, P. C. Griffiths and D. J. Adams, *Soft Matter*, 2015, **11**, 927-935.
10. D. J. Adams, *Gels*, 2018, **4**, 32.
11. T. Das, M. Haering, D. Haldar and D. Diaz Diaz, *Biomater. Sci.*, 2017, **6**, 38-59.
12. J. D. Hartgerink, E. Beniash and S. I. Stupp, *Proc. Nat. Acad. Sci. USA*, 2002, **99**, 5133-5138.
13. X.-Q. Dou and C.-L. Feng, *Adv. Mater.*, 2017, **29**, 1604062.
14. Q. Zhao, Y. Chen and Y. Lie, *Chin. Chem. Lett.*, 2018, **29**, 84-86.
15. Z. Wei, J. H. Yang, X. J. Du, F. Xu, M. Zrinyi, Y. Osada, F. Li and Y. M. Chen, *Macromol. Rapid Commun.*, 2013, **34**, 1464-1470.
16. H. Wang, D. Mao, Y. Wang, K. Wang, X. Yi, D. Kong, Z. Yang, Q. Liu and D. Ding, *Sci. Rep.*, 2015, **5**, 1-10.
17. B. Hu, C. Owh, P. L. Chee, W. R. Leow, X. Liu, Y.-L. Wu, P. Guo, X. J. Loh and X. Chen, *Chem. Soc. Rev.*, 2018, **47**, 6917-6929.
18. E. J. Howe, B. O. Okesola and D. K. Smith, *Chem. Comm.*, 2015, **51**, 7451-7454.
19. S. Marullo, C. Rizzo, N. T. Dintcheva, F. Giannici and F. D'Anna, *Colloid Interface*, 2018, **517**, 182-193.
20. Yamanaka, M., *J. Incl. Phenom. Macrocycl. Chem.*, 2013, **77**, 33-48.
21. T. Giraud, P. Hoschtettler, G. Pickaert, M.-C. Averlant-Petit and L. Stefan, *Nanoscale*, 2022, **14**, 4908-4921.
22. Y. Feng, Z.-X. Liu, H. Chen and Q.-H. Fan, *Chem. Comm.*, 2022, **58**, 8736-8753.
23. O. Gronwald and S. Shinkai, *Chem. Eur. J.*, 2001, **7**, 4328-4334.
24. A. Y.-Y. Tam and V. W.-W. Yam, *Chem. Comm.*, 2013, **42**, 1540-1567.
25. E. K. Johnson, D. J. Adams and P. J. Cameron, *J. Mater. Chem.*, 2011, **21**, 2024-2027.
26. L. Chen, G. Pont, K. Morris, G. Lotze, A. Squires, L. C. Serpell and D. J. Adams, *Chem. Comm.*, 2011, **47**, 12071-12073.
27. G. Fichman and E. Gazit, *Acta Biomater.*, 2014, **10**, 1671-1682.
28. Y. Li, M. Qin, Y. Cao and W. Wang, *Sci. China Phys. Mech.*, 2014, **57**, 849-858.
29. M. A. Khalily, M. Goktas and M. O. Guler, *Org. Biomol. Chem.*, 2015, **13**, 1983-1987.
30. Y. Ding, Y. Li, M. Qin, Y. Cao and W. Wang, *Langmuir*, 2013, **29**, 13299-13306.

31. L. Saunders and P. X. Ma, *Macromol. Biosci.*, 2019, **19**, 1800313
32. H. Jian, M. Wang, Q. Dong, J. Li, A. Wang, X. Li, P. Ren and S. Bai, *ACS Appl. Mater. Interfaces*, 2019, **11**, 46419-46426.
33. K. Basu, A. Baral, S. Basak, A. Dehsorkhi, J. Nanda, D. Bhunia, S. Ghosh, V. Castelletto, I. W. Hamley and A. Banerjee, *Chem. Comm.*, 2016, **52**, 5045-5048.
34. Z. Yang, G. Liang, M. Ma, Y. Gao and B. Xu, *J. Mater. Chem.*, 2006, **17**, 850-854.
35. J. Shi, Y. Gao, Z. Yang and B. Xu, *Beilstein J. Org. Chem.*, 2011, **7**, 167-172.
36. H. M. Wang, C. H. Yang, M. Tan, L. Wang, D. L. Kong and Z. M. Yang, *Soft Matter*, 2011, **7**, 3897–3905.
37. L. Chen, K. Morris, A. Laybourn, D. Elias, M. R. Hicks, A. Rodger, L. Serpell and D. J. Adams, *Langmuir*, 2010, **26**, 5232-5242.
38. Z. Yang, G. Liang, L. Wang and B. Xu, *J. Am. Chem. Soc.*, 2006, **128**, 3038-3043.
39. V. Jayawarna, S. M. Richardson, A. R. Hirst, N. W. Hodson, A. Saiani, J. E. Gough and R. V. Ulijn, *Acta Biomater.*, 2009, **5**, 934-943.
40. V. Jayawarna, M. Ali, T. A. Jowitt, A. F. Miller, A. Saiani, J. E. Gough and R. V. Ulijn, *Adv. Mater.*, 2006, **18**, 611-614.
41. A. Mahler, M. Reches, M. Rechter, S. Cohen and E. Gazit, *Adv. Mater.*, 2006, **18**, 1365-1370.
42. T. Liebmann, S. Rydholm, V. Akpe and H. Brismar, *BMC Biotechnol.*, 2007, **7**, 1-11.
43. Yan Zhang, Zhimou Yang, Fang Yuan, Hongwei Gu, a. Ping Gao and Bing Xu*, *J. Am. Chem. Soc.*, 2004, **126**, 15028-15029.
44. J. Li, X. Du, S. Hashim, A. Shy and B. Xu, *J. Am. Chem. Soc.*, 2017, **139**, 71-74.
45. S. Mukherjee, T. Kar and P. K. Das, *Chem. Asian J.*, 2014, **9**, 2798-2805.
46. A. H. Conney, R. L. Chang, D. M. Jerina and S. J. C. Wei, *Drug Metab. Rev.*, 1994, **26**, 125-163.
47. M. A. Hossain and S. M. Salehuddin, *Arab. J. Chem.*, 2012, **5**, 391-396.
48. L. Chen, S. Revel, K. Morris, L. C. Serpell and D. J. Adams, *Langmuir*, 2010, **26**, 13466-13471.
49. G. Cheng, V. Castelletto, C. M. Moulton, G. E. Newby and I. W. Hamley, *Langmuir*, 2010, **26**, 4990-4998.

50. H. Xu, A. K. Das, M. Horie, M. S. Shaik, A. M. Smith, Y. Luo, X. Lu, R. Collins, S. Y. Liem, A. Song, P. L. A. Popelier, M. L. Turner, P. Xiao, I. A. Kinloch and R. V. Ulijn, *Nanoscale*, 2010, **2**, 960-966.
51. E. K. Johnson, D. J. Adams and P. J. Cameron, *J. Mater. Chem.*, 2011, **21**, 2024-2027.
52. Z. Yang, L. Wang, J. Wang, P. Gao and B. Xu, *J. Mater. Chem.*, 2010, **20**, 2128-2132.
53. C. J. Bowerman, D. M. Ryan, D. A. Nissan and B. L. Nilsson, *Mol. Biosyst.*, 2009, **5**, 1058-1069.
54. R. C. Hayward and D. J. Pochan, *Macromol.*, 2010, **43**, 3577-3584.
55. A. K. Patterson and D. K. Smith, *Chem. Comm.*, 2020, **56**, 11046-11049.
56. C. C. Piras and D. K. Smith, *Chem. Eur. J.*, 2019, **25**, 11318-11326.
57. Z. Yang, H. Gu , D. Fu, P. Gao , J. Lam and B. Xu, *Adv. Mater.*, 2004, **16**, 1440-1440.
58. S. Toledano, R. J. Williams, V. Jayawarna and R. V. Ulijn, *J. Am. Chem. Soc.*, 2006, **128**, 1070-1071.
59. C. Maity, W. E. Hendriksen, J. H. van Esch and R. Eelkema, *Angew. Chem. Int. Ed.*, 2015, **54**, 998-1001.
60. C. B. P. Oliveira, S. R. S. Veloso, E. M. S. Castanheira, P. R. Figueiredo, A. T. P. Carvalho, L. Hilliou, R. B. Pereira, D. M. Pereira, J. A. Martins, P. M. T. Ferreira and P. J. Jervis, *Soft Matter*, 2022, **18**, 3955-3966.
61. D. M. Murali and G. Shanmugam, *New J. Chem.*, 2019, **43**, 12396-12409.
62. E. R. Draper, M. Wallace, R. Schweins, R. J. Poole and D. J. Adams, *Langmuir*, 2017, **33**, 2387-2395.
63. K. L. Morris, L. Chen, J. Raeburn, O. R. Sellick, P. Cotanda, A. Paul, P. C. Griffiths, S. M. King, R. K. O'Reilly, L. C. Serpell and D. J. Adams, *Nat. Commun.*, 2013, **4**, 1480.
64. S. Roy, N. Javid, J. Sefcik, P. J. Halling and R. V. Ulijn, *Langmuir*, 2012, **28**, 16664-16670.
65. E. Mattia and S. Otto, *Nat. Nanotechnol.*, 2015, **10**, 111-119.
66. D. B. Amabilino, D. K. Smith and J. W. Steed, *Chem. Soc. Rev.*, 2017, **46**, 2404-2420.
67. B. A. K. Kriebisch, C. M. E. Kriebisch, A. M. Bergmann, C. Wanzke, M. Tena-Solsona and J. Boekhoven, *ChemSystemsChem*, 2023, **5**, e202200035

68. C. Colquhoun, E. R. Draper, R. Schweins, M. Marcello, D. Vadukul, L. C. Serpell and D. J. Adams, *Soft Matter*, 2017, **13**, 1914-1919.
69. M. A. Greenfield, J. R. Hoffman, M. O. de la Cruz and S. I. Stupp, *Langmuir*, 2010, **26**, 3641-3647.
70. D. J. Adams, M. F. Butler, W. J. Frith, M. Kirkland, L. Mullen and P. Sanderson, *Soft Matter*, 2009, **5**, 1856-1862.
71. D. J. Adams, L. M. Mullen, M. Berta, L. Chen and W. J. Frith, *Soft Matter*, 2010, **6**, 1971-1980.
72. C. Tang, A. M. Smith, R. F. Collins, R. V. Ulijn and A. Saiani, *Langmuir*, 2009, **25**, 9447-9453.
73. Y. Chen, H. X. Gan and Y. W. Tong, *Macromol.*, 2015, **48**, 2647-2653.
74. J. Li, W.-Y. Wong and X.-m. Tao, *Nanoscale*, 2020, **12**, 1281-1306.
75. F. Tantakitti, J. Boekhoven, X. Wang, R. V. Kazantsev, T. Yu, J. Li, E. Zhuang, R. Zandi, J. H. Ortony, C. J. Newcomb, L. C. Palmer, G. S. Shekhawat, M. O. de la Cruz, G. C. Schatz and S. I. Stupp, *Nat. Mater.*, 2016, **15**, 469-476.
76. K. A. Houton, K. L. Morris, L. Chen, M. Schmidtmann, J. T. A. Jones, L. C. Serpell, G. O. Lloyd and D. J. Adams, *Langmuir*, 2012, **28**, 9797-9806.
77. G. Ben Messaoud, P. Le Griel, D. Hermida-Merino, S. L. K. W. Roelants, W. Soetaert, C. V. Stevens and N. Baccile, *Chem. Mater.*, 2019, **31**, 4817-4830.
78. D. McDowall, M. Walker, M. Vassalli, M. Cantini, N. Khunti, C. J. C. Edwards-Gayle, N. Cowieson and D. J. Adams, *Chem. Comm.*, 2021, **57**, 8782-8785.
79. S. Zhang, M. A. Greenfield, A. Mata, L. C. Palmer, R. Bitton, J. R. Mantei, C. Aparicio, M. O. de la Cruz and S. I. Stupp, *Nat. Mater.*, 2010, **9**, 594-601.
80. M. Reches and E. Gazit, *Science*, 2003, **300**, 625-627.
81. A. Saiani, A. Mohammed, H. Frielinghaus, R. Collins, N. Hodson, C. M. Kielty, M. J. Sherratt and A. F. Miller, *Soft Matter*, 2009, **5**, 193-202.
82. R. Orbach, L. Adler-Abramovich, S. Zigerson, I. Mironi-Harpaz, D. Seliktar and E. Gazit, *Biomacromolecules*, 2009, **10**, 2646-2651.
83. D. M. Ryan, S. B. Anderson, F. T. Senguen, R. E. Youngman and B. L. Nilsson, *Soft Matter*, 2010, **6**, 475-479.
84. S. M. M. Reddy, P. Dorishetty, G. Augustine, A. P. Deshpande, N. Ayyadurai and G. Shanmugam, *Langmuir*, 2017, **33**, 13504-13514.
85. S. Fleming, S. Debnath, P. W. J. M. Frederix, T. Tuttle and R. V. Ulijn, *Chem. Comm.*, 2013, **49**, 10587-10589.
86. J. E. Hein and D. G. Blackmond, *Acc. Chem. Res.*, 2012, **45**, 2045-2054.

87. J. L. Bada, *Nature*, 1995, **374**, 594-595.
88. S. Marchesan, C. D. Easton, F. Kushaki, L. Waddington and P. G. Hartley, *Chem. Comm.*, 2012, **48**, 2195-2197.
89. S. Biswas and A. K. Das, *Langmuir*, 2019, **35**, 2383-2391.
90. J. H. Jung, Y. Ono, K. Hanabusa and S. Shinkai, *J. Am. Chem. Soc.*, 2000, **122**, 5008-5009.
91. K. J. C. van Bommel, A. Friggeri and S. Shinkai, *Angew. Chem. Intl. Ed.*, 2003, **42**, 980-999.
92. K. Sugiyasu, S. Tamaru, M. Takeuchi, D. Berthier, I. Huc, R. Oda and S. Shinkai, *Chem. Comm.*, 2002, **11**, 1212-1213.
93. S. Marchesan, K. E. Styan, C. D. Easton, L. Waddington and A. V. Vargiu, *J. Mater. Chem. B*, 2015, **3**, 8123-8132.
94. S. Marchesan, C. D. Easton, K. E. Styan, L. J. Waddington, F. Kushkaki, L. Goodall, K. M. McLean, J. S. Forsythe and P. G. Hartley, *Nanoscale*, 2014, **6**, 5172-5180.
95. S. Marchesan, L. Waddington, C. D. Easton, D. A. Winkler, L. Goodall, J. Forsythe and P. G. Hartley, *Nanoscale*, 2012, **4**, 6752-6760.
96. T. Koga, M. Matsuoka and N. Higashi, *J. Am. Chem. Soc.*, 2005, **127**, 17596-17597.
97. K. J. Nagy, M. C. Giano, A. Jin, D. J. Pochan and J. P. Schneider, *J. Am. Chem. Soc.*, 2011, **133**, 14975–14977.
98. Z. Dzolic, K. Wolsperger and M. Zinic, *New J. Chem.*, 2006, **30**, 1411-1419.
99. S. Cicchi, G. Ghini, L. Lascialfari, A. Brandi, F. Betti, D. Berti, P. Baglioni, L. Di Bari, G. Pescitelli, M. Mannini and A. Caneschi, *Soft Matter*, 2010, **6**, 1655-1661.
100. R. J. Swanekamp, J. T. M. DiMaio, C. J. Bowerman and B. L. Nilsson, *J. Am Chem. Soc.*, 2012, **134**, 5556-5559.
101. S. Bera, B. Xue, P. Rehak, G. Jacoby, W. Ji, L. J. W. Shimon, R. Beck, P. Kral, Y. Cao and E. Gazit, *ACS Nano*, 2020, **14**, 1694-1706.
102. S. Basak, I. Singh, A. Ferranco, J. Syed and H.-B. Kraatz, *Angew. Chem. Int. Ed.*, 2017, **56**, 13288-13292.
103. S. Prasanthkumar, S. Ghosh, V. C. Nair, A. Saeki, S. Seki and A. Ajayaghosh, *Angew. Chem. Int. Ed.*, 2015, **54**, 946-950.

104. J. Lopez-Andarias, M. Jose Rodriguez, C. Atienza, J. Luis Lopez, T. Mikie, S. Casado, S. Seki, J. L. Carrascosa and N. Martin, *J. Am. Chem. Soc.*, 2015, **137**, 893-897.
105. H. Shigemitsu, T. Fujisaku, W. Tanaka, R. Kubota, S. Minami, K. Urayama and I. Hamachi, *Nat. Nanotechnol.*, 2018, **13**, 165-172.
106. K. Sugiyasu, S. I. Kawano, N. Fujita and S. Shinkai, *Chem. Materi.*, 2008, **20**, 2863-2865.
107. E. R. Draper and D. J. Adams, *Chem. Soc. Rev.*, 2018, **47**, 3395-3405.
108. C. Colquhoun, E. R. Draper, E. G. Eden, B. N. Cattoz, K. L. Morris, L. Chen, T. O. McDonald, A. E. Terry, P. C. Griffiths, L. C. Serpell and D. J. Adams, *Nanoscale*, 2014, **6**, 13719-13725.
109. B. Escuder, M. Llusar and J. F. Miravet, *J. Org. Chem.*, 2006, **71**, 7747-7752.
110. D. J. Cornwell, O. J. Daubney and D. K. Smith, *J. Am. Chem. Soc.*, 2015, **137**, 15486-15492.
111. Y. E. Shapiro, *Prog. Polym. Sci.*, 2011, **36**, 1184-1253.
112. Mo, H. and Pochapsky, T.C., *Prog. Nucl. Magn. Res. Spec.*, 1997, **30**, 1-38.
113. B. O. Okesola, Y. Wu, B. Derkus, S. Gani, D. Wu, D. Knani, D. K. Smith, D. J. Adams and A. Mata, *Chem. Mater.*, 2019, **31**, 7883-7897.
114. A. M. Brizard, M. C. A. Stuart and J. H. van Esch, *Faraday Discuss.*, 2009, **143**, 345-357.
115. J. Zhan, X. Liao, X. Fan, J. Zhang, H. Li, Y. Cai and X. Qiu, *Compos. B Eng.*, 2022, **236**, 109794.
116. L. L. E. Mears, E. R. Draper, A. M. Castilla, H. Su, Zhuola, B. Dietrich, M. C. Nolan, G. N. Smith, J. Doutch, S. Rogers, R. Akhtar, H. Cui and D. J. Adams, *Biomacromolecules*, 2017, **18**, 3531-3540.
117. J.-B. Guilbaud and A. Saiani, *Chem. Soc. Rev.*, 2011, **40**, 1200-1210.
118. E. R. Draper, B. Dietrich, K. McAulay, C. Brasnett, H. Abdizadeh, I. Patmanidis, S. J. Marrink, H. Su, H. Cui, R. Schweins, A. Seddon and D. J. Adams, *Matter*, 2020, **2**, 764-778.
119. M. J. Hollamby, *Phys. Chem. Chem. Phys*, 2013, **15**, 10566-10579.
120. C. Yan, A. Altunbas, T. Yucel, R. P. Nagarkar, J. P. Schneider and D. J. Pochan, *Soft Matter*, 2010, **6**, 5143-5156.
121. K. McAulay, L. Thomson, L. Porcar, R. Schweins, N. Mahmoudi, D. J. Adams and E. R. Draper, *Org. Mater.*, 2020, **02**, 108-115.

122. C. C. Horgan, A. L. Rodriguez, R. Li, K. F. Bruggeman, N. Stupka, J. K. Raynes, L. Day, J. W. White, R. J. Williams and D. R. Nisbet, *Acta Biomater.*, 2016, **38**, 11-22.
123. Lay-Theng Lee* and B. Cabane‡, *Macromolecules*, 1997, **30**, 6559-6566.
124. C. Yan and D. J. Pochan, *Chem. Soc. Rev.*, 2010, **39**, 3528-3540.
125. V. J. Nebot and D. K. Smith, in *Functional Molecular Gels*, eds. B. Escuder and J. F. Miravet, Royal Society of Chemistry, 2013, ch. Techniques for the characterisation of molecular gels, pp. 30-66.
126. S. Boothroyd, A. Saiani and A. F. Miller, *Biopolymers*, 2014, **101**, 669-680.
127. S. Fleming and R. V. Ulijn, *Chem. Soc. Rev.*, 2014, **43**, 8150-8177.
128. X. Che, B. Bai, T. Zhang, C. Zhang, C. Zhang, P. Zhang, H. Wang and M. Li, *New J. Chem.*, 2017, **41**, 8614-8619.
129. T. Xia, W. Liu and L. Yang, *J. Biomed. Mater. Res. A*, 2017, **105**, 1799-1812.
130. R. G. Weiss, *J. Am. Chem. Soc.*, 2014, **136**, 7519-7530.
131. L. E. Buerkle, Z. Li, A. M. Jamieson and S. J. Rowan, *Langmuir*, 2009, **25**, 8833-8840.
132. L. E. Buerkle, R. Galleguillos and S. J. Rowan, *Soft Matter*, 2011, **7**, 6984-6990.
133. Y. M. Abul-Haija, S. Roy, P. W. J. M. Frederix, N. Javid, V. Jayawarna and R. V. Ulijn, *Small*, 2014, **10**, 973-979.
134. A. Heeres, C. van der Pol, M. C. A. Stuart, A. Friggeri, B. L. Feringa and J. van Esch, *J. Am. Chem. Soc.*, 2003, **125**, 14252-14253.
135. A. Brizard, M. Stuart, K. van Bommel, A. Friggeri, M. de Jong and J. van Esch, *Angew. Chem. Int. Ed.*, 2008, **47**, 2063-2066.
136. S. Fleming, S. Debnath, P. W. J. M. Frederix, N. T. Hunt and R. V. Ulijn, *Biomacromolecules* 2014, **15**, 1171-1184.
137. J. W. Sadownik, J. Leckie and R. V. Ulijn, *Chem. Comm.*, 2011, **47**, 728-730.
138. W. Wang and Y. Chau, *Chem. Comm.*, 2011, **47**, 10224-10226.
139. J. Boekhoven, A. M. Brizard, M. C. A. Stuart, L. Florusse, G. Raffy, A. Del Guerzo and J. H. van Esch, *Chem. Sci.*, 2016, **7**, 6021-6031.
140. Y. J. Adhia, T. H. Schloemer, M. T. Perez and A. J. McNeil, *Soft Matter*, 2012, **8**, 430-434.
141. L. Chen, S. Revel, K. Morris, D. G. Spiller, L. C. Serpell and D. J. Adams, *Chem. Comm.*, 2010, **46**, 6738-6740.
142. G. Pont, L. Chen, D. G. Spiller and D. J. Adams, *Soft Matter*, 2012, **8**, 7797-7802.

143. J. Wang, Z. Wang, J. Gao, L. Wang, Z. Yang, D. Kong and Z. Yang, *J. Mater. Chem.*, 2009, **19**, 7892-7896.
144. R. Huang, W. Qi, L. Feng, R. Su and Z. He, *Soft Matter*, 2011, **7**, 6222-6230.
145. B. Fan, K. Zhang, Q. Liu and R. Eelkema, *ACS Macro Lett.*, 2020, **9**, 776-780.
146. S. Panja, S. Bianco, B. Dietrich and D. J. Adams, *Mater. Chem. Front.*, 2022, **6**, 2703-2708.
147. S. Panja and D. J. Adams, *Chem. Comm.*, 2022, **58**, 5622-5625.
148. L. Chronopoulou, Y. Toumia, B. Cerroni, D. Pandolfi, G. Paradossi and C. Palocci, *New Biotechnol.*, 2017, **37**, 138-143.
149. A. Maslovskis, J. B. Guilbaud, I. Grillo, N. Hodson, A. F. Miller and A. Saiani, *Langmuir*, 2014, **30**, 10471-10480.
150. H. Shigemitsu, R. Kubota, K. Nakamura, T. Matsuzaki, S. Minami, T. Aoyama, K. Urayama and I. Hamachi, *Nat. Comm.*, 2020, **11**, 3859.
151. D. J. Cornwell, B. O. Okesola and D. K. Smith, *Angew. Chem. Int. Ed.*, 2014, **53**, 12461-12465.
152. S. Onogi, H. Shigemitsu, T. Yoshii, T. Tanida, M. Ikeda, R. Kubota and I. Hamachi, *Nat. Chem.*, 2016, **8**, 743-752.
153. R. Yu, N. Lin, W. Yu and X. Y. Liu, *CrystEngComm*, 2015, **17**, 7986-8010.
154. S. A. Abbah, L. M. Delgado, A. Azeem, K. Fuller, N. Shologu, M. Keeney, M. J. Biggs, A. Pandit and D. I. Zeugolis, *Adv. Healthc. Mater.*, 2015, **4**, 2488-2499.
155. M. M. Smith and D. K. Smith, *Soft Matter*, 2011, **7**, 4856-4860.
156. J. R. Moffat and D. K. Smith, *Chem. Comm.*, 2009, **3**, 316-318.
157. L. Thomson, R. Schweins, E. R. Draper and D. J. Adams, *Macromol. Rapid Commun.*, 2020, **41**, e2000093.
158. J. Raeburn, B. Alston, J. Kroeger, T. O. McDonald, J. R. Howse, P. J. Cameron and D. J. Adams, *Mater. Horiz.*, 2014, **1**, 241-246.
159. H. Du, J. Liu, B. Pan, H.-Y. Yang, G.-B. Liu and K. Lu, *Food Hydrocoll.*, 2022, **131**, 107751.
160. J. G. Hardy, A. R. Hirst, I. Ashworth, C. Brennan and D. K. Smith, *Tetrahedron*, 2007, **63**, 7397-7406.
161. D. M. Ryan, T. M. Doran and B. L. Nilsson, *Langmuir*, 2011, **27**, 11145-11156.
162. D. Li, Y. Shi and L. Wang, *Chin. J. Chem.*, 2014, **32**, 123-127.
163. K. V. Rao and S. J. George, *Chem. Eur. J.*, 2012, **18**, 14286-14291.
164. A. Das and S. Ghosh, *Chem. Comm.*, 2011, **47**, 8922-8924.

165. M. M. Safont-Sempere, G. Fernandez and F. Wuerthner, *Chem. Rev.*, 2011, **111**, 5784-5814.
166. R. I. Petrova, R. Patel and J. A. Swift, *Cryst. Growth Des.*, 2006, **6**, 2709-2715.
167. R. I. Petrova and J. A. Swift, *J. Am. Chem. Soc.*, 2004, **126**, 1168-1173.
168. H. Li and L. A. Estroff, *CrystEngComm*, 2007, **9**, 1153-1155.
169. H. J. Nickl and H. K. Henisch, *J. Electrochem. Soc.*, 1969, **116**, 1258.
170. Garcıa-Ruiz, J.M., Gavira, J.A., Otálora, F., Guasch, A. and Coll, M., *Mater. Res. Bull.*, 1998, **33**,1593-1598.
171. Hartgerink, J.D., Beniash, E. and Stupp, S.I., *Science*, 2001, **294**, 1684-1688.
172. T. D. Clark, K. Kobayashi and M. R. Ghadiri, *Chem. Eur. J.*, 1999, **5**, 782-792.
173. H. K. Henisch and J. M. Garciaruiz, *J. Cryst. Growth*, 1986, **75**, 203-211.
174. H. K. Henisch and J. M. Garciaruiz, *J. Cryst. Growth*, 1986, **75**, 195-202.
175. S. S. Jayabhavan, J. W. Steed and K. K. Damodaran, *Cryst. Growth Des.*, 2021, **21**, 5383-5393.
176. J. van Esch, R. M. Kellogg and B. L. Feringa, *Tetrahedron Lett.*, 1997, **38**, 281-284.
177. D. K. Kumar and J. W. Steed, *Chem. Soc. Rev.*, 2014, **43**, 2080-2088.
178. J. A. Foster, K. K. Damodaran, A. Maurin, G. M. Day, H. P. G. Thompson, G. J. Cameron, J. C. Bernal and J. W. Steed, *Chem. Sci.*, 2017, **8**, 78-84.
179. A. Dawn, K. S. Andrew, D. S. Yufit, Y. Hong, J. P. Reddy, C. D. Jones, J. A. Aguilar and J. W. Steed, *Crys. Growth Des.*, 2015, **15**, 4591-4599.
180. S. R. Kennedy, C. D. Jones, D. S. Yufit, C. E. Nicholson, S. J. Cooper and J. W. Steed, *CrystEngComm*, 2018, **20**, 1390-1398.
181. B. Saikia, M. T. Mulvee, I. Torres-Moya, B. Sarma and J. W. Steed, *Cryst. Growth Des.*, 2020, **20**, 7989-7996.
182. J. A. Foster, M.-O. M. Piepenbrock, G. O. Lloyd, N. Clarke, J. A. K. Howard and J. W. Steed, *Nat. Chem.*, 2010, **2**, 1037-1043.
183. J. A. Gavira, A. E. S. Van Driessche and J.-M. Garcia-Ruiz, *Crys. Growth Des.*, 2013, **13**, 2522-2529.
184. Y. Ma, Q. Feng and X. Bourrat, *Mater. Sci. Eng. C Mater. Biol. Appl.*, 2013, **33**, 2413-2420.
185. M.-O. M. Piepenbrock, G. O. Lloyd, N. Clarke and J. W. Steed, *Chem. Comm.*, 2008, **23**, 2644-2646.
186. D. Giuri, L. J. Marshall, C. Wilson, A. Seddon and D. J. Adams, *Soft Matter*, 2021, **17**, 7221-7226.

187. D. K. Kumar, D. A. Jose, A. Das and P. Dastidar, *Chem. Comm.*, 2005, **32**, 4059-4061.
188. Y. Xu, C. Kang, Y. Chen, Z. Bian, X. Qiu, L. Gao and Q. Meng, *Chem. Eur. J.*, 2012, **18**, 16955-16961.
189. J. Cui, Z. Shen and X. Wan, *Langmuir*, 2010, **26**, 97-103.
190. P. Zhu, X. Yan, Y. Su, Y. Yang and J. Li, *Chem. Eur. J.*, 2010, **16**, 3176-3183.
191. R. K. Das, R. Kandanelli, J. Linnanto, K. Bose and U. Maitra, *Langmuir*, 2010, **26**, 16141-16149.
192. D. Giuri, L. J. Marshall, B. Dietrich, D. McDowall, L. Thomson, J. Y. Newton, C. Wilson, R. Schweins and D. J. Adams, *Chem. Sci.*, 2021, **12**, 9720-9725.
193. M. Zhou, A. M. Smith, A. K. Das, N. W. Hodson, R. F. Collins, R. V. Ulijn and J. E. Gough, *Biomater.*, 2009, **30**, 2523-2530.
194. E. V. Alakpa, V. Jayawarna, A. Lampel, K. V. Burgess, C. C. West, S. C. J. Bakker, S. Roy, N. Javid, S. Fleming, D. A. Lamprou, J. Yang, A. Miller, A. J. Urquhart, P. W. J. M. Frederix, N. T. Hunt, B. Peault, R. V. Ulijn and M. J. Dalby, *Chem*, 2016, **1**, 512-512.
195. A. Singh and J. Elisseeff, *J. Mater. Chem.*, 2010, **20**, 8832-8847.
196. E. R. Cross, S. Sproules, R. Schweins, E. R. Draper and D. J. Adams, *J. Amer. Chem. Soc.*, 2018, **140**, 8667-8670.
197. W. Tanaka, H. Shigemitsu, T. Fujisaku, R. Kubota, S. Minami, K. Urayama and I. Hamachi, *J. Amer. Chem. Soc.*, 2019, **141**, 4997-5004.
198. L. Chen, S. Revel, K. Morris and D. J. Adams, *Chem. Comm.*, 2010, **46**, 4267-4269.

Chapter 2

Using gelator-structurally similar non-gelator multicomponent systems to achieve new behaviours in the micellar and gel states

This chapter is adapted from the following publication:

"Hierarchical Composite Self-Sorted Gel Noodles"

Advanced materials, **2023**, 35, 2211277.

L. J. Marshall, M. Wallace, N. Mahmoudi, G. Ciccone, C. Wilson, M. R. Vassalli, & D. J. Adams.

L. J. Marshall synthesised and characterised the gelators under investigation, performed the rheological experiments, N. Mahmoudi aided collection and processing of SANS data, G. Ciccone collected and processed nanoindentation data and C. Wilson collected and processed XRD data. B. Dietrich synthesised d-2Nap-dd-FF.

2.1 Introduction

Multicomponent systems composed of two structurally similar but behaviourally different components can be used to gain extra control over supramolecular systems and provide an easy method for introducing new properties and functionality into a system.[1, 2] Such multicomponent systems can conceptually form a range of different possible structures; they can self-sort, where each self-assembled structure formed only contains one of the components, or co-assemble, where each structure formed contains a mixture of the components (Figure 2.1a).[3-6] Co-assembly can be orthogonal, cooperative or destructive.[7] During orthogonal co-assembly, the components assemble independently in the presence of one another, forming distinct structural components.[7] In cooperative co-assembly, the structures formed contain an intimate mixture of each component.[7] The arrangement of the components in such assemblies can be ordered, as is the case with donor-acceptor systems,[8,9] or may be random.[10] Disruptive co-assembly occurs where the co-assembly of a mixture of components reduces the ability of the system to form self-assembled structures.[7] Each of these possibilities comes with potential for preparing new types of system that cannot be accessed when using a single component.

Co-assembled systems are useful for many applications. For example, bioactive peptides can be incorporated into a multicomponent gel network to improve cell culture viability.[11] Different modes of co-assembly are suited for certain applications. Cooperative co-assembly between structurally similar peptides can be used to achieve supramolecular charge transfer within stacked structures containing alternating donor and acceptor molecules for optoelectronic applications.[12] Alternatively, self-sorting of two components can be exploited to form interpenetrating networks of bulk heterojunctions containing domains of each individual component. Such architecture is desirable for p-n heterojunction photovoltaics.[13,14]

Here, we describe multicomponent systems composed of structurally similar *N*-functionalised dipeptides: 2NapLG (Figure 2.1bi), PhOLL (Figure 2.1ci) and 2NapVG (Figure 2.1cii) with the well-studied LMWG 2NapFF (Figure 2.1bii). Multicomponent systems composed of 2NapFF and 2-naphthoxyacetic acid (2Nap-OH, Figure 2.1ciii) were also studied to aid in understanding the assembly of these systems. We will focus the discussion on 2NapLG owing to its ability to consistently form high quality crystals in the presence and absence of 2NapFF under specific conditions.

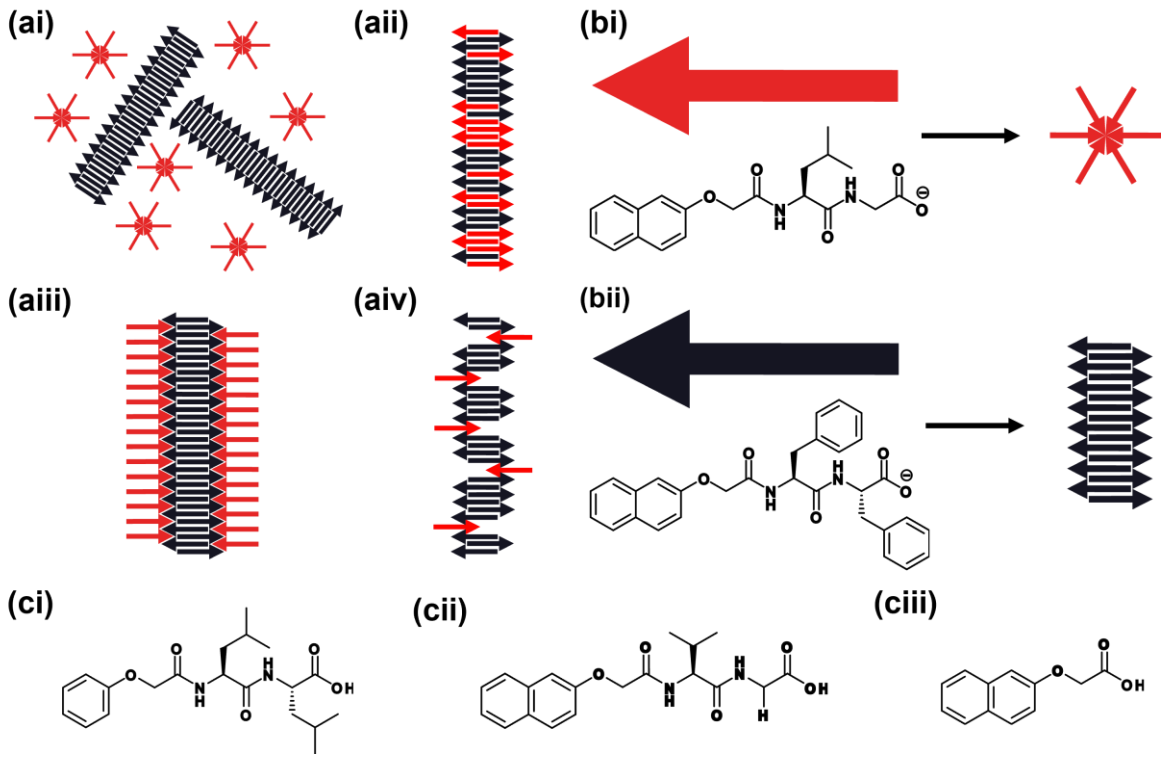

Figure 2.1. (a) Schematic representations of (i) self-sorting, (ii) co-operative co-assembly (iii) orthogonal co-assembly and (iv) disruptive co-assembly in a two-component system. (b) Chemical structures of (i) 2NapLG (shown schematically as a red arrow) which self-assembles to form non-persistent micelles at high pH and (ii) 2NapFF (shown schematically as a black arrow) which self-assembles to form long one-dimensional structures (worm-like micelles) at high pH at the concentrations discussed here. (c) Chemical structures of (i) PhOLL, (ii) 2NapVG and (iii) 2Nap-OH.

For two components to effectively co-assemble, they must share a common mode of assembly.[7, 15] There is therefore potential for 2NapLG, 2NapVG, PhOLL and 2Nap-OH to co-assemble with 2NapFF at high pH in their micellar states as they all contain an *N*-terminal aromatic group and a *C*-terminal carboxylic acid. Aromatic rings drive assembly through the formation of π-π interactions and the hydrophobic effect.[16] In such functionalised dipeptide-based systems, the carboxylic acid is used to trigger self-assembly via a reduction in pH[17] or by formation of salt bridges on addition of divalent cations.[18] Since all the dipeptides to be studied have different amino acid residues in their peptide chain, we expected co-assembly to take place in an orthogonal manner (Figure 2.1aiii). *N*-Functionalised dipeptides with a free carboxylic acid at the *C*-terminus behave like surfactants in solution at high pH.[4, 7, 19] Surfactants have previously been used to control the self-assembly behaviour of peptides.[2, 4, 7, 20] Each dipeptide studied here has the capability to control the assembly of the other component via its surfactant-like properties.

2.2 Results and Discussion

2.2.1 Viscosity of solutions at high pH

Despite their structural similarities, 2NapFF has very different behaviour in aqueous solution at high pH (see below) compared to the other *N*-functionalised dipeptides studied here. Co-assembly of two components with different behaviours provides an avenue for tuning the properties of micellar solutions and any resulting gel phases.

2NapFF forms worm-like micelles in solution at high pH.[19] Such solutions have a viscosity greater than that of water and exhibit shear-thinning behaviour (Figure A1.1.1, Appendix 1.1).[21] 2NapLG forms non-viscous solutions. This suggests that non-persistent micelles are formed by 2NapLG in solution at high pH.[22] Solutions containing a mixture of 2NapFF and 2NapLG at concentration ratios of 2.5 mg/mL:2.5 mg/mL and 2.5 mg/mL:5 mg/mL (2NapLG:2NapFF) show greater viscosity than either component alone at the same concentrations at pH 10.5 (Figure 2.2a). This is particularly interesting since 2NapLG alone shows no shear-thinning behaviour (Figure A1.1.1, Appendix 1.1) and is considerably less viscous than 2NapFF (Figure 2.2a). These data strongly imply that the mixtures of 2NapFF and 2NapLG are not operating in a self-sorting fashion (where simple dilution of the 2NapFF would be expected to lead to a significant decrease in viscosity). 2NapVG, PhOLL and 2Nap-OH show the same behaviour as 2NapLG in solution at high pH (Figure 2.2).

All solutions (single and multicomponent) showed increased viscosity at reduced temperatures (Figure 2.2). Decreasing temperature is known to increase the viscosity of solutions, with temperature having a greater effect on non-Newtonian fluids and at higher concentrations.[23] The structural changes occurring at low temperature must be reversible since a reproducible increase and decrease in viscosity over three cycles of decreasing the temperature to 10 °C and returning it to 25 °C was observed in each system (Figure 2.2, inserts). The 2NapVG:2NapFF and 2Nap-OH:2NapFF systems showed lower reproducibility. The structures present in these systems may need more time to recover from the decrease in temperature than the other two systems.

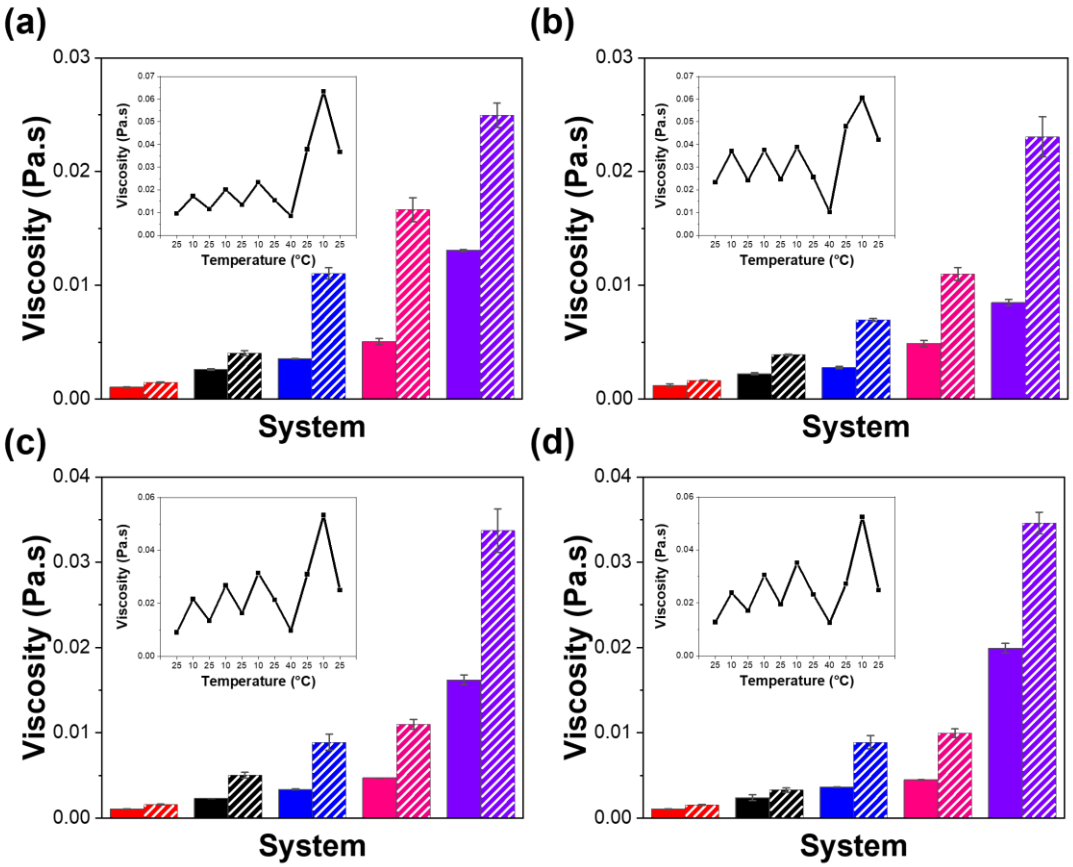

Figure 2.2. (a) Average viscosity values recorded at a shear rate of 10 s^{-1} for each system, where X = (a) 2NapLG, (b) PhOLL, (c) 2NapVG, and (d) 2Nap-OH in H_2O at pH 10.5; X 2.5 mg/mL (red), 2NapFF 2.5 mg/mL (black), X 2.5 mg/mL:2NapFF 2.5mg/mL (blue), 2NapFF 5 mg/mL (pink) and X 2.5 mg/mL:2NapFF 5 mg/mL (purple). Measurements were recorded in duplicate at 25 °C (shaded) and 10 °C (striped) with a fresh sample for each repeat. The error bars show the standard deviation between the samples. The inserts show the viscosity values collected from single samples of the 2.5 mg/mL:5 mg/mL multicomponent systems collected at a shear rate of 10 s^{-1} during the heat-cool cycles shown in chronological order along the *x*-axis. Full data can be found in Appendix 1.1.

Previous work shows that heating the self-assembled structures formed by 2NapFF results in irreversible structural changes.[24] On heating the multicomponent systems to 40 °C, the viscosity of the solution decreased due to dissolution of the assembled molecules (Figure 2.2, inserts). As observed previously with heat-cool cycles, cooling the resulting solution to 25 °C caused a dramatic increase in viscosity in the 2NapLG and PhOLL multicomponent systems as compared to the starting solutions.[24] Further reducing the temperature to 10 °C resulted in an even further increase in viscosity, showing that reducing the temperature is

still able to exert the same changes on the self-assembled structures achieved during previous heat-cool cycles.

Returning the temperature to 25 °C caused the viscosity to return to a similar value to that measured at 25 °C after the 25-40-25 °C heat-cool cycle. This further confirms the irreversible change in viscosity caused by heating and reversible change caused by cooling. The structures formed at 25 °C may be in a kinetically trapped state. Heating results in disassembly of the self-assembled structures. On re-cooling, the melted structures re-assemble in a more thermodynamically favourable fashion.[25] It is interesting that such heat-cool behaviour is not observed in 2NapFF alone at 5 mg/mL (Figure 2.3a). We are therefore able to achieve behaviours normally attributed to higher 2NapFF concentrations (10 mg/mL, Figure 2.3b) by incorporating a second component.

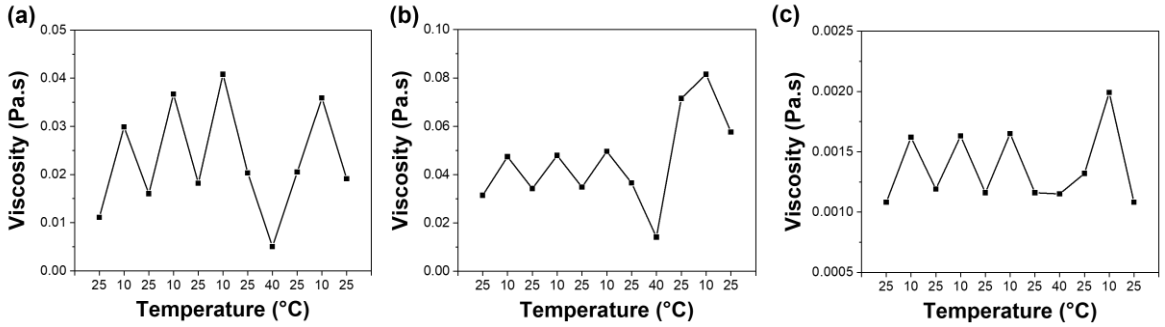

Figure 2.3. Viscosity values collected at a shear rate of 10 s^{-1} on a single sample during the heat-cool cycles shown in chronological order along the *x*-axis of (a) 2NapFF (5 mg/mL), (b) 2NapFF (10 mg/mL) and (c) 2NapLG (2.5 mg/mL) in H_2O at pH 10.5. Full data is shown in Appendix 1.1.

2NapFF alone at a concentration of 5 mg/mL (Figure 2.3a) does not show the same considerable jump in viscosity on returning to 25 °C after heating to 40 °C that is observed in the samples composed of 2NapFF alone at 10 mg/mL (Figure 2.3b) and in the multicomponent systems (Figure 2.2). This shows that the presence of a second component causes 2NapFF to behave as though its concentration has effectively doubled. 2NapLG alone (2.5 mg/mL, Figure 2.3c) does not show the same changes in viscosity throughout the heat-cool cycle (25-40-25 °C), showing that it is the interaction between the two components that causes the observed behaviours. Perhaps the transient nature of the micelles formed by 2NapLG prevents heating from having a significant effect on the structures formed while cooling causes the lifetime of any structures formed to increase, resulting in an increase in viscosity on a reduction in temperature.

The 2NapVG and 2Nap-OH 2.5 mg/mL:2NapFF 5 mg/mL multicomponent systems show intermediate behaviour between 2NapFF alone at concentrations of 5 mg/mL and 10 mg/mL. This agrees with previous studies into the behaviour of 2NapVG:2NapFF that showed that 2NapVG follows a template of assembly prepared by 2NapFF.[26] Instead of achieving new behaviours from the multicomponent system, the 2NapVG causes the system to behave as though the concentration of 2NapFF has been increased. We selected 2NapVG as a form of control as it is very similar in chemical structure to 2NapLG (the main focus of this project) and also forms non-viscous solutions at high pH. Thus far, it appears that despite differing in only a single amino acid residue, 2NapLG and 2NapVG have very different behaviours when mixed with 2NapFF.

2.2.2 CD spectroscopy

2NapFF alone assembles to form long, chiral structures in solution (Figure 2.4). The CD signal from these structures increases with increasing 2NapFF concentration as more 2NapFF molecules are available to form chiral structures. There are also slight shifts in the peaks arising from the structures, showing that the structures formed by 2NapFF at a concentration of 2.5 mg/mL have a different chiral arrangement to those formed at 5 mg/mL.

The peaks observed in the CD spectra of these systems arise from the naphthalene and phenylalanine rings, both of which have high extinction coefficients compared to the moieties usually found within peptides, being arranged into chiral environments during the self-assembly of these systems.[18] 2NapLG, PhOLL, 2NapVG and 2Nap-OH do not form chiral structures alone in solution at high pH and show little to no CD signal.

The CD spectra are complicated due to fact that all components in each system contain the same or similar absorbing groups.[18, 27] The contributions from each chromophore can be identified using the absorbance data (inserts), with signals in the range 180-215 nm arising from the chiral arrangement of phenylalanine rings and signals in the range 215-260 nm arising from the chiral arrangement of naphthalene rings.[28, 29] Amplification of the contributions from both the naphthalene and phenylalanine rings in the 2NapLG and 2Nap-OH multicomponent systems shows that these are not simply additive data sets of the two components.[30] This further implies co-assembly between these components and 2NapFF, rather than self-sorting. The signals from the naphthalene rings show a positive Cotton effect, likely caused by interaction between naphthalene rings in the self-assembled structures.[29,

[31,32] From previous work, the sign of the Cotton effect, and therefore the handedness of the chiral structures formed, depends on the identity of the amino acids in the peptide chain.[29]

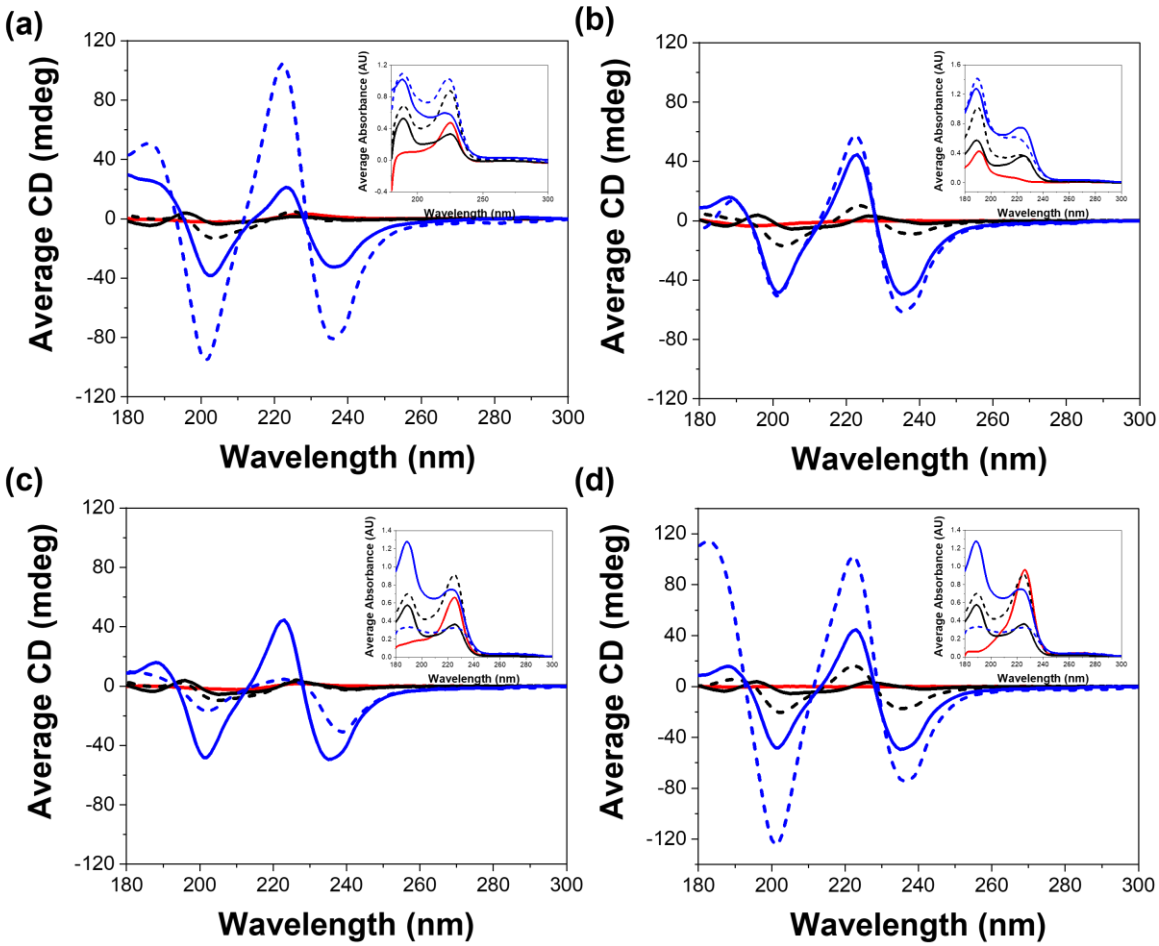

Figure 2.4. CD spectra and absorbance spectra (inserts) collected from samples containing (a) 2NapLG, (b) PhOLL, (c) 2NapVG and (d) 2Nap-OH. Spectra were recorded of each component alone at a concentration of 2.5 mg/mL (red), 2NapFF alone at concentrations of 2.5 mg/mL (black) and 5 mg/mL (blue), multicomponent systems at concentration ratios 2.5 mg/mL:2NapFF 2.5 mg/mL (black dashed), and 2.5 mg/mL:2NapFF 5 mg/mL (blue dashed) in H_2O at pH 10.5. All data was collected in triplicate and averaged. The inserts show the corresponding absorbance spectra for each system. These were recorded concurrently with the CD spectra. High tension (HT) data are shown in Appendix 1.2.

The CD spectra clearly show an amplification in the CD signals in all the multicomponent systems, as compared to their corresponding single component systems, the only exception being 2NapVG. This agrees with our conclusion from the viscosity data that, instead of diluting the chiral structures formed by 2NapFF, the presence of 2NapLG, 2Nap-OH, and to a lesser extent PhOLL, amplifies the CD signal, suggesting co-assembly resulting in a greater concentration of chiral, self-assembled structures.

Unlike the other second components, 2NapVG is incorporated into the structures formed by 2NapFF in a "sergeants and soldiers" fashion, as previously reported.[26] This appears to negatively impact the chirality of the structures formed in the 2NapVG 2.5 mg/mL:2NapFF 5 mg/mL system. The CD data illustrates that 2NapVG does not co-assemble with 2NapFF in the same manner as 2NapLG and PhOLL and that the effect that 2NapVG has on assembly changes as the 2NapFF concentration increases.

The intensity of the positive peak at 190 nm is unchanged in the PhOLL 2.5 mg/mL:2NapFF 5 mg/mL multicomponent system and is significantly reduced in the 2NapVG 2.5 mg/mL:2NapFF 5 mg/mL multicomponent system. This shows the importance of both the *N*-terminal group and the amino acid residues chosen for the second component in these systems. The single aromatic ring in PhOLL is less effective at co-assembly with 2NapFF than the naphthalene ring in 2NapLG. However, while 2NapVG also contains a naphthalene ring at the *N*-terminus, the replacement of the L residue in 2NapLG with the V residue in 2NapVG results in disruption of the chiral arrangement of the structures formed by self-assembly of 2NapFF.

2Nap-OH alone has a similar effect to 2NapLG on the CD signals, highlighting that the CD signals arise from the chiral stacking of the naphthalene rings. It also shows that the L residue in 2NapLG has a significantly different effect on assembly than the V residue in 2NapVG. 2NapLG allows the naphthalene rings to favourably stack together, while 2NapVG disrupts the chiral structures formed by 2NapFF at a concentration of 5 mg/mL.

It is possible that more fine structure is present in the spectrum. However, this may be masked by the intense signals from the naphthalene and phenylalanine chromophores owing to their effective π-π coupling.[33] Due to the instrumentation available to us, it was not possible to rule out any LD effects.[29]

CD data collected on heating a solution of 2NapFF (5 mg/mL) alone and a solution of 2NapLG 2.5 mg/mL:2NapFF 5 mg/mL show that the signal intensities persist to higher temperatures in the multicomponent system as compared to the single component system (Figure 2.5). The structures formed by the 2NapLG 2.5 mg/mL:2NapFF 5 mg/mL multicomponent system are therefore more thermally stable than those formed by the 2NapFF 5 mg/mL single component system.[34] This increases the utility and tuneability of the multicomponent system compared to the single component system of the same 2NapFF concentration.

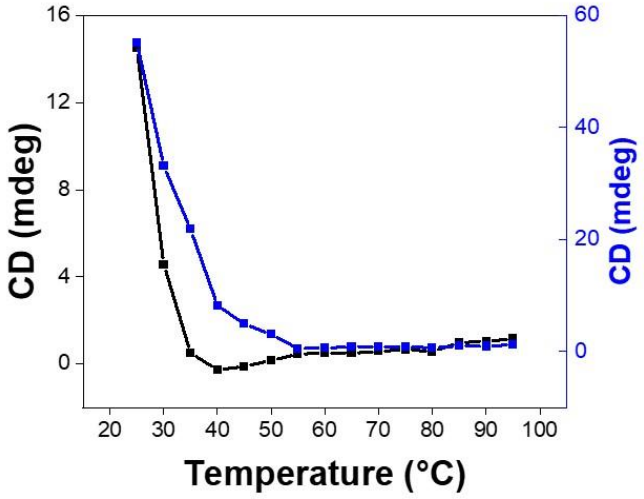

Figure 2.5. CD values recorded at 220 nm (arbitrary value selected based on proximity to a positive peak present in both systems) during variable-temperature CD spectroscopy experiments performed on micellar solutions of 2NapFF alone 5 mg/mL (black) and 2NapLG 2.5 mg/mL:2NapFF 5 mg/mL (blue) at pH 10.5. The temperature of the samples was increased in 5 °C increments from 25 °C to 95 °C, as shown in chronological order on the *x*-axis. Full data is shown in Figure A1.2.3, Appendix 1.2

2.2.3 NMR spectroscopy

We confirmed that 2NapLG forms physical interactions with the structures formed by 2NapFF in solution at high pH using nuclear Overhauser effect (NOE) nuclear magnetic resonance (NMR) experiments. In samples of 2NapLG alone, we observed a positive NOE difference to the β and γ protons when the methyl resonance was selectively inverted (Figure 2.6ai and aii). This confirms that 2NapLG behaves like a small molecule in solution at high pH, i.e., does not form persistent structures.[26, 35] However, in the presence of 2NapFF at 25 °C, a negative NOE difference was observed between the γ proton and the aromatic protons of 2NapFF (Figure 2.6aiii). These observations show that the 2NapLG is interacting with the large structures formed by 2NapFF.

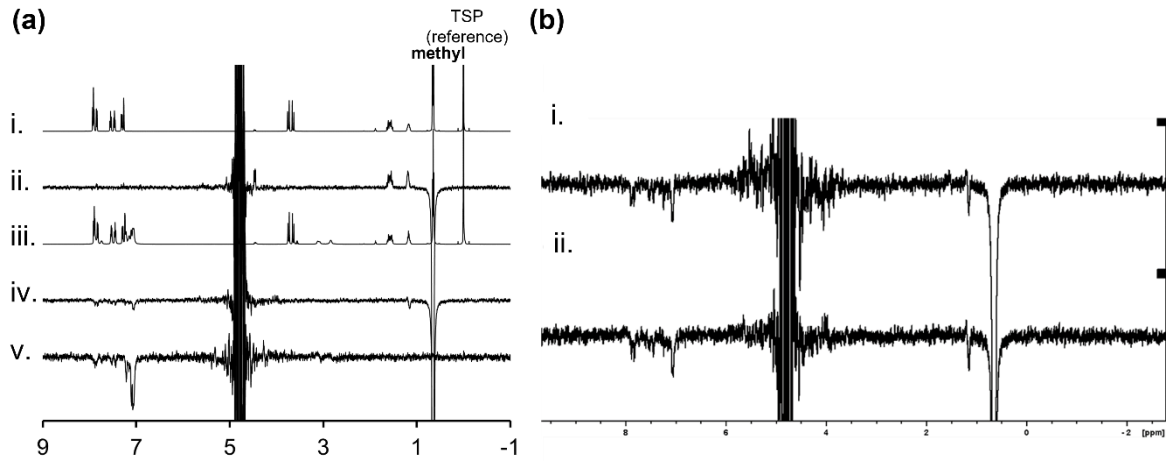

Figure 2.6. (a) ^{1}H NMR spectra of (i) 2NapLG 2.5 mg/mL, (ii) 2NapLG 2.5 mg/mL showing the NOE difference when methyl resonance inverted, (iii) 2NapLG 2.5 mg/mL:2NapFF 5 mg/mL and, (iv) 2NapLG 2.5 mg/mL:2NapFF 5 mg/mL showing the NOE difference when methyl resonance inverted and when phenylalanine aromatic resonance inverted (v). (b) NOE difference spectrum of 2NapLG 2.5 mg/mL:2NapFF 5 mg/mL at 25 °C before (i) and after (ii) full heat cycle. NMR data was collected and processed by M. Wallace (UEA, UK).

For 2NapFF, when the aromatic signal (most likely from the aromatic rings on the phenylalanine residues) is selectively inverted, we observe NOE to other aromatic protons and to the **CH$_2$**Ph groups of 2NapFF. The NOE difference is negative, as we would expect from the formation of worm-like micelles (Figure 2.6a, v). [26] No difference in the NOE was observed after heating to 40 °C (Figure 2.6b), showing that 2NapLG is still incorporated in the re-assembled structures after disassembly at high temperature.

We probed the co-assembly of 2NapLG with 2NapFF further using ^{1}H NMR spectroscopy. The integrals corresponding to protons on 2NapFF measured by ^{1}H NMR are smaller in the presence of 2NapLG, showing that more 2NapFF molecules are assembled in the multicomponent system (Figure 2.7).[36] This agrees with the increased CD signals observed both as 2NapFF concentration increases and as 2NapLG is added to the system (Figure 2.4a). All these data show that 2NapLG is influencing the self-assembly behaviour of 2NapFF. The ^{1}H integral of 2NapLG was the same in the presence and absence of 2NapFF, within experimental uncertainty (Figure 2.7). Therefore, the mobility of 2NapLG molecules on an NMR timescale do not change going from the single component to multicomponent system.

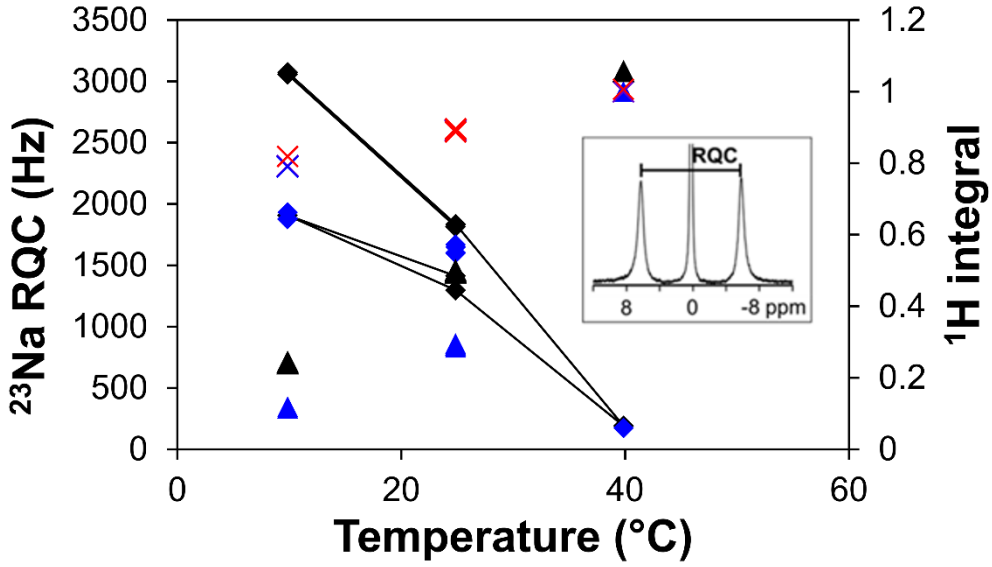

Figure 2.7. Plot of RQC of $^{23}Na^{+}$ (diamonds) and the ^{1}H integral of 2NapLG CH_3 (crosses) and of 2NapFF **CH_2**Ph (triangles) in 2NapLG 2.5 mg/mL:2NapFF 5 mg/mL (blue) and 2NapFF 5 mg/mL (black) and 2NapLG 2.5 mg/mL (red). The ^{1}H integrals were normalised to the value measured at 40 °C in the 2NapLG 2.5 mg/mL:2NapFF 5 mg/mL sample. The sample was subjected to a temperature cycle of 25-10-25-10-25-40-25-10-25 °C (the same as the viscosity heat-cool cycle). Inset: definition of ^{23}Na RQC, equal to double the residual quadrupolar coupling constant.[37] NMR data was collected and processed by M. Wallace (UEA, UK).

The integrals of selected peaks corresponding to 2NapFF and 2NapLG decrease going from 25 °C to 10 °C, showing that more molecules are in the assembled state at 10 °C than at 25 °C (Figure 2.7). This explains the reversible increase in viscosity observed at 10 °C: decreasing the temperature will decrease the rate at which the molecules exchange between self-assembled and free states. We expect that the self-assembled state is more energetically favourable resulting in more worm-like micelles being present at lower temperatures. No hysteresis was observed in the integrals of the protons on either 2NapFF or 2NapLG during the temperature cycles.

^{23}Na nuclei are present in the systems due to the addition of NaOH during preparation of the solutions at high pH (see Experimental Methods, Chapter 5). This allows us to measure the residual quadrupolar coupling (RQC) between the structures present in solution and ^{23}Na nuclei by ^{23}Na NMR experiments.[38] The ^{23}Na RQC increased with decreasing temperature, showing increased alignment in a magnetic field at lower temperatures (Figure 2.7).[38] This

agrees with the increased viscosity and decreased proton integrals observed on going from 25 °C to 10 °C, corresponding to a greater degree of assembly of the 2NapFF.

Measurements of RQC with ^{23}Na nuclei by ^{23}Na NMR experiments show that when 2NapFF 5 mg/mL alone is heated to 40 °C, the RQC does not recover while in the 2NapLG 2.5 mg/mL:2NapFF 5 mg/mL mixed system, the RQC lost on heating to 40 °C is always recovered when the temperature is returned to 25 °C. Prior to heating to 40 °C the RQC is much higher with 2NapFF 5 mg/mL alone. There is therefore a considerable change in the behaviour of 2NapFF in the presence of 2NapLG. A 2NapFF concentration of 5 mg/mL was selected based on previous work.[39] It is interesting that despite showing an irreversible increase in viscosity following a heat-cool cycle, the multicomponent system can recover alignment with the spectrometer field and exhibit a similar ^{23}Na RQC.

2.2.4 SANS

Small angle neutron scattering (SANS) data provide further evidence that 2NapLG is interacting with the structures formed by 2NapFF at high pH. 2NapLG (2.5 mg/mL in D_2O) alone does not scatter well enough to produce data of suitable quality for fitting (Figure 2.8b). This agrees with viscosity and NMR data and confirms that 2NapLG alone does not form persistent structures in aqueous solution. This makes it even more intriguing that 2NapLG has such a pronounced effect on the assembly behaviour of 2NapFF. 2NapFF alone forms long cylindrical structures in solution, commonly referred to as worm-like micelles. At a concentration of 2.5 mg/mL, data collected from a sample of 2NapFF (2.5 mg/mL in D_2O) were fitted to a cylinder model with a radius of 28 Å. A summary of all the parameters obtained from fitting SANS data can be found in Table 2.1.

D_2O was used as a solvent instead of H_2O to provide sufficient contrast between the solvent and the structures for high quality data to be collected.[40] Viscosity and CD experiments were repeated in D_2O to confirm that the same behaviour observed in H_2O is also observed in D_2O (Appendices 1.1 and 1.2).

SANS data collected from the 2NapLG 2.5 mg/mL:2NapFF 5 mg/mL multicomponent system were fitted to a hollow cylinder model (Figure 2.8). The hollow cylinder had a radius of 13 Å and a thickness of 22 Å. This shows that co-assembly with 2NapLG completely changes the structures formed by 2NapFF as the structures begin to resemble those formed at higher 2NapFF concentrations,[41] despite 2NapLG alone not forming cylindrical structures.

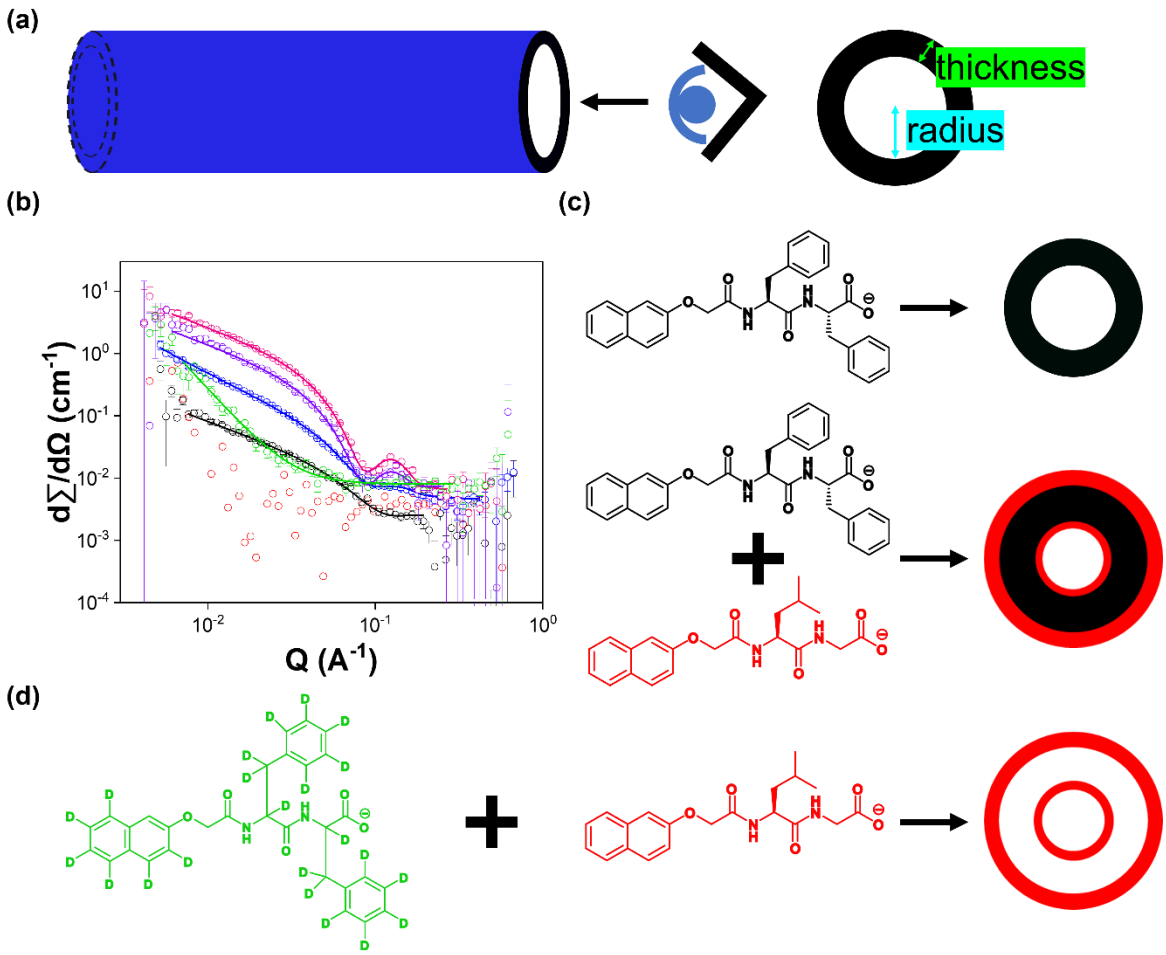

Figure 2.8. (a) Schematic visualising a hollow cylinder and what the thickness and radius parameters from SANS data correspond to in the context of a hollow cylinder. (b) Plots of SANS data (circles) from 2NapLG 2.5 mg/mL (red), 2NapFF 2.5 mg/mL (black), 2NapLG 2.5 mg/mL :2NapFF 2.5 mg/mL (blue), 2NapFF 5 mg/mL (pink), 2NapLG 2.5 mg/mL:2NapFF 5 mg/mL (purple) and 2NapLG 2.5 mg/mL:d2Nap-dd-FF 5 mg/mL (green). The fits are shown as solid lines, with the models used and parameters described in Table 2.1. (c) Schematic representations of how the systems studied here self-assemble, looking down the length of the hollow cylinders formed. (d) Schematic representation of the source of scattering from the sample composed of 2NapLG 2.5 mg/mL:d-2Nap-dd-FF 5 mg/mL (green).

When the concentration of 2NapFF was increased to 5 mg/mL, the scattering data were fitted to a hollow cylinder model giving a radius of 15 Å and thickness of 22 Å. The SANS data from the 2NapLG 2.5 mg/mL:2NapFF 5 mg/mL multicomponent system were also fitted to a hollow cylinder model.

The presence of 2NapLG resulted in changes to the structures as compared to those formed from 2NapFF alone. The radius of the inner core of the hollow cylinder decreased to 12 Å

and the thickness of the outer tube increased to 28 Å (Table 2.1). From comparison with similar work reported by Abul-Haija *et al.*,[2] we suggest that 2NapLG is behaving like a surfactant and is coating the inner and outer surfaces of the hollow cylinders formed by 2NapFF (Figure 2.8c). Co-assembly of gelator and surfactant molecules results in the formation of functionalised nanofibers, with the functional groups exposed on the surfaces of the fibres.[7] Despite partial incorporation of the surfactant into the self-assembled structures, Abul-Haija *et al*. reported that the core structure formed by the peptide-based gelator was unaffected by the presence of the surfactant-like component. Such systems can be thought of as undergoing orthogonal co-assembly.

Sample	2NapFF 2.5 mg/mL 25 ℃	2NapLG 2NapFF 2.5 mg/mL 25 ℃	2NapFF 5 mg/mL 25 ℃	2NapFF 5 mg/mL 10 ℃	2NapLG 2NapFF 5 mg/mL 25 ℃	2NapLG 2NapFF 5 mg/mL 10 ℃
Model	Cylinder	Hollow cylinder	Hollow cylinder	Hollow cylinder	Hollow cylinder	Hollow cylinder
Scale	7.55×10^{-5}	1.85×10^{-4}	0.0015	0.0022	0.0019	0.0023
Scale error	*3.55×10^{-6}*	*2.71×10^{-6}*	*3.73×10^{-5}*	*7.33×10^{-5}*	*4.75×10^{-5}*	*5.81×10^{-5}*
Background	0.0024	0.044	0.0080	0.011	0.0060	0.015
Radius	28.2	13.0	14.8	14.4	14.8	14.3
Radius error	*0.73*	-	*0.45*	*0.59*	*0.46*	*0.48*
Thickness	-	22.0	23.5	23.7	23.9	24.6
Thickness error	-	-	*0.68*	*0.91*	*0.70*	*0.74*
Length	5000	5000	5000	5000	5000	5000
Reduced χ^2	**1.13**	**4.38**	**4.49**	**1.09**	**2.85**	**2.21**

Table 2.1. Summary of the parameters obtained from fitting the SANS data. 2NapLG always had a concentration of 2.5mg/mL. Fitting parameters were obtained from SasView model fitting of the SANS data. Parameter errors are fitting errors. Length was set to 5000 as the length of the structures under investigation is beyond the length scale measurable by SANS. 2NapFF 2.5 mg/mL was best fit to a cylinder model. All other data sets were best fit to a hollow cylinder model. These models were selected as they provided the best fits to the data by eye and according to χ^2 values.

Selective deuteration of 2NapFF allowed us to probe how 2NapLG alone scatters in the multicomponent system.[40] The mostly deuterated analogue, d2Nap-dd-FF (Figure 2.8d), forms viscous solutions like 2NapFF, but does not scatter well by SANS, as expected due to the lack of contrast. Interestingly, samples composed of 2NapLG:d2Nap-dd-FF at either concentration ratio do not scatter well. From ^{1}H NMR spectra, we are confident that the deuterated 2NapFF defined in Figure 2.8d was present in the samples studied. The loss of

scattering intensity on removal of the scattering contribution from 2NapFF suggests that 2NapLG is forming weakly scattering shells on the inner and outer surfaces of the structures formed by 2NapFF (Figure 2.8d).

This behaviour is different to that previously observed in a similar multicomponent system composed of 2NapFF and 2NapVG.[26] Like 2NapLG, 2NapVG alone forms spherical micelles in solution at high pH. Unlike 2NapLG, 2NapVG does not alter the structures formed by 2NapFF in solution at high pH. Instead, 2NapVG behaves in the same way as additional 2NapFF molecules. This was described as a "sergeants and soldiers" manner of assembly where 2NapFF directs the assembly of 2NapVG.[26] This mode of assembly fits under the umbrella of cooperative co-assembly.

SANS data shows that reducing temperature did not significantly affect the structures (Table 2.1), despite increasing the viscosity of the solutions. This supports the hypothesis that reducing temperature increases the effective concentration of the self-assembled structures without causing structural changes.

The SANS data from systems containing PhOLL showed that PhOLL had a similar effect on the self-assembled structures to 2NapLG, although less pronounced (Figure 2.9a). This agrees with the changes in behaviour recorded during viscosity measurements and CD spectroscopy. The behaviours observed using 2NapLG can therefore be achieved using other, similar molecules.

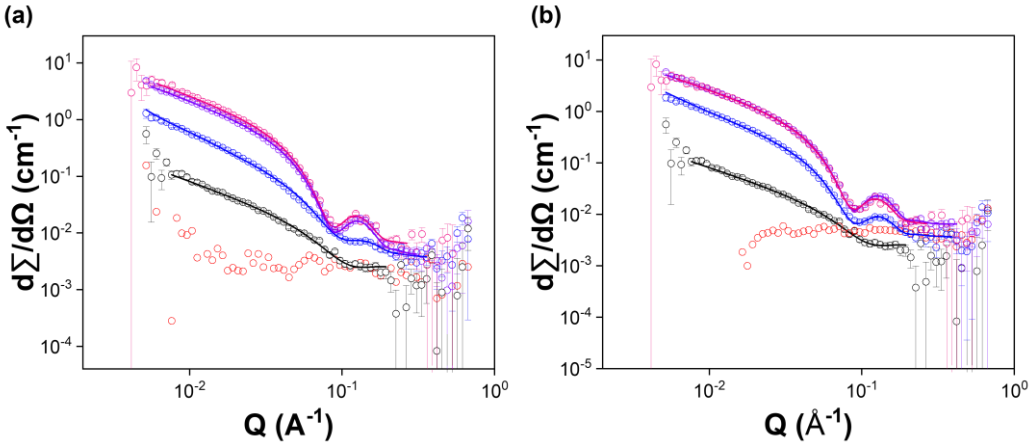

Figure 2.9. Plots of SANS data (circles) from 2NapFF 2.5 mg/mL (black) and 2NapFF 5 mg/mL (pink) alongside (a) PhOLL and (b) 2Nap-OH alone 2.5 mg/mL (red) and mixed with 2NapFF at concentration rations of 2.5 mg/mL:2.5 mg/mL (blue) and 2.5 mg/mL: 5 mg/mL (purple). Fits are shown as solid lines, with the models used and parameters described in Table 2.2.

Sample	PhOLL 2NapFF 2.5 mg/mL 25 ℃	PhOLL 2NapFF 5 mg/mL 25 ℃	2Nap-OH 2NapFF 2.5 mg/mL 25 ℃	2Nap-OH 2NapFF 5 mg/mL 25 ℃
Model	Hollow cylinder + power law	Hollow cylinder	Hollow cylinder + power law	Hollow cylinder
A Scale	2.09 x10^{-4}	0.0014	5.18 x10^{-4}	0.0021
Scale error	*2.86 x10^{-6}*	*1.85 x10^{-6}*	*3.61 x10^{-6}*	*2.26 x10^{-5}*
Background	0.0034	0.0042	0.0035	0.0065
Radius	13.0	16.3	15.1	17.4
Radius error	-	*0.038*	-	*0.13*
Radius polydispersity	0.13	0.25	-	0.18
Thickness	21.0	18.8	21.9	18.0
Thickness error	-	-	-	*0.21*
Length	5000	5000	5000	5000
B scale	6.31 x10^{-5}	-	2.58 x10^{-5}	-
B scale error	*3.42 x10^{-6}*	-	*2.15 x10^{-6}*	-
B power	1.78	-	1.96	-
B power error	*0.012*	-	*0.018*	-
Reduced χ^2	**5.56**	**6.29**	**6.66**	**10.78**

Table 2.2. Fitting parameters were obtained from SasView model fitting of the SANS data. Parameter errors are fitting errors. All data in the above was fit to a hollow cylinder model (with or without a power law) as this model provided the best fit by eye and according to χ^2 values. Length was set to 5000 as the length of the structures under investigation is beyond the length scale measurable by SANS.

We used 2Nap-OH:2NapFF multicomponent systems as a control for the SANS data. Like 2NapLG, 2Nap-OH does not scatter well alone (Figure 2.9b). When mixed with 2NapFF, we saw increased scattering compared to 2NapFF alone at the same 2NapFF concentrations, showing that 2Nap-OH is incorporated into the 2NapFF structures in a similar fashion to 2NapLG. However, we did not observe the same decrease in radius and increase in thickness as was seen with 2NapLG (Table 2.2). This further proves that the LG residues from 2NapLG are left exposed on the inner and outer surfaces of the hollow cylinders formed by the co-assembled multicomponent systems.

2.2.5 Supramolecular gel noodles

2NapFF can form gels using calcium ions as a trigger.[18] The divalent cations form cross-links between deprotonated carboxylic acid groups on neighbouring worm-like micelles, resulting in formation of a network.[18] The 2NapLG 2.5 mg/mL:2NapFF 5 mg/mL

multicomponent system also formed stable gels using a calcium trigger (Figure 2.10). The 2NapLG 2.5 mg/mL:2NapFF 5 mg/mL multicomponent gels had similar stiffness (G′) to the 2NapFF (5 mg/mL) single-component gels but notably higher strength (determined by the strain value at which G″ crosses over G′, Figure 2.10).

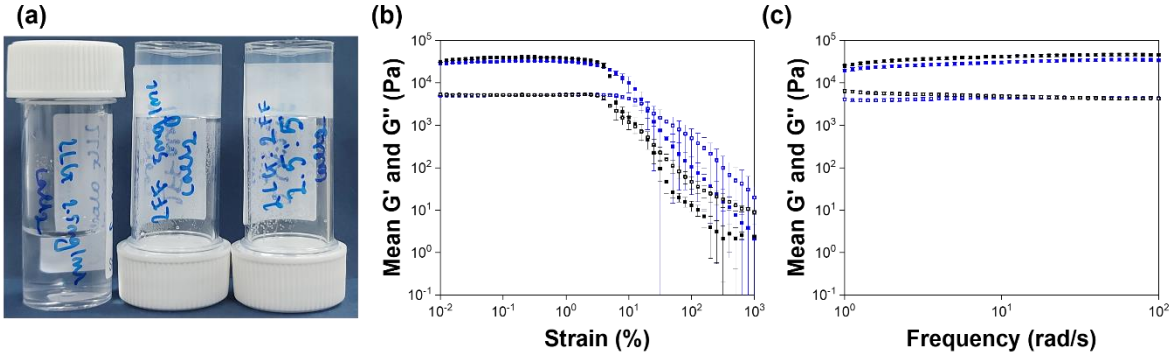

Figure 2.10. (a) Photographs of 2NapLG 2.5 mg/mL, 2NapFF 5 mg/mL and 2NapLG 2.5 mg/mL:2NapFF 5 mg/mL solutions (left to right) on addition of 2 molar equivalents of $CaCl_2$. (b) Strain sweeps and (c) frequency sweeps of gels formed from 2NapFF 5 mg/mL (black) and 2NapLG 2.5 mg/mL:2NapFF 5 mg/mL using $CaCl_2$ as a trigger. Samples were collected in triplicate and averaged. Error bars show the standard deviation between samples.

Interest is growing in supramolecular noodles, first reported by Zhang *et al*,[42] for optoelectronics,[43] regenerative medicine,[44] and as tough, flexible materials.[45] The ability of the 2NapLG 2.5 mg/mL:2NapFF 5 mg/mL multicomponent system to form gels using $CaCl_2$ as a trigger was a good indication that this system would form supramolecular noodles. The higher viscosity in the solution phase and greater mechanical strength in the gel state of the multicomponent system compared to 2NapFF alone led us to hypothesise that the inclusion of 2NapLG would allow formation of more robust supramolecular noodles than those formed by 2NapFF alone.

Noodles were prepared using the syringe-pump and spin-coater setup as previously described (Figure 2.11a).[46] The noodles formed were sufficiently robust to be transferred from the plastic petri dish in which they were formed to a glass surface to allow nanoindentation measurements to be performed (Figure 2.11b). However, it was clear that the 2NapFF noodles were less mechanically robust than the multicomponent noodles (Figure A1.3.1, Appendix 1.3). We recorded maps of indentations,[47] along the length of several noodles prepared from the 2NapFF 5 mg/mL single component system and from the 2NapLG 2.5 mg/mL:2NapFF 5 mg/mL multicomponent system; and quantified the mechanical response by fitting force-indentation data with the Hertz model to obtain the Young's modulus, as explained in the Experimental Methods (Chapter 5).

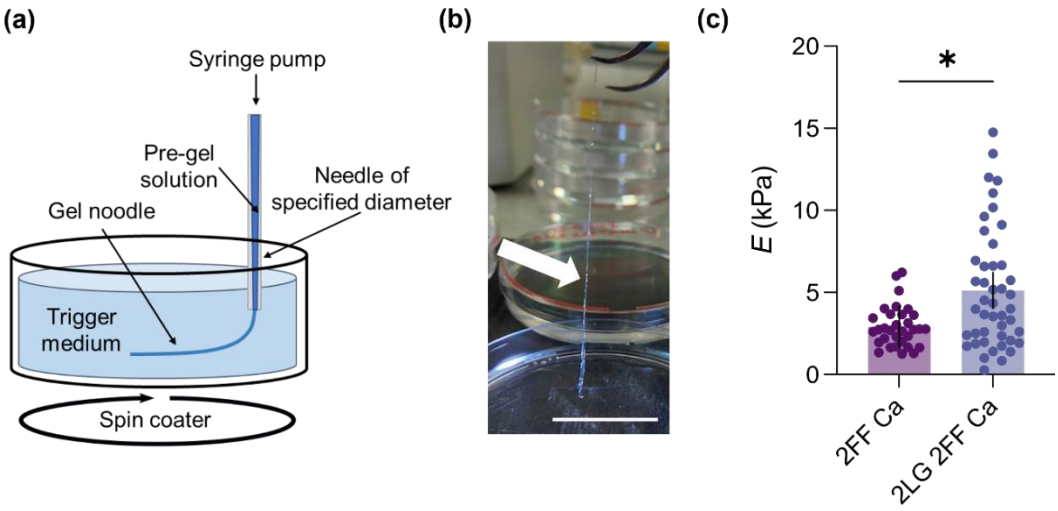

Figure 2.11. (a) Schematic showing how the noodles were prepared using the syringe pump and spin coater set up. $CaCl_2$ (0.5 M, aqueous solution) was used as the trigger medium by providing Ca^{2+} ions which cross-link the gelator molecules, allowing formation of a gel network. (b) Photograph of 2NapLG 2.5 mg/mL:2NapFF 5 mg/mL supramolecular noodle during transfer from its trigger medium (noodle highlighted by white arrow for clarity). The scale bar shows 300 mm. (c) Young's modulus (*E*) of noodles composed of 2NapFF 5 mg/mL (2FF Ca) and 2NapLG 2.5 mg/mL:2NapFF 5 mg/mL (2LG 2FF Ca). Mean ± 95% CI, n=33 for 2FF Ca, n=48 for 2LG 2FF Ca obtained from at least two separate noodles, *p<0.05, two-tailed Mann-Whitney test.

Multicomponent noodles have greater Young's modulus than the single component noodles (Figure 2.11c), showing how the mechanical properties of such gel noodles can be modulated by the addition of a second component. We were able to achieve the same outcomes using a similar second component to 2NapLG, PhOLL (Figure 2.12), thus showing that this is not an exceptional case.

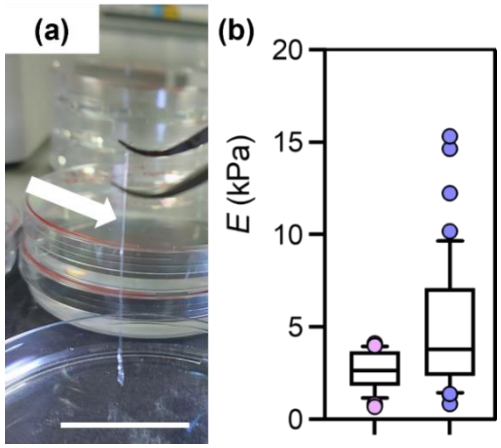

Figure 2.12. (a) Photograph of a noodle formed from PhOLL 2.5 mg/mL:2NapFF 5 (noodle highlighted by white arrow for clarity). (b) Results from nanoindentation of noodles composed of 2NapFF 5 mg/mL (pink) and PhOLL 2.5 mg/mL:2NapFF 5 mg/mL (purple).

2.2.6 Composite supramolecular gel noodles

Micellar dispersions of 2NapFF at high pH form supramolecular hydrogels on a reduction in pH using glucono-δ-lactone (GdL).[48] 2NapLG forms crystals under the same conditions (Figure 2.13). By slightly reducing the pH of the environment surrounding pre-formed 2NapLG:2NapFF gel noodles to just below that of the first apparent pK_a of the system (Figure 2.14), we were able to form crystals within the gel noodles (Figure 2.15a and Figure A1.3.2, Appendix 1.3). The formation of crystals within the gel noodles shows that the system is transitioning from co-assembly to self-sorted assembly when the pH is reduced below a critical value. Crystals were able to form at pH values as high as 8.0 by simply transferring the noodles from the $CaCl_2$ solution in which they were formed to a bath of deionised H_2O (pH 7-8).

The starting pH of all solutions used to prepare crystals was 10.5. On addition of 20 mg/mL of solid GdL, the medium in which the crystals were formed had a final pH of ~3.5 for both the single and multicomponent systems. To further investigate the ability of 2NapLG to form crystals at high pH, we attempted to form crystals from a solution of 2NapLG alone using $CaCl_2$ as a trigger. Addition of 2 molar equivalents of Ca^{2+} ions (with respect to 2NapLG) to a solution of 2NapLG alone resulted in formation of crystals within a medium with a final pH of ~10.0. No crystals were obtained on addition of $CaCl_2$ to 2NapLG:2NapFF multicomponent systems. Co-assembly of 2NapLG and 2NapFF at high pH therefore prevents crystal formation. While no polymorphism was observed between the different 2NapLG crystals formed in the presence and absence of 2NapFF at low (pH ~3.5), 2NapLG crystals formed at higher pH (pH ~10.0) on addition of $CaCl_2$ had different morphology (Figure 2.13a-c) and powder X-ray diffraction (PXRD) pattern (Figure 2.13e) to those formed at low pH. We were unable to obtain a single crystal diffraction pattern from the 2NapLG crystals formed *via* addition of $CaCl_2$ and were therefore unable to confirm whether polymorphism was taking place. From these results, we expect that Ca^{2+} ions present in the noodles may be helping 2NapLG to form crystals within the gel noodles.

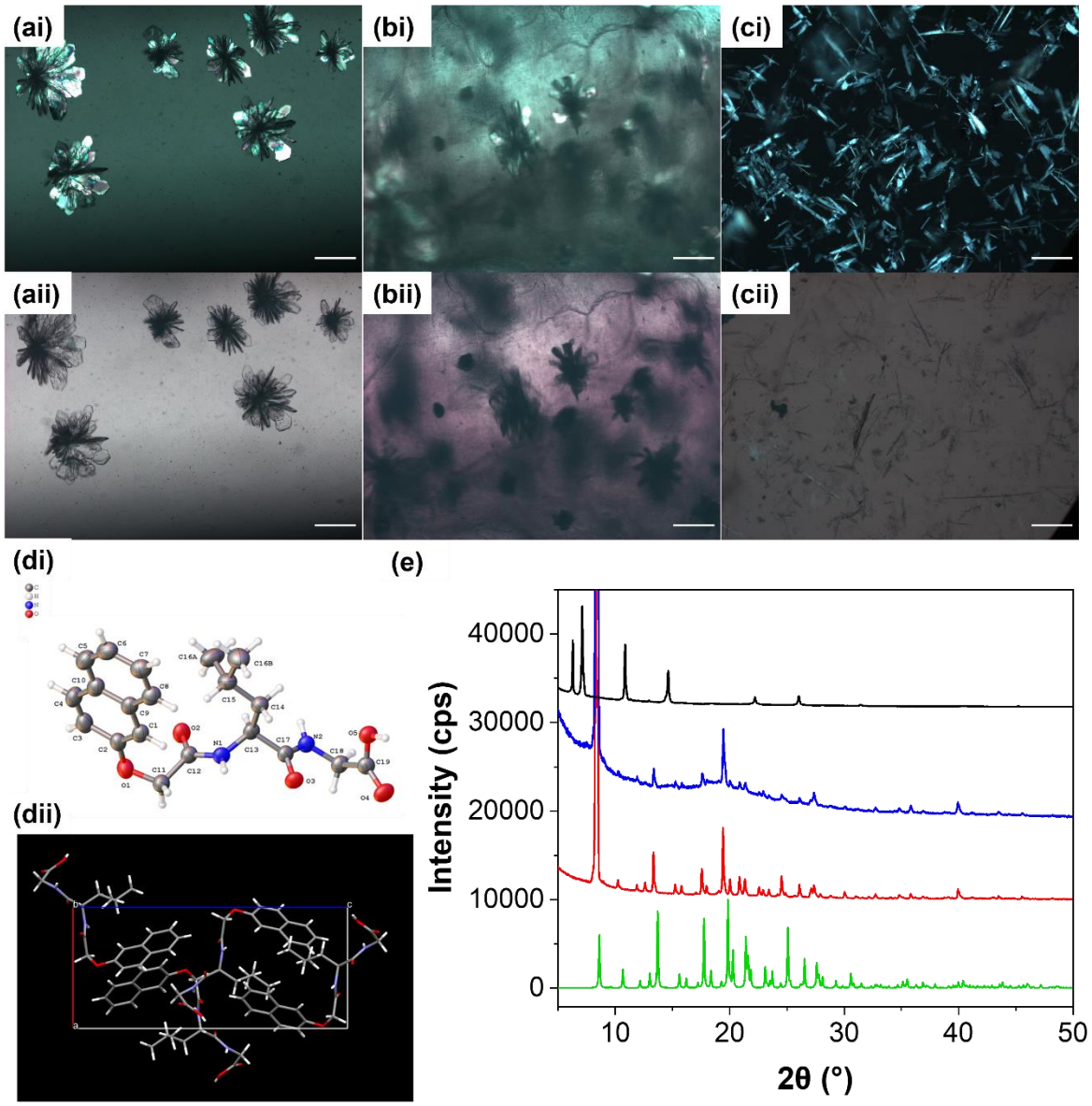

Figure 2.13. Crystals formed from aqueous solutions of (a) 2NapLG alone and (b) 2NapLG and 2NapFF formed by a reduction in pH (from 10.5 to ~3.5) using GdL as a trigger and (c) 2NapLG alone using $CaCl_2$ as a trigger. Images were collected under (i) cross-polarised and (ii) non-polarised light. Scale bars represent 300 µm. (di) Single crystal structure and (ii) crystal packing of 2NapLG obtained from crystals prepared *via* reduction in pH using GdL. (b) Comparison of the single crystal (green) and PXRD patterns obtained from 2NapLG crystals formed alone (red) and in the presence of 2NapFF (blue) in aqueous conditions on a reduction in pH using GdL showing the absence of any polymorphism in when the crystals are formed in conjunction with a 2NapFF gel. A PXRD pattern was also obtained from crystals formed from 2NapLG alone in aqueous conditions on addition of 2 molar equivalents of $CaCl_2$ (200 mg/mL, aqueous solution, black). Single crystal data for 2NapLG is shown in Table A1.4.1, Appendix 1.4.

We expect that the same effect as observed in similar multicomponent systems, where charge is removed from the component with the higher apparent pK_a first,[49, 50] is allowing the system to transition from co-assembly to self-sorting on a reduction in pH. Such charge removal drives self-assembly of the first component, while the second component still carries its charge and thereby remains dispersed in solution. The pH change on transfer of the gel noodles from the $CaCl_2$ solution in which they are formed to deionised H_2O allows the system to spend sufficient time at a pH value that is below the apparent pK_a of the first component (in this case 2NapFF, Figure 2.14b) and above the apparent pK_a of the second (2NapLG, Figure 2.14a), resulting in a preference for self-sorting.

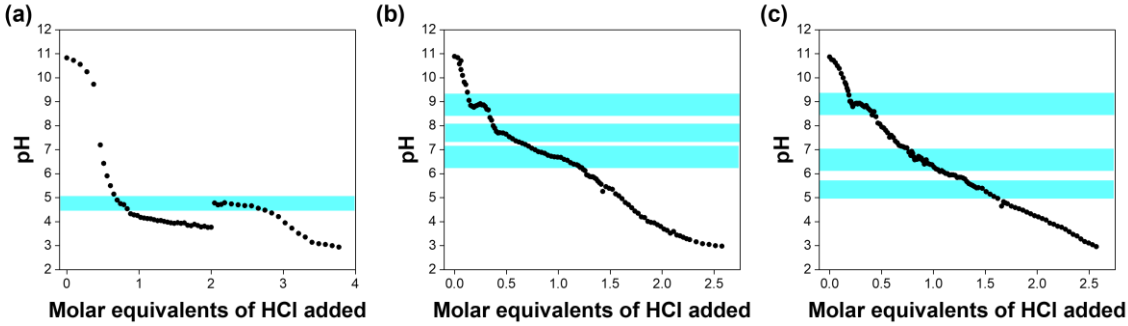

Figure 2.14. pH titrations of (a) 2NapLG 2.5 mg/mL, (b) 2NapFF (5 mg/mL) and (c) 2NapLG 2.5 mg/mL:2NapFF 5 mg/mL. The blue shading highlights the plateaus from which the pK_a values were extrapolated. Raw values from pH titrations are shown in Appendix 1.5.

The kinetics of pH reduction therefore plays an important role in crystal formation. For example, no crystal formation was observed when the multicomponent noodles were transferred directly into acidic solution e.g., 0.1 M HCl. Such fast pH reduction does not allow sufficient time at the appropriate pH value for self-sorting to occur. It is possible that secondary nucleation occurs in the co-assembled structure, but this is a difficult aspect to probe.

The fact that 2NapLG alone can form crystals on addition of $CaCl_2$ but when mixed with 2NapFF, addition of $CaCl_2$ results in formation of a stable gel with no visible crystals is evidence for co-assembly between 2NapFF and 2NapLG within specific pH values. Presumably, the incorporation of the 2NapLG molecules in the assembled structures makes them unavailable for crystal formation. After a sufficient reduction in pH, self-sorting allows 2NapLG to form crystals (Figure 2.15a).

Nanoindentation was used to investigate the effect of crystal formation on the mechanical properties of the noodles. Figure 2.15b clearly shows a marked increase in the slope of the indentation curves (apparent stiffness)[52] when transitioning from a region with the gel only

to an area where crystals are present. We were unable to perform nanoindentation measurements on the single component noodles following a reduction in pH as reducing the pH causes the noodles to become more brittle and break during transfer to the surface required form indentations to be performed.

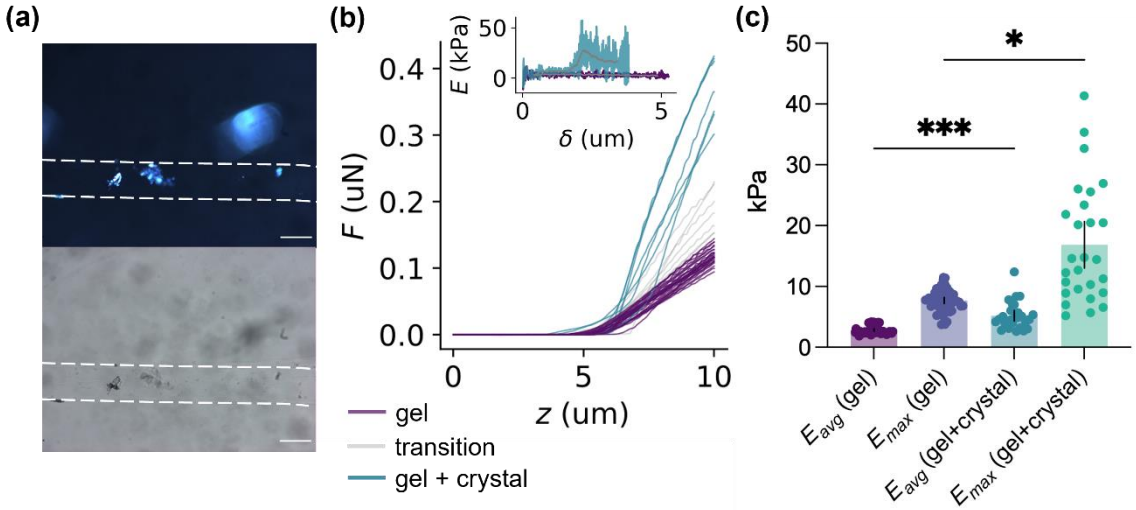

Figure 2.15. (a) Optical microscope images collected under cross-polarised (top) and non-polarised light (bottom). White dashed lines highlight the outer edges of the noodles. Scale bars show 300 μm. (b) Representative force (F)-distance (z) nanoindentation curves of a composite noodle transitioning from a region devoid of crystal (gel, purple) to a region containing a crystal (gel + crystal, green). The increased slope represents an increase in stiffness. Inset shows *E* as a function of indentation depth, δ, obtained using the elasticity spectra approach[51] for a region devoid of crystal (purple) and for a region containing a crystal (green). Gray traces are smoothed data. (c) Young's modulus (*E*) of composite noodles containing crystals obtained using the elasticity spectra approach. Data were collected from regions without crystals (gel) and from regions containing crystals (gel + crystal) and the *E* calculated as a function of the indentation depth. The bars show for each condition the value of the soft (E_{avg}) and stiff components (E_{max}) (see Experimental Methods). Mean ± 95% CI, n=51 for gel and n=27 for gel+crystal obtained from at least 2 separate noodles, * p=0.0337, *** p = 0.0005, One-way ANOVA with Kruskal-Wallis multiple comparison test.

Because of the non-homogeneous nature of the sample, we calculated the elasticity spectra, computing Young's modulus as a function of indentation depth[51] for regions containing the gel only and the gel plus crystal (Figure 2.15b). To obtain quantifiable metrics of the elasticity of the system, we computed the soft (E_{avg}) and hard (E_{max}) components of each elasticity spectrum (see Experimental Methods, Chapter 5). As observed in Figure 2.15c, the

crystals impact on the mechanical properties of both phases, and, as expected, the increase in the rigid component is much more pronounced.

PhOLL also forms crystals alone and in the presence of 2NapFF on a reduction in pH using GdL. The number and size of these crystals is greatly reduced in the presence of 2NapFF (Figure 2.16). We also observed small, sparse crystals in PhOLL:2NapFF noodles. These crystals were too small to be investigated using nanoindentation. However, these observations further prove that 2NapLG is not a special case. It should therefore be possible to prepare crystals in noodles using similar multicomponent systems provided one component forms crystals under the same conditions that the second forms gels.

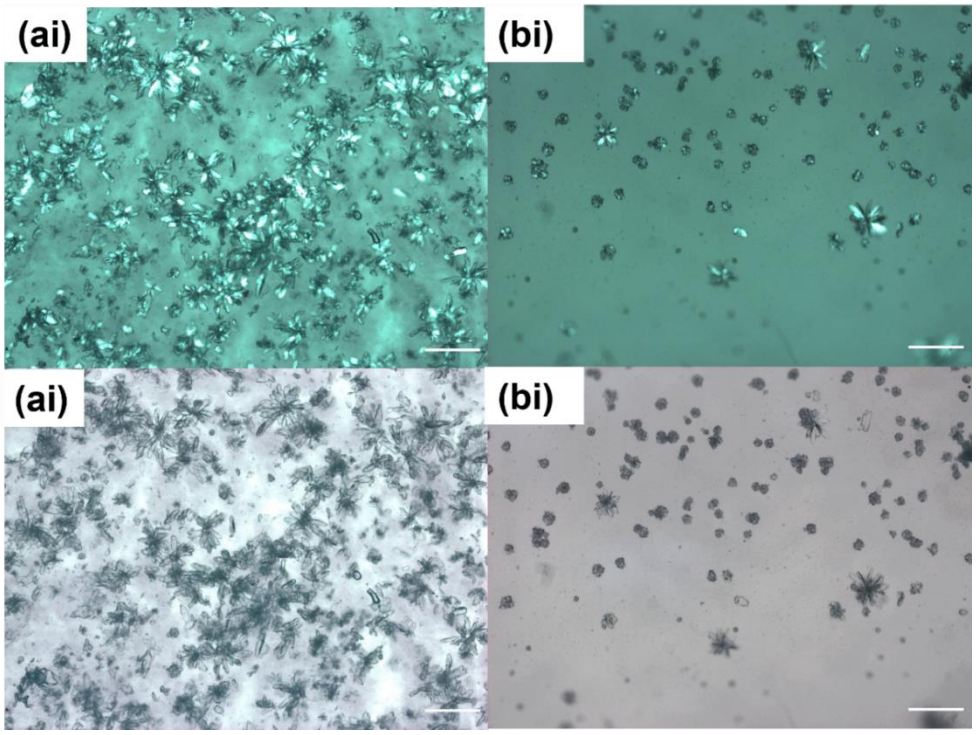

Figure 2.16. Crystals formed from aqueous solutions of (a) PhOLL alone and (b) PhOLL and 2NapFF formed by a reduction in pH using GdL as a trigger. The starting pH of all solutions was 10.5. Addition of 20 mg/mL of GdL gave a final pH of 3. Images were collected under cross-polarised (top) and non-polarised (bottom) light. Scale bars represent 300 μm.

The formation of crystals/removal of 2NapLG molecules from the bulk gel network causes the network to shrink and expel the solvent, a process known as syneresis (Figure A1.6.1, Appendix 1.6). Reducing the temperature at which the bulk gels were formed increased the lifetime of the stable gel phase but did not prevent syneresis. Syneresis is not observed in the noodles, where crystals were formed at significantly higher pH than the bulk gels formed on a reduction in pH using GdL. We suspect the smaller proportion of 2NapLG molecules

being involved in crystal formation prevents disruption of the gel network (Figure A1.6.5, Appendix 1.6). The same behaviours are observed in PhOLL:2NapFF multicomponent systems (Figure A1.6.6, Appendix 1.6).

We expect there is potential for spatial and temporal control over crystal formation within the noodles, for example, through use of a photoacid trigger that provides appropriate pH reduction.[53] There is also potential for further control over the properties of the gel noodles using temperature, for example, by exposing the pre-gel solution to a heat-cool cycle prior to noodling.[24, 54]

2.3 Conclusions

We have shown how the preparation of multicomponent systems from two structurally similar, but behaviorally different components can be used to modulate the properties of a LMWG in both the sol and gel phases. The properties of such systems can be tuned further using temperature. Using these multicomponent systems, we have exemplified the potential of multicomponent supramolecular noodles and how the interesting behavior of the individual components can be exploited to achieve new behaviors. We were able to achieve the same outcomes using a similar second component to 2NapLG, PhOLL, thus showing that 2NapLG is not an exceptional case. We can harness the crystal-forming behavior of one component and the supramolecular gel noodle-forming behavior of a second component to achieve a composite material with both solid and viscoelastic behavior. These unusual materials significantly expand the scope of such soft materials.

2.4 References

1. V. Jayawarna, S. M. Richardson, A. R. Hirst, N. W. Hodson, A. Saiani, J. E. Gough and R. V. Ulijn, *Acta Biomater.*, 2009, **5**, 934-943.
2. Y. M. Abul-Haija, S. Roy, P. W. J. M. Frederix, N. Javid, V. Jayawarna and R. V. Ulijn, *Small*, 2014, **10**, 973-979.
3. E. R. Draper and D. J. Adams, *Chem. Soc. Rev.*, 2018, **47**, 3395-3405.
4. P. Makam and E. Gazit, *Chem. Soc. Rev.*, 2018, **47**, 3406-3420.
5. B. Adelizzi, N. J. Van Zee, L. N. J. de Windt, A. R. A. Palmans and E. W. Meijer, *J. Am. Chem. Soc.*, 2019, **141**, 6110-6121.

6. M. M. Safont-Sempere, G. Fernandez and F. Wuerthner, *Chem. Rev.*, 2011, **111**, 5784-5814.
7. S. Fleming, S. Debnath, P. W. J. M. Frederix, N. T. Hunt and R. V. Ulijn, *Biomacromolecules*, 2014, **15**, 1171-1184.
8. K. V. Rao and S. J. George, *Chem. Eur. J.*, 2012, **18**, 14286-14291.
9. C. Wang, Y. Guo, Z. Wang and X. Zhang, *Langmuir*, 2010, **26**, 14509-14511.
10. H. A. Behanna, K. Rajangam and S. I. Stupp, *J. Am. Chem. Soc.*, 2007, **129**, 321-327.
11. W. Liyanage, K. Vats, A. Rajbhandary, D. S. W. Benoit and B. L. Nilsson, *Chem. Comm.*, 2015, **51**, 11260-11263.
12. M. Pandeeswar, S. P. Senanayak, K. S. Narayan and T. Govindaraju, *J. Am. Chem. Soc.*, 2016, **138**, 8259-8268.
13. H. Kar and S. Ghosh, *Isr. J. Chem.*, 2019, **59**, 881-891.
14. K. Sugiyasu, S. I. Kawano, N. Fujita and S. Shinkai, *Chem. Mater.*, 2008, **20**, 2863-2865.
15. M. Halperin-Sternfeld, M. Ghosh, R. Sevostianov, I. Grigoriants and L. Adler-Abramovich, *Chem. Comm.*, 2017, **53**, 9586-9589.
16. G. Fichman and E. Gazit, *Acta Biomater.*, 2014, **10**, 1671-1682.
17. D. J. Adams, M. F. Butler, W. J. Frith, M. Kirkland, L. Mullen and P. Sanderson, *Soft Matter*, 2009, **5**, 1856-1862.
18. L. Chen, G. Pont, K. Morris, G. Lotze, A. Squires, L. C. Serpell and D. J. Adams, *Chem. Comm.*, 2011, **47**, 12071-12073.
19. K. McAulay, P. A. Ucha, H. Wang, A. M. Fuentes-Caparros, L. Thomson, O. Maklad, N. Khunti, N. Cowieson, M. Wallace, H. Cui, R. J. Poole, A. Seddon and D. J. Adams, *Chem. Comm.*, 2020, **56**, 4094-4097.
20. L. E. Buerkle and S. J. Rowan, *Chem. Soc. Rev.*, 2012, **41**, 6089-6102.
21. B. Arenas-Gomez, C. Garza, Y. Liu and R. Castillo, *J. Colloid Interface Sci.*, 2020, **560**, 618-625.
22. K. McAulay, L. Thomson, L. Porcar, R. Schweins, N. Mahmoudi, D. J. Adams and E. R. Draper, *Org. Mater.*, 2020, **02**, 108-115.
23. G. D. Saravacos, *J. Food Sci.*, 1970, **35**, 122-125.
24. E. R. Draper, H. Su, C. Brasnett, Poole, R. J., S. Rogers, H. Cui, A. Seddon and D. J. Adams, *Angew. Chem.*, 2017, **129**, 10603-10606.

25. S. Roy, N. Javid, J. Sefcik, P. J. Halling and R. V. Ulijn, *Langmuir*, 2012, **28**, 16664-16670.
26. E. R. Draper, M. Wallace, R. Schweins, R. J. Poole and D. J. Adams, *Langmuir*, 2017, **33**, 2387-2395.
27. Strickla.Eh, J. Horwitz and C. Billups, *Biochem.*, 1969, **8**, 3205-3213.
28. K. Bakshi, M. R. Liyanage, D. B. Volkin, C. R. Middaugh, *Therapeutic Peptides: Methods and Protocols*, Ed. Nixon, A. E., 2014, **1088**, Ch. Circular Dichroism of peptides, 247-253.
29. K. L. Morris, L. Chen, A. Rodger, D. J. Adams and L. C. Serpell, *Soft Matter*, 2015, **11**, 1174-1181.
30. C. Colquhoun, E. R. Draper, E. G. Eden, B. N. Cattoz, K. L. Morris, L. Chen, T. O. McDonald, A. E. Terry, P. C. Griffiths, L. C. Serpell and D. J. Adams, *Nanoscale*, 2014, **6**, 13719-13725.
31. H. Nobuyuki, Y. Takuma and H. Uda, *J. Am. Chem. Soc.*, 1978, **100**, 4029-4036.
32. S. Kaneyoshi, T. Zou, S. Ozaki, R. Takeuchi, A. Udou, T. Nakahara, K. Fujimoto, S. Fujii, S. Sato and S. Takenaka, *Chem. Eur. J.*, 2020, **26**, 139-142.
33. L. Chen, K. Morris, A. Laybourn, D. Elias, M. R. Hicks, A. Rodger, L. Serpell and D. J. Adams, *Langmuir*, 2010, **26**, 5232-5242.
34. N. J. Greenfield, *TrAC Trends Anal. Chem.*, 1999, **18**, 236-244.
35. A. L. Skinner and J. S. Laurence, *J. Pharm. Sci.*, 2008, **97**, 4670-4695.
36. B. Escuder, M. Llusar and J. F. Miravet, *J. Org. Chem.*, 2006, **71**, 7747-7752.
37. P. W. Kuchel, B. E. Chapman, N. Mueller, W. A. Bubb, D. J. Philp and A. M. Torres, *J. Magn. Reason.*, 2006, **180**, 256-265.
38. M. Wallace, J. A. Iggo and D. J. Adams, *Soft Matter*, 2015, **11**, 7739-7747.
39. D. Giuri, L. J. Marshall, B. Dietrich, D. McDowall, L. Thomson, J. Y. Newton, C. Wilson, R. Schweins and D. J. Adams, *Chem. Sci.*, 2021, **12**, 9720-9725.
40. E. R. Draper, B. Dietrich, K. McAulay, C. Brasnett, H. Abdizadeh, I. Patmanidis, S. J. Marrink, H. Su, H. Cui, R. Schweins, A. Seddon and D. J. Adams, *Matter*, 2020, **2**, 764-778.
41. C. Colquhoun, E. R. Draper, R. Schweins, M. Marcello, D. Vadukul, L. C. Serpell and D. J. Adams, *Soft Matter*, 2017, **13**, 1914-1919.
42. S. Zhang, M. A. Greenfield, A. Mata, L. C. Palmer, R. Bitton, J. R. Mantei, C. Aparicio, M. O. de la Cruz and S. I. Stupp, *Nat. Mater.*, 2010, **9**, 594-601.

43. B. D. Wall, S. R. Diegelmann, S. Zhang, T. J. Dawidczyk, W. L. Wilson, H. E. Katz, H.-Q. Mao and J. D. Tovar, *Adv. Mater.*, 2011, **23**, 5009-5014.
44. T. J. Deming, *Nat. Mater.*, 2010, **9**, 535-536.
45. T. Christoff-Tempesta, Y. Cho, D.-Y. Kim, M. Geri, G. Lamour, A. J. Lew, X. Zuo, W. R. Lindemann and J. H. Ortony, *Nat. Nanotechnol.*, 2021, **16**, 447-454.
46. D. McDowall, M. Walker, M. Vassalli, M. Cantini, N. Khunti, C. J. C. Edwards-Gayle, N. Cowieson and D. J. Adams, *Chem. Comm.*, 2021, **57**, 8782-8785.
47. G. Ciccone, M. A. G. Oliva, N. Antonovaite, I. Luchtefeld, M. Salmeron-Sanchez and M. Vassalli, *JoVE J. Vis. Exp.*, 2022, **179**, e63401.
48. J. Raeburn, G. Pont, L. Chen, Y. Cesbron, R. Levy and D. J. Adams, *Soft Matter*, 2012, **8**, 1168-1174.
49. P. R. A. Chivers and D. K. Smith, *Chem. Sci.*, 2017, **8**, 7218-7227.
50. K. L. Morris, L. Chen, J. Raeburn, O. R. Sellick, P. Cotanda, A. Paul, P. C. Griffiths, S. M. King, R. K. O'Reilly, L. C. Serpell and D. J. Adams, *Nat. Comm.*, 2013, **4**, 1480.
51. I. Luchtefeld, A. Bartolozzi, J. Mejia, O. Dobre, M. Basso, T. Zambelli and M. Vassalli, *J. Nanobiotechnol.*, 2020, **18**, 1-11.
52. M. Krieg, G. Flaschner, D. Alsteens, B. M. Gaub, W. H. Roos, G. J. L. Wuite, H. E. Gaub, C. Gerber, Y. F. Dufrene and D. J. Mueller, *Nat. Rev. Phys.*, 2019, **1**, 41-57.
53. L. Thomson, R. Schweins, E. R. Draper and D. J. Adams, *Macromol. Rapid Comm.*, 2020, **41**, e2000093.
54. L. Thomson, D. McDowall, L. Marshall, O. Marshall, H. Ng, W. J. A. Homer, D. Ghosh, W. Liu, A. M. Squires, E. Theodosiou, P. D. Topham, L. C. Serpell, R. J. Poole, A. Seddon and D. J. Adams, *ACS Nano.*, 2022, **16**, 20497-20509.

Chapter 3

Multicomponent systems composed of two structurally similar gelators

3.1 Introduction

The work discussed in this chapter investigates the behaviour of multicomponent systems composed of two gelators with the same basic structural design: an *N*-terminal aromatic group followed by two amino acid residues. Such peptide-based low molecular weight gelators (LMWGs) generally contain at least one phenylalanine (F) residue since the presence of additional aromatic rings contributes to self-assembly through π-π stacking and the hydrophobic effect.[1, 2]

Here, we investigate multicomponent systems containing one of two possible stereoisomers (*RS* and *SS*) of the well-studied peptide-based LMWG 2NapFF mixed with a variety of *N*-functionalised (*SS*)-dipeptide based gelators (Figure 3.1). Most studies focus on 2Nap-(*SS*)-FF.[3-9] We have included 2Nap-(*RS*)-FF to highlight the effect of changing chirality and show how this can be a powerful tool in tuning the properties of these systems. One diastereomer of 2NapFF is included in all the multicomponent systems to exemplify a range of possible properties accessible using multicomponent systems.

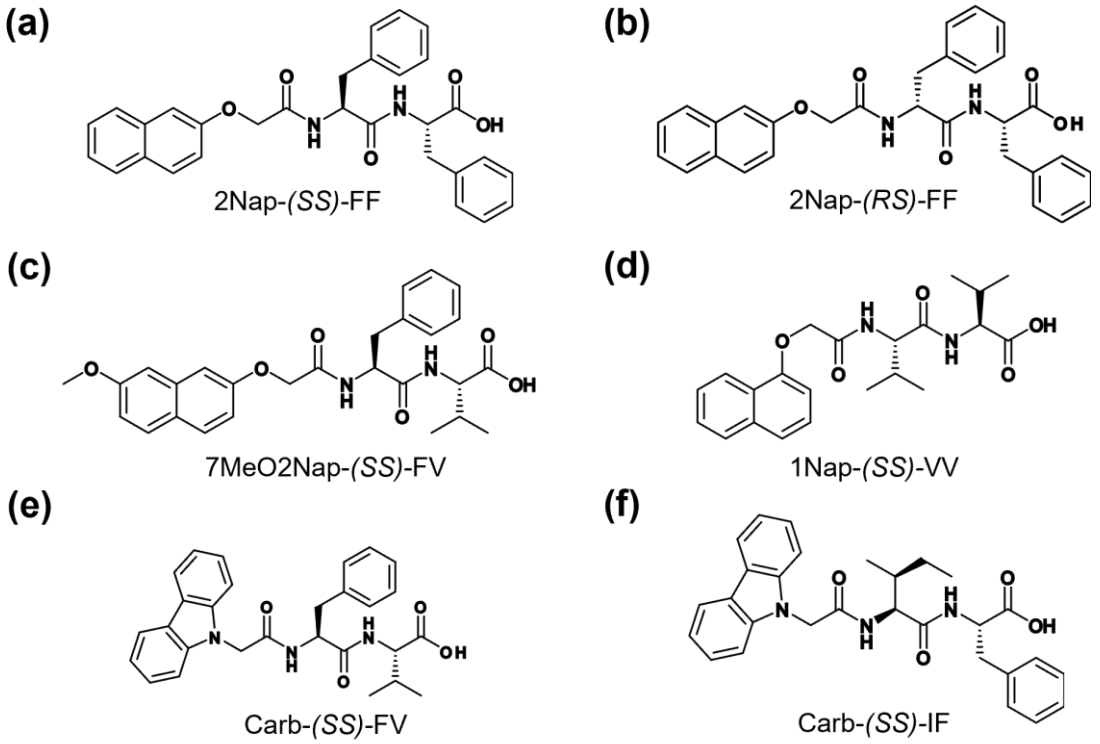

Figure 3.1. Chemical structures of the components studied here: (a) 2Nap-(*SS*)-FF, (b) 2Nap-(*RS*)-FF, (c) 7MeO2Nap-(*SS*)-FV, (d), 1Nap-(*SS*)-VV, (e) Carb-(*SS*)-FV and (f) Carb-(*SS*)-IF. The chirality of the second component will be omitted throughout the rest of this chapter to allow ease of reading.

Gelator-gelator multicomponent systems are commonly prepared at ratios of 1:1. Here, we investigate several different concentration ratios to investigate how the outcome of a multicomponent system can be influenced by changing the concentration ratio while maintaining the same total gelator concentration (10 mg/mL). This provides an easy method for tuning the mechanical properties of a system while keeping the same desired components.

Peptide-based LMWGs tend to self-assemble to form long, one-dimensional structures in aqueous solution through the formation of directional non-covalent interactions such as hydrogen bonds and π-π stacking interactions (Figure 3.2a).[10] Mixing two such gelators in aqueous solution results in a range of possible outcomes in both the solution and gel states. We have exemplified some of the possible outcomes in Figure 3.2. The two LMWGs may prefer to interact only with themselves, resulting in self-sorting (Figure 3.2b). On gelation the self-sorted structures formed may interact through entanglements (Figure 3.2bi)[11, 12] or narcissistic self-sorting may continue, resulting in the formation of two completely independent interpenetrating gel networks (Figure 3.2bii).[13] Alternatively, the two LMWGs may co-assemble into the same secondary structures pre-gelation (Figure 3.2c). The arrangement of the gelator molecules within the secondary structures may be random[14, 15] or result in an alternating pattern of the two gelators[16, 17] depending on gelator design. If the gelators exhibit some degree of self-discrimination, the resulting secondary structures may contain sections that contain only one (or a higher proportion of one) gelator. This could result in preferential entanglement in specific sections of the gel network (Figure 3.2cii).[18] This would change the cross-linking density and thereby the mechanical properties of the final gel.

Mixing two LMWGs allows fine control over material properties. Sequential assembly based on the pK_a of peptide-based LMWGs has been shown to allow some predictability over the system.[19, 20] The LMWGs studied here have similar pK_a values, making such predictions difficult.

As discussed in Chapter 1, the chirality of the amino acids in peptide-based LMWGs provides a potential tool for changing of the behaviour of these systems. Previous work has stated the importance of homochirality in allowing like-with-like intermolecular interactions that allow self-assembly of peptide-based systems and ultimately control the properties of the resulting materials.[21] Homochiral systems were found to be more thermally and mechanically stable compared to their heterochiral equivalents.[21] Homochiral peptide

systems formed more uniform assemblies while heterochiral systems formed self-sorted, heterogenous assemblies.[21]

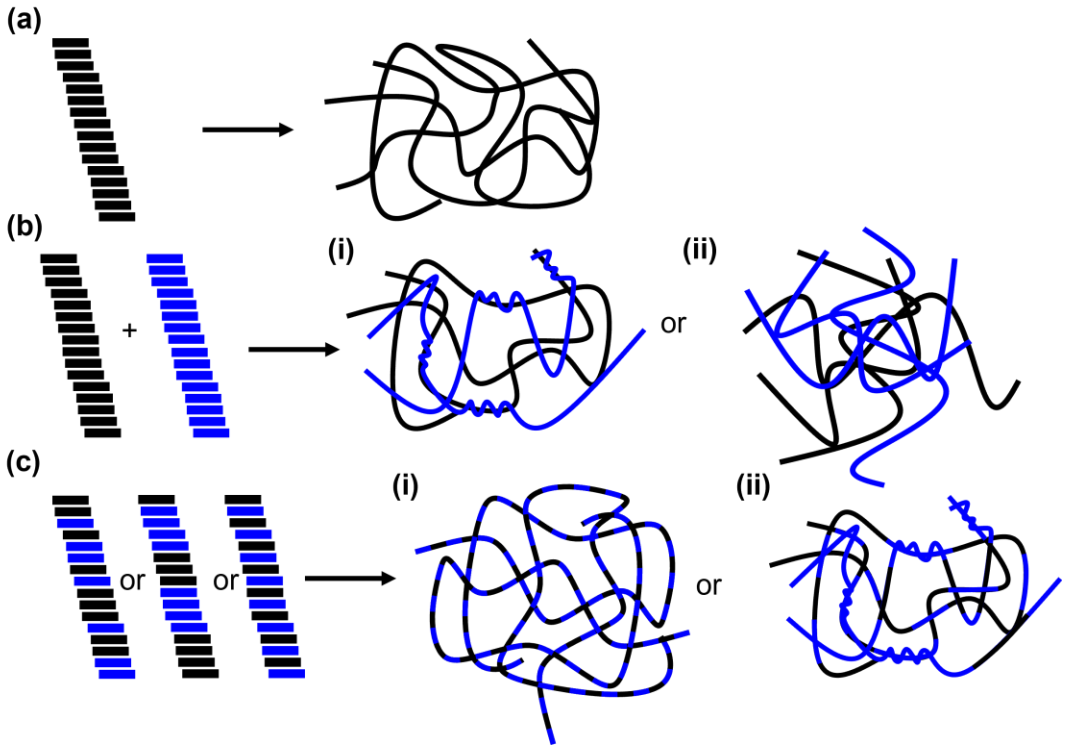

Figure 3.2. (a) Cartoon showing the possible outcomes of assembly of (a) a single gelator, (b) two gelators that self-sort to individually form fibres that may (i) interact or (ii) form independent interpenetrating networks, and (c) two gelators that co-assemble into the same fibres. This can be completely random, or the components may have a slight preference for self-self interaction, resulting in formation of blocks of each component, or the two components may alternate in an ordered manner. Entanglements in such networks may be (i) random or (ii) have preferential entanglement between specific sections of the primary fibres that make up the gel network.

Other work demonstrates the preference of β-sheet forming peptides for homochiral pairing over heterochiral pairing.[22] Although the (*S*)- and (*R*)-β-sheets have the same pattern of hydrogen-bond donors and acceptors, the amino acid side chains point in opposite directions. This means that the heterochiral systems will have less favourable alignment for further interactions, such as π-π stacking of aromatic groups. This was expressed as a preference for homochiral assembly and hence self-sorting in the heterochiral systems.[22] Such heterochiral self-sorting is unusual and highlights the importance of considering steric effects as well as intermolecular interactions when designing peptide-based systems. However, it is hard to predict how molecules are going to interact. From the above work, one could predict that the

2Nap-(*SS*)-FF multicomponent systems are more likely to co-assemble, while the 2Nap-(*RS*)-FF multicomponent systems are more likely to self-sort since all the second components have (*SS*)-configuration.

3.2 Results and Discussion

3.2.1 Multicomponent assembly at high pH

Stock suspensions of each component were prepared at a concentration of 10 mg/mL. These suspensions were allowed to stir overnight to ensure homogenous dispersal of the gelators. The resulting suspensions were adjusted to pH 10.5 before mixing for 2 hours with a stock suspension of the second component to give multicomponent systems with the following concentration ratios (second component:2NapFF): 7.5:2.5, 5:5 and 2.5:7.5 (mg/mL:mg/mL). The multicomponent suspensions were adjusted to pH 10.5 before use. All systems had a total gelator concentration of 10 mg/mL, with only the concentration ratio of second component:2NapFF being changed. To ensure the data for each technique was readily comparable, the same stock suspensions were used to prepare all samples for each individual technique to reduce batch-to-batch variability.

3.2.1.1 Viscosity at high pH

7MeO2NapFV, 1NapVV and CarbFV all form non-viscous solutions that do not exhibit shear-thinning behaviour at a concentration of 10 mg/mL (Figures 3.3 and 3.4). These components therefore do not form long, one-dimensional structures in solution at high pH when alone.[23] When preparing multicomponent suspensions, 7MeO2NapFV and 1NapVV effectively dilute 2NapFF, with their viscosity and shear-thinning behaviour decreasing as the concentration of 2NapFF decreases. This would suggest self-sorting is taking place between these components and 2NapFF at high pH.

The CarbFV multicomponent systems show different behaviours depending on the chirality of 2NapFF. When mixed with 2Nap-(*SS*)-FF, the resulting suspensions were significantly more viscous than that of CarbFV alone (Figure 3.3c). The CarbFV 5 mg/mL:2Nap-(*SS*)-FF 5 mg/mL multicomponent system had similar viscosity to 2Nap-(*SS*)-FF (10 mg/mL). The CarbFV 2.5 mg/mL:2Nap-(*SS*)-FF 7.5 mg/mL suspension had greater viscosity than the

2Nap-(*SS*)-FF 10 mg/mL single component system. The assembly of these systems is therefore concentration-dependent, suggesting the scenario is more complicated than the suggested self-sorting observed in the 7MeO2NapFV and 1NapVV multicomponent systems.

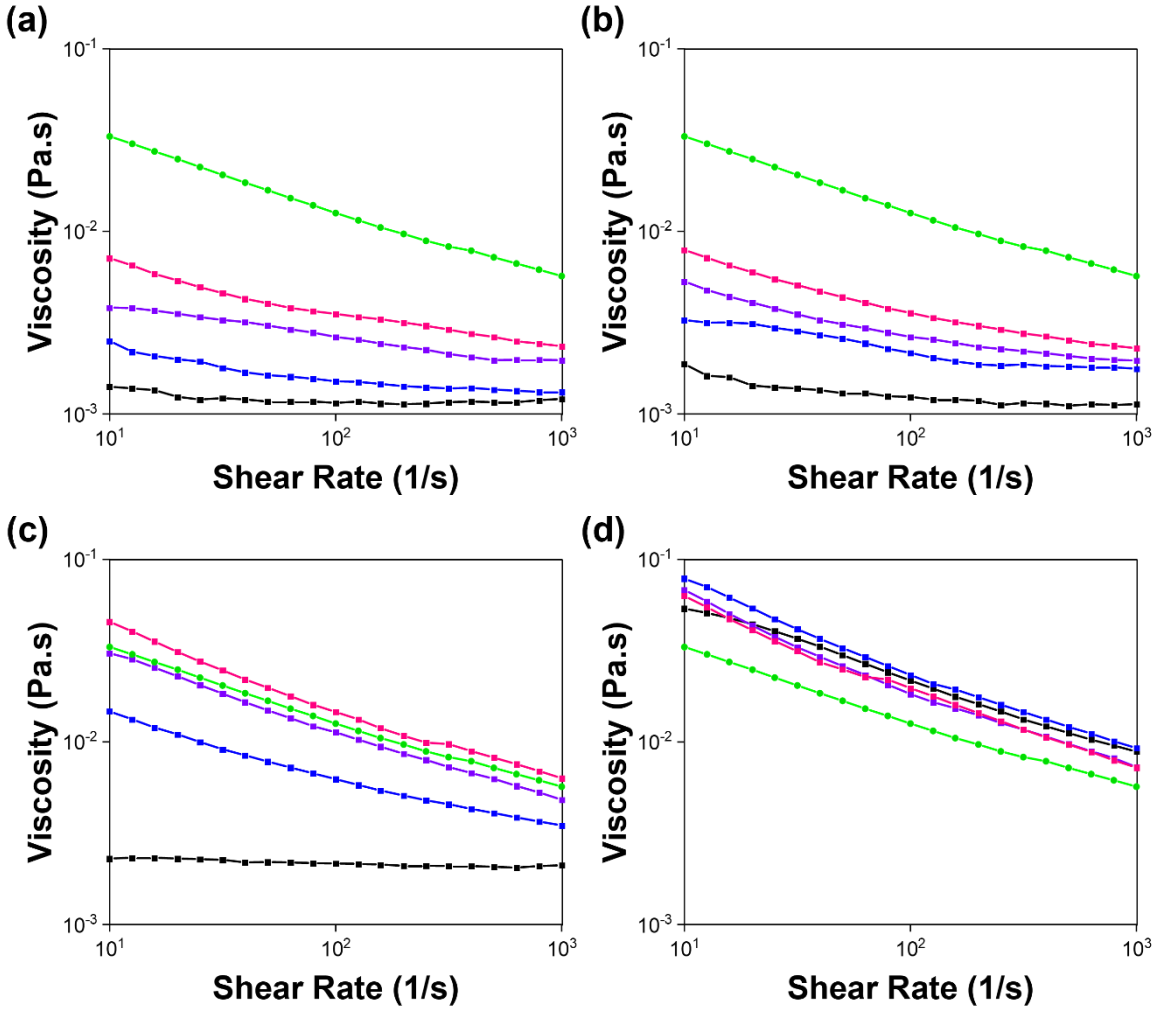

Figure 3.3. Viscosity values recorded from single and multicomponent systems of (a) 7MeO2NapFV, (b) 1NapVV, (c) CarbFV and (d) CarbIF at concentration ratios (second component:2Nap-(*SS*)-FF): 10 mg/mL:0 mg/mL (black), 7.5 mg/mL:2.5 mg/mL (blue), 5 mg/mL:5 mg/mL (purple) and 2.5 mg/mL:7.5 mg/mL (pink). 2Nap-(*SS*)-FF 10 mg/mL (green) is shown in each for easy comparison. Viscosity data were collected on a single sample of each system to probe behaviour at high pH.

The 2.5 mg/mL:7.5 mg/mL and 7.5 mg/mL:2.5 mg/mL CarbFV:2Nap-(*RS*)-FF multicomponent systems had similar viscosity values that lay between CarbFV 10 mg/mL and 2Nap-(*RS*)-FF and 10 mg/mL (Figure 3.4c). The 5 mg/mL CarbFV:5 mg/mL 2Nap-(*RS*)-FF multicomponent system had even greater viscosity than 2Nap-(*RS*)-FF 10 mg/mL.

This behaviour could result from co-assembly, or from self-sorted fibres interacting at longer length scales causing an increase in viscosity.

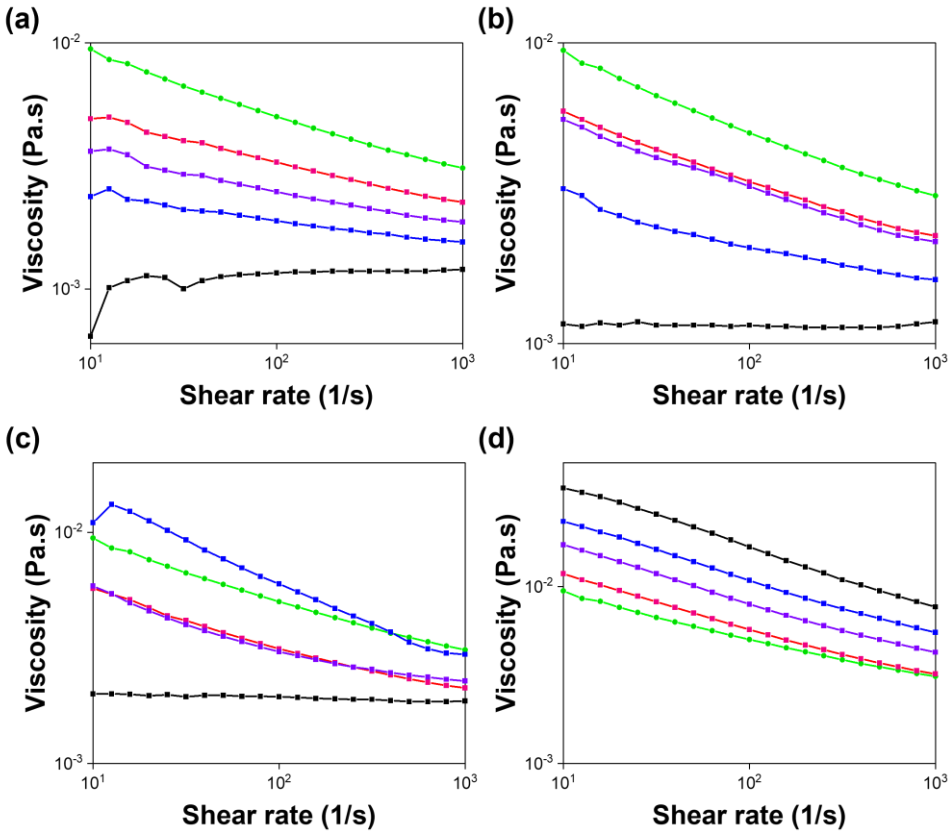

Figure 3.4. Viscosity values recorded from single and multicomponent systems of (a) 7MeO2NapFV, (b) 1NapVV, (c) CarbFV and (d) CarbIF at concentration ratios (second component:2Nap-(*RS*)-FF): 10 mg/mL:0 mg/mL (black), 7.5 mg/mL:2.5 mg/mL (blue), 5 mg/mL:5 mg/mL (purple) and 2.5 mg/mL:7.5 mg/mL (pink). 2Nap-(*RS*)-FF 10 mg/mL (green) is shown in each for easy comparison. Viscosity was collected on a single sample of each system to quickly probe behaviour at high pH.

CarbIF (10 mg/mL) is the only component with greater viscosity than 2NapFF (10 mg/mL) of either chirality (Figures 3.3 and 3.4). 2Nap-(*RS*)-FF appears to dilute CarbIF, indicating self-sorting. All the CarbIF:2Nap-(*SS*)-FF multicomponent systems have similar viscosity. As with the CarbFV:2Nap-(*RS*)-FF systems, we cannot conclude from the viscosity data alone whether self-sorting or co-assembly is taking place.

Figure 3.5 shows the viscosity values of solutions diluted from a single 10 mg/mL stock solution of each diastereomer of 2NapFF to allow comparison between the multicomponent systems of each concentration ratio and the corresponding diluted 2NapFF single component system of the same 2NapFF concentration.

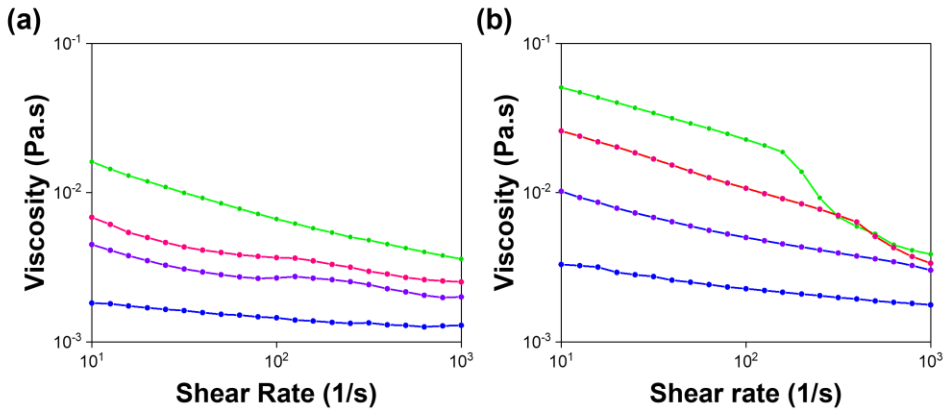

Figure 3.5. Viscosity values recorded for (a) 2Nap-(*SS*)-FF and (b) 2Nap-(*RS*)-FF at concentrations of 10 mg/mL (green), 7.5 mg/mL (pink), 5 mg/mL (purple) and 2.5 mg/mL (blue).

3.2.1.2 UV-Vis and CD spectroscopy at high pH

UV-Vis spectroscopy performed on samples prepared in DMSO shows the absorbance from molecules in each system as all the components under study are soluble in DMSO (Figures 3.6 and 3.7). Here, we observe a concentration-dependent change in absorbance: as the concentration of one component decreases, its contribution to absorbance also decreases while that of the second component increases with increasing concentration. We collected data from each component individually at 10 mg/mL for comparison. The noisy data recorded between 200 and ~230 nm is due to absorbance by DMSO. Absorbance from the carbazole group dominates absorbance in the systems that contain a component with a carbazole group at the *N*-terminus. UV-Vis collected in the micellar phase at high pH show the same general trends as the data collected in the solution phase in DMSO (Figures 3.6 and 3.7).

Circular dichroism (CD) spectroscopy was used to investigate the effect of mixing the two components of each system on the secondary structure of the self-assemblies formed (Figures 3.8 and 3.9). The maximum in the CD data centred at 225-230 nm stems from π-π stacking of aromatic phenylalanine residues.[24] The remaining signals most likely come from interactions between the aromatic *N*-terminal capping groups during self-assembly to form chiral structures.

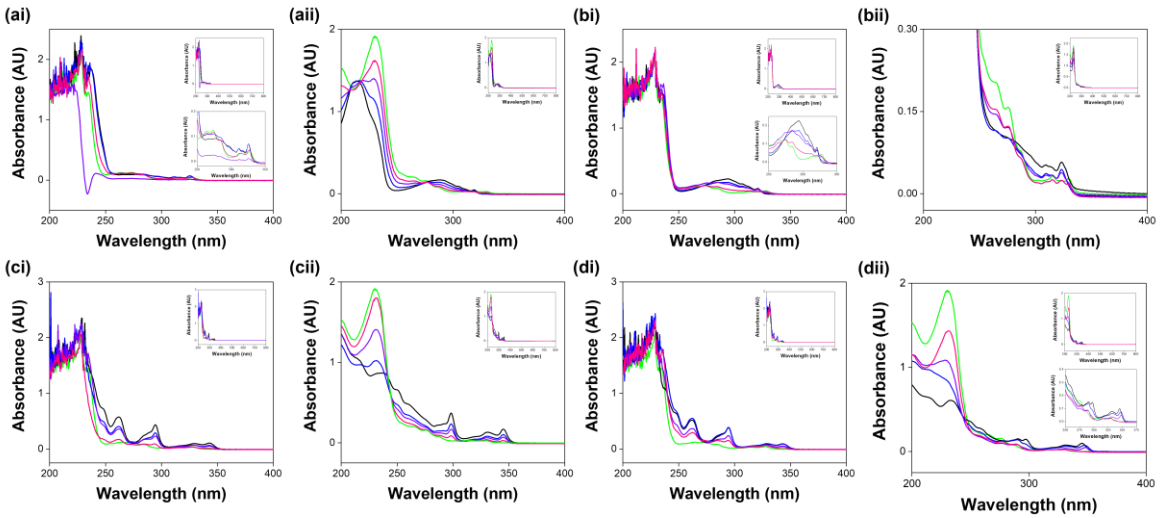

Figure 3.6. UV-Vis absorption spectra recorded from single and multicomponent systems of (a) 7MeO2NapFV, (b) 1NapVV, (c) CarbFV and (d) CarbIF at concentration ratios second component:2Nap-(*SS*)-FF (mg/mL:mg/mL) of 10:0 (black), 7.5:2.5 (blue), 5:5 (purple) and 2.5:7.5 (pink) collected in (i) DMSO and (ii) H_2O at pH 10.5. The data recorded from 2Nap-(*SS*)-FF 10 mg/mL (green) is shown in each spectrum for easy comparison with the multicomponent systems. The inserts show the entire spectrum (top) and selected regions to make them more visible (bottom).

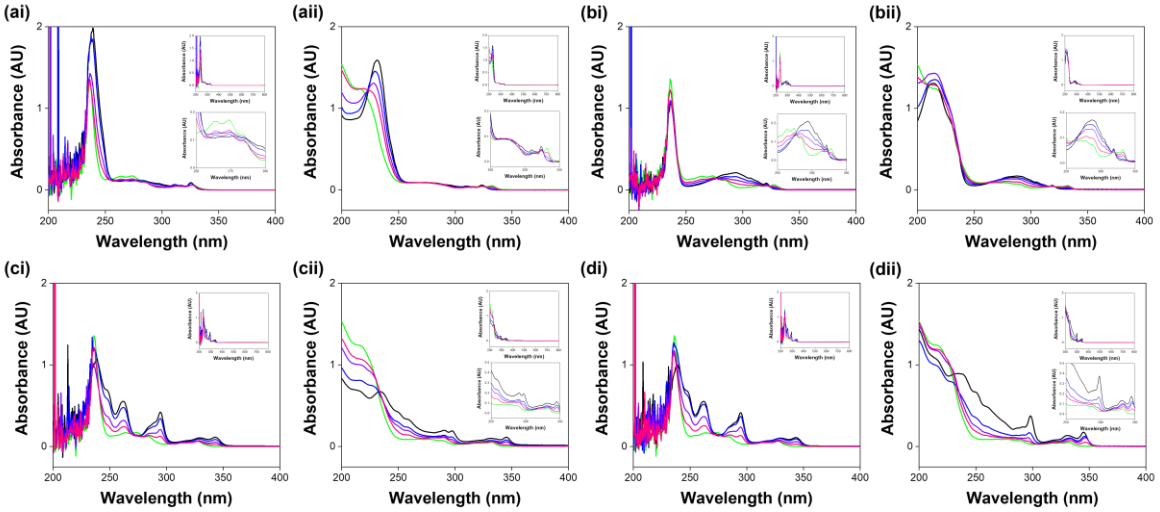

Figure 3.7. UV-Vis absorption spectra recorded from single and multicomponent systems of (a) 7MeO2NapFV, (b) 1NapVV, (c) CarbFV and (d) CarbIF at concentration ratios second component:2Nap-(*RS*)-FF (mg/mL:mg/mL) of 10:0 (black), 7.5:2.5 (blue), 5:5 (purple) and 2.5:7.5 (pink) collected in (i) DMSO and (ii) H_2O at pH 10.5. The data recorded from 2Nap-(*RS*)-FF 10 mg/mL (green) is shown in each spectrum for easy comparison with the multicomponent systems. The inserts show the entire spectrum (top) and selected regions to make them more visible (bottom).

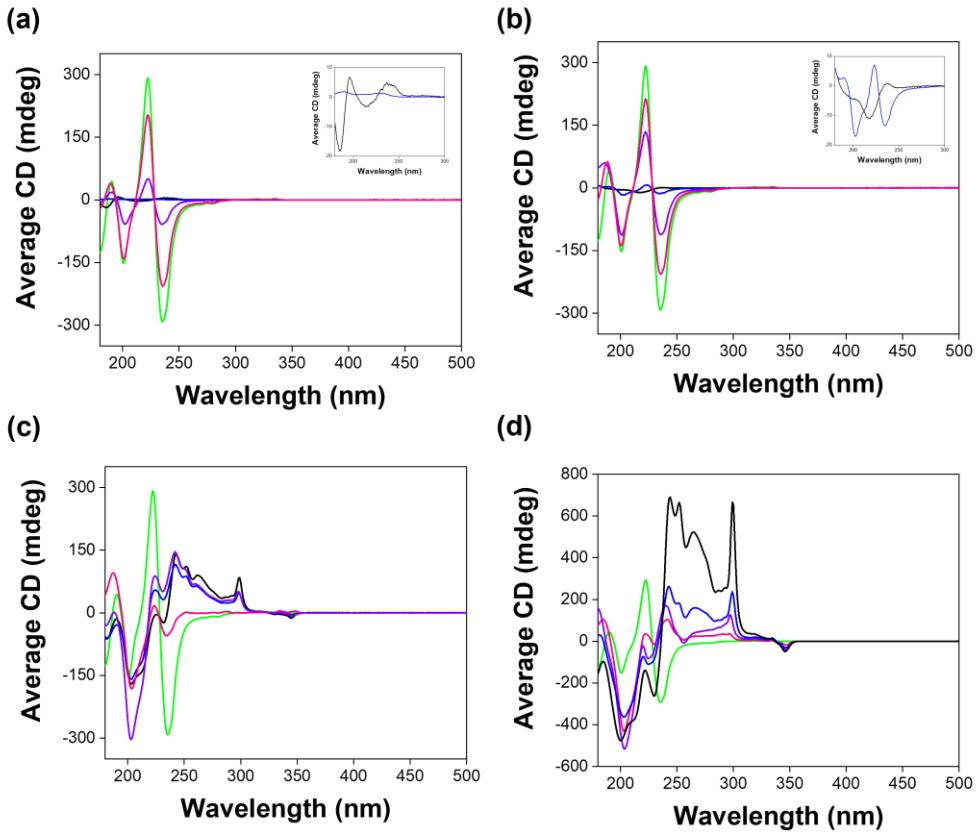

Figure 3.8. CD spectra recorded from single and multicomponent systems of (a) 7MeO2NapFV, (b) 1NapVV, (c) CarbFV and (d) CarbIF at concentration ratios second component:2Nap-(*SS*)-FF of 10 mg/mL:0 mg/mL (black), 7.5 mg/mL:2.5 mg/mL (blue), 5 mg/mL:5 mg/mL (purple) and 2.5 mg/mL:7.5 mg/mL (pink) at pH 10.5. The CD spectrum recorded from 2Nap-(*SS*)-FF 10 mg/mL (green) is shown in each spectrum for easy comparison with the multicomponent systems. All data was collected in triplicate and averaged. Absorbance and high tension (HT) data were recorded concurrently with the CD spectra (Appendix 2.2). Inserts showing CD data collected from 7MeO2NapFV and 1NapVV alone at 10 mg/mL and in a 7.5 mg/mL:2.5 mg/mL 2Nap-(*SS*)-FF multicomponent system are shown to make this data more easily visible.

CD data collected at high pH shows that 7MeO2NapFV and 1NapVV form far fewer chiral structures than 2Nap-(*SS*)-FF and 2Nap-(*RS*)-FF, with the intensity of the peaks corresponding to 7MeO2NapFV and 1NapVV alone being far lower than any of the other systems (Figures 3.8 and 3.9). The chirality provided by 2NapFF begins to dominate the CD spectra recorded from these multicomponent systems at even the lowest 2NapFF concentrations, with the line shapes resembling those from 2NapFF. Very little contribution from 7MeO2NapFV or 1NapVV is observed in the multicomponent systems. 7MeO2NapFV 7.5 mg/mL:2Nap-(*SS*)-FF 2.5 mg/mL is the only exception (Figure 3.8a insert), where the

intensity of the CD peaks is almost completely disrupted. This suggests that 7MeO2NapFV disrupts the chirality of the structures formed when present at high enough concentrations.

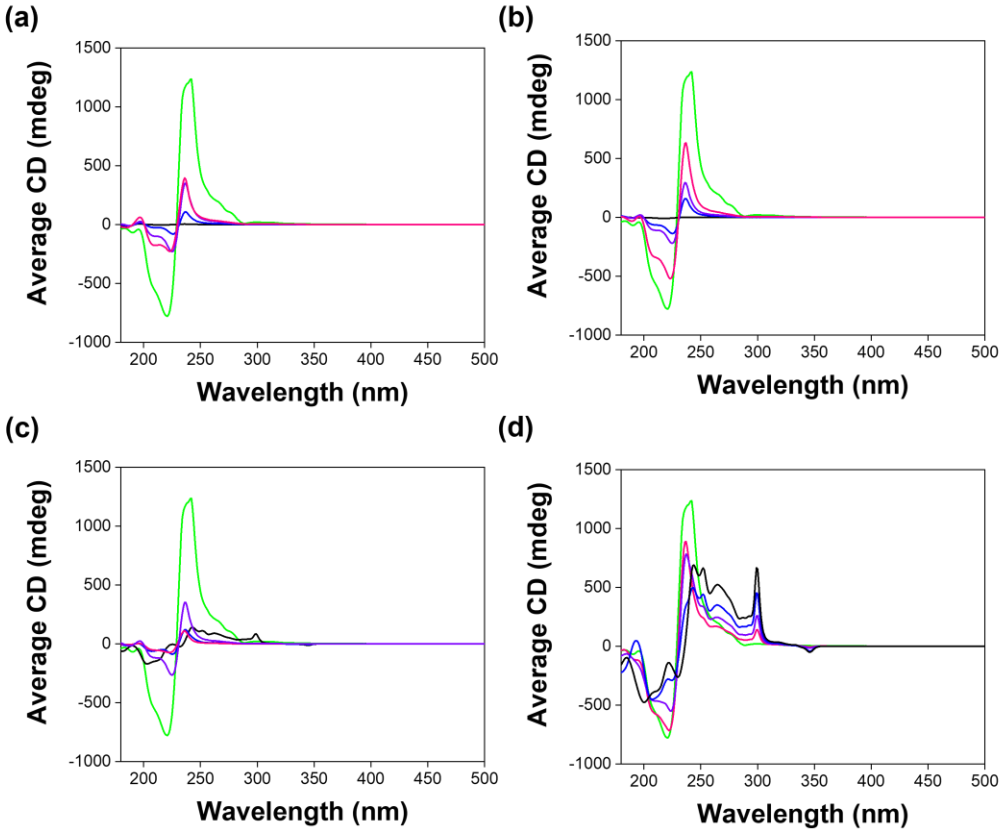

Figure 3.9. CD spectra recorded from single and multicomponent systems of (a) 7MeO2NapFV, (b) 1NapVV, (c) CarbFV and (d) CarbIF at concentration ratios second component:2Nap-(RS)-FF of 10 mg/mL:0 mg/mL (black), 7.5 mg/mL:2.5 mg/mL (blue), 5 mg/mL:5 mg/mL (purple) and 2.5 mg/mL:7.5 mg/mL (pink) at pH 10.5. The CD spectrum recorded from 2Nap-(RS)-FF 10 mg/mL (green) is shown in each spectrum for easy comparison with the multicomponent systems. All data was collected in triplicate and averaged. Absorbance and HT data were recorded concurrently with the CD spectra (Appendix 2.2).

This behaviour could be related to observations made during simulations performed by Isaacs *et al.*[25] When the concentration of one component is significantly greater than the concentration of the second component, a preference for co-assembly arises due to the increased probability of the component with the lower concentration coming into contact with the component with the higher concentration. The greatest efficiency of self-sorting always occurred when the concentrations of the two components are equal.[25] This suggests that the most efficient self-sorting takes place in the 5 mg/mL:5 mg/mL multicomponent systems. However, results from small angle neutron scattering (SANS, see below) suggest

that (in 5 mg/mL:5 mg/mL system at least) 7MeO2NapFV and 2Nap-(*SS*)-FF actually co-assemble. It is possible that this co-assembly is concentration-dependent, and that self-sorting takes place in the 2.5 mg/mL:7.5 mg/mL system. SANS experiments on this system would be required to confirm this suggestion.

The intensity of the CD peaks increases with increasing 2NapFF concentration and never exceeds that measured from 2NapFF alone at 10 mg/mL (Figures 3.8 and 3.9). This suggests that the presence of 7MeO2NapFV and 1NapVV molecules perturbs the chirality of the structures formed. However, the intensity of the CD signals is enhanced compared to CD data collected from a 2Nap-(*SS*)-FF single component system at the same 2Nap-(*SS*)-FF concentration (Figure 3.10), showing that the total concentration of chiral structures in the multicomponent systems is greater than in the 2Nap-(*SS*)-FF single component systems. This is further evidence for co-assembly.

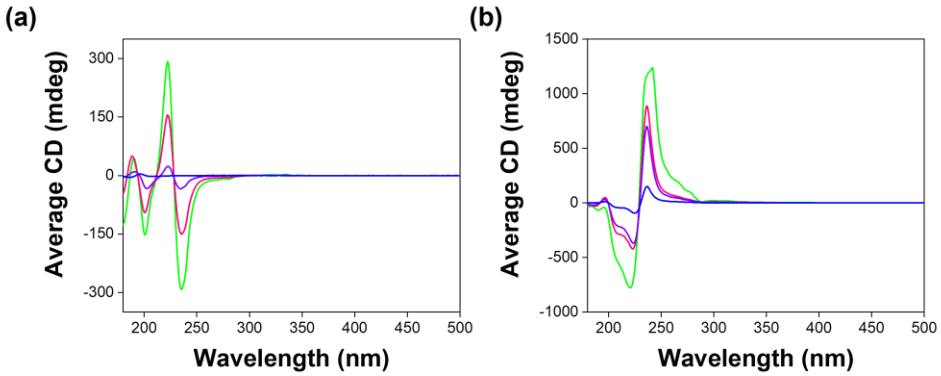

Figure 3.10. CD spectra recorded from single component systems composed of (a) 2Nap-(*SS*)-FF and (b) 2Nap-(*RS*)-FF at concentrations of 10 mg/mL (green), 7.5 mg/mL (pink), 5 mg/mL (purple) and 2.5 mg/mL (blue) at pH 10.5. All data was collected in triplicate and averaged. Absorbance and HT data were recorded concurrently with the CD spectra (Appendix 2.2).

We cannot completely rule out self-sorting of these systems from CD data alone as it is possible that peaks from 7MeO2NapFV and 1NapVV are present, they are just masked by the intense peaks measured from 2NapFF. However, if self-sorting were taking place, the CD spectrum would be the sum of the spectra from the two components individually.[13, 26] This differs from the conclusions drawn from viscosity data.

The CarbFV:2Nap-(*RS*)-FF multicomponent systems (Figure 3.9c) shows similar behaviour to the 7MeO2NapFV and 1NapVV systems, suggesting CarbFV is undergoing co-assembly with 2Nap-(*RS*)-FF directing assembly. CD signals from the CarbFV 5 mg/mL:2Nap-(*RS*)-FF 5 mg/mL multicomponent system are more intense than those from the other two

multicomponent systems, suggesting that this is the optimum concentration ratio for the co-assembly of these components. This agrees with observations from the viscosity data.

The CarbFV:2Nap-(*SS*)-FF multicomponent systems maintain similar CD intensity regardless of concentration ratio (apart from CarbFV 2.5 mg/mL:2Nap-(*SS*)-FF 7.5 mg/mL). This suggests co-assembly is taking place rather than self-sorting. The intensity and line shape of the signals are very similar to CarbFV 10 mg/mL, suggesting CarbFV is conducting assembly with 2Nap-(*SS*)-FF almost entirely co-assembled with CarbFV to give the same effective concentration of structures as CarbFV 10 mg/mL (Figure 3.8c).

Contributions from both components are observed in the CD spectra collected from the CarbIF multicomponent systems (Figures 3.8d and 3.9d). This indicates self-sorting, despite the behaviour reminiscent of co-assembly observed in the viscosity measurements. As the concentration of one component in the CarbIF:2NapFF multicomponent systems decreases, its contribution to the CD intensity diminishes while that of the second component increases as its concentration increases. This is further evidence for self-sorting.

The amplification of CD signal in the multicomponent systems compared to 2Nap-(*SS*)-FF single component systems of the same 2Nap-(*SS*)-FF concentration is not observed when comparing the 2Nap-(*RS*)-FF multicomponent systems (Figure 3.9) to 2Nap-(*RS*)-FF single component systems (Figure 3.10). This could be due to less effective packing of (*SS*)-dipeptides with 2Nap-(*RS*)-FF compared to (*SS*)-dipeptides with 2Nap-(*SS*)-FF.

3.2.1.3 SANS at high pH

SANS data was collected from each component alone at 10 mg/mL and from 5 mg/mL:5 mg/mL multicomponent systems. We attempted to fit each data set to all available standard cylinder models to identify the most suitable model for each. SANS data collected in the micellar phase at high pH from most of the systems studied were best fitted to a hollow cylinder model. The two exceptions were 7MeO2NapFV 10 mg/mL (fitted to an elliptical cylinder plus a power law) and 1NapVV 10 mg/mL (fitted to a power law). The inability of 1NapVV to form cylindrical structures pre-gelation is most likely due to the hydrophobicity of 1NapVV, causing it to instead form irregular aggregates.[27]

The axis ratio obtained for the 7MeO2NapFV 10 mg/mL single component system was almost exactly 2 (Figure 3.11). This suggests that the SANS data corresponds to two

cylinders laterally associated with one another which could explain the difficulty faced fitting this data. It is also possible that 7MeO2NapFV 10 mg/mL forms helical tapes as previous work has shown that the best fit for these structures arises from an elliptical cylinder model.[28] Since the SANS data from the 1NapVV 10 mg/mL single component system was fit to a power law only we expect that the structures formed by 1NapVV are too large to be measured by SANS or that the structures are not sufficiently persistent to provide a strong scattering signal.[11]

(a)

Sample	2Nap-(*SS*)-FF 10 mg/mL	7MeO2NapFV 10 mg/mL	7MeO2NapFV:2 Nap-(*SS*)-FF 5:5 mg/mL	1NapVV 10 mg/mL	1NapVV: 2Nap-(*SS*)-FF 5:5 mg/mL
Model	Hollow cylinder	Elliptical cylinder + power law	Hollow cylinder + power law	Power law	Hollow cylinder + power law
Background	0.018	0.067	0.028	0.072	0.025
A scale	0.0049	3.32 x10^{-4}	0.0017	5.79 x10^{-8}	0.0019
A scale error	*4.46 x10^{-5}*	*2.47 x10^{-6}*	*6.03 x10^{-5}*	*5.32 x10^{-9}*	*5.93 x10^{-5}*
A radius	18.0	141.6	18.4	-	18.6
A radius error	*0.11*	*1.00*	*0.43*	-	*0.33*
A radius polydispersity	0.1	0.3	-	-	-
A thickness	17.7	-	17.6	-	16.6
A thickness error	*0.18*	-	*0.73*	-	*0.58*
A axis ratio	-	1.99	-	-	-
A axis ratio error	-	*0.06*	-	-	-
A length	5000	745.8	744.5	-	5000
A length error	-	*4.39*	*98.7*	-	-
B scale	-	0.0016	7.07 x10^{-4}	-	7.86 x10^{-5}
B scale error	-	*6.97 x10^{-5}*	*7.41 x10^{-5}*	-	*1.37 x10^{-5}*
B power	-	0.93	1.45	3.64	1.86
B power error	-	*0.017*	*0.035*	*0.020*	*0.042*
Reduced χ^2	**10.68**	**23.63**	**1.08**	**9.04**	**1.36**

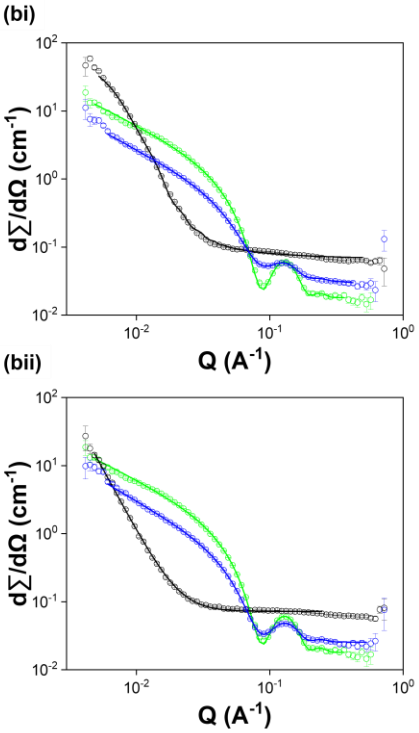

Figure 3.11. (a) Summary of the fitting parameters obtained from SasView[29] model fitting of the SANS data. Parameter errors are fitting errors. (b) Plots of SANS data (circles) and fits (solid lines) obtained from 2Nap-(*SS*)-FF 10 mg/mL (green), (i) 7MeO2NapFV 10 mg/mL (black) and 7MeO2NapFV 5 mg/mL:2Nap-(*SS*)-FF 5 mg/mL (blue) and (ii) 1NapVV 10 mg/mL (black) and 1NapVV 5 mg/mL:2Nap-(*SS*)-FF 5 mg/mL (blue) at high pH.

Inclusion of a power law component improved the quality of the fit for several of the systems. A power law was only included when necessary to fully capture the data to avoid overfitting. A superior fit was achieved for many of the systems studied when the length was set to an arbitrary value outside the range available by SANS. Here we use 5000 Å. Inclusion of polydispersity in the radius parameter allowed us to fully capture the data at Q ≈ 0.1 Å^{-1} for several data sets. In all cases, the background value for the fit was entered manually.

The parameters obtained for 7MeO2NapFV 5 mg/mL:2Nap-(*SS*)-FF 5 mg/mL at high pH are within fitting error of those obtained for 2Nap-(*SS*)-FF 10 mg/mL (Figure 3.11). This suggests complete co-assembly of the two components with 2Nap-(*SS*)-FF directing assembly.[19] This disagrees with the conclusion we drew from the viscosity data, where the behaviour observed suggested self-sorting was taking place. A power law component was included to completely capture the SANS data collected from the 7MeO2NapFV 5 mg/mL:2Nap-(*SS*)-FF 5 mg/mL sample. Inclusion of a power law suggests there are more interactions occurring at longer length scales in the multicomponent system. The length of the 7MeO2NapFV 5 mg/mL:2Nap-(*SS*)-FF 5 mg/mL sample could be fit to a value within the range of SANS. This could be the fitting software picking up on the Kuhn length of the sample as we would expect that the structures formed by these systems would have lengths out with the range accessible by SANS.[30] The inclusion of polydispersity of the radius was no longer required in the 7MeO2NapFV 5 mg/mL:2Nap-(*SS*)-FF 5 mg/mL sample, suggesting increased homogeneity of the structures in the multicomponent system.

SANS data collected from 2Nap-(*RS*)-FF systems were challenging to fit and often gave high χ^2 values, despite the fits being reasonable by eye. Fitting the 7MeO2NapFV 5 mg/mL:2Nap-(*RS*)-FF 5 mg/mL SANS data to a hollow cylinder model combined with a power law provided the best fit (Figure 3.12). Attempts to fit all parameters at once gave high error for the A scale and an unrealistically small value for the thickness, which would suggest the structures are not actually hollow. However, none of the other models or combinations of models gave good quality fits according to residuals, error values and the proximity of the fit to the data by eye. Inputting the parameters from 2Nap-(*RS*)-FF 10 mg/mL gave a reasonable fit apart from at low Q. Inclusion of a power law component to the hollow cylinder parameters from 2Nap-(*RS*)-FF RS 10 mg/mL further improved the fit. Manually increasing the power law value improved the fit at low Q but slightly reduced the quality of fit at high Q. From the final fit, we expect co-assembly is taking place with 2Nap-(*RS*)-FF directing assembly. Attempts to fit this data to a combination of cylinder models did not improve the quality of the fit, confirming that 7MeO2NapFV and 2Nap-(*RS*)-FF are not self-sorting, again disagreeing with our observations from the viscosity data.

As with 7MeO2NapFV, the SANS data collected from the 1NapVV multicomponent systems were fit to the same hollow cylinder model as the 2Nap-(*SS*)-FF 10 mg/mL (Figure 3.11) and 2Nap-(*RS*)-FF 10 mg/mL (Figure 3.12) single component systems with the inclusion of a power law to allow capture of the data at low Q. The parameters obtained from

fits of the multicomponent systems are very similar to those obtained for the 2NapFF single component systems of the corresponding chirality, suggesting co-assembly with 2NapFF directing assembly.

(a)

Sample	2Nap-(*RS*)-FF 10 mg/mL	7MeO2NapFV 10 mg/mL	7MeO2NapFV:2 Nap-(*RS*)-FF 5:5 mg/mL	1NapVV 10 mg/mL	1NapVV: 2Nap-(*RS*)-FF 5:5 mg/mL
Model	Hollow cylinder	Elliptical cylinder + power law	Hollow cylinder + power law	Power law	Hollow cylinder + power law
Background	0.065	0.067	0.060	0.072	0.063
A scale	0.0042	3.32 x10^{-4}	0.0022	5.79 x10^{-8}	0.0049
A scale error	*6.27 x10^{-5}*	*2.47 x10^{-6}*	*1.04 x10^{-5}*	*5.32 x10^{-9}*	*2.08 x10^{-4}*
A radius	128.3	141.6	128.8	-	130.4
A radius error	*0.12*	*1.0*	-	-	*0.18*
A radius polydispersity	-	0.3	0.05	-	0.05
A thickness	14.1	-	14.1	-	7.9
A thickness error	*0.22*	-	-	-	*0.35*
A axis ratio	-	1.99	-	-	-
A axis ratio error	-	*0.06*	-	-	-
A length	555.2	745.8	555.2	-	539.3
A length error	*4.20*	*4.39*	-	-	*4.29*
B scale	-	0.0016	1.73 x10^{-5}	-	4.09 x10^{-9}
B scale error	-	*6.97 x10^{-5}*	*2.805 x10^{-7}*	-	*1.52 x10^{-10}*
B power	-	0.93	2.4	3.64	4.1
B power error	-	*0.017*	-	*0.020*	-
Reduced χ^2	**22.09**	**23.63**	**49.30**	**9.04**	**14.53**

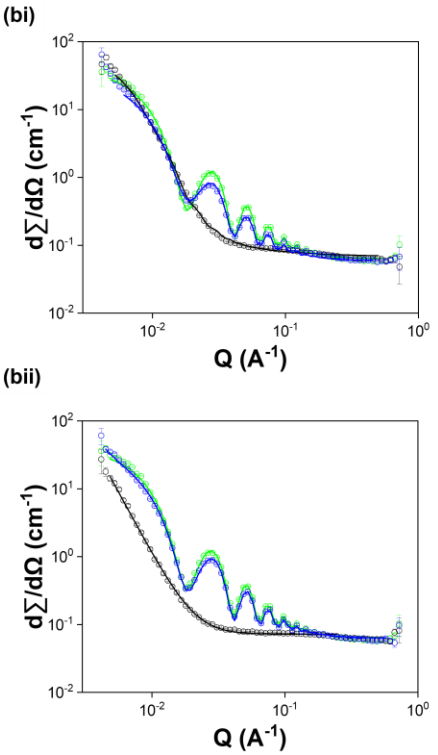

Figure 3.12. (a) Summary of the fitting parameters obtained from SasView model fitting of the SANS data. Parameter errors are fitting errors. (b) Plots of SANS data (circles) and fits (solid lines) obtained from 2Nap-(*RS*)-FF 10 mg/mL (green), (i) 7MeO2NapFV 10 mg/mL (black) and 7MeO2NapFV 5 mg/mL:2Nap-(*RS*)-FF 5 mg/mL (blue) and (ii) 1NapVV 10 mg/mL (black) and 1NapVV 5 mg/mL:2Nap-(*RS*)-FF 5 mg/mL (blue) at high pH.

Slight differences are observed in the 1NapVV multicomponent systems compared to the 2NapFF single component systems. Fits of the structures in the 1NapVV 5 mg/mL:2Nap-(*RS*)-FF 5 mg/mL multicomponent system gave almost half the thickness of those in the 2Nap-(*RS*)-FF 10 mg/mL single component system. Polydispersity was included to improve the quality of the fit obtained for the multicomponent system (Figure 3.12). This suggests the presence of cylinders with a range of values for the radius. A power law component was included in the fits for the multicomponent systems of both 2NapFF diastereomer. The values for the power law were set manually as this provided a fit of better quality at low Q (by eye) than the value obtained from automatic fitting.

From these data, we conclude that 7MeO2NapFV and 1NapVV co-assemble with both diastereomers of 2NapFF. As with the CD data, this disagrees with the conclusions drawn

from viscosity data, where mixing with 7MeO2NapFV or 1NapVV caused reduction in viscosity with decreasing 2NapFF, suggesting dilution of the structures formed by 2NapFF. We concluded from this behaviour that these systems were self-sorting. It is unclear why co-assembly between these components results in reduction in viscosity, despite maintaining the same structures formed by 2NapFF alone. We suspect that the component with the greatest susceptibility for self-assembly will control assembly. This likely comes from a multitude of factors, such as the free energy associated with the interactions formed during self-assembly. Here, the 2NapFF diastereomers are the stronger candidates for self-assembly.

The SANS data collected from the CarbFV 5 mg/mL:2Nap-(*SS*)-FF 5 mg/mL multicomponent system could be fitted to both a hollow cylinder model and a hollow cylinder + hollow cylinder combined model (Figure 3.13). When fitting to a combined model (hollow cylinder + hollow cylinder), we used the parameters obtained from each component alone at a concentration of 5 mg/mL as a starting point.

Despite providing a fit of similar quality by eye to the hollow cylinder + power law model (Figure 3.13), the hollow cylinder + hollow cylinder combined model fit had a higher χ^2 value and had larger parameter error values. The CD spectra of the CarbFV multicomponent systems did not show the expected behaviour for a self-sorted system and instead indicates that CarbFV and 2Nap-(*SS*)-FF undergo co-assembly directed by CarbFV. This is further corroborated by the similarities between the parameters obtained from fitting SANS data from CarbFV 10 mg/mL and SANS data from CarbFV 5 mg/mL:2Nap-(*SS*)-FF 5 mg/mL. We therefore conclude that CarbFV undergoes co-assembly with 2Nap-(*SS*)-FF. It should be noted that self-sorting may also be occurring to some degree.

The occurrence of CarbFV-directed co-assembly suggests that the structures formed by CarbFV are more stable than those formed by 2Nap-(*SS*)-FF, perhaps due to more favourable interactions between CarbFV molecules than between 2Nap-(*SS*)-FF molecules. We do not know how the two molecules are arranged in the structures. As shown in Figure 3.2, this could be completely random, or the two components may form blocks within the co-assembled structures.

(a)

Sample	2Nap-(*SS*)-FF 10 mg/mL	2Nap-(*SS*)-FF 5 mg/mL	CarbFV 10 mg/mL	CarbFV 5 mg/mL	CarbFV: 2Nap-(*SS*)-FF 5:5 mg/mL	CarbFV: 2Nap-(*SS*)-FF 5:5 mg/mL
Model	Hollow cylinder	Hollow cylinder + power law	Hollow cylinder + power law	Hollow cylinder + power law	Hollow cylinder + power law	Hollow cylinder + hollow cylinder
Background	0.018	0.0030	0.063	0.0050	0.016	0.019
A scale	0.0049	0.0013	0.0022	0.0011	0.0031	0.0016
A scale error	*4.46 x10^{-5}*	*4.74 x10^{-5}*	*1.88 x10^{-5}*	*2.15 x10^{-5}*	*2.38 x10^{-5}*	*1.97 x10^{-4}*
A radius	18.0	15.5	18.7	28.5	17.6	10.9
A radius error	*0.11*	*0.50*	*0.16*	*0.36*	*0.15*	*1.82*
A radius polydispersity	0.1	-	-	-	-	-
A thickness	17.7	20.2	29.5	28.72	28.3	21.5
A thickness error	*0.18*	*0.82*	*0.26*	*0.60*	*0.24*	*7.32*
A length	5000	5000	161.9	337.5	290.6	5000
A length error	-	-	*1.37*	*10.9*	*4.07*	-
B scale	-	7.76 x10^{-4}	4.45 x10^{-4}	1.85 x10^{-4}	2.72 x10^{-4}	0.0032
B scale error	-	*1.46 x10^{-4}*	*5.97 x10^{-6}*	*9.89 x10^{-5}*	*1.13 x10^{-5}*	*1.35 x10^{-4}*
B radius	-	-	-	-	-	24.1
B radius error	-	-	-	-	-	*3.2*
B thickness	-	-	-	-	-	20.2
B thickness error	-	-	-	-	-	*3.5*
B length	-	-	-	-	-	1088.7
B length error	-	-	-	-	-	*94.2*
B power	-	0.99	2.09	1.94	1.94	-
B power error	-	*0.088*	*0.0039*	*0.015*	*0.013*	-
Reduced χ^2	**10.68**	**1.33**	**5.98**	**2.28**	**1.83**	**2.96**

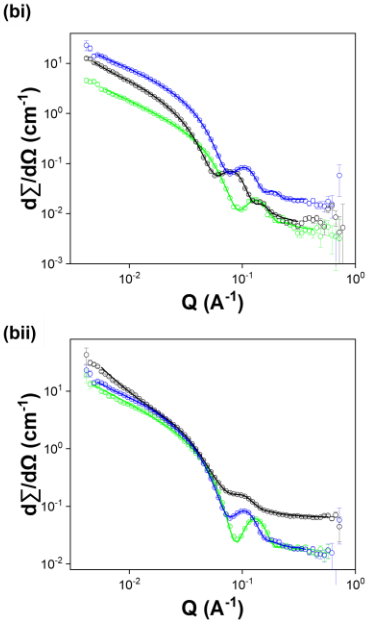

Figure 3.13. (a) Summary of the fitting parameters obtained from SasView model fitting of the SANS data. Parameter errors are fitting errors. (b) Plots of SANS data (circles) and fits (solid lines) obtained from 2Nap-(*SS*)-FF 10 mg/mL (green), (i) CarbFV 5 mg/mL (black), 2Nap-(*SS*)-FF 5 mg/mL (green) and CarbFV 5 mg/mL:2Nap-(*SS*)-FF 5 mg/mL fit to a hollow cylinder + hollow cylinder combined model (blue) and (ii) CarbFV 10 mg/mL (black), 2Nap-(*SS*)-FF 10 mg/mL (green) and CarbFV 5 mg/mL:2Nap-(*SS*)-FF 5 mg/mL fit to a hollow cylinder model (blue) at high pH.

Fitting the SANS data from the CarbIF 5 mg/mL:2Nap-(*SS*)-FF 5 mg/mL multicomponent system to a hollow cylinder model provided the best quality fit compared to all other cylinder models (Figure 3.14). The parameters obtained did not resemble those from either system alone. This could be mean co-assembly is taking place, resulting in the formation of new structures, or that the two components are self-sorting, and the reduced concentration is having a significant effect on the structures formed by each component.

To probe this further, we first fit the data from each component alone at concentrations of 5 mg/mL to match the concentrations present in the multicomponent system (Figure 3.14). Both CarbIF and 2Nap-(*SS*)-FF were fitted to a hollow cylinder model. We then fitted the data from the multicomponent system to a hollow cylinder + hollow cylinder combined model, using the fits from the 5 mg/mL single component systems as a starting point. The resulting fit was a great match to the data by eye, had low parameter error values and had a

lower χ^2 value than the hollow cylinder single model fit. This suggests self-sorting is taking place, with each component forming similar structures to those formed when alone. There are some slight changes to the dimensions of the cylinders, suggesting that assembly in the presence of a second component affects self-sorted assembly. We note that without imaging of the structures formed, it is impossible to say definitively how the components are assembling in the presence of one another.

(a)

Sample	2Nap-(*SS*)-FF 10 mg/mL	2Nap-(*SS*)-FF 5 mg/mL	CarbIF 10 mg/mL	CarbIF 5 mg/mL	CarbIF: 2Nap-(*SS*)-FF 5:5 mg/mL	CarbIF: 2Nap-(*SS*)-FF 5:5 mg/mL
Model	Hollow cylinder	Hollow cylinder + power law	Hollow cylinder + power law	Hollow cylinder	Hollow cylinder	Hollow cylinder + hollow cylinder
Background	0.018	0.0030	0.068	0.0060	0.026	0.026
A scale	0.0049	0.0013	0.0069	0.0025	0.0049	*0.0048*
A scale error	*4.46 x10^{-5}*	*4.74 x10^{-5}*	*2.60 x10^{-5}*	*2.26 x10^{-5}*	*4.24 x10^{-5}*	*7.52 x10^{-5}*
A radius	18.0	15.5	23.1	21.8	11.8	11.7
A radius error	*0.11*	*0.50*	*0.047*	*0.14*	*0.13*	*0.17*
A radius polydispersity	0.1	-	-	-	0.2	-
A thickness	17.7	20.2	20.9	22.7	19.2	18.64
A thickness error	*0.18*	*0.82*	*0.081*	*0.24*	*0.20*	*0.38*
A length	5000	5000	363.0	480.26	5000	5000
A length error	-	-	*2.89*	*13.4*	-	-
B scale	-	7.76 x10^{-4}	5.443 x10^{-6}	-	-	4.66 x10^{-4}
B scale error	-	*1.46 x10^{-4}*	*8.42 x10^{-7}*	-	-	*6.48 x10^{-7}*
B radius	-	-	-	-	-	19.4
B radius error	-	-	-	-	-	*2.1*
B thickness	-	-	-	-	-	23.0
B thickness error	-	-	-	-	-	*2.1*
B length	-	-	-	-	-	244.5
B length error	-	-	-	-	-	*20.7*
B power	-	0.99	2.70	-	-	-
B power error	-	*0.088*	*0.034*	-	-	-
Reduced χ^2	**10.68**	**1.33**	**31.04**	**2.45**	**6.16**	**4.40**

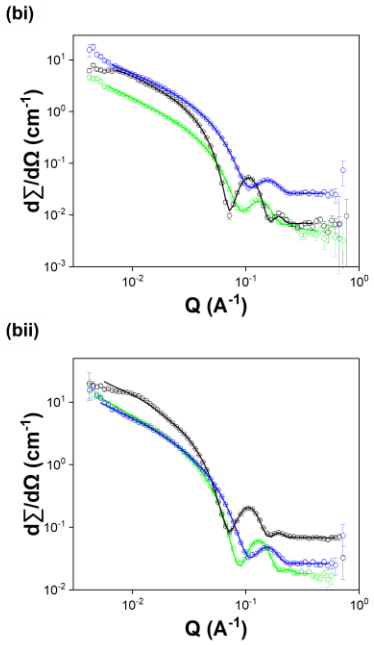

Figure 3.14. (a) Summary of the fitting parameters obtained from SasView model fitting of the SANS data. Parameter errors are fitting errors. (b) Plots of SANS data (circles) and fits (solid lines) obtained from (i) CarbIF 5 mg/mL (black), 2Nap-(*SS*)-FF 5 mg/mL (green) and CarbIF 5 mg/mL:2Nap-(*SS*)-FF 5 mg/mL fit to a hollow cylinder + hollow cylinder combined model (blue) and (ii) CarbIF 10 mg/mL (black), 2Nap-(*SS*)-FF 10 mg/mL (green) and CarbIF 5 mg/mL:2Nap-(*SS*)-FF 5 mg/mL fit to a hollow cylinder model (blue) at high pH.

The SANS data from the CarbFV 5 mg/mL: and CarbIF 5 mg/mL:2Nap-(*RS*)-FF multicomponent systems only provided reasonable fits to a hollow cylinder model combined with a second hollow cylinder model (Figure 3.15). This is strong evidence for self-sorting. To start fitting, we input parameters from each component alone. In both cases this gave a reasonable fit. We then fit all the parameters together. The multicomponent systems only

contain 5 mg/mL of each component. We expect concentration to affect the structures formed and may result in different secondary structures being formed.

(a)

Sample	2Nap-(*RS*)-FF 10 mg/mL	CarbFV 10 mg/mL	CarbFV: 2Nap-(*RS*)-FF 5:5 mg/mL	CarbIF 10 mg/mL	CarbIF: 2Nap-(*RS*)-FF 5:5 mg/mL
Model	Hollow cylinder	Hollow cylinder + power law	Hollow cylinder + hollow cylinder	Hollow cylinder + power law	Hollow cylinder + hollow cylinder
Background	0.065	0.063	0.058	0.068	0.061
A scale	0.0042	0.0022	0.030	0.0069	0.0020
A scale error	*6.27 x10^{-5}*	*1.88 x10^{-5}*	*5.61 x10^{-5}*	*2.60 x10^{-5}*	*5.71 x10^{-5}*
A radius	128.3	18.7	127.6	23.1	127.7
A radius error	*0.12*	*0.16*	*0.16*	*0.047*	*0.25*
A thickness	14.1	29.5	13.2	20.9	14.7
A thickness error	*0.22*	*0.26*	*0.27*	*0.081*	*0.48*
A length	555.2	161.9	463.7	363.0	448.3
A length error	*4.20*	*1.37*	*4.72*	*2.89*	*6.48*
B scale	-	4.45 x10^{-4}	0.0026	5.443 x10^{-6}	0.0030
B scale error	-	*5.97 x10^{-6}*	*3.457 x10^{-5}*	*8.42 x10^{-7}*	*5.84 x10^{-5}*
B radius	-	-	23.8	-	26.7
B radius error	-	-	*0.15*	-	*0.16*
B thickness	-	-	13.2	-	13.9
B thickness error	-	-	*0.27*	-	*0.29*
B length	-	-	261.2	-	552.8
B length error	-	-	*5.43*		*15.70*
B power	-	2.09	-	2.70	-
B power error	-	*0.0039*	-	*0.034*	-
Reduced χ^2	**22.09**	**5.98**	**202.45**	**31.04**	**55.75**

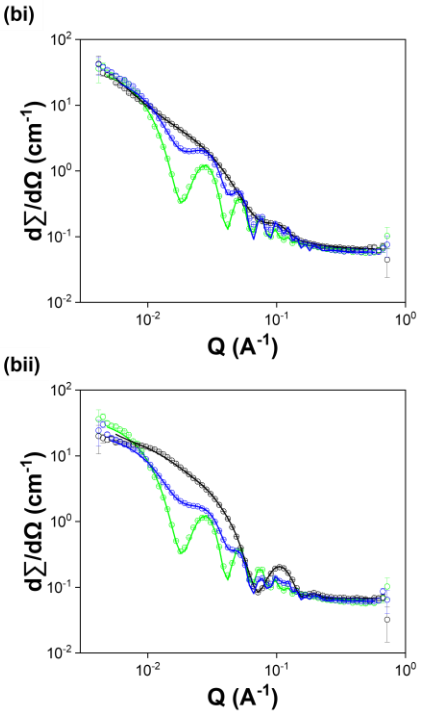

Figure 3.15. (a) Summary of the parameters obtained from fitting the SANS data using SasView model fitting. Parameter errors are fitting errors. (b) Plots of SANS data (circles) and fits (solid lines) obtained from 2Nap-(*RS*)-FF 10 mg/mL (green), (i) CarbFV 10 mg/mL (black) and CarbFV 5 mg/mL:2Nap-(*RS*)-FF 5 mg/mL (blue) and (ii) CarbIF 10 mg/mL (black) and CarbIF 5 mg/mL:2Nap-(*RS*)-FF 5 mg/mL (blue) at high pH.

The CD data from the CarbFV 5 mg/mL:2Nap-(*RS*)-FF 5 mg/mL multicomponent systems suggests co-assembly is taking place. However, we were unable to obtain reasonable fits when fitting the CarbFV 5 mg/mL:2Nap-(*RS*)-FF 5 mg/mL SANS data to a single hollow cylinder model. The CD signals from CarbFV may be completely masked by those from 2Nap-(*RS*)-FF, making the data resemble a co-assembled system.

The results from the SANS data can be partially rationalised by considering the molecular structures of the components. 7MeO2NapFV and 1NapVV have a naphthalene at the *N*-terminus, as does 2NapFF. It is easy to imagine that the naphthalene rings stacking on top of each other within the co-assembled structures. CarbFV and CarbIF have a different *N*-terminal group, making it more difficult for these components to effectively co-assemble

with 2NapFF. It is therefore preferable for them to self-sort. However, this does not explain the suspected co-assembly between CarbFV and 2Nap-(*SS*)-FF.

3.2.2 Multicomponent assembly during gelation

Molecular assembly going from high pH to low pH was probed using ^{1}H nuclear magnetic resonance (NMR) spectroscopy. At high pH, most of the dipeptides studied are visible in the ^{1}H NMR spectrum, apart from 2Nap-(*RS*)-FF and CarbIF. As the pH is reduced on addition of GdL, the chosen trigger for gelation, self-assembly of the dipeptides into fibrous structures causes them to become NMR invisible.[19] We can therefore correlate the disappearance of peaks from the NMR spectrum to the percentage of the corresponding dipeptide that is self-assembled into solid-like fibres. The percentage free molecule from the NMR data can be compared to pH data collected during gelation. Assembly begins just below the pK_a value of the gelator. The NMR data matches with the plateaus in the pH data which corresponds to the pK_a values of the components.[20]

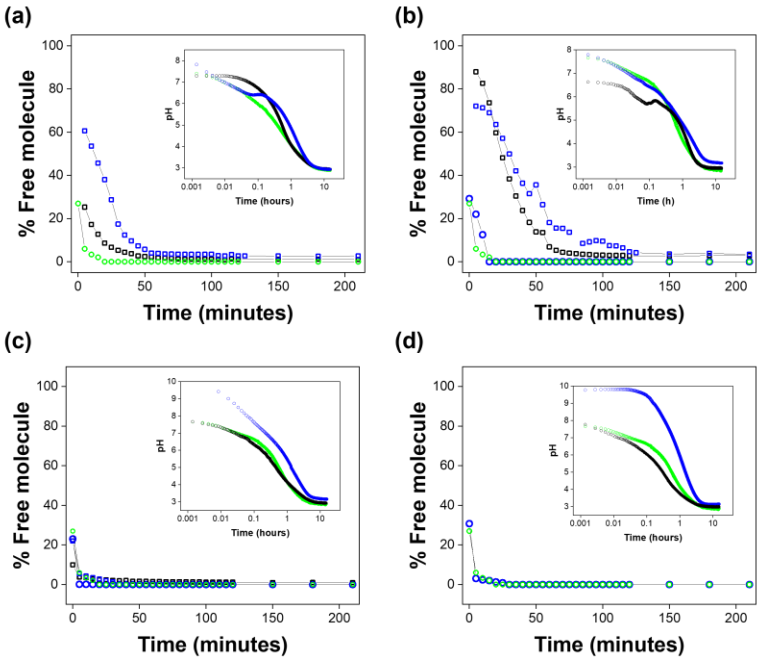

Figure 3.16. Results from kinetic ^{1}H NMR spectroscopy experiments and measurements of pH with time (inserts) during gelation using GdL as a trigger for (a) 7MeO2NapFV, (b) 1NapVV, (c) CarbFV and (d) CarbIF. Data was collected for each second component alone at a concentration of 10 mg/mL (black), in a multicomponent system with a concentration ratio of 5 mg/mL:5 mg/mL (second component = blue square, 2NapFF = blue circle) and for 2Nap-(*SS*)-FF 10 mg/mL (green).

In all cases, peaks from both components start to disappear at the same pH. This suggests that the pK_a values of each component are too close for effective self-sorting *via* a slow pH change as previously described.[20] The components will therefore be assembling at the same time as each other. How the assembly of each component will be affected by concurrent assembly of the other is hard to determine. CarbFV, CarbIF and 2NapFF all disappear rapidly (Figures 3.16 and 3.17). 7MeO2NapFV and 1NapVV assemble more slowly. 7MeO2NapFV assembles more slowly in the presence of 2NapFF, showing that the presence of a second component is altering the self-assembly. However, none of these observations confirm that co-assembly is taking place. The CarbIF integrals in all experiments were too small to measure.

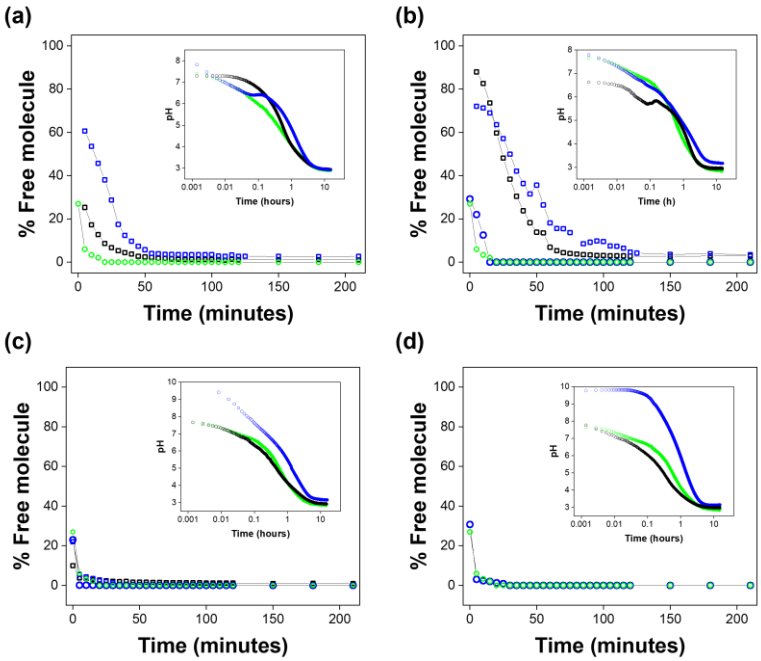

Figure 3.17. Results from kinetic NMR spectroscopy experiments and measurements of pH with time (inserts) during gelation using GdL as a trigger for (a) 7MeO2NapFV, (b) 1NapVV and (c) CarbFV. Data was collected for each second component alone at a concentration of 10 mg/mL (black), in a multicomponent system with a concentration ratio of 5 mg/mL:5 mg/mL (2NapFF = blue circle, second component = blue square) and for 2Nap-(*RS*)-FF 10 mg/mL (green).

In a similar study investigating the multicomponent assembly of a series of dipeptides functionalised with *N*-terminal naphthalene derivatives, signals from the ^{1}H NMR spectra initially disappeared at similar rates.[19] At longer times, the % free molecule recorded for 2NapFF decreases faster. This implies that co-assembly isn't uniform throughout the

process. The rates of assembly of both components in each system are similar but 2NapFF doesn't need as much time to be fully assembled.

The integrals corresponding to 2Nap-(*RS*)-FF were too small to be measured. Since we could not measure 2Nap-(*RS*)-FF, we only have the differences between the single and multicomponent systems to rely on. For the same reason, we were also unable to measure CarbIF so these data were not included. This made probing assembly in the CarbIF:2Nap-(*RS*)-FF systems impossible. Assembly will be affected by concentration of component. It would therefore be helpful to have NMR kinetics data of the single component systems at 5 mg/mL in addition to 10 mg/mL in case this is having an effect.

3.2.3 Multicomponent assembly in the gel state at low pH

Gels were prepared from each single and multicomponent system using GdL as a trigger.[31] Suspensions were prepared as described in section 3.2.1. Each gel was prepared by pipetting 2 mL of the required suspension into a 7 mL Sterilin vial containing pre-weighed solid GdL (16 mg/mL). The sample was swirled briefly by hand to dissolve the GdL. The samples were then left undisturbed for a minimum of 16 hours to allow gel formation before analysis. The final pH of all gels were between 3.2 and 3.5.

3.2.3.1 CD spectroscopy at low pH

Data from UV-Vis spectroscopy of the gels could not be used due to the turbidity of the samples. CD spectra at low pH show less obvious trends than those at high pH. The HT values measured concurrently with CD data are very high (Appendix 2.2). We therefore need to be cautious about the conclusions we draw from this data. The data collected from 2Nap-(*SS*)-FF and 2Nap-(*RS*)-FF follow the opposite trend to that expected with CD signal increasing with decreasing concentration (Figure 3.18). This makes the data complicated to rationalise.

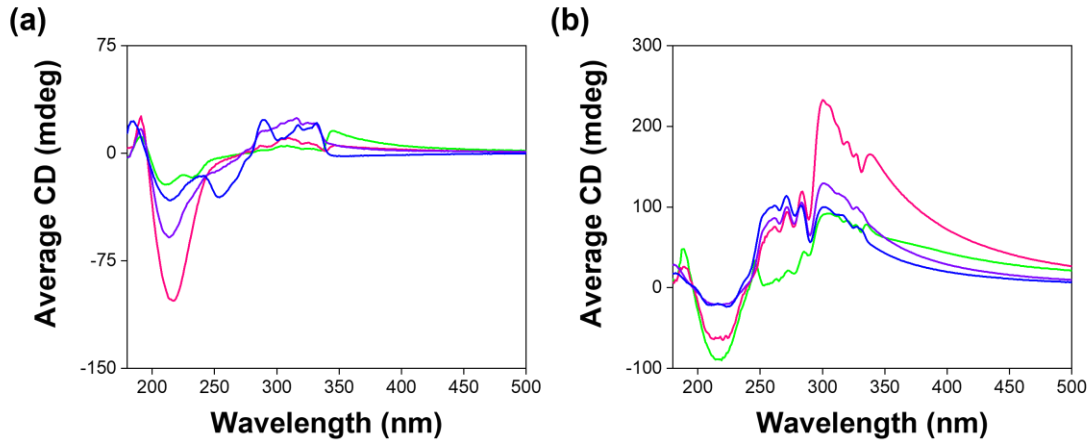

Figure 3.18. CD spectra recorded from single component systems composed of (a) 2Nap-(*SS*)-FF and (b) 2Nap-(*RS*)-FF at concentrations of 10 mg/mL (green), 7.5 mg/mL (pink), 5 mg/mL (purple) and 2.5 mg/mL (blue) in the gel state at low pH. All data was collected in triplicate and averaged. Absorbance and HT data were recorded concurrently with the CD spectra (Appendix 2.2).

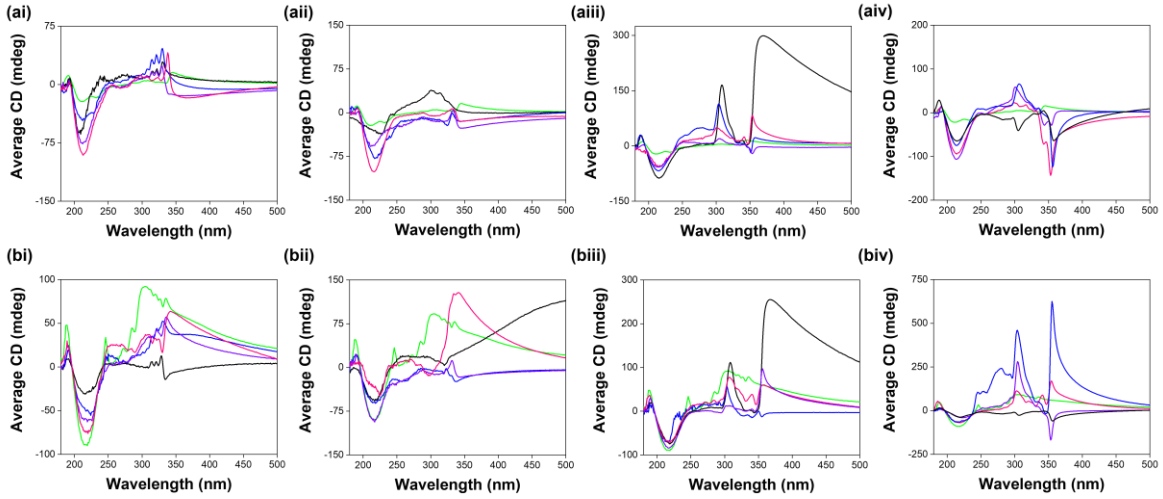

Figure 3.19. CD spectra recorded from single and multicomponent systems of (i) 7MeO2NapFV, (ii) 1NapVV, (iii) CarbFV and (iv) CarbIF at concentration ratios second component:(a) 2Nap-(*SS*)-FF and (b) 2Nap-(*RS*)-FF of 10 mg/mL:0 mg/mL (black), 7.5 mg/mL:2.5 mg/mL (blue), 5 mg/mL:5 mg/mL (purple) and 2.5 mg/mL:7.5 mg/mL (pink) at low pH in the gel state. The CD spectra recorded from the appropriate 2NapFF diastereomer at 10 mg/mL (green) is shown in each spectrum for easy comparison with the multicomponent systems. All data was collected in triplicate and averaged. Absorbance and HT data were recorded concurrently with the CD spectra (Appendix 2.2).

3.2.3.2 SANS at low pH

As with the SANS data collected from samples at high pH, we attempted to fit all data sets to all available standard cylinder models in order to identify the most suitable model for each set of data. Fitting SANS data collected from the 2Nap-(*SS*)-FF 10 mg/mL gel sample did not yield the expected parameters based on previous work.[3, 32] Manually entering the expected values greatly decreased the quality of the fit. We do not know the reason behind this. Inclusion of polydispersity in the radius parameter allowed us to fully capture the data at Q = 0.1 $Å^{-1}$. This was necessary for most of the systems in the gel state.

In most cases, the value obtained for length during fitting was beyond the scale available by neutron scattering. As before, we set the length for these data sets to 5000 Å. Changing from this value does not significantly affect the quality of the fit. Inclusion of a power law helps us to capture scattering contribution from the gel network.[32] The power law is dominant at low Q. The values for axis ratio in elliptical models might originate from lateral association of fibres in the gel network.[33]

Fitting the SANS data from the 2Nap-(*SS*)-FF 10 mg/mL single component system to a flexible elliptical cylinder model combined with a power law provided the best fit (Figure 3.20). The 7MeO2NapFV 10 mg/mL single component system was also best fit to a flexible elliptical cylinder model but without the power law component (Figure 3.20). Since 2Nap-(*SS*)-FF directs assembly at high pH, it would be reasonable to expect that 2Nap-(*SS*)-FF would also direct assembly at low pH. However, using the parameters obtained from fitting the 2Nap-(*SS*)-FF single component system did not match the data. Fitting all the parameters together after inputting the values from the 2Nap-(*SS*)-FF single component fit gave an axis ratio of 1 suggesting the structures formed in the multicomponent system are not elliptical and are therefore fundamentally different to those formed by the single component systems. The 7MeO2NapFV 5 mg/mL:2Nap-(*SS*)-FF 5 mg/mL multicomponent system was instead fitted to a flexible cylinder model (Figure 3.20). Co-assembly of the two components is therefore causing a significant difference in assembly on a reduction in pH and therefore the secondary structures of the gel network.

(a)

Sample	2Nap-(*SS*)-FF 10 mg/mL	7MeO2NapFV 10 mg/mL	7MeO2NapFV: 2Nap-(*SS*)-FF 5:5 mg/mL	1NapVV 10 mg/mL	1NapVV: 2Nap-(*SS*)-FF 5:5 mg/mL
Model	Flexible elliptical cylinder + power law	Flexible elliptical cylinder	Flexible cylinder + power law	Flexible elliptical cylinder	Flexible elliptical cylinder + power law
Background	0.022	0.081	0.024	0.068	0.028
A scale	3.31×10^{-4}	5.05×10^{-4}	0.0032	0.0025	3.94×10^{-4}
A scale error	*1.15×10^{-5}*	*2.10×10^{-5}*	*3.98×10^{-5}*	*2.93×10^{-5}*	*7.34×10^{-6}*
A radius	22.5	60.3	31.6	177.9	30.4
A radius error	*0.35*	*0.73*	*0.092*	*0.68*	*0.21*
A radius polydispersity	0.15	0.5	0.1	0.3	-
A axis ratio	3.42	3.78	-	1.67	1.93
A axis ratio error	*0.060*	*0.11*	-	*0.018*	*0.021*
A Kuhn length	15.6	132.1	60.9	422.3	-
A Kuhn length error	*0.62*	*4.83*	*0.0029*	*7.50*	-
A length	5000	5000	608.6	5000	5000
A length error	-	-	*8.75*	-	-
B scale	2.04×10^{-5}	-	4.56×10^{-5}	-	3.49×10^{-5}
B scale error	*2.84×10^{-6}*	-	*3.25×10^{-6}*	-	*1.93×10^{-6}*
B power	2.75	-	2.53	-	2.71
B power error	*0.027*	-	*0.0014*	-	*0.011*
Reduced χ^2	**12.81**	**6.55**	**6.83**	**10.01**	**6.12**

(bi)

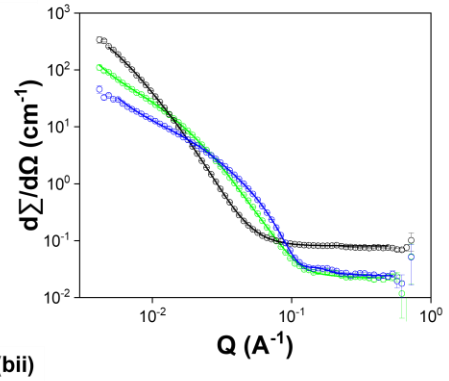

(bii)

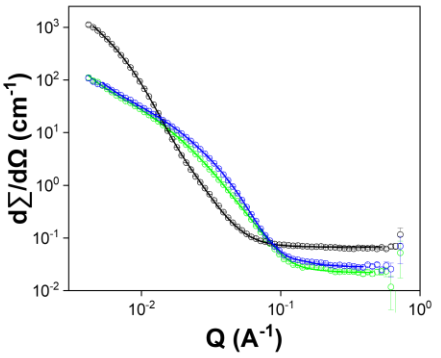

Figure 3.20. (a) Summary of the parameters obtained from fitting the SANS data using SasView model fitting. Parameter errors are fitting errors. (b) Plots of SANS data (circles) and fits (solid lines) obtained from 2Nap-(*SS*)-FF 10 mg/mL (green), (i) 7MeO2NapFV 10 mg/mL (black) and 7MeO2NapFV 5 mg/mL:2Nap-(*SS*)-FF 5 mg/mL (blue) and (ii) 1NapVV 10 mg/mL (black) and 1NapVV 5 mg/mL:2Nap-(*SS*)-FF 5 mg/mL (blue) in the gel state at low pH.

The 1NapVV 10 mg/mL gel has high polydispersity (Figure 3.20). This implies that not all secondary structures present in the gel have the same radius. The SANS data from the 1NapVV 5 mg/mL:2Nap-(*SS*)-FF multicomponent system was fitted by first inputting the parameters from 2Nap-(*SS*)-FF single component system then fitting all the parameters together (Figure 3.20). This method of fitting provided the best fit according to χ^2 value, parameter errors, residuals and how the fit looked by eye. This suggests that the 2Nap-(*SS*)-FF directed co-assembly observed at high pH persists in the gel state at low pH. Despite having similar behaviour at high pH, the 1NapVV and 7MeO2NapFV multicomponent systems exhibit different behaviour on a reduction in pH.

The reduced χ^2 values obtained from fitting SANS data from 2Nap-(*RS*)-FF single and multicomponent systems are high in both the sol and gel states. However, the fits obtained look reasonable by eye and the parameters obtained from the fits have small error values. It

is interesting that 2Nap-(*RS*)-FF maintains a hollow cylinder structure going from the sol state at high pH to the gel state at low pH as this is not observed with 2Nap-(*SS*)-FF. The only parameter that changes considerably going from the sol state to the gel state is the thickness of the hollow cylinder, which almost doubles (Figure 3.21). This could indicate lateral association of the fibres during formation of the gel network.[33] Experiments following small angle scattering with time during gelation could be helpful in the future.

(a)

Sample	2Nap-(*RS*)-FF 10 mg/mL	7MeO2NapFV 10 mg/mL	7MeO2NapFV: 2Nap-(*RS*)-FF 5:5 mg/mL	1NapVV 10 mg/mL	1NapVV: 2Nap-(*RS*)-FF 5:5 mg/mL
Model	Hollow cylinder	Flexible elliptical cylinder	Hollow cylinder + power law	Flexible elliptical cylinder	Flexible elliptical cylinder
Background	0.092	0.081	0.065	0.068	0.069
A scale	0.0035	5.05×10^{-4}	4.81×10^{-4}	0.0025	0.0035
A scale error	*2.02×10^{-5}*	*2.10×10^{-5}*	*7.30×10^{-6}*	*2.93×10^{-5}*	*1.88×10^{-5}*
A radius	125.1	60.3	106.8	177.9	37.8
A radius error	*0.11*	*0.73*	*0.61*	*0.68*	*0.082*
A radius polydispersity	-	0.5	-	0.3	0.2
A thickness	25.3	-	64.4	-	-
A thickness error	*0.17*	-	*0.95*	-	-
A axis ratio	-	3.78	-	1.67	-
A axis ratio error	-	*0.11*	-	*0.018*	-
A Kuhn length	-	132.08	-	422.33	376.83
A Kuhn length error	-	*4.83*	-	*7.50*	*0.082*
A length	575.2	5000	494.2	5000	815.2
A length error	*4.07*	-	*12.58*	-	*15.28*
B scale	-	-	-	-	-
B scale error	-	-	-	-	-
B power	-	-	-	-	-
B power error	-	-	-	-	-
Reduced χ^2	**61.07**	**6.55**	**9.98**	**10.01**	**12.37**

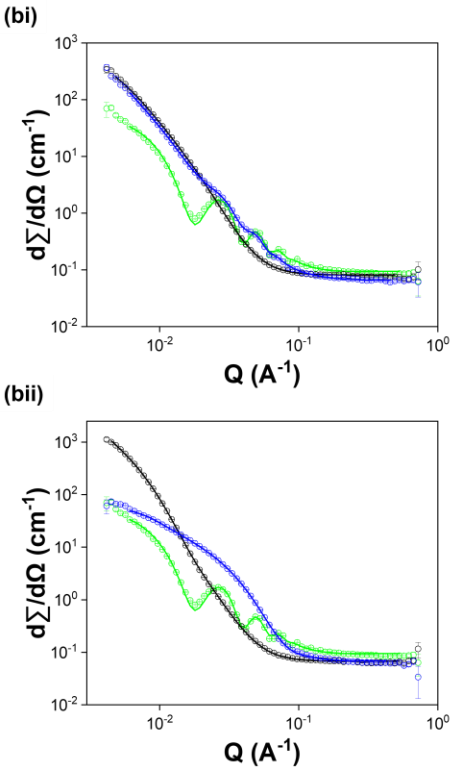

Figure 3.21. (a) Summary of the parameters obtained from fitting the SANS data using SasView model fitting. Parameter errors are fitting errors. (b) Plots of SANS data (circles) and fits (solid lines) obtained from 2Nap-(*RS*)-FF 10 mg/mL (green), (i) 7MeO2NapFV 10 mg/mL (black) and 7MeO2NapFV 5 mg/mL:2Nap-(*RS*)-FF 5 mg/mL (blue) and (ii) 1NapVV 10 mg/mL (black) and 1NapVV 5 mg/mL:2Nap-(*RS*)-FF 5 mg/mL (blue) in the gel state at low pH.

Co-assembly of 2Nap-(*RS*)-FF 5 mg/mL with 7MeO2NapFV 5 mg/mL causes significant changes to the parameters of the fit as compared to the 2Nap-(*RS*)-FF 10 mg/mL single component system (Figure 3.21). The model used to fit the SANS data from the multicomponent system is the same as the model used for the 2Nap-(*RS*)-FF 10 mg/mL single component system, suggesting 2Nap-(*RS*)-FF is directing assembly at low pH.

However, the parameters obtained from the fit are notably different to those obtained from the 2Nap-(*RS*)-FF 10 mg/mL single component system, showing that co-assembly with 7MeO2NapFV changes the structures formed.

The SANS data from the 1NapVV 5 mg/mL:2Nap-(*RS*)-FF 5 mg/mL multicomponent system was fitted to a flexible elliptical cylinder, the same model as was used for the 1NapVV single component system, suggesting that 1NapVV rather than 2Nap-(*RS*)-FF is directing assembly at low pH (Figure 3.21). Co-assembly of 1NapVV with 2Nap-(*RS*)-FF resulted in formation of structures with significantly smaller radii than those formed by 1NapVV alone. We were also able to fit the length of these structures, rather than setting it to 5000 Å. It appears that, although 2Nap-(*RS*)-FF seems to direct assembly at high pH, 1NapVV takes over at low pH.

We tried to combine cylinder models for the CarbFV 5 mg/mL:2Nap-(*SS*)-FF 5 mg/mL system to investigate whether the self-sorting is taking place at low pH. While the fits looked good by eye and had low χ^2 values (~2) for flexible elliptical cylinder + cylinder model, flexible cylinder and flexible elliptical cylinder models, the values obtained for the axis ratios were unreasonably high (between 7 and 11), depending on the models chosen. The data was best fitted to an elliptical cylinder combined with a power law (Figure 3.22); this is different to either component alone. This information suggests that co-assembly is taking place between these components at low pH.

The CarbFV 5 mg/mL:2Nap-(*RS*)-FF 5 mg/mL multicomponent system showed the same behaviour as its 2Nap-(*SS*)-FF counterpart: we achieved the best quality fit for the CarbFV 5 mg/mL:2Nap-(*RS*)-FF 5 mg/mL multicomponent system using an elliptical cylinder model combined with a power law (Figures 3.22 and 3.23). We tried fitting the data to the same models as each component alone, starting with the parameters obtained for the corresponding component. Neither provided suitable fits for the multicomponent data. This shows that co-assembly is resulting in the formation of new structures that do not resemble either component. From SANS data collected at high pH, it appears that co-assembly is arising on gelation from an initially self-sorted system.

(a)

Sample	2Nap-(*SS*)-FF 10 mg/mL	CarbFV 10 mg/mL	CarbFV: 2Nap-(*SS*)-FF 5:5 mg/mL	CarbIF 10 mg/mL	CarbIF: 2Nap-(*SS*)-FF 5:5 mg/mL
Model	Flexible elliptical cylinder + power law	Flexible cylinder + power law	Elliptical cylinder + power law	Flexible cylinder + power law	Flexible cylinder + power law
Background	0.022	0.071	0.025	0.079	0.025
A scale	3.31×10^{-4}	0.0020	0.0036	0.0029	0.0019
A scale error	*1.15×10^{-5}*	*3.45×10^{-5}*	*1.89×10^{-5}*	*3.21×10^{-5}*	*9.62×10^{-5}*
A radius	22.5	52.7	34.7	48.5	38.9
A radius error	*0.35*	*0.017*	*0.25*	*0.13*	*0.19*
A radius polydispersity	0.15	-	0.1	-	-
A axis ratio	3.42	-	1.43	-	-
A axis ratio error	*0.060*	-	*0.020*	-	-
A Kuhn length	15.6	84.8	-	80.2	39.9
A Kuhn length error	*0.62*	*2.95*	-	*1.81*	*3.40*
A length	5000	5000	5000	3370.8	909.5
A length error	-	-	-	*90.99*	*51.98*
B scale	2.043×10^{-5}	2.68×10^{-4}	7.76×10^{-5}	7.95×10^{-4}	5.58×10^{-5}
B scale error	*2.84×10^{-6}*	*1.04×10^{-5}*	*4.09×10^{-6}*	*4.14×10^{-5}*	*1.86×10^{-6}*
B power	2.75	2.09	2.31	1.66	2.59
B power error	*0.027*	*0.015*	*0.011*	*0.0023*	*0.0070*
Reduced χ^2	**12.81**	**19.74**	**3.54**	**21.77**	**8.56**

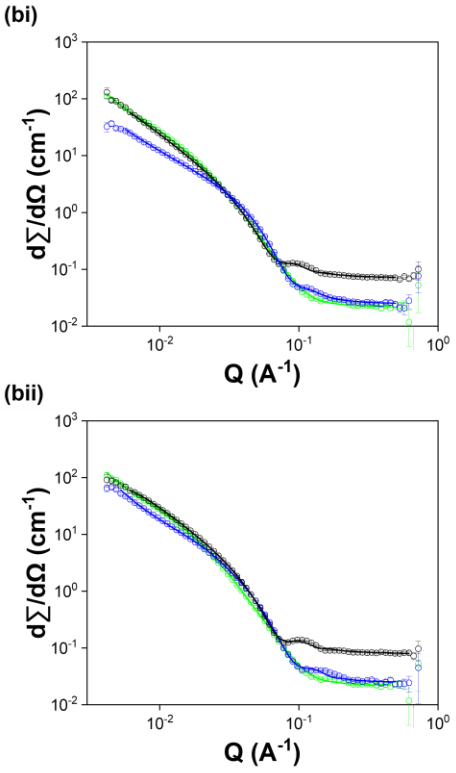

Figure 3.22. (a) Summary of the parameters obtained from fitting the SANS data using SasView model fitting. Parameter errors are fitting errors. (b) Plots of SANS data (circles) and fits (solid lines) obtained from 2Nap-(*SS*)-FF 10 mg/mL (green), (i) CarbFV 10 mg/mL (black) and CarbFV 5 mg/mL:2Nap-(*SS*)-FF 5 mg/mL fit to hollow cylinder model combined with a power law (blue) and to a hollow cylinder combined with a hollow cylinder (pink) and (ii) CarbIF 10 mg/mL (black) and CarbIF 5 mg/mL:2Nap-(*SS*)-FF 5 mg/mL (blue) in the gel state at low pH.

A flexible cylinder model combined with a power law gave the best fit for the SANS data from CarbIF 5 mg/mL:2Nap-(*SS*)-FF 5 mg/mL multicomponent system compared to all other single cylinder models. We note that the fit did not capture the line shape exactly at low Q (Figure 3.22). Fitting the data to a hollow cylinder model combined with a flexible elliptical cylinder model allowed us to capture the line shape more accurately at high Q, but the fit had a higher χ^2 value. The radius and thickness values for the hollow cylinder component had to be entered manually to better emulate the line shape between 0.1 and 0.3 Q. This was the only combined cylinder model we were able to achieve the correct line shape with. It is difficult to rationalise how hollow cylinders may be forming from this system. It is also important to be cautious of over-fitting as combined models add extra parameters. We therefore conclude that the CarbIF 5 mg/mL:2Nap-(*SS*)-FF 5 mg/mL multicomponent system also transitions from self-sorting in the micellar phase at high pH to co-assembly at

low pH in the gel state. Without selectively deuterated experiments and some form of imaging, we cannot conclude for certain what is happening in these systems.

(a)

Sample	2Nap-(*RS*)-FF 10 mg/mL	CarbFV 10 mg/mL	CarbFV: 2Nap-(*RS*)-FF 5:5 mg/mL	CarbIF 10 mg/mL	CarbIF: 2Nap-(*RS*)-FF 5:5 mg/mL
Model	Hollow cylinder	Flexible cylinder + power law	Elliptical cylinder + power law	Flexible cylinder + power law	Flexible cylinder + power law
Background	0.092	0.071	0.066	0.079	0.070
A scale	0.0035	0.0020	0.0027	0.0029	0.0026
A scale error	*2.02 x10^{-5}*	*3.45 x10^{-5}*	*1.35 x10^{-5}*	*3.21 x10^{-5}*	*1.36 x10^{-5}*
A radius	125.1	52.7	45.1	48.5	58.8
A radius error	*0.11*	*0.017*	*0.11*	*0.13*	*0.08*
A radius polydispersity	-	-	-	-	-
A thickness	25.3	-	-	-	-
A thickness error	*0.17*	-	-	-	-
A axis ratio	-	-	1.56	-	-
A axis ratio error	-	-	*0.013*	-	-
A Kuhn length	-	84.81	81.0	80.18	176.7
A Kuhn length error	-	*2.95*	*2.51*	*1.81*	*0.0015*
A length	575.2	5000	5000	3370.8	706.9
A length error	*4.07*	-	-	*90.99*	*23.8*
B scale	-	2.68 x10^{-4}	8.43 x10^{-5}	7.95 x10^{-4}	9.44 x10^{-5}
B scale error	-	*1.04 x10^{-5}*	*1.39 x10^{-6}*	*4.14 x10^{-5}*	*4.08 x10^{-5}*
B power	-	2.09	2.60	1.66	2.41
B power error	-	*0.015*	*0.0042*	*0.0023*	*0.017*
Reduced χ^2	**61.07**	**19.74**	**25.00**	**21.77**	**10.05**

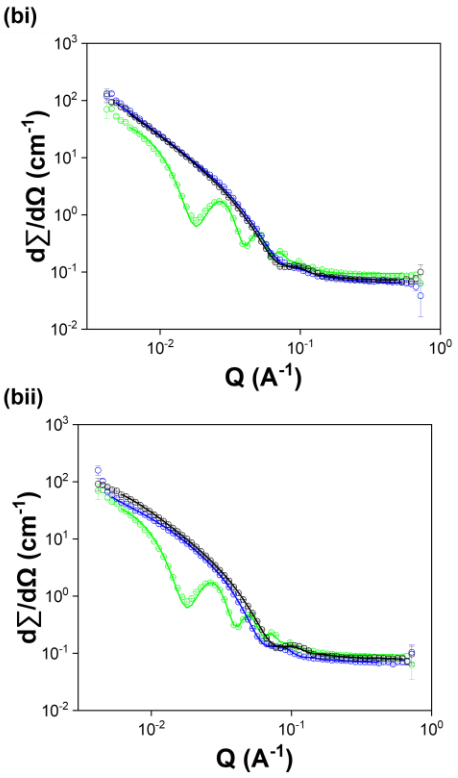

Figure 3.23. (a) Summary of the parameters obtained from fitting the SANS data using SasView model fitting. Parameter errors are fitting errors. (b) Plots of SANS data (circles) and fits (solid lines) obtained from 2Nap-(RS)-FF 10 mg/mL (green), (i) CarbFV 10 mg/mL (black) and CarbFV 5 mg/mL:2Nap-(RS)-FF 5 mg/mL fit to hollow cylinder model combined with a power law (blue) and to a hollow cylinder combined with a hollow cylinder (pink) and (ii) CarbIF 10 mg/mL (black) and CarbIF 5 mg/mL:2Nap-(RS)-FF 5 mg/mL (blue) in the gel state at low pH.

The CarbIF 5 mg/mL:2Nap-(*RS*)-FF 5 mg/mL multicomponent system showed the same behaviour as the CarbFV multicomponent systems. The SANS data from this system were best fit to a flexible cylinder model combined with a power law (Figure 3.23). While combining two cylinder models gave fits of similar quality according to χ^2 value, error values and evaluating the fit by eye, the values obtained for the axis ratios were unusually high (between 7 and 11). We therefore conclude that, like the CarbFV 5mg/mL:2Nap-(*RS*)-FF 5 mg/mL multicomponent system, CarbIF 5mg/mL:2Nap-(*RS*)-FF transitions from self-sorting at high pH to co-assembly with 2Nap-(*RS*)-FF when the pH is reduced.

All these data show the effect of the identity of the second gelling component as well as the chirality of the first gelling component. While previous work highlighting the preference for homochiral interactions[22] would suggest the 2Nap-(*SS*)-FF multicomponent systems would be more likely to undergo co-assembly and the 2Nap-(*RS*)-FF multicomponent systems would undergo self-sorting, we think something else is at play in these systems.

3.2.3.3. Rheology at low pH

We investigated the mechanical properties of the gels formed from of all the single and multicomponent systems using rheology. A comparison to the same diastereomer of 2NapFF as is in the multicomponent systems is included in each graph for easy comparison. The rheological data clearly shows the importance of concentration ratio in determining the mechanical properties of the final gel. The relative concentration of components therefore provides an important tool for tuning the properties of a given multicomponent gel. That said, the effect of concentration on mechanical properties does not follow an obvious trend, making it difficult to predict the outcome of altering concentration ratio.

It would be reasonable to expect that the self-sorted multicomponent systems with secondary structures that closely resemble one of the components to have rheological properties that also resemble that component. However, the length scales investigated using SANS do not take into account the interactions that take place at longer length scales within the gel network, for example entanglements and cross-links between individual structures. It is therefore important to be cautious when relating the results from rheological measurements to the secondary structures observed using SANS.

The 7MeO2NapFV 10 mg/mL single component system forms gels with higher stiffness (G')[34] and elasticity (G''/G')[34] than 2Nap-(*SS*)-FF 10 mg/mL (Figure 3.24a). The 7MeO2NapFV 7.5 mg/mL:2Nap-(*SS*)-FF 2.5 mg/mL multicomponent gels have even greater stiffness and elasticity than the 7MeO2NapFV 10 mg/mL gels. Incorporating a small proportion of 2Nap-(*SS*)-FF into the system therefore increases the solid-like behaviour of the system. As 2Nap-(*SS*)-FF concentration increases, the stiffness and elasticity of the gels decreases. The 7MeO2NapFV 2.5 mg/mL:2Nap-(*SS*)-FF 7.5 mg/mL multicomponent gels have similar G' and G'' values to the 2Nap-(*SS*)-FF 10 mg/mL single component gels, suggesting 2Nap-(*SS*)-FF dictates assembly at this concentration ratio.

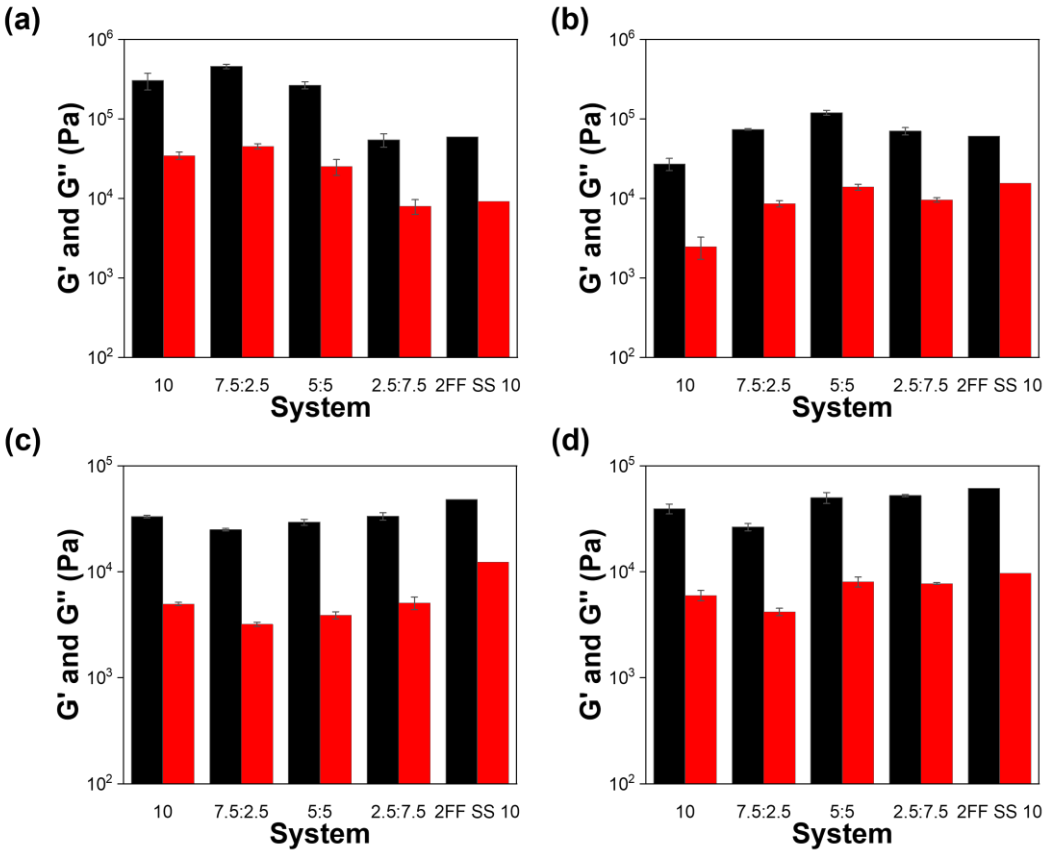

Figure 3.24. Average G′ (black) and G″ (red) values for (a) 7MeO2NapFV, (b) 1NapVV, (c) CarbFV and (d) CarbIF single and 2Nap-(*SS*)-FF multicomponent systems. Moduli were calculated from frequency sweeps using the values for the moduli at a frequency of 10 rad/s. Error bars show the standard deviation between samples. The full rheology data used to calculate the values shown can be found in Appendix 2.3.

1NapVV 10 mg/mL gels have lower stiffness and elasticity than 2Nap-(*SS*)-FF 10 mg/mL (Figure 3.24b). All the 1NapVV multicomponent systems have greater stiffness and elasticity than the single component systems, with 1NapVV 5 mg/mL:2Nap-(*SS*)-FF 5 mg/mL having the highest G′ and G″ values. This exemplifies how preparation of multicomponent systems and optimisation of concentration ratio can be used to enhance the mechanical properties of a chosen system. The 7MeO2NapFV and 1NapVV systems exhibit different behaviour in the gel state, despite their similarities in the sol state. 1NapVV being less similar to 2Nap-(*SS*)-FF than 7MeO2NapFV at the molecular level and the differences in the secondary structures formed by these molecules in the gel state likely contribute to these differences to some extent.

CarbFV 10 mg/mL and CarbIF 10 mg/mL have lower G′ and G″ values than 2Nap-(*SS*)-FF 10 mg/mL (Figure 3.24). All the CarbFV multicomponent systems have lower G′ and

elasticity than the single component systems. G′ increases with increasing 2Nap-(*SS*)-FF concentration. This example shows that preparation of multicomponent systems can also be used to reduce the stiffness of a system and, again, concentration ratio of components can be used to fine-tune the changes in mechanical properties. The CarbIF multicomponent systems showed a similar trend in stiffness and elasticity. This highlights the importance of the *N*-terminal capping groups chosen for each component during design of gelator-gelator multicomponent systems.

Strain sweeps provide valuable information about the mechanical properties of a gel in addition to moduli values. The strain value at which G′ begins to deviate from linear (the critical strain)[35] tells us the strain at which the gel network begins to break down. The strain value at which G″ crosses over G′ (the crossover point) tells us where the gel network has completely broken down and transitioned from a viscoelastic solid to a liquid.[36] These values therefore tell us about the strength of the gel network.

Gels formed from 7MeO2NapFV alone have a greater crossover point than those formed from 2Nap-(*SS*)-FF alone, but a lower critical strain (Figure 3.25a). This suggests that while the network of 7MeO2NapFV gels begins to break down at a lower strain value, the network does not completely collapse until much greater strain is applied. Different behaviour in response to applied strain can be useful in different situations. Preparation of 7MeO2NapFV:2Nap-(*SS*)-FF multicomponent systems with concentration ratios 7.5:2.5 and 5:5 (mg/mL:mg/mL) reduces the mechanical strength of the gels formed compared to the single component systems. The 7MeO2NapFV 2.5 mg/mL:2Nap-(*SS*)-FF 7.5 mg/mL gels had the same critical strain and crossover point values to the 2Nap-(*SS*)-FF gels, further confirming that 2Nap-(*SS*)-FF has completely taken over assembly at this concentration ratio. This highlights the importance of the concentration of each component.

1NapVV alone has a considerably higher crossover point than all the other systems (Figure 3.25b). Incorporation of 2Nap-(*SS*)-FF into the system reduces the crossover point considerably. As the 2Nap-(*SS*)-FF concentration increases in the 7MeO2NapFV and 1NapVV multicomponent systems, the values for all mechanical properties measured begin to resemble those from 2Nap-(*SS*)-FF alone. This could be related to the conclusions drawn from SANS, which shows that these systems co-assemble to form secondary structures that resemble those formed by 2Nap-(*SS*)-FF alone at the same total gelator concentration.

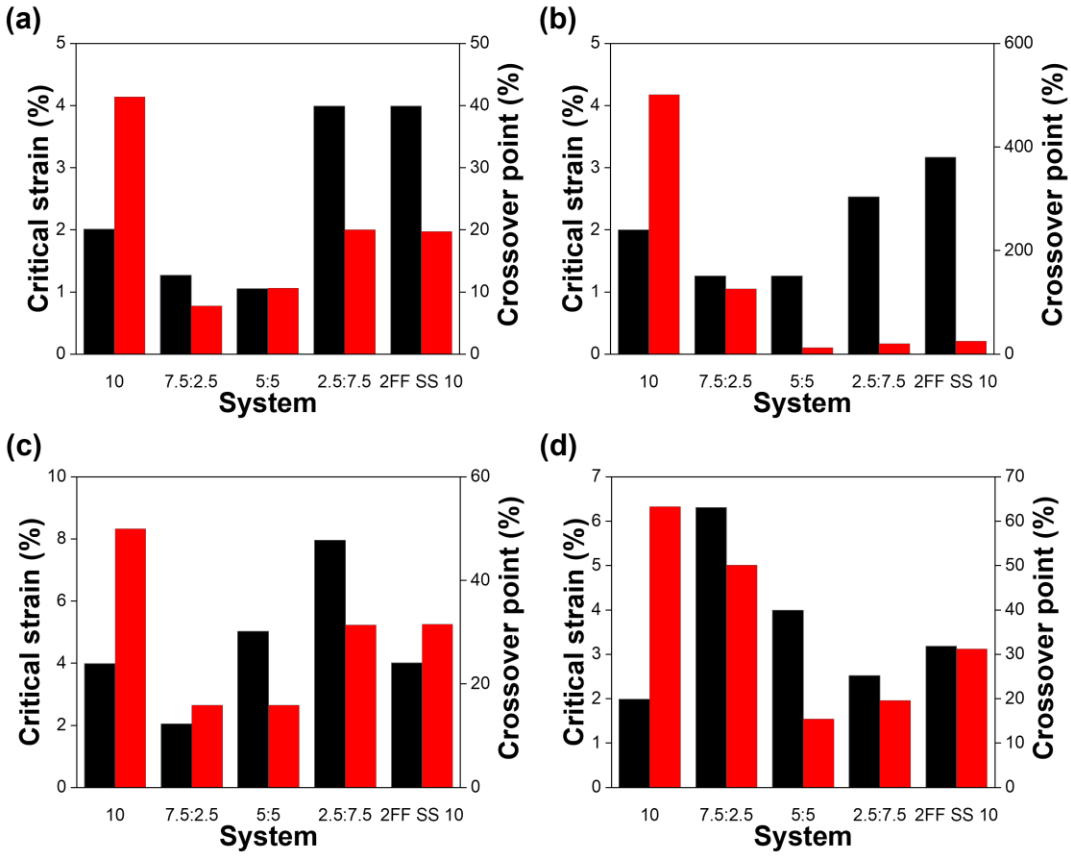

Figure 3.25. Critical strain (black) and crossover point (red) values for (a) 7MeO2NapFV, (b) 1NapVV, (c) CarbFV and (d) CarbIF single and 2Nap-(*SS*)-FF multicomponent systems calculated from strain sweeps. All full rheology data can be found in Appendix 2.3.

The gels formed by CarbFV and CarbIF require high strain for the gel network to be completely broken down, signified by the larger crossover point (Figure 3.25c and d). The CarbFV 7.5 mg/mL:2Nap-(*SS*)-FF 2.5 mg/mL gels had lower critical strain and crossover points than CarbFV alone (Figure 3.25c). As 2Nap-(*SS*)-FF concentration increases, both the critical strain and the crossover point increase, resulting in the CarbFV 2.5 mg/mL:2Nap-(*SS*)-FF 7.5 mg/mL system having higher critical strain and a similar crossover point to 2Nap-(*SS*)-FF 10 mg/mL. While co-assembly at lower 2Nap-(*SS*)-FF concentrations disrupts the strength of the gel network, it is possible to achieve enhanced mechanical strength by optimising the concentration ratio of the two components while maintaining the total gelator concentration.

The CarbIF 7.5 mg/mL:2Nap-(*SS*)-FF 2.5 mg/mL multicomponent system has significantly greater critical strain and crossover point than either component alone (Figure 3.25d). As 2Nap-(*SS*)-FF concentration increases, critical strain and crossover point decrease. While the CarbIF 5 mg/mL:2Nap-(*SS*)-FF 5 mg/mL system has higher critical strain than 2Nap-

(*SS*)-FF alone, it has lower crossover point. The CarbIF 2.5 mg/mL:2Nap-(*SS*)-FF 7.5 mg/mL system has lower critical strain and crossover point than either component alone. Again, the concentration ratio of the two components is clearly influencing the mechanical strength of the gels.

7MeO2NapFV 10 mg/mL also has higher stiffness and elasticity than 2Nap-(*RS*)-FF (Figure 3.26a). As the concentration of 2Nap-(*RS*)-FF in the system increases, G′ and elasticity decrease. Gels formed from the 2.5 mg/mL 7MeO2NapFV:7.5 mg/mL 2Nap-(*RS*)-FF 7.5 mg/mL multicomponent system have almost identical moduli values to 2Nap-(*RS*)-FF 10 mg/mL. This is the same as what was observed in the 7MeO2NapFV:2Nap-(*SS*)-FF multicomponent systems and agrees with observations from SANS data showing that 7MeO2NapFV co-assembles with 2Nap-(*RS*)-FF to form structures that resemble those formed by 2Nap-(*RS*)-FF alone.

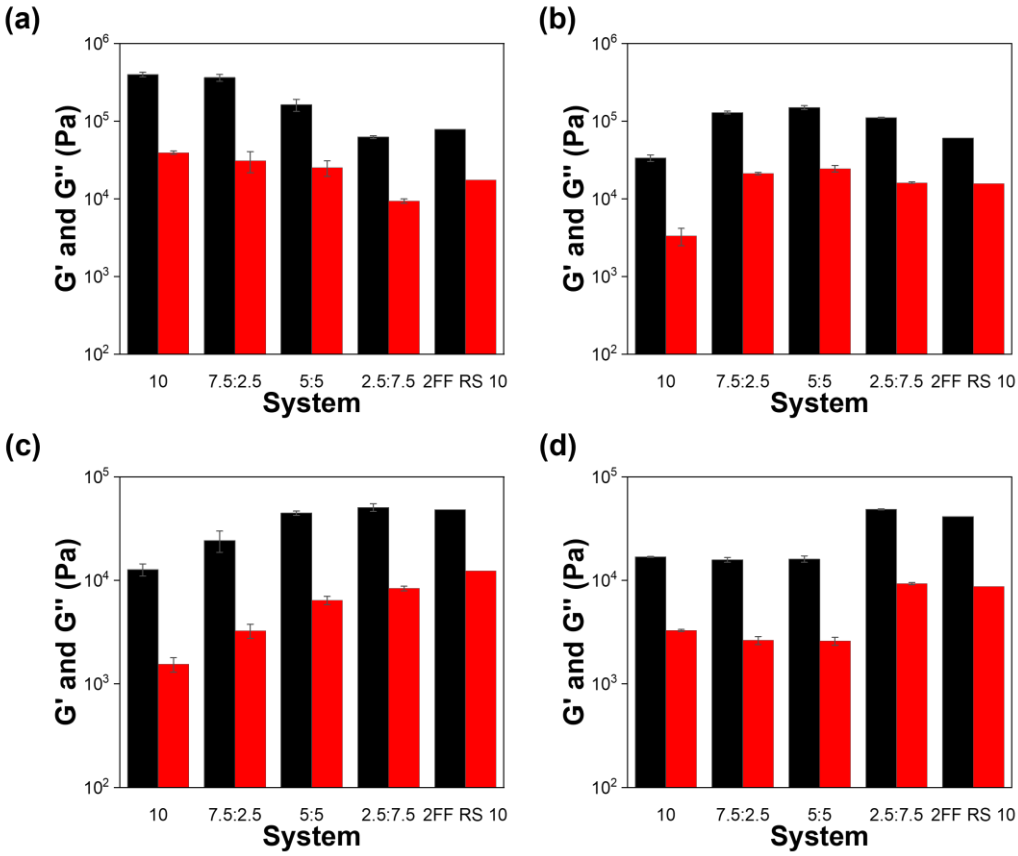

Figure 3.26. Average G′ (black) and G″ (red) values for (a) 7MeO2NapFV, (b) 1NapVV, (c) CarbFV and (d) CarbIF single and 2Nap-(*RS*)-FF multicomponent systems. Moduli were calculated from frequency sweeps using the values for the moduli at a frequency of 10 rad/s. Error bars show the standard deviation between samples. All full rheology data can be found in Appendix 2.3.

1NapVV 10 mg/mL gels have much lower stiffness and elasticity than 2Nap-(*RS*)-FF 10 mg/mL (Figure 3.26b). The moduli values of the multicomponent gels are greater than those of the single component gels. The 1NapVV 5 mg/mL:2Nap-(*RS*)-FF 5 mg/mL has the highest moduli values, suggesting this is the optimum concentration ratio for maximising the mechanical properties of the gels. As with the 7MeO2NapFV multicomponent systems, changing the chirality of 2NapFF does not significantly change the trends observed in the mechanical properties of the gels.

The CarbFV:2Nap-(*RS*)-FF multicomponent gels show a clear trend of increasing moduli values with increasing 2Nap-(*RS*)-FF concentration (Figure 3.26c). As the concentration of 2Nap-(*RS*)-FF increases and the concentration of CarbFV decreases, the rheological properties of the gels change from resembling CarbFV to resembling 2Nap-(*RS*)-FF, which could suggest self-sorting. However, the moduli values exceed what would be expected from two separate additive networks (i.e. values in between the maximum concentrations of either component), suggesting co-assembly is taking place. This would agree with SANS experiments, where the data was best fit to a single model, showing that the two components are undergoing co-assembly.

The moduli values of the CarbIF:2Nap-(*RS*)-FF multicomponent systems are almost identical to CarbIF alone, until the CarbIF 2.5 mg/mL:2Nap-(*RS*)-FF 7.5 mg/mL system, which has very similar moduli values to 2Nap-(*RS*)-FF alone (Figure 3.26d). SANS data suggests the CarbIF 5 mg/mL:2Nap-(*RS*)-FF 5 mg/mL system at least undergoes co-assembly. CarbIF therefore appears to direct co-assembly until the 2Nap-(*RS*)-FF concentration exceeds the CarbIF concentration. At which point 2Nap-(*RS*)-FF takes over.

The strength of the 2Nap-(*RS*)-FF multicomponent gels are strongly concentration dependent. The effect of concentration ratio varies depending on the identity of the second component despite all undergoing co-assembly, according to SANS data. The crossover points of the 7MeO2NapFV:2Nap-(*RS*)-FF multicomponent gels increase with increasing 2Nap-(*RS*)-FF concentration (Figure 3.27a). While co-assembly reduces the strength of the gels at higher 7MeO2NapFV concentrations, the 2.5 mg/mL 7MeO2NapFV:2Nap-(*RS*)-FF 7.5 mg/mL system has similar critical strain and considerably higher crossover point compared to the 2Nap-(*RS*)-FF 10 mg/mL gels.

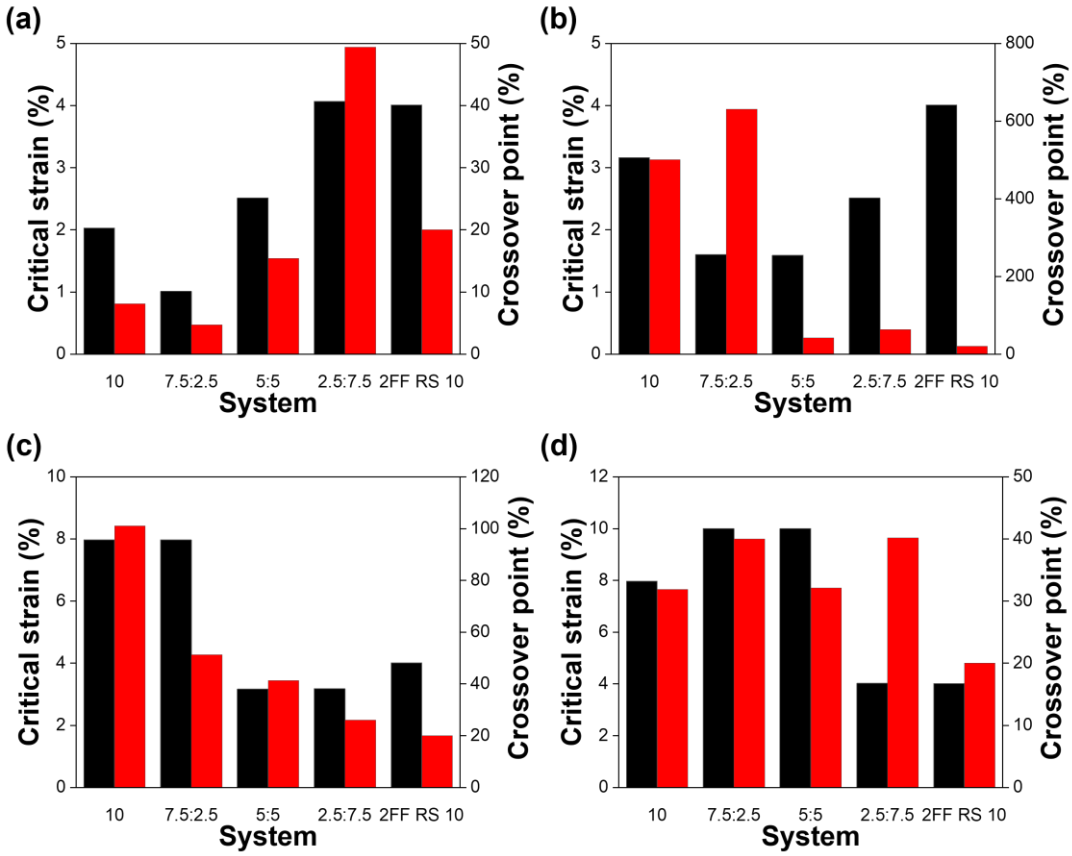

Figure 3.27. Critical strain (black) and crossover point (red) values for (a) 7MeO2NapFV, (b) 1NapVV, (c) CarbFV and (d) CarbIF single and 2Nap-(R*S*)-FF multicomponent systems calculated from strain sweeps. All full rheology data can be found in Appendix 2.3.

The increased stiffness of the 1NapVV:2Nap-(*RS*)-FF multicomponent gels (Figure 3.26b) seems to compromise their strength, as seen by the considerably lower values obtained for the critical strain and crossover point compared to the single component gels (Figure 3.27b). As with 7MeO2NapFV, critical strain increases with increasing 2Nap-(*RS*)-FF concentration. The 1NapVV 7.5 mg/mL:2Nap-(*RS*)-FF 2.5 mg/mL has an unexpectedly high crossover point. There is no obvious reason for this.

CarbFV 10 mg/mL single component gels have significantly higher critical strain and crossover point then 2Nap-(*RS*)-FF 10 mg/mL single component gels (Figure 3.27c). As 2Nap-(*RS*)-FF concentration in the multicomponent systems increases, the critical strain and crossover point of the gels decrease. The 5 mg/mL:5 mg/mL and 2.5 mg/mL:7.5 mg/mL CarbFV:2Nap-(*RS*)-FF gels have lower strength than 2Nap-(*RS*)-FF alone. As with the 1NapVV multicomponent systems, this could be due to increased stiffness compromising gel strength.

The strength of the CarbIF multicomponent systems follow a similar trend to their stiffness. The multicomponent systems with CarbIF concentration greater than or equal to 2Nap-(*RS*)-FF concentration show enhanced strength that more closely resembles the strength of CarbIF alone at the same total gelator concentration (Figure 3.27d). The critical strain of CarbIF 2.5 mg/mL:2Nap-(*RS*)-FF 7.5 mg/mL multicomponent gels was very similar to that of the 2Nap-(*RS*)-FF 10 mg/mL single component gels. The crossover point of these gels was unexpectedly high. In a mirror of the 1NapVV and CarbFV multicomponent systems, the increased strength of select CarbIF systems is paired with a reduction in stiffness.

The rheology data shows the vast array of possible outcomes from preparing multicomponent systems using a variety of gelators and by changing the chirality of one of the components. As already discussed, while we can achieve a wide variety of mechanical properties, it is practically impossible to predict the outcome of preparing multicomponent systems.

3.3 Conclusions

This work highlights the importance of considering the concentration ratio of components when preparing multicomponent systems. A range of mechanical properties can be accessed from a single two-gelator system by varying the concentration ratio. This allows preparation of a system from two essential components that also has the desired mechanical properties. While the ideal situation is to be able to design a system with predetermined properties, we have shown the importance of testing a variety of conditions.

Our results show that preparing multicomponent systems using two components with different *N*-terminal capping groups does not guarantee self-sorting, as was seen with the CarbFV:2NapFF systems. The identity and order of amino acids in the peptide chain clearly also play a role in determining how the two components in the system assemble in the presence of one another and thereby the properties of the resulting system. While the techniques used here provide evidence for self-sorting or co-assembly at the molecular and fibre levels of self-assembly, we cannot draw conclusions about interactions between the two components at the gel network level.

We have shown how altering the chirality of a single amino acid residue in one of the components can greatly increase the variety of structures and therefore properties available to two-component gelator-gelator systems. It is interesting that, despite previous work

demonstrating a preference for homochiral assembly in peptide-based multicomponent supramolecular systems, no significant disruption to assembly was observed in the 2Nap-(*RS*)-FF multicomponent systems and in some cases, these systems had enhanced mechanical properties compared to their 2Nap-(*SS*)-FF counterparts. There was also no change from co-assembly to self-sorting when 2Nap-(*SS*)-FF was replaced with 2Nap-(*RS*)-FF. This suggests that the propensity for 2NapFF of either chirality to self-assemble into ordered structures outweighs any preference for homochiral assembly in the systems studied.

We expect that the component with the greatest propensity for self-assembly will direct co-assembly. For example, CarbFV appears to have stronger self-assembly at high pH than 2Nap-(*SS*)-FF, based on CD data. Co-assembly of these two components with 2Nap-(*SS*)-FF therefore results in formation of structures that more closely resemble CarbFV and CarbIF. When two components have similar abilities to self-assemble, for example CarbIF and 2Nap-(*RS*)-FF, self-sorting is more likely to take place.

3.4 References

1. T. Das, M. Haering, D. Haldar and D. Diaz Diaz, *Biomater. Sci.*, 2017, **6**, 38-59.
2. D. M. Murali and G. Shanmugam, *New J. Chem.*, 2019, **43**, 12396-12409.
3. C. Colquhoun, E. R. Draper, R. Schweins, M. Marcello, D. Vadukul, L. C. Serpell and D. J. Adams, *Soft Matter*, 2017, **13**, 1914-1919.
4. K. McAulay, P. A. Ucha, H. Wang, A. M. Fuentes-Caparros, L. Thomson, O. Maklad, N. Khunti, N. Cowieson, M. Wallace, H. Cui, R. J. Poole, A. Seddon and D. J. Adams, *Chem. Comm.*, 2020, **56**, 4094-4097.
5. E. R. Draper, H. Su, C. Brasnett, Poole, R. J., S. Rogers, H. Cui, A. Seddon and D. J. Adams, *Angew. Chem.*, 2017, **129**, 10603-10606.
6. A. Z. Cardoso, L. E. Mears, B. N. Cattoz, P. C. Griffiths, R. Schweins and D. J. Adams, *Soft Matter*, 2016, **12**, 3612-3621.
7. L. Thomson, R. Schweins, E. R. Draper and D. J. Adams, *Macromol. Rapid Comm.*, 2020, **41**, e2000093.
8. D. Giuri, L. J. Marshall, B. Dietrich, D. McDowall, L. Thomson, J. Y. Newton, C. Wilson, R. Schweins and D. J. Adams, *Chem. Sci.*, 2021, **12**, 9720-9725.
9. F. Avino, A. B. Matheson, D. J. Adams and P. S. Clegg, *Org. Biomol. Chem.*, 2017, **15**, 6342-6348.

10. F. Sheehan, D. Sementa, A. Jain, M. Kumar, M. Tayarani-Najjaran, D. Kroiss and R. V. Ulijn, *Chem. Rev.*, 2021, **121**, 13869-13914.
11. B. O. Okesola, Y. Wu, B. Derkus, S. Gani, D. Wu, D. Knani, D. K. Smith, D. J. Adams and A. Mata, *Chem. Mater.*, 2019, **31**, 7883-7897.
12. A. M. Brizard, M. C. A. Stuart and J. H. van Esch, *Faraday Discuss.*, 2009, **143**, 345-357.
13. H. Shigemitsu, T. Fujisaku, W. Tanaka, R. Kubota, S. Minami, K. Urayama and I. Hamachi, *Nat. Nanotechnol.*, 2018, **13**, 165-172.
14. L. N. J. de Windt, C. Kulkarni, H. M. M. ten Eikelder, A. J. Markvoort, E. W. Meijer and A. R. A. Palmans, *Macromol.*, 2019, **52**, 7430-7438.
15. M. Zhou, A. M. Smith, A. K. Das, N. W. Hodson, R. F. Collins, R. V. Ulijn and J. E. Gough, *Biomater.*, 2009, **30**, 2523-2530.
16. A. Das and S. Ghosh, *Chem. Comm.*, 2011, **47**, 8922-8924.
17. N. S. S. Kumar, M. D. Gujrati and J. N. Wilson, *Chem. Comm.*, 2010, **46**, 5464-5466.
18. N. Singh, A. Lopez-Acosta, G. J. M. Formon and T. M. Hermans, *J. Am. Chem. Soc.*, 2022, **144**, 410-415.
19. C. Colquhoun, E. R. Draper, E. G. Eden, B. N. Cattoz, K. L. Morris, L. Chen, T. O. McDonald, A. E. Terry, P. C. Griffiths, L. C. Serpell and D. J. Adams, *Nanoscale*, 2014, **6**, 13719-13725.
20. K. L. Morris, L. Chen, J. Raeburn, O. R. Sellick, P. Cotanda, A. Paul, P. C. Griffiths, S. M. King, R. K. O'Reilly, L. C. Serpell and D. J. Adams, *Nat. Comm.*, 2013, **4**, 1480.
21. S. Basak, I. Singh, A. Ferranco, J. Syed and H.-B. Kraatz, *Angew. Chem. Int. Ed.*, 2017, **56**, 13288-13292.
22. D. M. Chung and J. S. Nowick, *J. Chem. Soc.*, 2004, **126**, 3062-3063.
23. P. Terech and R. G. Weiss, *Chem. Rev.*, 1997, **8**, 3133-3160.
24. S. Marchesan, C. D. Easton, F. Kushaki, L. Waddington and P. G. Hartley, *Chem. Comm.*, 2012, **48**, 2195-2197.
25. A. X. Wu and L. Isaacs, *J. Am. Chem. Soc.*, 2003, **125**, 4831-4835.
26. K. Sugiyasu, S. I. Kawano, N. Fujita and S. Shinkai, *Chem. Mater.*, 2008, **20**, 2863-2865.
27. L. Chen, T. O. McDonald and D. J. Adams, *RSC Adv.*, 2013, **3**, 8714-8720.
28. A. Ruter, S. Kuczera, D. J. Pochan and U. Olsson, *Langmuir*, 2019, **35**, 5802-5808.
29. https://www.sasview.org.

30. K. McAulay, B. Dietrich, H. Su, M. T. Scott, S. Rogers, Y. K. Al-Hilaly, H. Cui, L. C. Serpell, A. M. Seddon, E. R. Draper and D. J. Adams, *Chem. Sci.*, 2019, **10**, 7801-7806.
31. D. J. Adams, M. F. Butler, W. J. Frith, M. Kirkland, L. Mullen and P. Sanderson, *Soft Matter*, 2009, **5**, 1856-1862.
32. E. R. Draper, M. Wallace, R. Schweins, R. J. Poole and D. J. Adams, *Langmuir*, 2017, **33**, 2387-2395.
33. E. R. Draper, B. Dietrich, K. McAulay, C. Brasnett, H. Abdizadeh, I. Patmanidis, S. J. Marrink, H. Su, H. Cui, R. Schweins, A. Seddon and D. J. Adams, *Matter*, 2020, **2**, 764-778.
34. S. Sathaye, A. Mbi, C. Sonmez, Y. Chen, D. L. Blair, J. P. Schneider and D. J. Pochan, *Wiley Interdiscip. Rev. Nanomed. Nanobiotechnol.*, 2015, **7**, 34-68.
35. D. I. Wilson, *Eye*, 2018, **32**, 179-183.
36. L. S. Mojarrad and A. Rafe, *J. Texture Stud.*, 2018, **49**, 320-327.

Chapter 4

Changing the mechanical properties of peptide-based supramolecular hydrogels by chemical cross-linking

This chapter is partially adapted from the following publication:

"Enhancement of the mechanical properties of lysine-containing peptide-based supramolecular hydrogels by chemical cross-linking"

Soft Matter, **2021**, 17, 8459-8464.

L. J. Marshall, O. Matsarskaia, R. Schweins, & D. J. Adams

L. J. Marshall synthesised and characterised the gelators under investigation and performed the rheological experiments and fitted all the SANS data. O. Matsarskaia and R. Schweins performed the SANS experiments due to COVID restrictions.

4.1 Introduction

Many methods have been employed to improve the mechanical stability of peptide-based supramolecular hydrogels including control of gelation to ensure formation of a homogenous gel network[1], physical cross-linking using ions[2, 3] or *via* exploitation of secondary nucleation processes[4], exploitation of the chiral nature of peptides[5], and mixing with polymer additives.[6-8] However, these techniques only have limited effects on gel properties. Recently, methods utilising chemical cross-linking to enhance the mechanical properties of supramolecular hydrogels have been explored. Such methods include native chemical ligation[9], disulfide formation[3, 10], tyrosine dimerisation[11] as well as the use of enzymes[12] and cross-linking agents such as glutaraldehyde (GTA)[13] and Genipin.[14]

While chemical cross-linking between gelator molecules in supramolecular hydrogels regularly increases gel stiffness, very few approaches also increase gel strength and some even decrease the gels' resistance to strain.[11] We therefore hope to expand the available methods for chemical cross-linking to further improve mechanical properties without compromising gel strength.

Previous work has successfully used GTA (Figure 4.1a) as a cross-linking agent via *in situ* formation of imine bonds.[13] We have used a similar approach here by incorporating a lysine (K) residue into the well-studied, peptide-based gelator 2NapFF (Figure 4.1b) to give three new gelators: 2NapFFK, 2NapKFF and 2NapFKF (Figure 4.1c, d and e). We expected that exposure to GTA would result in cross-linking between primary amines on the side chains of K residues on neighbouring fibres or within individual fibres and thereby alter the mechanical properties of the gels.

Previous work has shown the power of the FF motif in driving self-assembly alongside aromatic *N*-terminal capping groups through π-π stacking and the hydrophobic effect.[15] The reported anti-parallel nature of peptide-based hydrogels containing FF may be beneficial as the self-assembled structures will be primed for easy cross-linking between adjacent fibrils, allowing self-assembly to facilitate cross-linking.[16, 17] We therefore primarily focus on 2NapFFK and 2NapKFF. We expected that the position of the K residue would play a role in the final properties of the gels formed. While altering the position of the amine will affect its accessibility for cross-linking, it may also disrupt the π-π stacking interactions between aromatic rings, altering the self-assembly and thereby the properties of the gels formed.

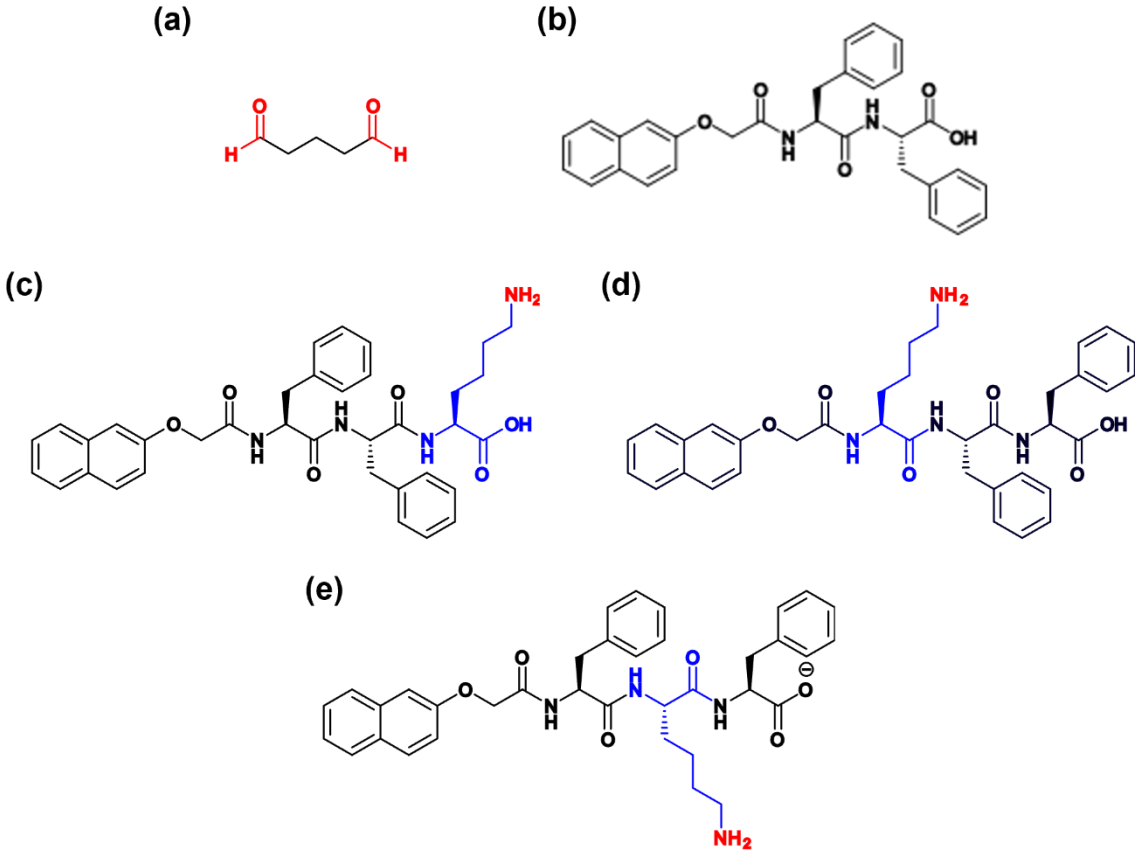

Figure 4.1. Chemical structures of **(a)** the cross-linking agent GTA, **(b)** the well-known peptide-based LMWG 2NapFF and the gelators studied here: **(c)** 2NapFFK, **(d)** 2NapKFF and **(e)** 2NapFKF. The K residues are highlighted in blue, and the groups involved in imine formation are highlighted in red.

It should be noted that the increased stability and possible changes in orientation of the gelator molecules caused by introduction of chemical bonds may drive self-assembly towards crystallisation rather than gel formation.[18, 19] All three molecules formed gels under the conditions discussed here. We can expect that the gelator molecules in the gel state are kinetically trapped and lack the energy required to overcome the energy barrier to a more thermodynamically stable, crystalline state.[20]

GTA is widely used as a cross-linking agent for materials such as collagen due to its high efficiency and low cost.[21] GTA introduces cross-links via imine bond formation between free amines in the material to be cross-linked and the aldehyde groups at either end of GTA (Figure 4.2).[22, 23] There are many advantages to using GTA as a cross-linking agent, particularly for supramolecular hydrogels. For example, the reaction can occur in aqueous medium and at room temperature, meaning that there will be no heat-cooling effects associated with the reaction.[24] This is important as previous work has shown that gels have

different properties depending on their thermal history. [25] There is no need for purification post cross-linking as no other chemical reagents are required and the only side-product is water.[13] Importantly, the reaction is reversible and so should not interfere with self-assembly.[13]

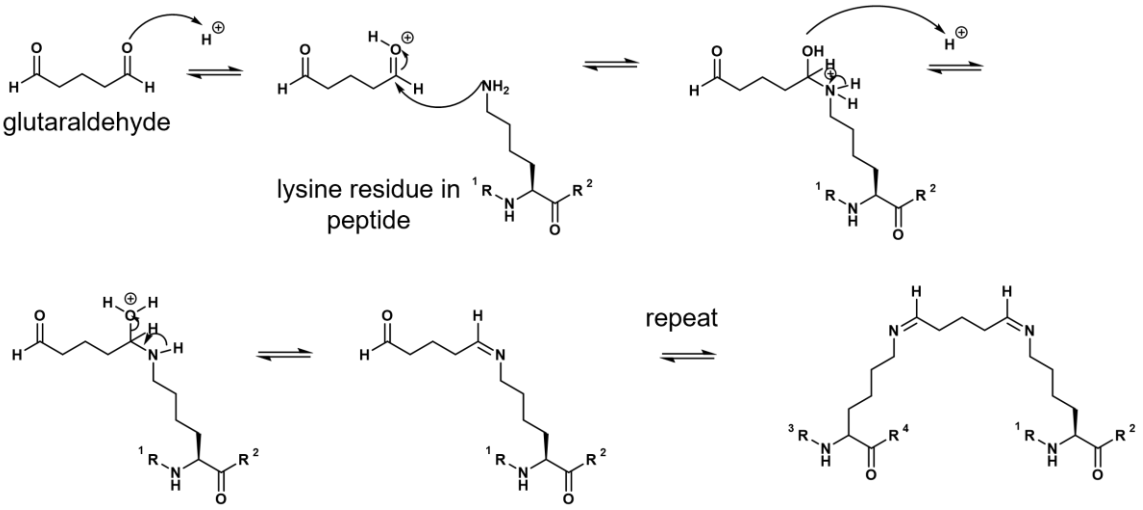

Figure 4.2. Proposed mechanism for cross-linking between GTA and K residues within a peptide, assuming GTA reacts in a monomeric state for simplicity.

GTA exhibits complex behaviour in solution and is likely to undergo cross-linking reactions in polymeric form.[26, 27] Previous work by Bowes and Cater showed that reactions between collagen and excess GTA resulted in new compounds where the ratio of GTA molecules to K residues greatly exceeded 1:1.[22] These results agree with other studies suggesting that GTA undergoes cross-linking in polymeric form.[28]

The packing of the molecules in the gels will need to allow for the amines to be cross-linked by GTA. This means that the amines will have to be spatially arranged in such a way that they are the appropriate distance apart for cross-linking. This will be especially hard to predict owing to the complex behaviour of GTA in aqueous solution. Bowes and Cater suggested that the number of cross-links introduced into a material is influenced by stereochemical factors. They noted that the efficiency of GTA in this regard is likely due to the fact that the distances that GTA (or its oligomers) can bridge are particularly suitable for cross-linking amine groups.[22] The work by Bowes and Cater,[22] among others,[13, 23, 26] confirms that GTA is a promising candidate as a cross-linking agent for the peptides to be studied here.

While this project hopes to form chemical cross-links between the supramolecular fibres in gel network (Figure 4.3). It is perhaps more likely that the cross-links will form within the

fibres, as seen in previous work by Draper *et al*.[29] Both of these possibilities will have different effects on the rheological properties of the gels.[30, 31] It will therefore be important to determine where and how the cross-linking is taking place within the gels.

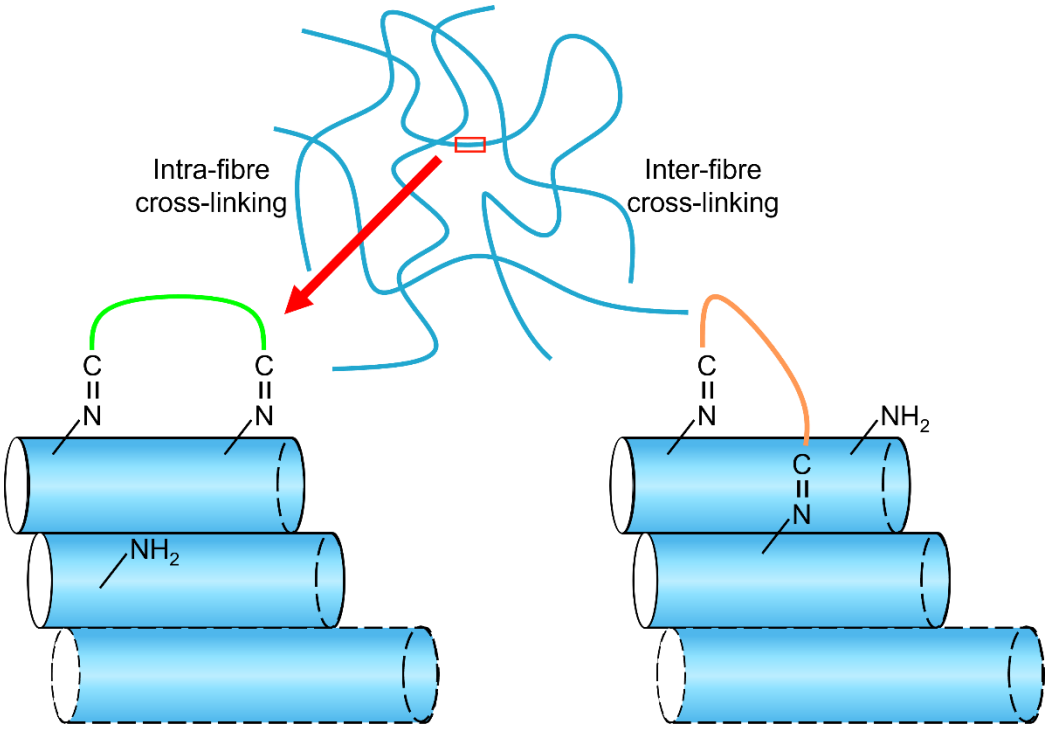

Figure 4.3. Cartoon close-up of a small cross-section of the gel network. The gel network is formed by lateral association of individual one-dimensional structures (blue). These one-dimensional structures were fit using SANS to a standard cylinder model combined with a power law. Chemical cross-linking between amines on K residues may occur within (green) individual fibres or between (orange) neighbouring fibres. The arrangement of the fibres shown is purely hypothetical.

As previously discussed, we can control the structure of the gel network by carefully selecting the method for gelation.[32] We hypothesised that using Ca^{2+} ions as a gelation trigger rather than glucono-δ-lactone (GdL) would be beneficial for chemical cross-linking as the fibres would already be aligned adjacent to one another, allowing facile formation of inter-fibre cross-links (Figure 4.4).[32] Gels were formed from these gelators by addition of salts to suspensions of the gelators at an initial pH of 11.7. Such a high pH was chosen to ensure the samples were well above the apparent pKa of the gelators. However, gels have been formed at lower pH values.[33, 34] The ability to form gels in a range of pH conditions greatly increases the utility of the gels formed by these gelators.

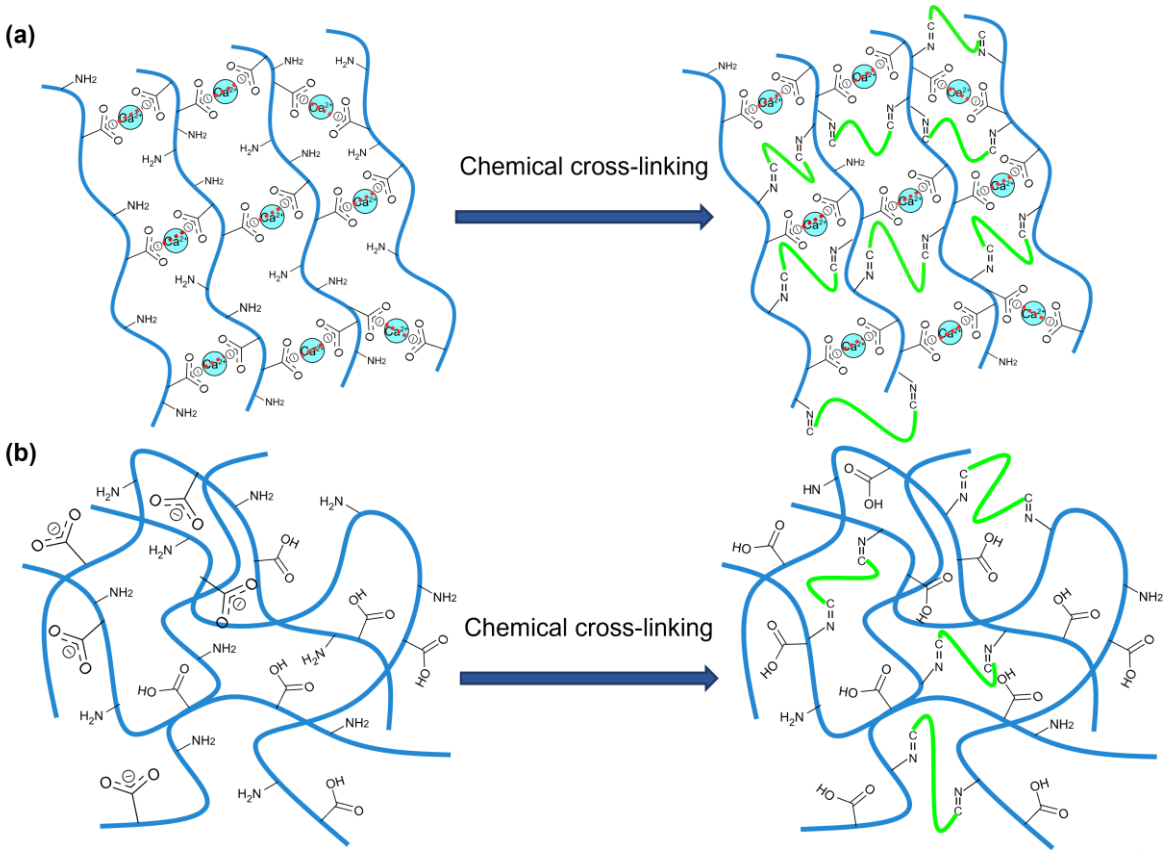

Figure 4.4. Schematic showing proposed more efficient chemical cross-linking in (a) Ca^{2+} triggered gels compared to (b) GdL-triggered gels. The blue lines represent individual fibres in the gel network. Salt bridges are depicted by red dashed lines and chemical cross-links are depicted by solid green lines. The arrangement of fibres and position of carboxylic acid groups are purely hypothetical.

Other groups have worked with similar LMWGs (specifically 2NapFFKK) for use as antifungal and antimicrobial agents.[35-37] Laverty *et al*. were able to prepare homogenous gels via pH trigger by dissolving 2NapFFKK in water at a pH of approximately 9 and increasing the pH by titration with NaOH. [37] The solution could then be titrated with HCl to a pH of 7.4, at which point a hydrogel was formed.[35, 37] The work by the Laverty group suggests that it was highly likely that the *N*-capped tripeptides to be studied here would be able to form hydrogels, under the appropriate pH conditions. However, it was important to closely monitor on the pH before, during and after gel formation.[31, 38, 39]

4.2 Results and Discussion

4.2.1 Synthesis of cross-linkable peptide-based gelators

Once the initial target molecules had been identified, a means to synthesise them was established. One of the most common protecting groups for the side-chain amine of K is *N*-carboxybenzyl (Cbz) which can be removed by Pd/C catalysed hydrogenation. To reduce the number of deprotection steps, we incorporated a *C*-terminal protecting group that could also be removed by hydrogenation. While benzyl ester (OBzl) protected F is readily available, its K(Cbz) equivalent is not. An extra deprotection step was therefore required for 2NapFFK, where K(Cbz)-OMe would be used instead. OMe is the methyl ester protecting group and can be removed by hydrolysis with a suitable base, such as LiOH. A full synthetic scheme can be found in Appendix 3.1, using 2NapFFK as an example.

The coupling method selected is one used frequently within the group where isobutyl chloroformate (IBCF) is used as the coupling agent and *N*-methyl morpholine (NMM) as a base (Figure 4.5).[40-43] The tert-butyloxy carbonyl (Boc) protecting group is then removed from the *N*-terminus by formation of the trifluoroacetic acid (TFA) salt. The resulting free amine can then be coupled to the next residue in the peptide chain, again using IBCF and NMM. This method was repeated until all that was left was removal of the final protecting groups from the side-chain amine of K and the *C*-terminus of the peptide.

After successful synthesis of 2NapK(Cbz)FF-OBzl, the final step in the synthesis was removal of both Cbz and OBzl by hydrogenation. The original hydrogenolysis method utilised 5 mol % of Pd/C (with respect to Pd content), EtOH as a solvent and a hydrogen atmosphere provided by balloons. This method was unsuccessful, perhaps since the starting material was able to self-assemble and form a gel in EtOH. Only starting material was obtained after stirring the reaction at room temperature overnight, suggesting that the reaction could not take place in the gel state (Figure 4.6). This prompted the use of an alternative solvent, THF, in which the starting material did not form a gel. However, this was also unsuccessful (Figure 4.7).

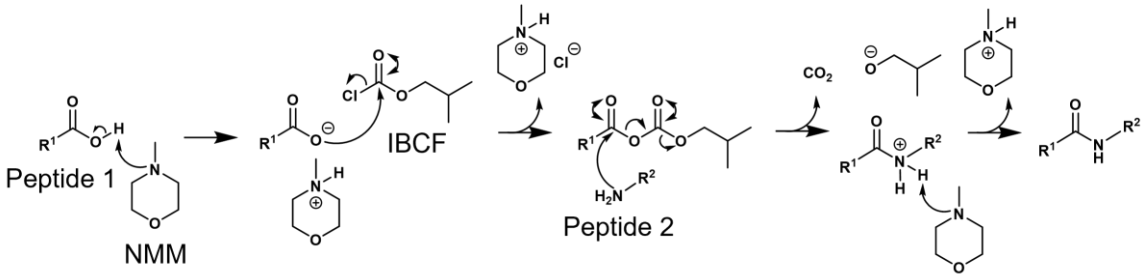

Figure 4.5. Peptide coupling mechanism using IBCF as a coupling agent and NMM as a base. NMM deprotonates the free carboxylic acid group on the first peptide (all other reactive groups in this peptide must be protected). This creates a nucleophilic centre that attacks the carbonyl group on IBCF. IBCF activates the acid by forming an anhydride which is an excellent leaving group. The activated acid is attacked by the free amine on the second peptide (again, all other reactive groups must be protected), creating an amide bond between peptides 1 and 2. NMM can then deprotonate the N atom in the amide bond to give the coupled product.

Previous studies suggest the need for much more intensive conditions than those used here. For example, Jain *et al*. used 30 mol % of catalyst, 8.27 bar of H_2, 4 equivalents of concentrated HCl and 72 hours reaction time (at room temperature).[44] This suggests that higher pressures and longer reaction times are required to remove Cbz, making this synthetic route less desirable than initially thought. It has also been suggested that hydrogenolysis of Cbz is highly solvent dependent and requires an acid additive of optimum strength. It may therefore take significant time and reagents to establish optimum conditions for this reaction.[45-47]

Further research into the employment of hydrogenolysis for the removal of Cbz indicated that, in some cases, an acid additive is required to initiate the reaction and to aid with dissolution of the starting material.[44, 45] Following this discovery, alternative conditions such as increased amount of catalyst to 10 mol %, use of fresh catalyst, different solvents, inclusion of TFA as an acid additive and increasing hydrogen pressure to 2 bar in a Parr Shaker were also attempted to no avail (Figure 4.7).

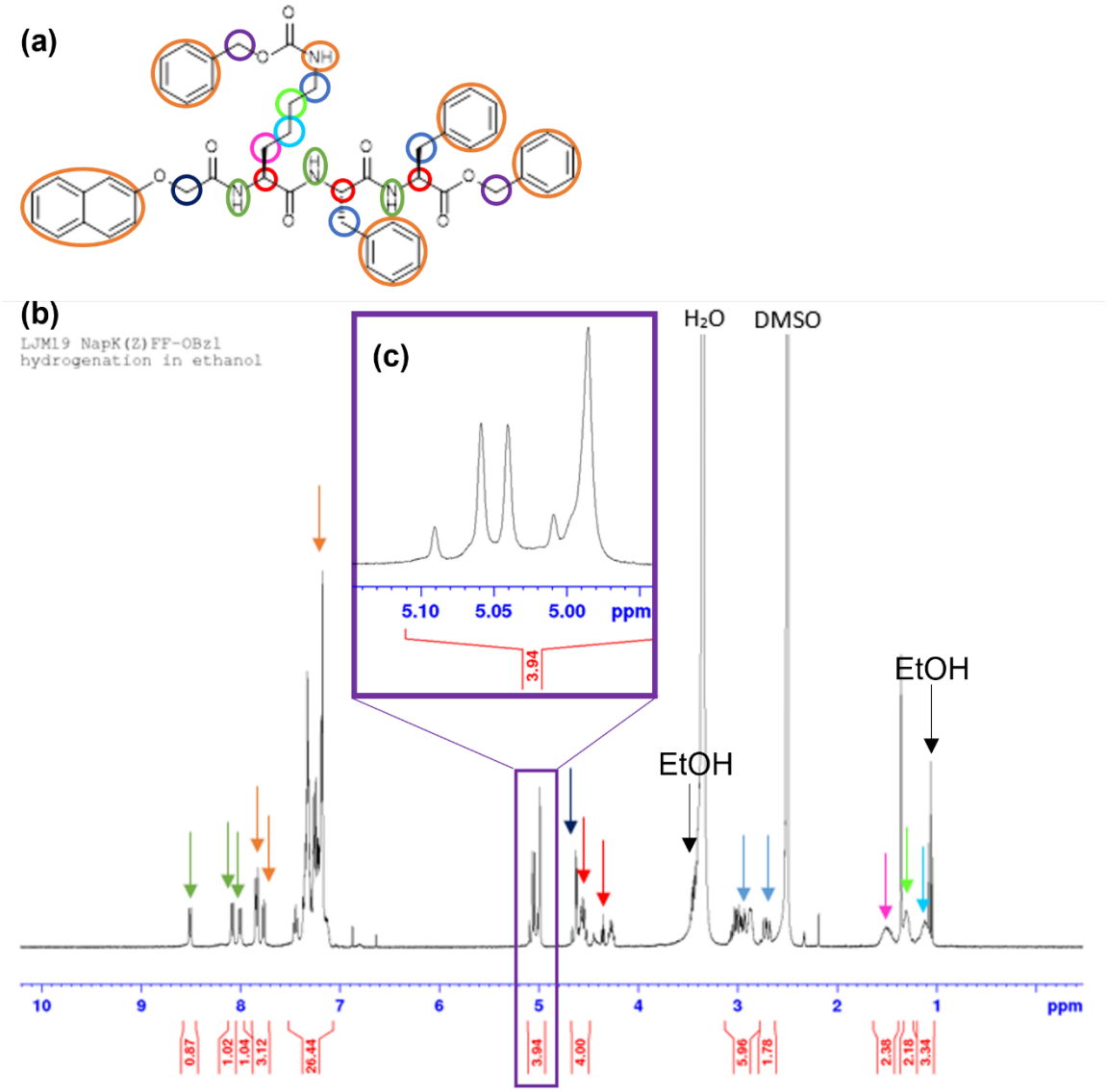

Figure 4.6. (a) Structure of 2NapK(Cbz)FF-OBzl colour coded to match the ^{1}H NMR spectrum. (b) ^{1}H NMR spectrum collected following hydrogenation in EtOH. (c) Expansion of the peaks corresponding to the $COOCH_2Ph$ atoms in the Cbz and OBzl groups, verifying both are still present. Full characterisation of each product can be found in Appendix 3.2.

It was thought that a simple way to reduce the pressure-dependence of the reaction would be to use a hydrogen transfer agent for *in situ* hydrogen generation rather than using hydrogen gas directly. This comes with the advantage of reduced fire risk as well as avoiding the additional safety concerns associated with use of a hydrogen cylinder. Previous work has also indicated that the use of $NaBH_4$ removes the need for an acid additive and, unlike other hydrogen transfer agents, $NaBH_4$ is not required in large stoichiometric excess, is not moisture sensitive and does not require high reaction temperatures.[48] The same study also reported very short reaction times (5 minutes) and high yields (98%), even with compounds

of diverse electronic and steric characteristics.[48] However, in order for $NaBH_4$ to release H_2, it requires polar protic solvents such as MeOH or EtOH. The ability of the starting material to form gels in both of these solvents may have contributed to the lack of success with this method (Figure 4.7).[48, 49]

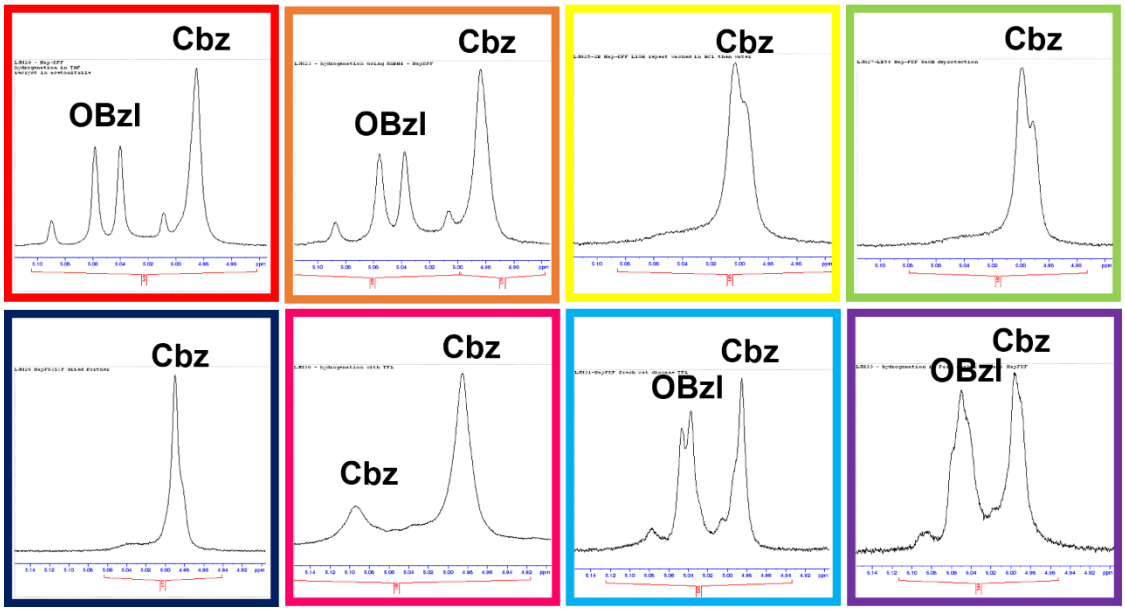

Figure 4.7. Region of ^{1}H NMR spectra containing the Cbz and OBzl COO**CH$_2$**Ph peaks from the products obtained following attempted deprotection of 2NapKFF (top row) and 2NapFKF (bottom row) in the following conditions: H_2 (balloon), 10 mol % Pd/C catalyst, THF solvent, 6 days (red), $NaBH_4$ as a hydrogen transfer agent, 10 mol % Pd/C, MeOH solvent, 16 hours (orange), LiOH (10 equiv.), refluxed at ~75 °C, THF/H_2O solvent mixture, 45 minutes (yellow), NaOH (10 equiv.), refluxed at ~80 °C, THF/H_2O solvent mixture, 16 hours (green), NaOH (10 equiv.), refluxed at ~80 °C, THF/H_2O solvent mixture, 45 minutes (navy blue), H_2 (balloon), 10 mol % Pd/C catalyst, TFA (3 equiv.) acid additive, 1,4-dioxane solvent, 5 days, OBzl already removed using NaOH (pink), H_2 (balloon), 10 mol % Pd/C catalyst (fresh), TFA (5 equiv.) acid additive, 1,4-dioxane solvent, 5 days (light blue), H_2 (2 bar) in Parr Shaker, 10 mol % Pd/C catalyst (fresh), TFA (3 equiv.) acid additive, EtOAc solvent, 4 hours (purple). Loss of OBzl was confirmed by the presence of a COOH peak at ~12.75.

To keep the number of synthetic steps required as low as possible, it was desirable to select an alternative deprotection method that could remove both OBzl and Cbz at the same time. It was therefore exciting to discover that strong bases have been used to remove Cbz as well as OBzl.[50-52] These studies suggest refluxing at 100°C in a MeOH/water solvent mixture.

Since the starting materials form gels in MeOH, THF was used in its place. There was also a concern that using a strong base such as KOH at high temperature would result in hydrolysis of the amide bonds within the peptide. Therefore, LiOH was used as a substitute as is a weaker base than KOH.[53] When the reaction using LiOH proved unsuccessful (Figure 4.7, only OBzl was removed), it was attempted with NaOH which has also previously been used to remove Cbz.[52]

The reaction was monitored by thin-layer chromatography (TLC) using a 1:1 EtOAc:DCM solvent system. After 45 minutes, the spot corresponding to the starting material was replaced by a single spot on the baseline of the TLC plate. It was therefore concluded that the reaction had gone to completion. The reaction was poured into a large excess of 1 M HCl and stirred vigorously overnight. The resulting precipitate was filtered under vacuum and washed with deionised water. Analysis of the ^{1}H nuclear magnetic resonance (NMR) spectrum of the solid suggested successful removal of the OBzl group. However, the Cbz group remained in place (Figure 4.7). It could be the case that NaOH is simply not strong enough to remove Cbz, or that the reaction was not given enough time. However, increasing the strength of the base used and/or the reaction time would also increase the likelihood of the peptide being hydrolysed.

Owing to the extended reaction times, the time-intensive task of developing optimum reaction conditions, the safety hazards associated with hydrogenation and the failure of alternative Cbz deprotection methods, it was decided to pursue an alternative synthetic route. Detailed analysis of the NMR spectra for the products at each stage of synthesis can be found in Appendix 3.2.

Following the failure of the original synthetic strategy, it was apparent that alternative protecting groups were required. The availability and cost of the amino acid derivatives required, the total number of synthetic steps and the ease of purification following removal of the protecting groups were all taken into consideration when devising the new synthetic strategy.

K(Boc)-OMe was identified as another readily available K derivative. Boc was an attractive choice of protecting group as is easily removed by reaction with an acid to form the corresponding salt and this deprotection method is commonly used within the group.[1, 40, 54, 55] Further, the acid aids in dissolution of protected starting material while the deprotected product can be obtained to high purity by precipitation in a suitable solvent. This means that

removal of Boc from the K side chain in the final synthetic step can double as purification of the final compound.

It was decided to also use Boc as the protecting group for the *N*-terminus of F. This meant that instead of building the peptide chain from *C*-terminus to *N*-terminus, as in the first synthetic strategy, the peptide would instead be synthesised from *N* to *C* (Figure 4.8). Once in place, the *N*-terminal capping group would act as a permanent "protecting group". It was also noted that by preparing FF-OMe in bulk, the synthesis of 2NapFFK and 2NapKFF could effectively be shortened by two steps and the peptide could be built like a jigsaw puzzle, rather than by coupling one amino acid at a time (Figure 4.8).

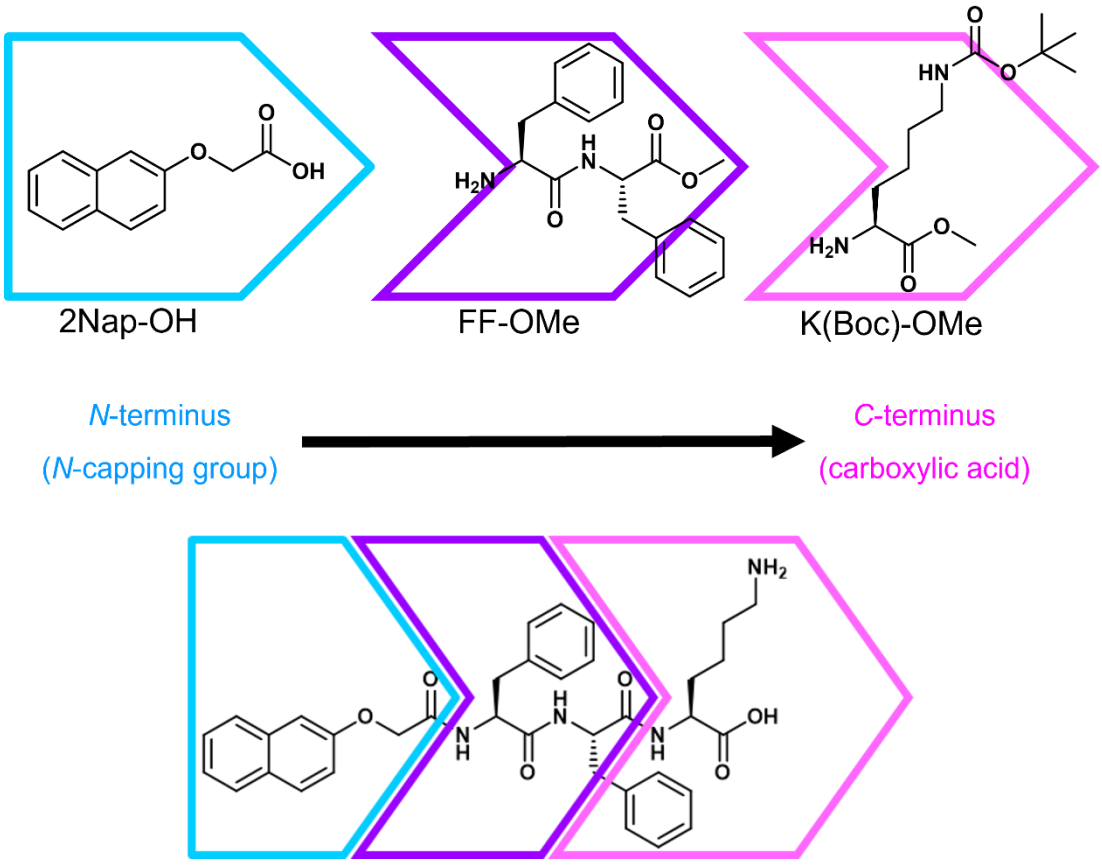

Figure 4.8. The structure of 2NapFFK highlighting synthesis of the tripeptide from the *N*-terminus to the C-terminus in a jigsaw-like fashion. Each jigsaw piece is shown in the form in which it is added to the peptide.

This synthetic method proved successful and all three *N*-capped tripeptides were obtained to >99 % purity (where the majority of impurities are residual solvents), as calculated from ^{1}H NMR spectra. The full synthetic route can be found in Appendix 3.3, using 2NapFFK as an example. The NMR spectroscopy data for the products at each stage of synthesis can be found in Appendix 3.4.

4.2.2 pH titrations of the target molecules

First, pH titrations were conducted on aqueous suspensions of each tripeptide, starting at pH 12, to determine the apparent pK_a values associated with each. Adams *et al*. showed that assembly begins at the first pK_a value of the peptide and that the pK_a of assembled peptides is greater than that of the same peptide free in solution.[56] It was expected that at least two pK_a values would be observed in the pH titration: one for the free amine on K and one for the *C*-terminal carboxylic acid.

The carboxylic acid groups on hydrophobic *N*-capped peptides generally have pK_a values of about 3.5.[38] However, previous work has shown that self-assembly causes this pK_a value to increase.[38, 57-59] One study investigating the self-assembly of FmocFF recorded two apparent pK_a shifts of ~2.2 and ~6.4 for a single *C*-terminal carboxylic acid group.[38] We expected that the pK_a of the free amine on the K residue of each gelator would also be shifted.

The apparent pK_a values of the *C*-terminal carboxylic acid groups of the dipeptides tested by Adams et al. were all higher than expected and were generally between 4 and 6.[56] Adams *et al*. also observed that the apparent pK_a values correlated with the hydrophobicity of the dipeptides studied. The more hydrophobic dipeptides gave higher apparent pK_a values. This meant that the apparent pK_a value of each dipeptide was reached at a different point during pH reduction. Thereby, the kinetics of assembly, controlled by deprotonation of the *C*-terminus, was different for each dipeptide.[56] It was expected that similar behaviour would be seen with the peptides studied here.

pK_a values for the side-chain amine on K residues within peptides ranging from 9.29-10.24 have been reported, depending on the identity of the peptide.[60, 61] Studies by Urry *et al*. suggest that in peptides containing F residues, the pK_a of the side-chain amine in K can be shifted from ~10 to ~7.[62] It is likely that the pK_a values of both the free amine on K and the *C*-terminal carboxylic acid groups are shifted as the peptide molecules begin to self-assemble. Thereby, each plateau in the pH titration shows the pH values at which the peptide molecules self-assemble into a different structure.[38, 63]

In previous studies, FmocFF exhibited two distinct pK_a transitions that were shown to be related to the structural transition of fibrils into tape-like structures that precipitated at low pH (pH < 2).[38] Different structures will be better suited to gelation and/or cross-linking. It is therefore possible to select pH conditions that encourage cross-linking between fibres and

to fine-tune the extent of cross-linking using pH conditions. However, as previously noted in the case of GTA, the mechanism by which the chosen cross-linking agent forms cross-links can also be pH-dependent. This could result in a trade-off between optimum cross-linking conditions and the optimum morphology for forming cross-links between fibres. It will also be important to select morphologies that result in the formation of strong hydrogels.

Previous work by Adams et. al used a series of Fmoc-dipeptides to investigate the influence of molecular structure on gelation behaviour.[56] This work shows the relationship between the apparent pK_a of peptide gelator molecules and the properties of the gels formed. The gels studied by Adams *et al*. were formed using GdL as a trigger.[56] The use of GdL as a pH trigger is advantageous as the rate of dissolution of GdL is greater than the rate of its hydrolysis into gluconic acid and a proton. This allows uniform dispersal of protons and formation of homogenous gels with reproducible properties, as previously discussed.[1] It is clear from the work by Adams *et al*. that, despite using the same peptide concentration and amount of GdL, each Fmoc-dipeptide behaved very differently on a reduction in pH and displayed different apparent pK_a values.[56] Each tripeptide studied here showed different apparent pK_a values (Figure 4.9) and were therefore expected to exhibit different behaviours on triggering gelation via a change in pH.

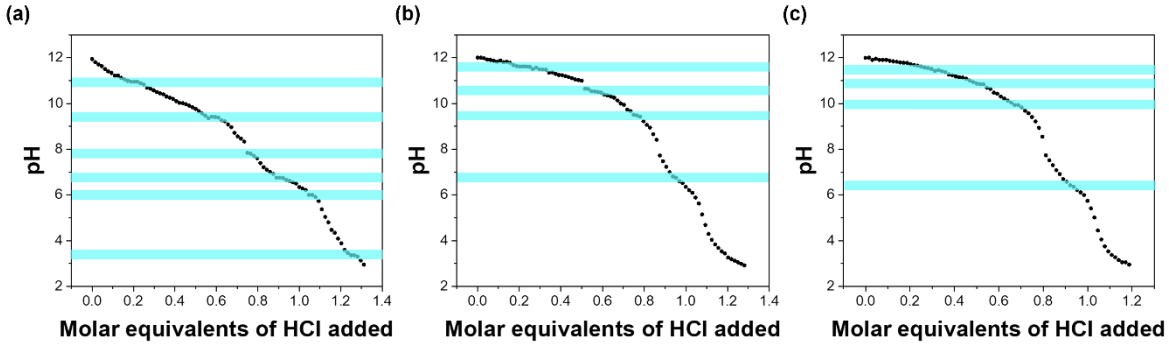

Figure 4.9. pH titrations recorded using 10 mg/mL suspensions of (a) 2NapFFK, (b) 2NapKFF and (c) 2NapFKF. The average temperature for the duration of the titrations was 25 °C. The plateaus in the pH curves that reveal possible pK_a values are highlighted in blue. The raw values for each pH titration are shown in Appendix 3.6.

Previous work has shown that a permanent, strong, 3D network can only be formed by the association of fibrils or by branching between fibres.[56] It is apparent from the study on Fmoc-dipeptides that increased hydrophobicity leads to increased gel strength. Since the apparent pK_a values for hydrophobic peptides shift to higher values under self-assembly conditions, at a given pH below this pK_a, the dipeptides with the highest pK_a values will be at an

effectively higher supersaturation. This higher supersaturation can in turn lead to a greater degree of branching within a gel network and thereby a stronger gel.[56] It is hoped that introducing cross-links between fibres in a pre-formed gel will increase the strength of the gel formed in a similar way to increasing supersaturation.

It is also possible that the rigidity of the fibrils making up the network is directly related to the hydrophobic interactions within the gel, which will in turn influence gel strength.[56] It is hypothesised that, by introducing cross-links within the fibres of a pre-formed gel, it will be possible to circumvent the use of highly hydrophobic amino acids to form gels with sufficient strength for a given application. Thereby, it will be possible to include residues required for a given application, even if these residues do not contribute to self-assembly or gel strength.

According to the pK_a titrations (Figure 4.9) there is at least one apparent pK_a between pH 10.5 and pH 11.5 in all three gelators. We attempted to form gels at low pH (using GdL as a trigger) from a suspension of 2NapFFK (5 mg/mL) starting at pH 10.5 and pH 11.5. The sample with a starting pH of 10.5 did not form a self-supporting gel while the sample with a starting pH of 11.5 did form a stable gel. We therefore decided to use pH 11.7 as the starting pH for all samples as this is above the highest apparent pK_a value for all three tripeptides. The apparent pK_a values of the gelators, the initial pH before gelation and thereby the structures present before triggering gelation are clearly of great importance in these systems.

4.2.3 Viscosity of the target molecules in suspension at high pH

To achieve the desired initial pH, two molar equivalents of NaOH (with respect to the tripeptide) were used to prepare the suspensions. NaOH was added in the form of 0.1 M NaOH. Deionised water was then added so that the concentration of the peptide was 10 mg/mL. The suspensions had to be stirred vigorously for at least 24 hours to ensure homogenous dispersal of the peptide molecules. It was important that all three peptide suspensions were stirred in the same way, as previous work has shown that gels triggered by changing pH are sensitive to the method of agitation used prior to gel formation.[64] All three suspensions were white in colour at pH 11.7, suggesting the formation of structures. Viscosity data showed that all three tripeptides exhibit shear-thinning behaviour at high pH (Figure 4.10), indicating the presence of one-dimensional structures, such as worm-like micelles.[33, 65, 66]

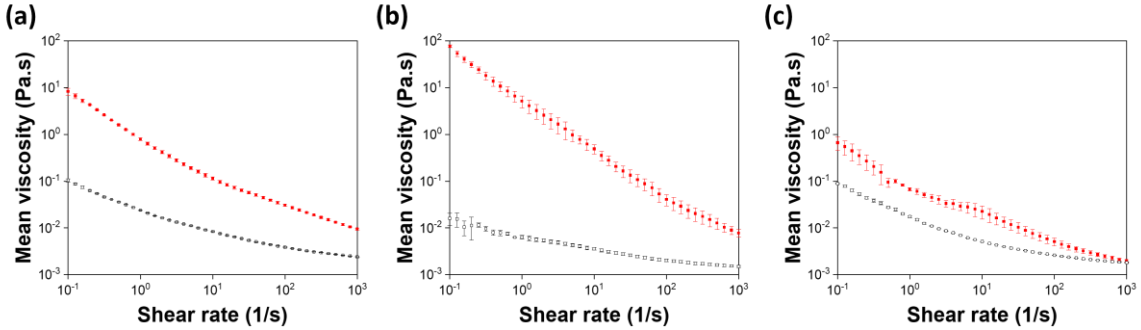

Figure 4.10. Viscosity data collected from (a) 2NapFFK, (b) 2NapKFF and (c) 2NapFKF at concentrations of 10 mg/mL at pH 11.7 without GTA (red) and after stirring 24 hours (black) without pH adjustment to replicate conditions in the cross-linking pre-gelation gels (pH >11.0).

All three tripeptides gave different viscosity values with 2NapKFF exhibiting the highest viscosity and 2NapFKF the lowest (Figure 4.10). This shows that the position of the K residue in the peptide chain alters the way that the molecules stack together into secondary structures at high pH. We expect that having the K residue sandwiched between the two F residues disrupts the formation of one-dimensional structures, resulting in the observed lower viscosity. However, all three tripeptides gave similar viscosity values after stirring with GTA, despite having different viscosities without GTA. Importantly, shear-thinning behaviour persists after stirring with GTA (Figure 4.10), showing the samples are still able to form worm-like micelles. GTA may be disrupting self-assembly, or the formation of cross-links may be causing defects in the structures formed.

We further confirmed the presence of worm-like micelles in the suspensions at high pH by forming gels at high pH using divalent cations.[33] As previously discussed, divalent cations can be used to trigger the gelation of peptides at high pH by forming electrostatic bridges between free carboxylate groups on adjacent worm-like micelles. In this manner, the peptides can form a network and trap the solvent, resulting in formation of a gel (Figure 4.4a).

After investigating the properties of the target molecules in the micellar phase at high pH, we were in a good position to begin investigating their properties in the gel phase and to design experiments examining the effect of chemical cross-linking with GTA on the properties of any resulting gels.

4.2.4 The effect of chemical cross-linking on the mechanical properties of GdL-triggered gels

Gels were prepared by first suspending the gelators in H_2O at high pH (~11.7) by addition of 2 molar equivalents of NaOH (0.1 M). Such high pH ensures deprotonation of both the *C*-terminal carboxylic acid group and the amine on the K side chain, rendering the molecules sufficiently polar to be dispersed in water.[39] Viscosity measurements of both gelators at high pH show shear-thinning behaviour, indicative of the presence of worm-like micelles.[33] While stirring with GTA at this pH reduces the viscosity of the micellar suspensions, the shear-thinning behaviour persists (Figure 4.10), showing that worm-like micelles are still present.

Gels were formed *via* a reduction in pH using GdL, as previously reported.[1] Reducing the pH of the suspensions results in protonation of the *C*-terminal carboxylic acid, decreasing the polarity of the molecules and driving further association of self-assembled structures to exclude water.[39] The amine is also protonated by reduction in pH, giving the molecule a positive charge. All the tripeptides were able to form gels despite the presence of this positive charge. We expect that during self-assembly the protonated amine will be positioned on the outside of the structures, allowing the amine to interact with water molecules and form hydrogen bonds with hydrogen acceptor groups as well as charge-dipole interactions. The self-assembled structures interact and entangle through the formation of non-covalent interactions as the pH continues to decrease until a 3D network is formed.[39, 67] Water is trapped within the network during self-assembly, giving the gel its viscoelastic properties.

The gelators were exposed to GTA (1 molar equivalent) under two different conditions (Figure 4.11): stirring in solution at high pH (pH ~11.7) for 24 hours before gelation and as gels at low pH (pH ~3.5). All samples were left for a minimum of 16 hours after addition of GdL to allow gel formation (time sweep data, Figure A3.5.1, Appendix 3.5). GTA was then added to the post-gelation samples, which were left undisturbed for a further 24 or 72 hours before rheology measurements. Since the GTA had to be added to the top of the sample, a gradient of cross-linking may have been present in the post-gelation samples. This will have affected the results obtained from rheology measurements and is a limitation to this experimental design.[68]

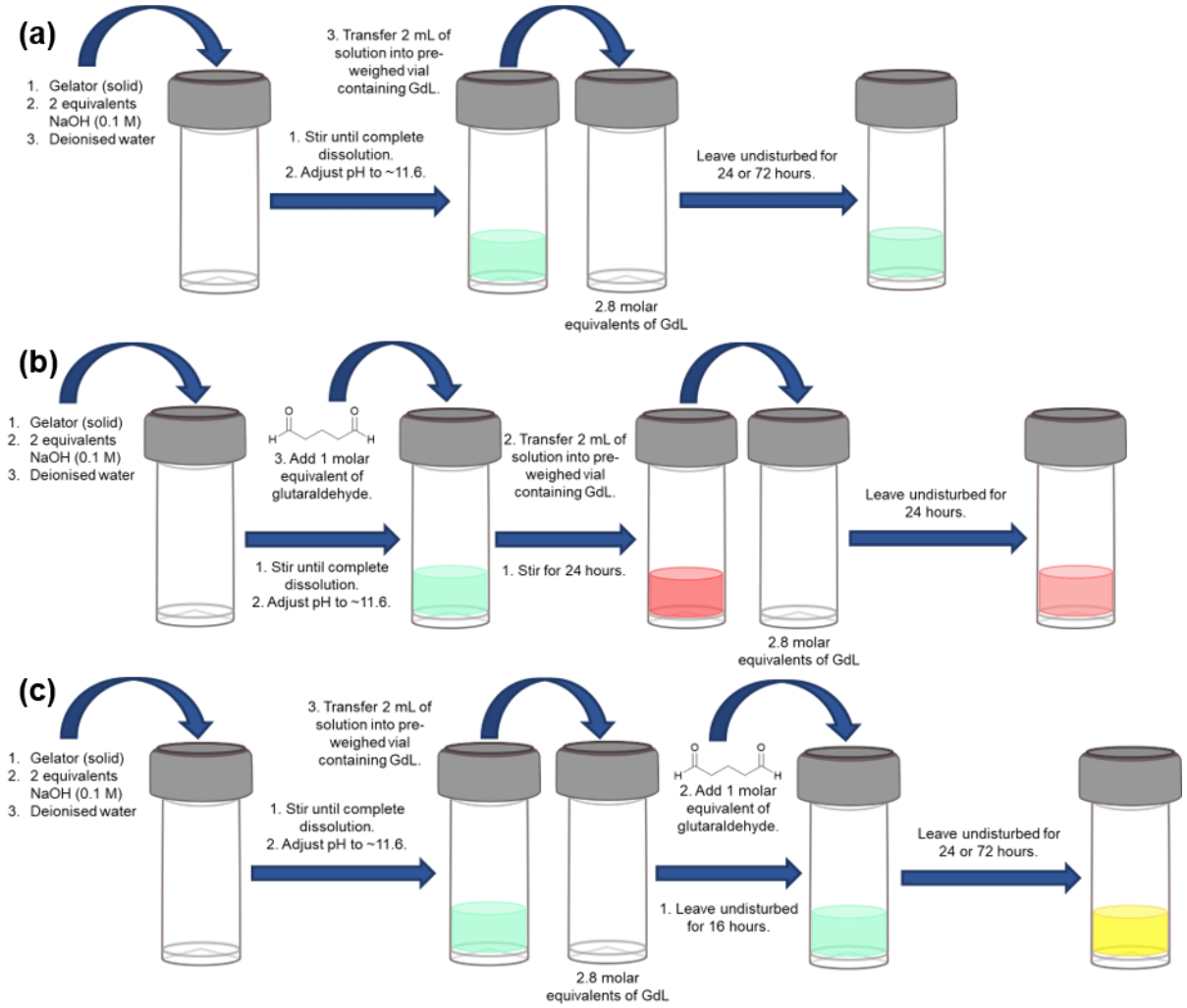

Figure 4.11. Schematic representations showing preparation of (a) control, (b) pre-gelation and (c) post-gelation samples.

The control experiments were designed to account for gel age as well as the presence of GTA.[69] Pre-gelation samples were left to sit for 24 hours before rheology to ensure they were the same age as the 24-hour post-gelation samples and the 24-hour controls. In most cases, the 24-hour and 72-hour control samples are not statistically different from a rheological perspective (Figure 4.12). Therefore, the differences between gels exposed to GTA post-gelation for 24 and 72 hours are due to the interaction of the gel with GTA and not the age of the gels. This allows direct comparison between 72-hour post-gelation samples and all others.

Only slight increases in stiffness (G′) were observed in 2NapFFK 5 mg/mL (Figure 4.12a) when comparing the control samples and the samples exposed to GTA for 24 hours post-gelation. This increase became more significant at a 2NapFFK concentration of 10 mg/mL (Figure 4.12 aii). The samples where GTA was added post-gelation and left to react for 72

hours showed even greater increases in stiffness compared to the controls. GTA is therefore able to interact with the gelators within the gel network at low pH, resulting in increased gel stiffness. The degree of this increase depends on how much time GTA is given to interact with the gels.

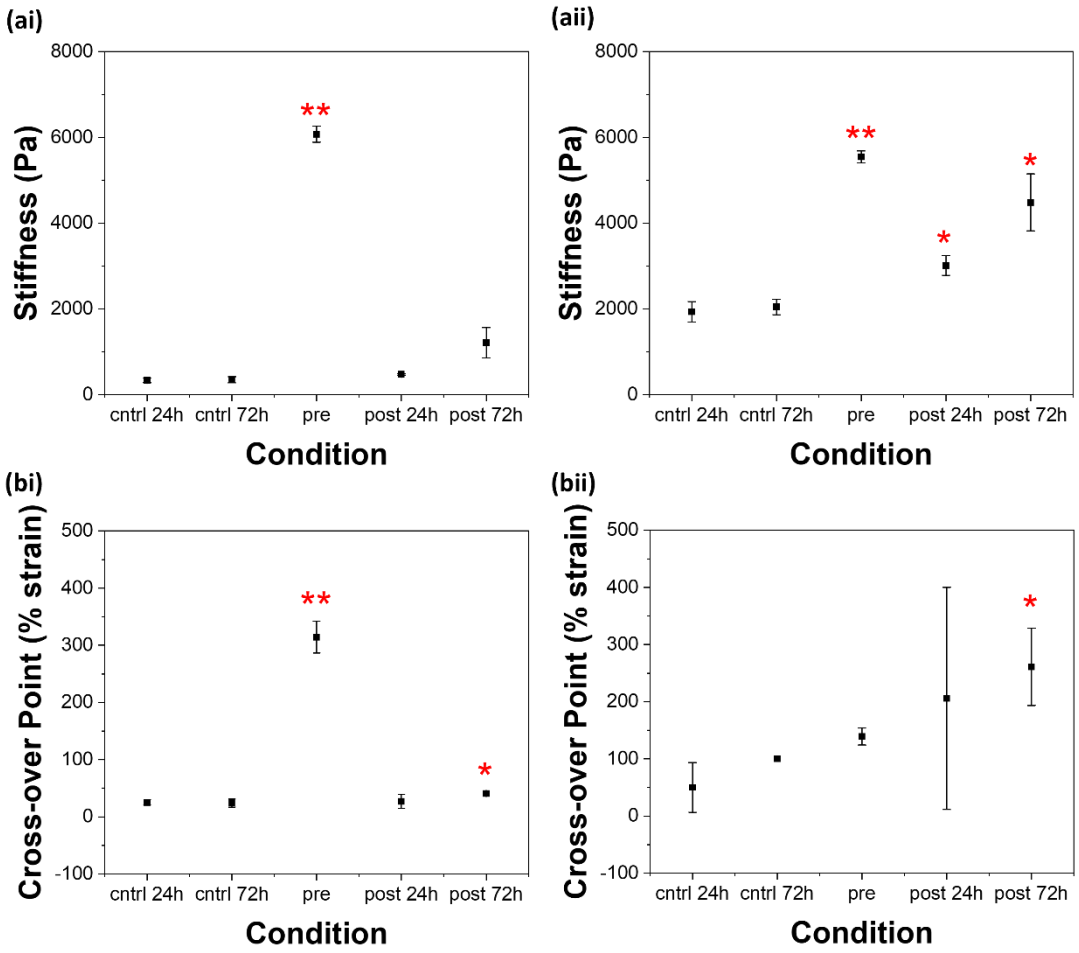

Figure 4.12. Scatter plots showing the (a) stiffness and (b) cross-over point of gels composed of 2NapFFK at concentrations of (i) 5 mg/mL and (ii) 10 mg/mL formed under different conditions. The stiffness was determined as the average G' value in a selected section of the LVR of the strain sweep (0.01-1 % strain). This section was selected as is applicable to all samples. The cross-over point was taken as strain value within the strain sweep where G″ crosses over G′. The points in the plot are the average from three samples. The error bars show the standard deviation between the three samples in each condition. Two-sample T-tests assuming unequal variances were performed between each triplicate of samples and the 24-hour control triplicate of samples. * = $p > 0.05$, ** $p > 0.01$.

Stirring 2NapFFK with GTA pre-gelation increased both the stiffness (G′) of the resulting gels and the strain required to completely break down the gel network (the strain at which

G′ crosses over G″ or the cross-over point, Figure 4.12). This can be explained by the pH at which GTA is interacting with the gelator molecules. At high pH, more deprotonated amines are available for imine formation, resulting in more cross-linking and thereby more notable changes in mechanical properties.[70] However, it is expected that pH is not the only factor contributing to this difference. At low pH the gel network has been formed, making it harder for GTA to diffuse through the sample and into the fibrous structure to interact with the amine groups.

At a higher gelator concentration (Figure 4.12b), there is a less notable difference between the pre- and post-gelation samples. We hypothesise that as the concentration increases it is harder for GTA to access the amine groups as the structures formed at high pH and the gel network will be denser. There could also be a change in morphology at a concentration between 5 and 10 mg/mL, making cross-linking more difficult.

It should be noted gels composed of 2NapFFK at a concentration of 5 mg/mL are not frequency independent at frequency values greater than 10 (Figure A3.5.3, Appendix 3.5). Cross-linking with GTA pre-gelation imparts frequency-independence on these gels.

Cross-linking 2NapFFK at 5 mg/mL pre-gelation leads to an increase in G′ greater than that achieved by increasing the gelator concentration to 10 mg/mL. A considerable increase in stiffness and resistance to strain can therefore be achieved without having to increase gelator concentration. Therefore, by cross-linking prior to gelation, it is possible to use lower gelator concentrations while maintaining the desired gel strength.

For 2NapKFF at a concentration of 5 mg/mL, the control samples and the 24-hour post-gelation samples are virtually identical, while the 72-hour post-gelation samples showed increased stiffness (Figure 4.13ai). 2NapKFF therefore needs more than 24 hours to sufficiently interact with GTA.

There is little difference between G′ and G″ values of the pre- and 72-hour post-gelation samples. However, the linear viscoelastic region (LVR) is notably longer in the pre-gelation samples (Figure 4.14bi). This shows that the pre-gelation gels can withstand higher strain before the gel network begins to break down and are therefore stronger than the post-gelation gels as well as the non-cross-linked (control) gels.[10, 71] This could be due to more efficient cross-linking at high pH, as previously discussed.

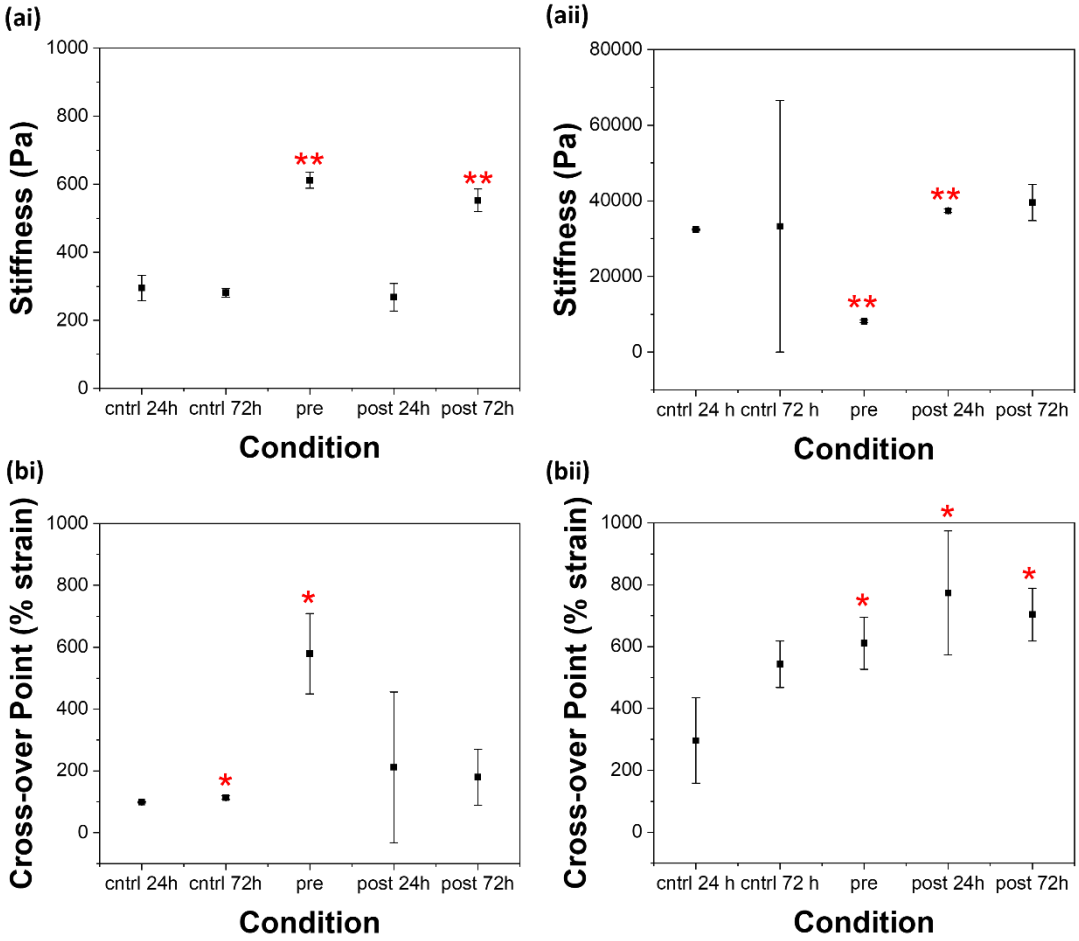

Figure 4.13. Scatter plots showing the (a) stiffness and (b) cross-over point of gels formed from 2NapKFF at concentrations of (i) 5 mg/mL and (ii) 10 mg/mL under different conditions. The stiffness was determined as the average G' value in the LVR of the strain sweep (0.01-1 % strain). This range was selected as is applicable to all samples. The cross-over point shows the strain value within the strain sweep where G″ crosses over G′. The points in the plot are the average from three samples. The error bars show the standard deviation between the three samples in each condition. Two-sample T-tests assuming unequal variances were performed between each triplicate of samples and the 24-hour control triplicate of samples. * = $p > 0.05$, ** $p > 0.01$. In the case where the 72-hour control samples were statistically different from 24-hour control, the 72-hour post samples were compared to the 72-hour controls in the statistical test.

Formation of cross-links prior to gel formation may also result in different gel morphology and thereby different properties. This observation is particularly exciting as most techniques previously used to modulate the mechanical properties of peptide-based supramolecular hydrogels result in increased stiffness (G′) but not increased mechanical strength. No increase in the length of the LVR of 2NapFFK is observed in any of the conditions tested

(Figure 4.14a), showing the importance of the position of the cross-linkable K residue in the outcome of chemical cross-linking.

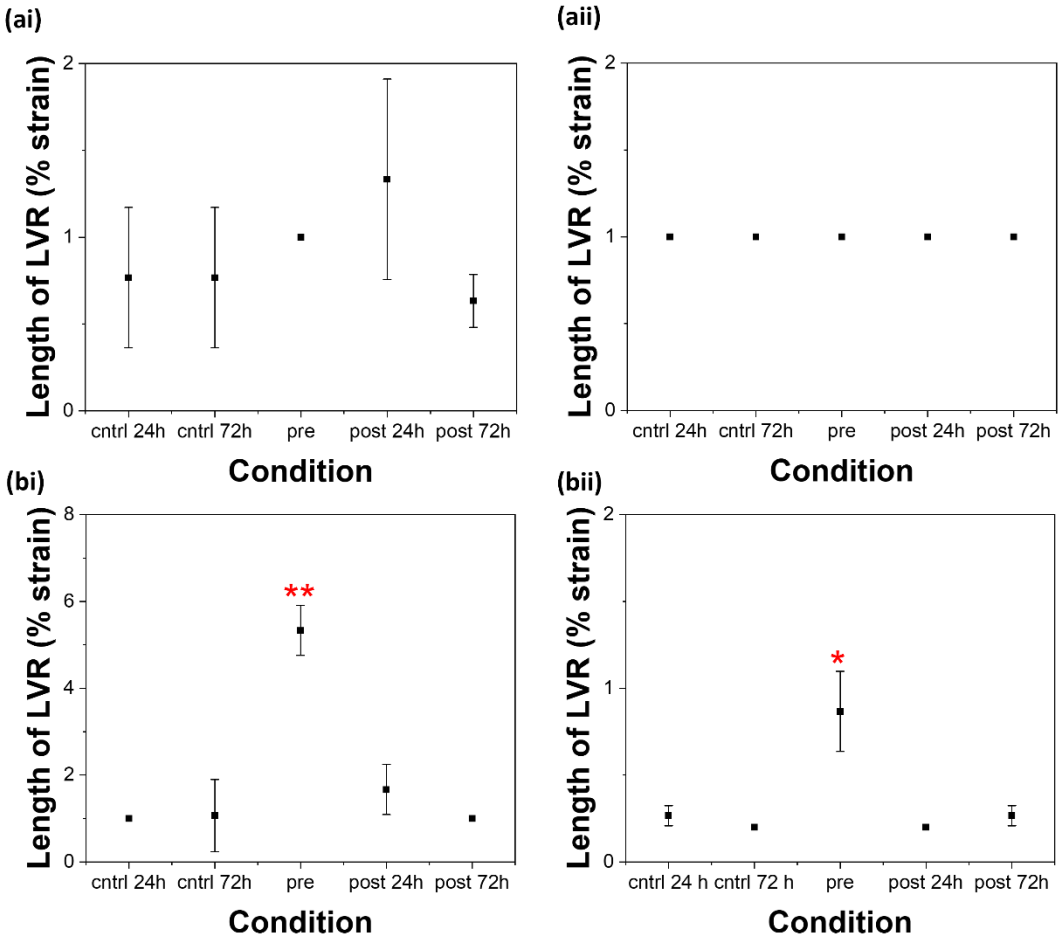

Figure 4.14. Scatter plots showing the length of the LVR recorded from gels composed of (a) 2NapFFK and (b) 2NapKFF at concentrations of (i) 5 mg/mL and (ii) 10 mg/mL in different conditions. The length of the LVR was taken as the strain value at which the G′ begins to decrease. The points in the plot are the average from three samples. The error bars show the standard deviation between the three samples in each condition. We note that for several samples the standard deviation is too small for the error bars to be visible. Two-sample T-tests assuming unequal variances were performed between each triplicate of samples and the 24-hour control triplicate of samples. * = $p > 0.05$, ** $p > 0.01$.

We highlight that for all these systems rheology was performed on samples a maximum of 14 days after gel formation. No evidence of crystallisation was observed in these samples with only slight changes in rheological properties. Samples left undisturbed at room temperature for over 1 month showed no visible evidence of crystal formation or precipitation.

At 10 mg/mL, 2NapKFF (Figure 4.13) showed very little difference between the 24-hour and 72-hour post-gelation samples. It could be that more time is needed at a higher concentration for this gelator to interact with GTA, owing to a denser gel network, or that the maximum increase in gel properties had already been reached within 24 hours. Interestingly, the post-gelation samples showed higher G′ values but similar G″ values compared to the control samples, suggesting greater elasticity.[13]

Slight increases in the length of the LVR were also observed, showing increased gel strength (Figure 4.14bii). The pre-gelation samples showed massive decreases in G′ and G″, signifying decreased stiffness. However, they also showed a considerable increase in the LVR (Figure 4.14bii). These observations suggest that while exposure to GTA pre-gelation reduced the stiffness of the gels, their resistance to strain was increased. This change in behaviour could be due to a transition in gel morphology or behaviour somewhere between 5 and 10 mg/mL. This change of properties is in opposition to what is usually seen following chemical cross-linking.[11]

The greater increase in mechanical properties in 2NapFFK at 5 mg/mL compared to 2NapKFF at 5 mg/mL is most likely due to the position of the K residue in the peptide chain. The K residue at the *C*-terminus is less sterically hindered and therefore more readily available for cross-linking.[10] This will increase the efficiency of cross-linking, resulting in the observed changes in mechanical properties. The drastic differences observed when comparing the pre-gelation samples of 2NapFFK and 2NapKFF at 10 mg/mL shows that the position of the K residue has a great effect on gel behaviour and provides a further level of control for tuning gel properties.

The tendency of this family of functionalised dipeptides to behave as surfactants[72, 73] may also play a role in the differences observed between gels depending on the position of the K residue. For 2NapFFK, we expect that the hydrophobic aromatic rings will be stacked together in the centre of the micellar structures with the hydrophilic carboxylic acid at the *C*-terminus and amine group on K exposed to maximise favourable like-with-like interactions with water. Such an arrangement is likely to be more difficult with the K residue sandwiched between the hydrophobic naphthalene ring at the *N*-terminus and the two phenyl rings in the FF motif. We therefore expect that the K residues in gels formed from 2NapKFF will be less accessible for cross-linking than those in gels formed from 2NapFFK.

We also synthesised and performed cross-linking on the final combination of the 2Nap capping group with two F residues and one K residue: 2NapFKF (Figure 4.1e). Our results further confirm the importance of the position of the K residue in the peptide-chain in determining the behaviour of the gelators on cross-linking as 2NapFKF behaved differently to both 2NapFFK and 2NapKFF following cross-linking. 2NapFFK showed increased stiffness in all cross-linking conditions and 2NapKFF showed increased stiffness following cross-linking in all conditions except pre-gelation at a 2NapKFF concentration of 10 mg/mL. The stiffness of 2NapFKF decreased significantly following cross-linking pre-gelation at 5 mg/mL and decreased slightly following cross-linking pre-gelation at 10 mg/mL (Figure 4.15). The cross-over point of gels formed from 2NapFKF increased following cross-linking pre-gelation and post-gelation at both 2NapFKF concentrations, similar to 2NapFFK. The length of the LVR increased slightly following cross-linking pre-gelation at a 2NapFKF concentration of 10 mg/mL. However, this increase was not as significant as observed in 2NapKFF.

Increasing gelator concentration to 10 mg/mL (Figure 4.15) changed the gels' response to cross-linking. Cross-linking post-gelation resulted in increased G′ and G″ as well as increased cross-over point. This resembles the behaviour observed for 2NapFFK at 10 mg/mL in H_2O, although markedly less extreme. Cross-linking post-gelation also resulted in decreased LVR length, this was not observed in any of the other conditions or gelators. Cross-linking pre-gelation resulted in slightly decreased stiffness and increased strength (cross-over point and length of LVR), similar to, but again less dramatic than, 2NapKFF at 10 mg/mL in H_2O.

We noticed a decrease in the tanδ (G″/G′) values of the gels formed from 2NaFKF depending on the conditions of cross-linking. G′ describes the solid-like properties of the material while G″ describes the liquid-like properties of the material.[74] Materials are considered "true gels" if they have a tanδ value lower than 0.1.[75] However, supramolecular hydrogels tend to have tanδ values of approximately 0.15. Different patterns in the tanδ values are observed depending on the position of the K residue in the peptide chain (Figure 4.16). The tanδ values of 2NapFFK gels increased on cross-linking, with cross-linking post-gelation giving the greatest increase at both 5 and 10 mg/mL while 2NapFKF shows the opposite trend. No such pattern was observed in 2NapKFF. This further shows that the response of the gelators to chemical cross-linking can be finely tuned using peptide sequence. This is important as it

will allow fine control over gel properties, allowing us to achieve the optimum behaviour required for a certain application.

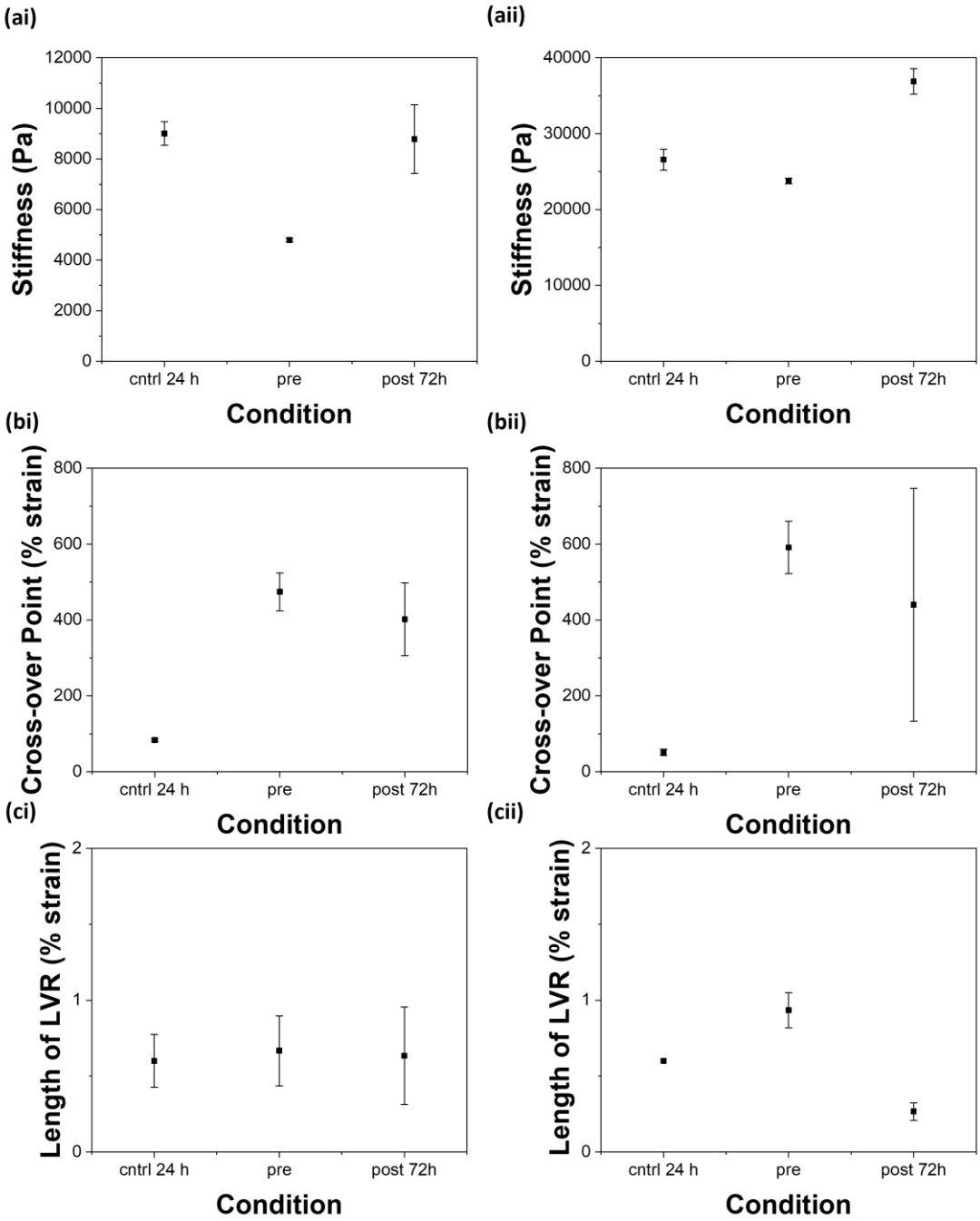

Figure 4.15. Scatter plots showing the (a) stiffness, (b) cross-over point and (c) length of the LVR of gels formed from 2NapFKF at concentrations of (i) 5 mg/mL and (ii) 10 mg/mL in different conditions. The points in the plot are the average from three samples. The error bars show the standard deviation between the three samples in each condition. Two-sample T-tests assuming unequal variances were performed between each triplicate of samples and the 24-hour control triplicate of samples.

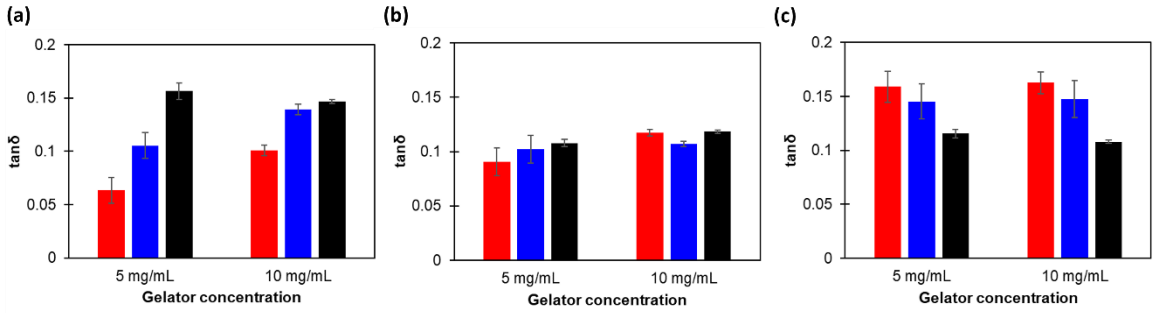

Figure 4.16. Graphs showing the tanδ values of gels formed from (a) 2NapFFK, (b) 2NapKFF and (c) 2NapFKF at concentrations of 5 mg/mL and 10 mg/mL without GTA (red), with GTA added post-gelation (blue) and GTA added pre-gelation (black). The tanδ values are the average calculated from the G′ and G″ values of three strain and three frequency sweeps on six separate samples at 0.1 % strain and 10 rad/s frequency. The error bars show the standard deviation between the tanδ values calculated from the six samples.

2NapFFK, 2NapKFF and 2NapFKF can all be cross-linked in a variety of conditions to achieve different mechanical properties, including increased gel strength. Our results show the potential for the position of the cross-linkable group in the peptide chain to be harnessed as a method for finely controlling the response of the gelator to cross-linking.

4.2.5 GTA concentration and cross-linking time post-gelation as parameters for controlling the effect of cross-linking on GdL-triggered gels

We investigated further some of the parameters involved in the preparation of our samples: GTA concentration and time allowed for cross-linking post-gelation. We initially began with a large excess of GTA in the hopes of ensuring cross-linking could occur and to account for the possibility of GTA interacting with the samples in polymeric form.[22] When a large excess of GTA was used, the effect of cross-linking post-gelation resulted in a similar outcome to using 1:1 molar ratio GTA:gelator (Figure 4.17a). However, for the pre-gelation samples, an even greater reduction in stiffness and increase in strength was observed in 2NapKFF (10 mg/mL). This suggests only so much GTA can react within the gel network while reaction in solution pre-gelation can be further amplified by increasing GTA concentration.

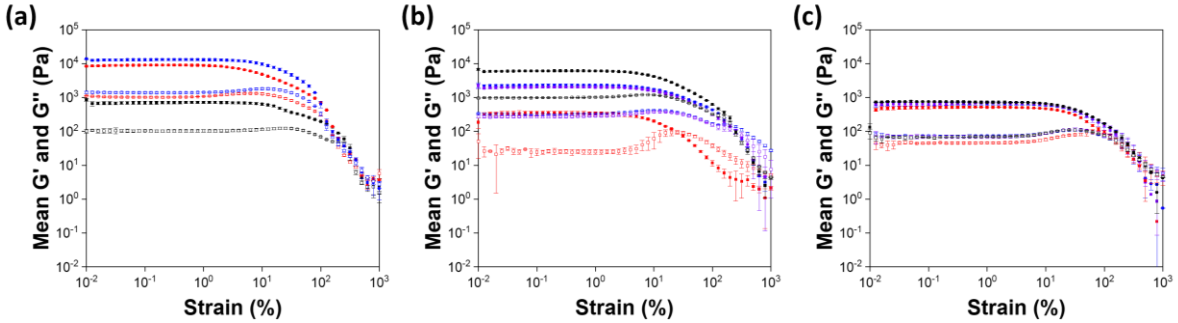

Figure 4.17. Strain sweeps from (a) 2NapKFF (10 mg/mL) without GTA (red) and with 50 molar equivalents of GTA added pre-gelation (black) and post-gelation and left to react for 72 hours (blue); (b) 2NapFFK (5 mg/mL) without GTA (red) and with GTA added pre-gelation at three different molar ratios (GTA:2NapFFK); 1:1 (black), 2:1 (blue) and 5:1 (purple) and (c) 2NapFFK (5 mg/mL) without GTA (red) and with GTA added post-gelation and left to react for 3 days (blue), 6 days (purple) and 10 days (black) before rheological measurements. All samples were prepared on the same day and from the same stock suspension. G′ (filled squares) and G″ (hollow squares) were calculated from the average of three samples. Error bars show the standard deviation between samples.

To further investigate this, we looked at 2NapFFK (5 mg/mL) as this is the gelator and concentration that shows the greatest changes in rheological properties on reaction with GTA. We reacted 2NapFFK in solution pre-gelation with GTA at three different molar ratios: 1:1, 2:1and 5:1(GTA:2NapFFK). The results in Figure 4.17b show that a molar ratio of 1:1 provides the optimum conditions for this gelator. Increasing the molar ratio reduced the degree to which stiffness (G′ and G″) increases. However, the length of the LVR and cross-over point increase to a similar extent at all molar ratios. This further exemplifies how the amount of cross-linking agent can be used to fine-tune the properties of the final gel.

Finally, we investigated the effect of time allowed for the cross-linking reaction to take place on the post-gelation samples. The post-gelation and control samples were prepared as normal and left for 3, 6 and 10 days. No change was seen in the controls during this time frame so only one set of control samples is shown for clarity. The rheology of the 3-day and 6-day post-gelation samples are almost identical (Figure 4.17c). There is a very slight increase in stiffness (G′) of the 10-day samples. However, leaving the samples for this long introduces more margins for change outside cross-linking, such as changes in temperature and degradation of the gel network with time, making leaving samples for this length of time

unappealing. We therefore kept the maximum number of days for the post-gelation samples at 3 days.

4.2.6 Effect of chemical cross-linking on GdL-triggered gels in D_2O

We studied the secondary structures within the gel networks using small angle scattering techniques. We hoped that small angle scattering would help us understand the structural changes brought about by cross-linking in different conditions in order to better understand how chemical cross-linking causes changes in mechanical properties.[76] Small angle scattering is used in favour of other techniques such as transmission electron microscopy (TEM), scanning electron microscopy (SEM) and atomic force microscopy (AFM) as there is no need to dry the samples which has been shown to result in drying artefacts and may result in structural changes.[77, 78]

Understanding the mechanism by which cross-linking is causing the observed changes in mechanical properties will help us apply this method of cross-linking to other gelators. Before performing small angle neutron scattering (SANS), it is important to ensure the same behaviour is observed when cross-linking in D_2O as in H_2O. SANS is performed in deuterated solvents to minimise scattering from solvent and allow sufficient contrast for useful information to be obtained.[79]

We performed cross-linking experiments on both gelators where cross-linking occurred either pre-gelation or post-gelation. We prepared suspensions of the gelators at concentrations of 5 mg/mL and 10 mg/mL at high pH by suspension in D_2O and addition of 2 molar equivalents of NaOD (0.1 M solution in D_2O). After stirring overnight to ensure complete dissolution, the pH of the suspensions was adjusted to ~11.7 by addition of either 1 M DCl or 1 M NaOD. The pre-gelation samples were prepared by stirring the gelator suspensions for 24 hours with 1 molar equivalent of GTA (50 % aqueous solution) at high pH before triggering gelation using GdL, as previously described.[1] The post-gelation samples were prepared by triggering gelation, leaving the gels to form overnight then adding 1 molar equivalent of GTA to the top of the gel and leaving the samples for 72 hours to react. The control samples were prepared without any GTA.

Preparation of the gels in D_2O did not have a significant effect on the properties of the control gels. It can be seen by comparing Figure A3.5.2 (Appendix 3.5) to Figure 4.18 that the effect

of cross-linking 2NapFFK gels pre- and post-gelation had similar effects at each concentration in both H_2O and in D_2O. Cross-linking pre-gelation consistently had the greatest impact on both gel stiffness (G′) and gel strength (the length of the LVR).

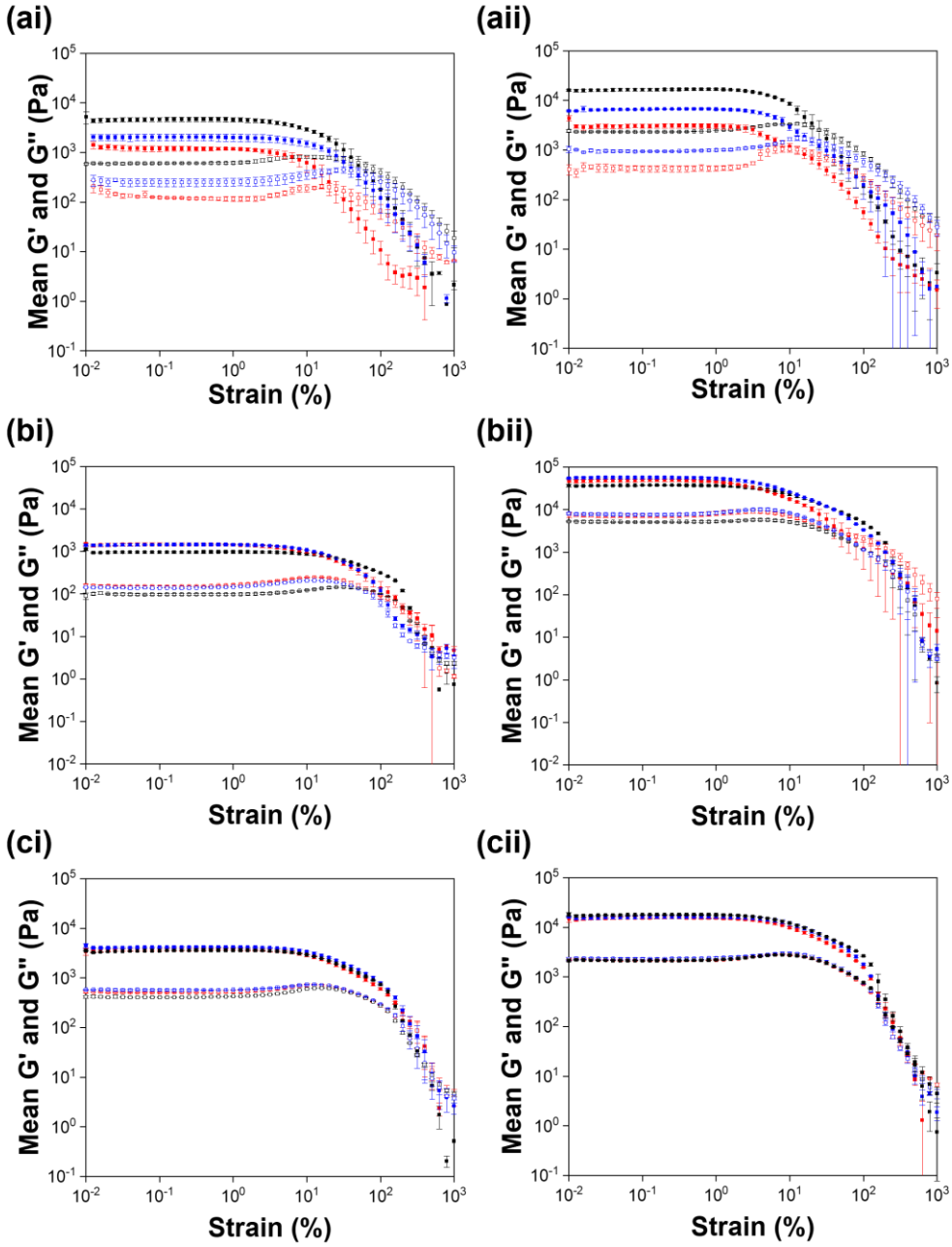

Figure 4.18: Strain sweeps of samples prepared in D_2O of (a) 2NapFFK, (b) 2NapKFF and (c) 2NapFKF at concentrations of (i) 5 mg/mL and (ii) 10 mg/mL with GTA added pre-gelation (black), GTA added post-gelation and left to react for 72 hours (blue) and control gels with no GTA (red). G′ (filled squares) and G″ (hollow squares) were calculated from the average of three samples. Error bars show the standard deviation between the three samples in each condition. The corresponding frequency sweeps can be found in Figure A3.5.4, Appendix 3.5.

For 2NapKFF at a concentration of 5 mg/mL in H_2O cross-linking post- and pre-gelation both resulted in increased gel stiffness and gel strength compared to the control samples. Cross-linking pre-gelation provided the greatest increase in mechanical properties. However, in D_2O (Figure 4.18bi), cross-linking post-gelation did not significantly alter the gels' properties. While cross-linking pre-gelation still caused a considerable increase in gels' resistance to strain, a slight decrease in gel stiffness was observed.

At a concentration of 10 mg/mL, both the stiffness and strength of 2NapKFF gels in H_2O (Figure 4.13bii) were increased following cross-linking post-gelation. Cross-linking pre-gelation caused an even greater increase in gel strength but also a considerable decrease in gel stiffness. In D_2O, cross-linking post-gelation caused slight increases in gel stiffness and gel strength (Figure 4.18bii). Cross-linking pre-gelation again caused an increase in gel strength but only a slight decrease in stiffness, compared to the massive decrease observed in samples of 2NapKFF at 10 mg/mL prepared in H_2O. Importantly, the linear viscoelastic regions of the cross-linked gels still notably increase for both gelators at both concentrations, showing cross-linking still imparts increased gel strength in D2O.

2NapFKF shows a similar trend to 2NapFFK and 2NapKFF in D_2O at 5 mg/mL (Figure 4.18ci) but showed very little change in rheology following cross-linking at 10 mg/mL (Figure 4.18cii), similar to the behaviour observed in H_2O. Samples of 2NapFKF cross-linked post-gelation at a concentration of 5 mg/mL in D_2O showed an increase in stiffness (G′) compared to in H_2O where stiffness decreased. The pre-gelation samples of 2NapFKF at 5 mg/mL in both H_2O and D_2O showed decreased stiffness. It is hypothesised that the K residues in gels formed from 2NapFKF are harder to access and therefore less prone to cross-linking.

As the cross-linking reaction is happening more slowly in D_2O, the GTA molecules have more time to diffuse through the sample and reach the increased number of amines available at higher concentration before reacting. This can be seen when comparing results from 2NapFFK gels at a concentration of 10 mg/mL in H_2O to D_2O. In H_2O, the post-gelation samples at a concentration of 5 mg/mL show much greater changes in rheological properties when compared to the control samples than at 10 mg/mL. It is suspected that this is due to the increased density of the network at 10 mg/mL, making it more difficult for GTA to diffuse through the sample and reach more of the amines. 2NapKFF and 2NapFKF do not

show great change in rheological properties at either concentration in both H_2O and D_2O, suggesting the K residues are harder for GTA to reach in gels formed from these gelators.

Figure 4.19 shows that, in both D_2O and H_2O, the post-gelation samples were considerably more yellow at the higher concentration (10 mg/mL), suggesting more cross-linking has taken place, in alignment with there being a greater number of amine groups available. Quantitative measurements of cross-linking density would be required to confirm this hypothesis.

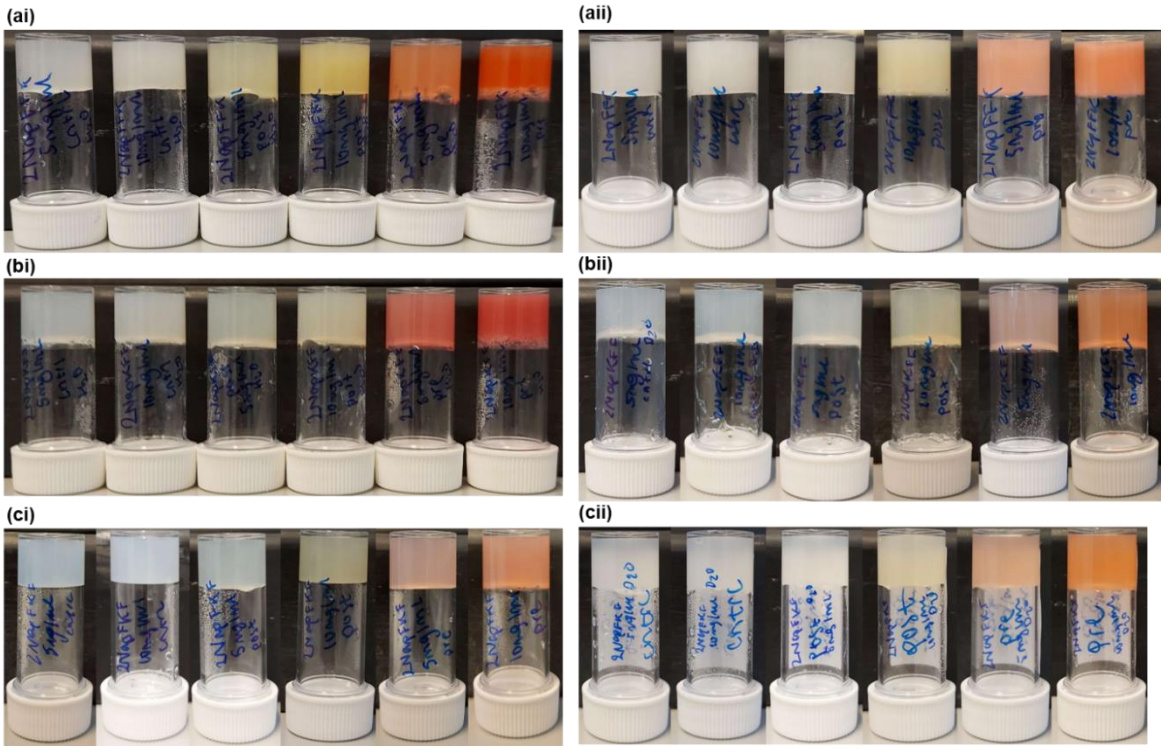

Figure 4.19. Photographs of gels formed from (a) 2NapFFK, (b) 2NapKFF and (c) 2NapFKF in (i) H_2O and (ii) D_2O, left to right alternating 5 mg/mL and 10 mg/mL: control (no GTA), GTA added post-gelation, stirred with GTA pre-gelation. Sample volumes are all 2 mL, prepared in 7 mL Sterilin vials.

Our results show that many variables can be used to alter the effect of cross-linking with GTA on gel mechanical properties, including concentration of the gelator and the conditions in which cross-linking takes place. We expected to observe some changes in D_2O compared to H_2O due to changes in the kinetics of both the cross-linking reaction and gelation using GdL as a trigger as reactions are generally slower in D_2O compared to H_2O due to the kinetic isotope effect.[80] This will cause the rate of hydrolysis of GdL to decrease in D_2O and thereby decrease the rate of self-assembly. This can then affect gel properties and in turn the effect of cross-linking on the gels.

Both SAXS performed in H_2O and SANS in D_2O will be needed to understand the changes in gel structure that result from cross-linking pre- and post-gelation at different concentrations and in D_2O compared to H_2O. H_2O does not have a sufficiently different neutron scattering length density (SLD) to the gelators and therefore there is not sufficient contrast between the medium and the self-assembled structures. The X-ray SLD of H_2O, however, is sufficiently different from gelators like those studied here to provide sufficient contrast and therefore collection of data of suitable quality to be fit. The high demand for synchrotron time makes it challenging to obtain data using both techniques.

4.2.7 Investigating the effect of cross-linking on the primary fibres in the gel network by SANS

SANS (performed at instrument D11, Institut Laue – Langevin (ILL), Grenoble, France) was used to determine the effect of cross-linking pre- and post-gelation on the secondary structures that constitute the gel network. The data from samples of 2NapFFK and 2NapKFF (Figures 4.22 and 4.23) suggests that cross-linking does not significantly change the nature of the fibres within the gel network as all three data sets within each gelator at each concentration could be fit to an elliptical cylinder model combined with a power law. However, cross-linking pre- and post-gelation did result in subtle changes in the morphologies of the cylinders that could account for some of the observed changes in rheological properties.

2NapFF acted as a control during our investigations since it is structurally similar to 2NapFFK and 2NapKFF but does not contain a cross-linkable amine group. We performed SANS experiments on samples composed of 2NapFF at concentrations of 5 and 10 mg/mL to investigate the effect of the presence of GTA pre- and post-gelation (Figure 4.24). This allowed us to compare changes to the morphology of the primary fibres within the gel network in the 2NapFF controls to those we observed on chemical cross-linking of 2NapFFK and 2NapKFF.

The 2NapFF samples at a concentration of 5 mg/mL were all best fit to a cylinder model combined with a power law while all the 10 mg/mL samples were best fit to a flexible elliptical cylinder combined with a power law (Figure 4.24). This shows that the presence of GTA does not affect the overall morphology of the fibres.

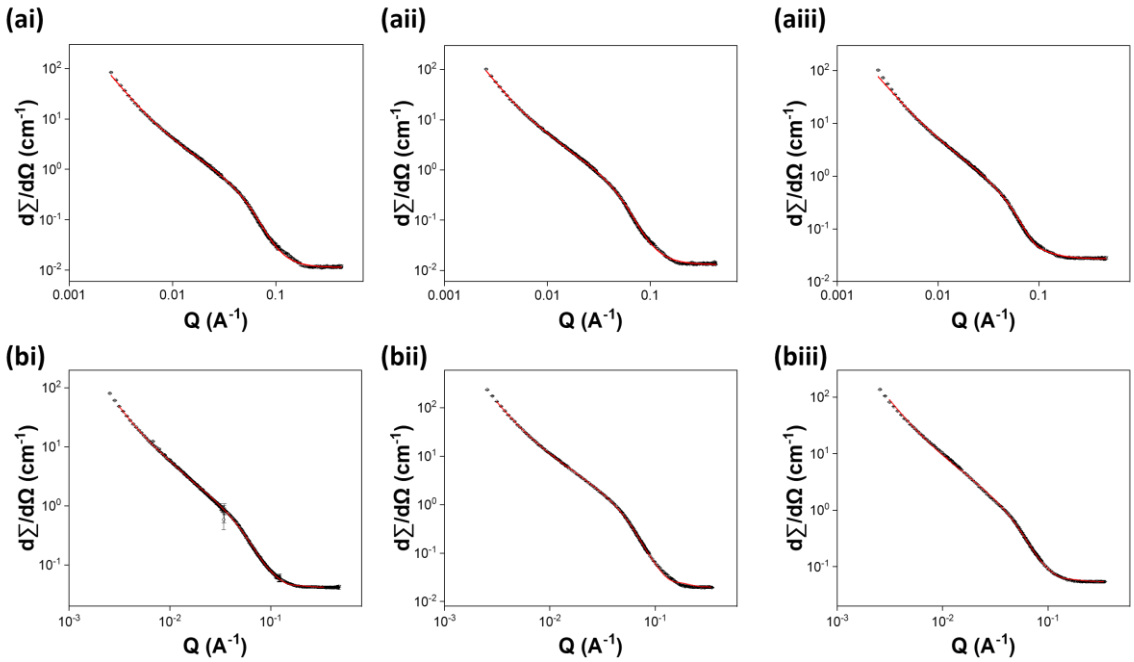

(c)

Sample	2NapFFK 5 mg/mL control	2NapFFK 5 mg/mL pre	2NapFFK 5 mg/mL post	2NapFFK 10 mg/mL control	2NapFFK 10 mg/mL pre	2NapFFK 10 mg/mL post
Cylinder Scale	0.0010	0.0014	0.0011	0.0021	0.0031	0.0026
Scale error	*6.49 x10^{-6}*	*6.93 x10^{-6}*	*5.66 x10^{-6}*	*6.54 x10^{-6}*	*9.25 x10^{-6}*	*8.96 x10^{-6}*
Background	0.011	0.013	0.026	0.041	0.019	0.053
Radius	26.7	26.0	30.0	20.6	24.2	24.3
Radius error	*0.0018*	*0.10*	*0.15*	*0.046*	*0.049*	*0.063*
Axis ratio	1.80	1.97	1.65	2.33	2.06	2.12
Axis ratio error	*0.018*	*0.0014*	*0.015*	*0.0091*	*0.049*	*0.010*
Length	389.2	397.2	296.1	432.6	5000	5000
Length error	*9.7*	*8.3*	*4.0*	*4.3*	-	-
Power Law scale	3.54 x10^{-5}	3.20 x10^{-5}	4.17 x10^{-5}	4.14 x10^{-5}	2.92 x10^{-5}	5.65 x10^{-5}
Scale error	*1.03 x10^{-5}*	*9.75 x10^{-7}*	*9.98 x10^{-7}*	*8.93 x10^{-7}*	*7.94 x10^{-7}*	*1.31 x10^{-6}*
Power Law	2.42	2.46	2.42	2.41	2.61	2.42
Power Law error	*1.03 x10^{-6}*	*0.0056*	*0.0044*	*0.0041*	*0.0050*	*0.0042*
Reduced χ^2	**12.7**	**11.5**	**9.63**	**13.6**	**18.3**	**22.5**

Figure 4.20. The SANS data collected (black) and fits (red) from (i) control, (ii) cross-linking pre-gelation and (iii) cross-linking post-gelation samples of 2NapFFK at concentrations of (a) 5 mg/mL and (b) 10 mg/mL. The data were fit to the range of a standard cylinder model combined with a power law. (c) Table summarising the parameters obtained from fitting.

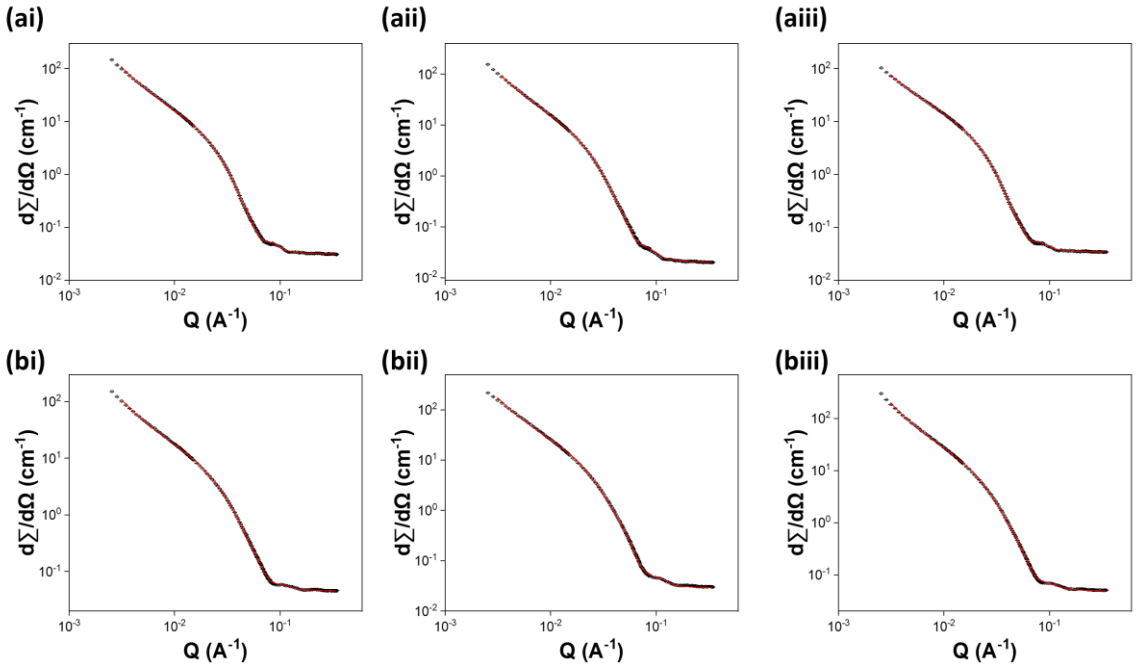

(c)

Sample	2NapKFF 5 mg/mL control	2NapKFF 5 mg/mL pre	2NapKFF 5 mg/mL post	2NapKFF 10 mg/mL control	2NapKFF 10 mg/mL pre	2NapKFF 10 mg/mL post
Cylinder Scale	0.0018	0.0016	0.0010	0.0035	0.0043	0.0047
Scale error	*3.23 x10^{-6}*	*2.94 x10^{-6}*	*1.74 x10^{-6}*	*5.93 x10^{-6}*	*6.23 x10^{-6}*	*6.75 x10^{-6}*
Background	0.031	0.020	0.034	0.045	0.029	0.048
Radius	52.8	51.8	53.8	40.3	42.4	42.9
Radius error	*0.062*	*0.069*	*0.063*	*0.044*	*0.039*	*0.038*
Axis ratio	1.96	2.28	1.98	2.28	2.49	2.37
Axis ratio error	*0.0053*	*0.0077*	*0.0056*	*0.0062*	*0.0067*	*0.0061*
Length	739.3	733.16	5000	5000	5000	5000
Length error	*14.0*	*13.7*	-	-	-	-
Power Law scale	3.73 x10^{-6}	6.77 x10^{-6}	6.41 x10^{-6}	8.99 x10^{-6}	1.05 x10^{-6}	9.25 x10^{-6}
Scale error	*1.52 x10^{-7}*	*1.88 x10^{-7}*	*2.56 x10^{-7}*	*3.71 x10^{-7}*	*2.86 x10^{-7}*	*2.62 x10^{-7}*
Power Law	2.89	2.80	2.63	2.69	2.76	2.81
Power Law error	*0.0079*	*0.0057*	*0.0079*	*0.0076*	*0.0052*	*0.0053*
Reduced χ^2	**8.75**	**8.74**	**3.84**	**10.9**	**21.4**	**26.3**

Figure 4.21. The SANS data collected (black) and fits (red) from (i) control, (ii) cross-linking pre-gelation and (iii) cross-linking post-gelation samples of 2NapKFF at concentrations of (a) 5 mg/mL and (b) 10 mg/mL. The data were fit to the range of a standard cylinder model combined with a power law. (c) Table summarising the parameters obtained from fitting.

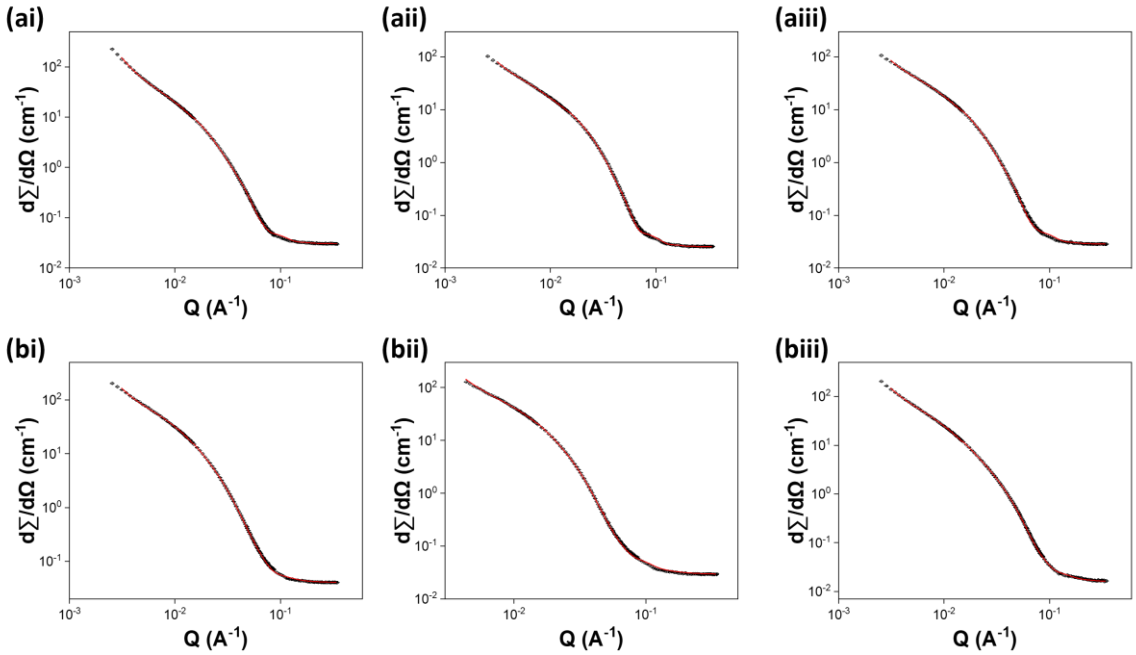

(c)

Sample	2NapFF 5 mg/mL control	2NapFF 5 mg/mL pre	2NapFF 5 mg/mL post	2NapFF 10 mg/mL control	2NapFF 10 mg/mL pre	2NapFF 10 mg/mL post
Cylinder Scale	0.0028	0.0027	0.0028	0.00046	0.00041	0.00068
Scale error	5.62 x10^{-6}	4.48 x10^{-6}	4.56 x10^{-6}	4.91 x10^{-6}	4.96 x10^{-6}	7.81 x10^{-6}
Background	0.030	0.025	0.028	0.040	0.029	0.016
Radius	45.1	48.9	46.9	36.7	46.0	31.1
Radius error	*0.055*	*0.055*	*0.056*	*0.069*	*0.060*	*0.078*
Axis ratio	2.83	2.20	2.60	2.22	1.85	1.95
Axis ratio error	*0.010*	*0.0061*	*0.0084*	*0.0079*	*0.0055*	*0.0080*
Kuhn length	-	-	-	17.82	10.13	23.44
Kuhn length error	-	-	-	*0.23*	*0.16*	*0.34*
Length	542.1	670.7	606.1	5000	5000	5000
Length error	*5.50*	*9.31*	*6.71*	-	-	-
Power Law scale	5.91 x10^{-6}	2.30 x10^{-6}	1.14 x10^{-6}	3.15 x10^{-6}	2.51 x10^{-5}	3.36 x10^{-5}
Scale error	*1.81 x10^{-7}*	*2.05 x10^{-7}*	*3.43 x10^{-7}*	*5.26 x10^{-7}*	*3.65 x10^{-7}*	*6.46 x10^{-7}*
Power Law	2.89	2.79	2.63	2.59	2.76	2.56
Power Law error	*0.0057*	*0.010*	*0.0064*	*0.0039*	*0.0049*	*0.0041*
Reduced χ^2	**15.7**	**10.3**	**13.5**	**7.61**	**11.1**	**5.78**

Figure 4.22. The SANS data collected (black) and fits (red) from (i) control, (ii) cross-linking pre-gelation and (iii) cross-linking post-gelation samples of 2NapFF at concentrations of (a) 5 mg/mL and (b) 10 mg/mL. The data were fit to the range of a standard cylinder model combined with a power law. (c) Table summarising the parameters obtained from fitting.

Despite not resulting in any chemical cross-links, stirring with GTA pre-gelation and addition of GTA to preformed gels caused structural changes to the fibres formed by 2NapFF compared to the controls with no GTA. At both concentrations, the presence of GTA both pre- and post-gelation caused the radii of the fibres to decrease and the axis ratio to increase. These changes were more notable in the pre-gelation samples. This was expected as there is more opportunity for GTA to interact with the fibres in the micellar phase than there is in the gel phase where a dense gel network is present.

The Kuhn length parameter in the flexible elliptical cylinder model allows us to directly compare the effect of GTA on the flexibility of the fibres formed by 2NapFF at 10 mg/mL. Stirring with GTA pre-gelation caused the flexibility of the fibres to increase while addition of GTA to pre-formed gels causes the flexibility of the fibres to decrease.

Despite these changes to the fibres that constitute the 2NapFF gel network, we did not see any considerable changes in the rheological properties of the gels. When compared to 2NapFF, chemical cross-linking in either condition did not cause any considerable changes to the secondary structures formed by 2NapFFK and 2NapKFF gels at 5 mg/mL or 10 mg/mL. Perhaps the ability of these gelators to maintain the integrity of their secondary structures allows them to reap the benefits of cross-linking using GTA. Rather than altering the secondary structure of the 3D gel network, it is more likely that the formation of chemical cross-links changes the way that the fibres in the gel network interact. We attempted to perform confocal microscopy on the gels studied here with and without cross-linking but could not find a suitable dye to allow imaging of the gel network.

4.2.8 Proof of chemical cross-linking by GTA via K residues

To determine whether the observed changes in rheological properties were due to reaction between the primary amine on the K residue and GTA, we performed a control experiment using the gelator 2NapFF (Figure 4.1b) which does not contain a K residue. The control was performed at a concentration of 5 mg/mL as this is the concentration at which the greatest changes in rheology were observed for the other systems. We tried reacting a 5 mg/mL suspension of 2NapFF with 1 molar equivalent of GTA at pH 11.7. No colour change was observed (Figure 4.23). It was therefore concluded that GTA is reacting with the amine group in the K-containing gelators, and this reaction causes the colour change from white to

pink in the pre-gelation samples and white to yellow in post-gelation samples. Previous work has shown similar colour changes on imine bond formation.[3, 81]

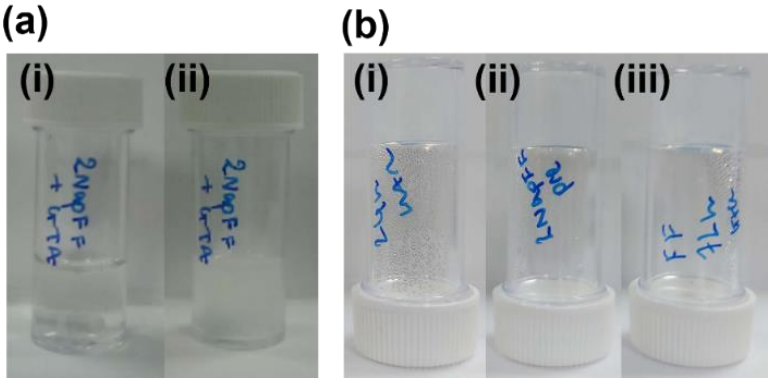

Figure 4.23. Photographs of (a) suspensions of 2NapFF (5 mg/mL) at pH 11.7 (i) before and (ii) after stirring with GTA for 24 hours, and (b) gels formed from 2NapFF (5 mg/mL): (i) control (no GTA), (ii) stirred with GTA for 24 hours pre-gelation (iii) GTA added post-gelation and left to react for 72 hours. All sample volumes are 2 mL, prepared in 7 mL Sterilin vials.

Figure 4.24 shows that the 2NapFF control and post-gelation samples were all almost identical in terms of rheology. Therefore, GTA does not alter the properties of gels formed from 2NapFF when added post-gelation. The pre-gelation samples showed a slight increase in stiffness (G′). However, the G″ of these samples was significantly increased, suggesting lower elasticity than the gels formed without GTA. There is also not an order of magnitude between G′ and G″, showing these samples were not "true gels".[82] Stirring with GTA pre-gelation therefore does impact gel properties, perhaps by interfering with self-assembly after addition of the trigger.[6] As previously mentioned, this may be similar to previous observations by the group of gels containing dextran.[83] The G″ of the gels containing dextran also increased, showing decreased elasticity, without any loss of gel strength. No increase in the cross-over point or length of the LVR of the 2NapFF gels was observed, showing that the increase in these rheological properties in the K-containing gelators is due to chemical cross-linking with GTA.

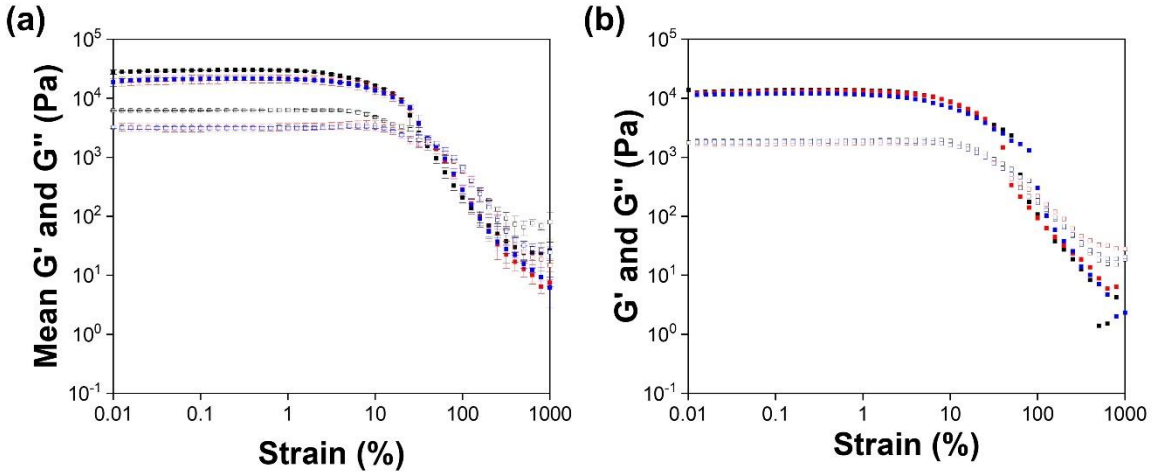

Figure 4.24: Strain sweeps of samples of 2NapFF (5 mg/mL) in (a) H_2O and (b) D_2O with GTA added pre-gelation (black), GTA added post-gelation and left to react for 72 hours (blue), control gels with no GTA (red). Mean G′ (filled squares) and G″ (hollow squares) for 2NapFF (5 mg/mL) were calculated from the average of three samples. Error bars show the standard deviation between samples. The strain sweeps in D_2O are also shown since SANS experiments were performed using 2NapFF as a control.

We also reacted a 2NapFFK suspension at pH 11.7 previously stirred with GTA for 24 hours and 2NapFFK gels exposed to GTA pre- and post-gelation with the reducing agent $NaBH_4$. If cross-linking had indeed occurred via imine bond formation, reaction with $NaBH_4$ would result in reduction of the imine bonds and thereby loss of colour. Khalily *et al*. showed that replacement of the dynamic cross-links provided by the imine bonds with purely covalent bonds resulted in collapse of the gels as the cross-links no longer allowed for the reversibility of the gel network.[13] Our gels showed the same behaviour and broke up after reacting with $NaBH_4$ for several hours. Loss of colour was also observed in both samples (Figure 4.25), showing reduction of any imine bonds, and further confirming that cross-linking via imine bond formation had occurred.

Finally, we performed ^1H NMR spectroscopy on samples of each K-containing gelator with and without stirring with GTA for 24 hours. The GTA samples all showed a distinct imine peak between 8.0 and 9.5 ppm (Figure 4.26), further confirming that cross-linking is indeed taking place via imine formation. These data confirm that the changes in mechanical properties observed in 2NapFFK and 2NapKFF is due to cross-linking between neighbouring K residues via GTA molecules.

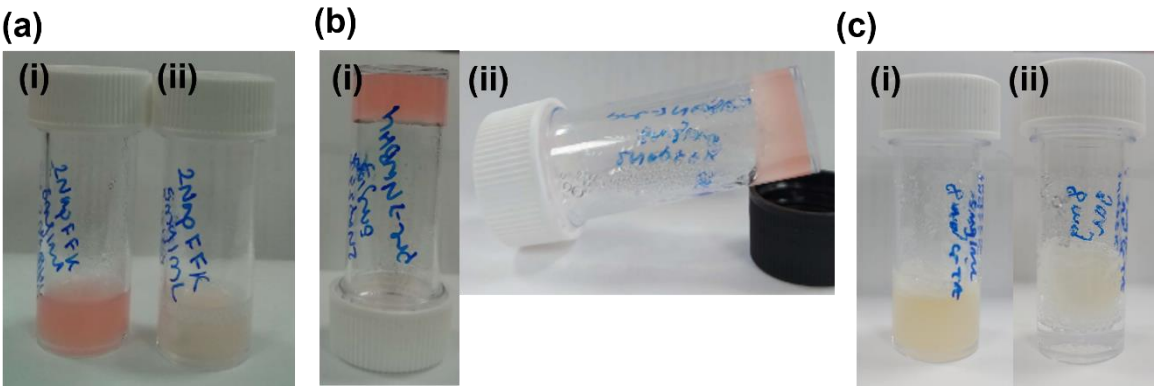

Figure 4.25. Photographs of 2NapFFK (5 mg/mL) (a) in the micellar phase at pH 11.7 (i) after stirring with GTA for 24 hours, (ii) after stirring with GTA for 24 hours followed by stirring with $NaBH_4$ for 16 hours, (bi) as a gel exposed to GTA pre-gelation, (ii) the same gel after addition of solid $NaBH_4$ to the top of the gel, (ci) as a gel exposed to GTA post-gelation and (ii) the same gel after addition of solid $NaBH_4$ to the top of the gel.

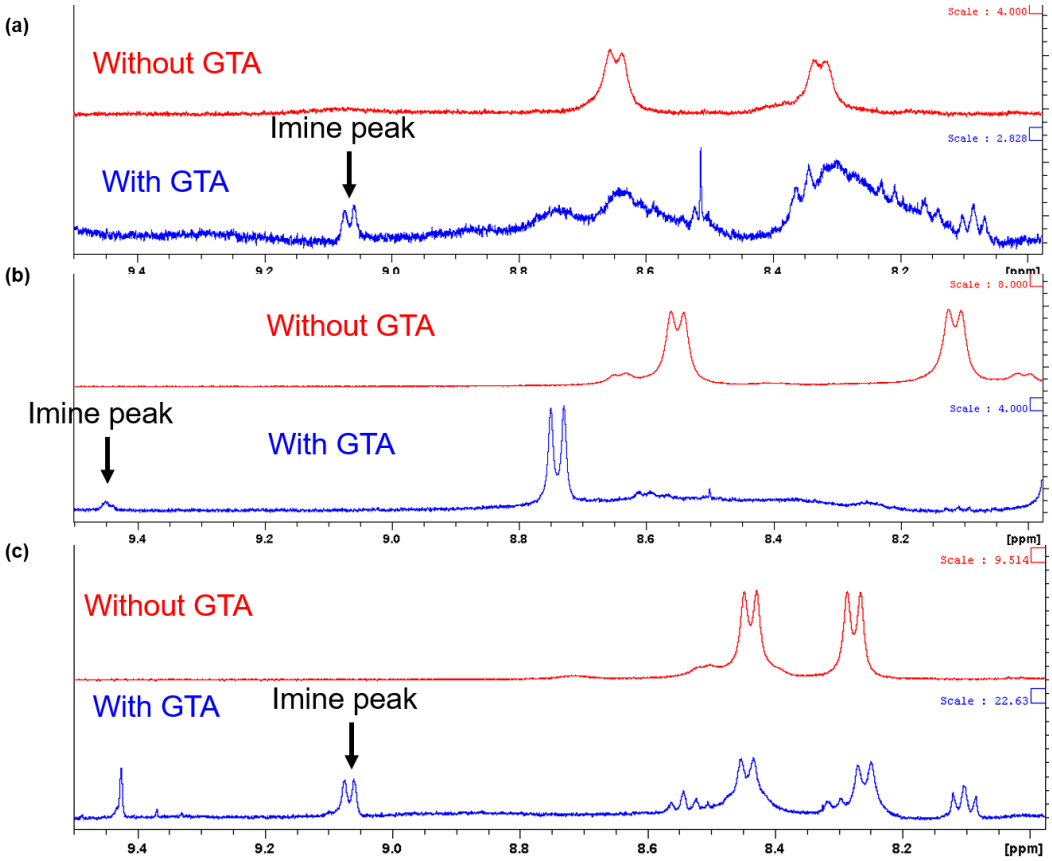

Figure 4.26. Expansion of ^1H NMR spectra of samples of (a) 2NapFFK, (b) 2NapKFF and (c) 2NapFKF without GTA (red) and after stirring with GTA at pH 11.7 for 24 hours (blue). The samples were prepared as aqueous suspensions at pH 11.7 then freeze-dried. $DMSO_{d6}$ was used as the solvent for NMR spectroscopy. The NMR spectra of the cross-linked samples clearly show the presence of an imine peak, confirming cross-linking is taking place via imine formation between K residues.

4.2.9 The effect of chemical cross-linking on the mechanical properties of cross-linking in Ca-triggered gels

Shear-thinning behaviour in viscosity data shows 2NapKFF and 2NapFFK both form worm-like micelles at high pH (Figure 4.10). It was therefore expected that these gelators would be able to form gels on addition of Ca^{2+} salts, in line with previous work by the Adams' group.[33, 65] Gelation induced by addition of divalent metal ions results in increased alignment of the fibres present in the gel network via the formation of salt bridges between carboxylate groups at the *C*-termini of the peptides. It was therefore hypothesised that the presence of these salt bridges would facilitate the formation of chemical bonds during cross-linking with GTA, as previously discussed (Figure 4.4).

Viscosity measurements were performed on suspensions of 2NapFFK and 2NapKFF at high pH following stirring with GTA for 24 hours showed reduction in viscosity and shear-thinning behaviour (Figure 4.10). We therefore suspected that the presence of GTA in solution at high pH was disrupting the formation worm-like micelles at high pH. Previous work has shown that the presence of additives, such as dextran (which is highly water soluble, like GTA), can interfere with self-assembly, resulting in formation of thinner fibres at high pH. [83] The authors suggest that the presence of dextran inhibits diffusion of gelator molecules and self-assembled fibres. This reduces lateral association and thereby reduces thickening of the fibres in the gel network.[83] It was therefore expected that Ca-triggered gels prepared from samples cross-linked pre-gelation would be mechanically weaker than those cross-linked post-gelation.

Suspensions of each gelator were prepared at high pH at a concentration of 5 mg/mL by addition of 2 molar equivalents of NaOH (0.1 M aqueous solution) in deionised water, as previously described. These suspensions were adjusted to a pH of ~11.7 by addition of small aliquots of HCl (1 M, aqueous solution) or NaOH (1 M, aqueous solution).

To prepare the pre-gelation samples, 2 mL of these suspensions was stirred with 1 molar equivalent of GTA (50 % aqueous solution) for 24 hours before triggering gelation. Gels were triggered by addition of 2 molar equivalents of $CaCl_2$ (200 mg/mL aqueous solution) on top of 2 mL of gelator suspension at high pH. The samples were left undisturbed at room temperature for 24 hours to ensure complete gel formation before rheology measurements.

1 molar equivalent of GTA was added to the top of the post-gelation gels and these were left for a further 72 hours to react before rheology measurements.

Gels were formed in all conditions (Figure 4.27). We used highly concentrated $CaCl_2$ solution to reduce the volume of salt solution required and thereby minimise changes to gelator concentration. $CaCl_2$ was added as a solution rather than as a solid because Chen *et al*. showed addition of salts as a solution produces more homogenous gels.[33] Divalent ions produce stronger gels than monovalent ions. [33] Within the chloride salts, the G′ values of the gels follow the Hofmeister series, with Ca^{2+} ions giving gels with the highest moduli.[33]

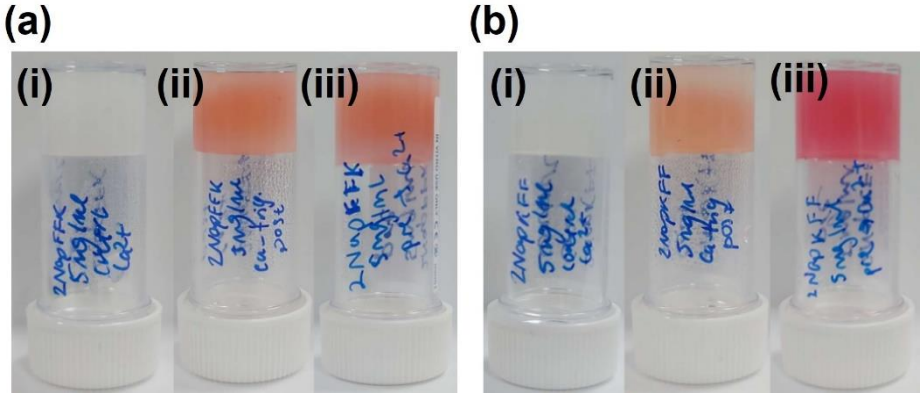

Figure 4.27. Gels formed from the gelators (a) 2NapFFK (5 mg/mL) and (b) 2NapKFF (5 mg/mL) using 2 molar equivalents of $CaCl_2$ (200 mg/mL aqueous solution) as a trigger (i) with no GTA (control), (ii) with GTA added post-gelation and (iii) stirred with GTA for 24 hours pre-gelation.

For gels formed by reduction in pH using GdL, the post-gelation samples were yellow while the pre-gelation samples were similar to the pink colour observed in Figure 4.27aii, aiii and bii. This confirms that the different colours observed in the GdL-triggered gels are due to the pH at which the GTA cross-linking reaction is taking place. Observation of the same colour change pre- and post-gelation at high pH confirms that cross-linking can take place in both sol and gel states. The ability of the pre-gelation samples to form gels suggest the worm-like micelles persist at high pH after stirring with GTA for 24 hours. Alternatively, the structures present may be able to rearrange into worm-like micelles with the ability to be cross-linked by Ca^{2+} ions.

The absence of colour change at the bottom of the vial suggests that GTA was unable to diffuse all the way through the post-gelation sample for 2NapKFF (Figure 4.27bii). This suggests that 2NapKFF forms a denser network than 2NapFFK, making the cross-linking reaction more diffusion limited. This may also affect reproducibility of samples. Previous

work in the Adams group has shown that data collecting using the vane geometry is dominated by the bottom layer of the sample.[68] Since the uncross-linked bottom layer is likely to be weaker than the rest of the sample, the rheological properties of the 2NapKFF gels cross-linked post-gelation may be even greater than the values recorded here. It may therefore be interesting to repeat these measurements using a parallel plate geometry in the future.

Results from rheology experiments show true gels were formed in each case (Figure 4.28).[75] The pH of each of the samples was measured after rheology experiments. A slight reduction in pH was observed following addition of $CaCl_2$, similar to that observed by Chen *et al.*[84] However, the reduction in pH was not sufficient to have caused the changes observed in the rheology measurements.

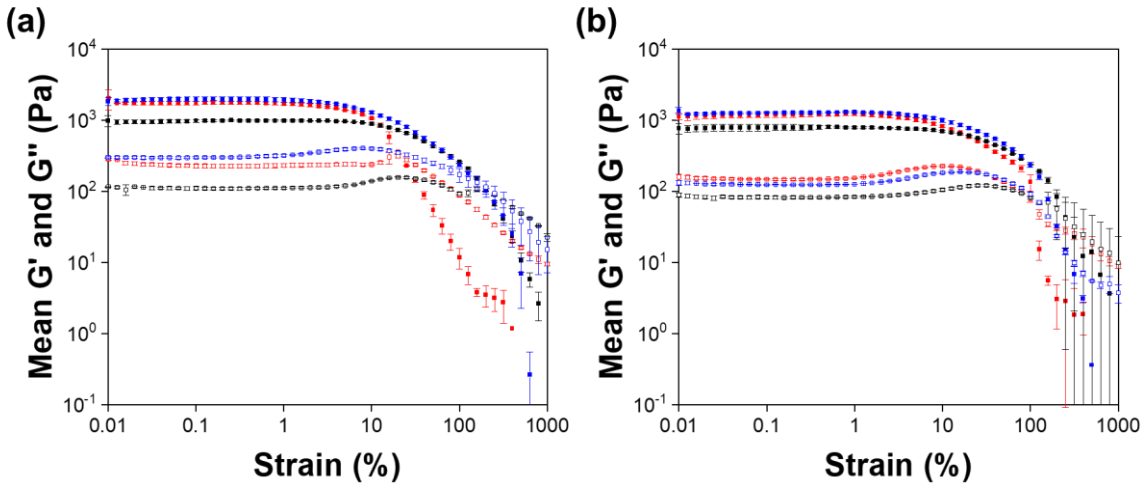

Figure 4.28. Strain sweeps from rheology measurements performed on gels formed from (a) 2NapFFK and (b) 2NapKFF at concentrations of 5 mg/mL using $CaCl_2$ as a trigger. Cross-linking was performed pre-gelation (black) and post-gelation (blue). The control with no cross-linking is shown in red. Mean G′ (filled symbols) and G″ (empty symbols) were calculated from three samples. The error bars show the standard deviation between the three samples.

Figure 4.28 shows that chemical cross-linking with GTA of the Ca-triggered gels post-gelation (blue) did not increase gel stiffness compared to the control gels, without chemical cross-linking (red). However, the LVR, and therefore the gels resistance to strain was increased to higher strain values than observed in the GdL-triggered gels. We expected to see an enhancement in the mechanical properties of post-gelation samples as salt bridges will already be present before addition of the cross-linking agent. The increased alignment

of the fibres can then facilitate the formation of chemical cross-links, making cross-linking more efficient and thereby having a greater effect on rheological properties than on gels prepared using a GdL trigger in the absence of Ca^{2+} ions. Such facilitation is not observed in the pre-gelation samples as most of the chemical cross-linking will already have occurred before formation of salt bridges on addition of $CaCl_2$. The pre-gelation samples (black) showed considerably decreased stiffness and increased resistance to strain, similar to the behaviour observed in the GdL-triggered gels.

The stiffness of the control gels formed from 2NapFFK increased when using $CaCl_2$ as a trigger compared to using GdL. The properties of the 2NapKFF control gels were similar using both $CaCl_2$ and GdL triggers. It is worth noting that the LVR appears to be longer in the Ca-triggered gels for both pre- and post-gelation samples compared to the GdL-triggered gels. This suggests the presence of physical cross-links in addition to chemical cross-links is further enhancing the strength of the gels. This provides a further level of control over gel properties, as well as increasing the range of pH values at which gels can be formed from these gelators, increasing their utility in many applications.

4.3 Conclusions

GTA clearly has a significant effect on the mechanical properties of the gels studied here, providing a simple strategy for tuning both strength and stiffness of peptide-based gelators. The position of the K residue in the gelator not only affects gel properties, but also how the gelator interacts with GTA. The ability to achieve different degrees of change in mechanical properties depending on gelator concentration and whether the gelators are exposed to GTA before or after gelation provides a further level of control. Such control is essential for fine-tuning gels for specific applications and increasing the potential uses of a single gelator. Expansion of known gelators is an attractive strategy due to the challenges associated with designing new gelators.[15] We expect to see similar results with other peptide-based gelators by simply incorporating a K residue into the peptide chain and performing cross-linking with GTA or a similar cross-linking agent.

Preparation of gels using $CaCl_2$ as a trigger instead of GdL allows access to the gel state at a wide range of pH values. This makes these gels appealing for applications that require specific applications e.g., cell and tissue culture engineering. pK_a titrations suggest each

gelator has several apparent pK_a values, meaning that different structures are being formed within different pH ranges. As long as the structures formed are long and anisotropic, divalent cations can be used as a trigger for gelation.[65] The pH (and thereby the type of structures constituting the gel network) will change the gel properties. This therefore provides a further opportunity for tuning gel properties via pH of gel formation and by extension the pH of cross-linking. This work greatly expands the choice of tools available for optimising the properties of peptide-based hydrogels for specific applications and circumvents the need to design entirely new gelators from scratch.

4.4 References

1. D. J. Adams, M. F. Butler, W. J. Frith, M. Kirkland, L. Mullen and P. Sanderson, *Soft Matter*, 2009, **5**, 1856-1862.
2. M. A. Greenfield, J. R. Hoffman, M. O. de la Cruz and S. I. Stupp, *Langmuir*, 2010, **26**, 3641-3647.
3. L. Aulisa, H. Dong and J. D. Hartgerink, *Biomacromolecules*, 2009, **10**, 2694-2698.
4. R. Laishram, S. Sarkar, I. Seth, N. Khatun, V. K. Aswal, U. Maitra and S. J. George, *J. Am. Chem. Soc.*, 2022, **144**, 11306-11315.
5. M. B. Taraban, Y. Feng, B. Hammouda, L. L. Hyland and Y. B. Yu, *Chem. Mater.*, 2012, **24**, 2299-2310.
6. P. R. A. Chivers and D. K. Smith, *Chem. Sci.*, 2017, **8**, 7218-7227.
7. D. J. Cornwell, B. O. Okesola and D. K. Smith, *Soft Matter*, 2013, **9**, 8730-8736.
8. J. Wang, Z. Wang, J. Gao, L. Wang, Z. Yang, D. Kong and Z. Yang, *J. Mater. Chem.*, 2009, **19**, 7892-7896.
9. J. P. Jung, J. L. Jones, S. A. Cronier and J. H. Collier, *Biomater*, 2008, **29**, 2143-2151.
10. W. Y. Seow and C. A. E. Hauser, *Adv. Healthc. Mater.*, 2013, **2**, 1219-1223.
11. Y. Ding, Y. Li, M. Qin, Y. Cao and W. Wang, *Langmuir*, 2013, **29**, 13299-13306.
12. Y. Li, Y. Ding, M. Qin, Y. Cao and W. Wang, *Chem. Comm.*, 2013, **49**, 8653-8655.
13. M. A. Khalily, M. Goktas and M. O. Guler, *Org. Biomol. Chem.*, 2015, **13**, 1983-1987.
14. L. Chronopoulou, Y. Toumia, B. Cerroni, D. Pandolfi, G. Paradossi and C. Palocci, *New Biotechnol.*, 2017, **37**, 138-143.

15. G. Fichman and E. Gazit, *Acta Biomater.*, 2014, **10**, 1671-1682.
16. A. N. Rissanou, E. Georgilis, E. Kasotakis, A. Mitraki and V. Harmandaris, *J. Phys. Chem. B*, 2013, **117**, 3962-3975.
17. S. Fleming, P. W. J. M. Frederix, I. R. Sasselli, N. T. Hunt, R. V. Ulijn and T. Tuttle, *Langmuir*, 2013, **29**, 9510-9515.
18. C. Yuan, W. Ji, R. Xing, J. Li, E. Gazit and X. Yan, *Nat. Rev. Chem.*, 2019, **3**, 567-588.
19. J. Li, R. Xing, S. Bai and X. Yan, *Soft Matter*, 2019, **15**, 1704-1715.
20. K. Nagy-Smith, E. Moore, J. Schneider and R. Tycko, *Proc. Natl. Acad. Sci USA*, 2015, **112**, 9816-9821.
21. E. Khor, *Biomater.*, 1997, **18**, 95-105.
22. J. H. Bowes and C. W. Cater, *Biochim. Biophys. Acta*, 1968, **168**, 341-352.
23. K. Okuda, I. Urabe, Y. Yamada and H. Okada, *J. Ferment. Bioeng.*, 1991, **71**, 100-105.
24. M. E. Belowich and J. F. Stoddart, *Chem.Soc. Rev.*, 2012, **41**, 2003-2024.
25. S. Debnath, S. Roy, Y. M. Abul-Haija, P. W. J. M. Frederix, S. M. Ramalhete, A. R. Hirst, N. Javid, N. T. Hunt, S. M. Kelly, J. Angulo, Y. Z. Khimyak and R. V. Ulijn, *Chem. Eur. J.*, 2019, **25**, 7881-7887.
26. I. Migneault, C. Dartiguenave, M. J. Bertrand and K. C. Waldron, *Biotechniques*, 2004, **37**, 798-802.
27. Y. Wine, N. Cohen-Hadar, A. Freeman and F. Frolow, *Biotechnol. Bioeng.*, 2007, **98**, 711-718.
28. S. Farris, J. Song and Q. Huang, *J. Agric. Food Chem.*, 2010, **58**, 998-1003.
29. E. R. Draper, T. O. McDonald and D. J. Adams, *Chem. Comm.*, 2015, **51**, 12827-12830.
30. R. G. Weiss, *J. Am. Chem. Soc.*, 2014, **136**, 7519-7530.
31. J. Raeburn, A. Z. Cardoso and D. J. Adams, *Chem. Soc. Rev.*, 2013, **42**, 5143-5156.
32. C. Colquhoun, E. R. Draper, R. Schweins, M. Marcello, D. Vadukul, L. C. Serpell and D. J. Adams, *Soft Matter*, 2017, **13**, 1914-1919.
33. L. Chen, G. Pont, K. Morris, G. Lotze, A. Squires, L. C. Serpell and D. J. Adams, *Chem. Comm.*, 2011, **47**, 12071-12073.
34. S. Roy, N. Javid, P. W. J. M. Frederix, D. A. Lamprou, A. J. Urquhart, N. T. Hunt, P. J. Halling and R. V. Ulijn, *Chem. Eur. J.*, 2012, **18**, 11723-11731.

35. A. A. Albadr, S. M. Coulter, S. L. Porter, R. R. S. Thakur and G. Laverty, *Gels*, 2018, **4**, 48.
36. A. P. McCloskey, M. Lee, J. Megaw, J. McEvoy, S. M. Coulter, S. Pentlavalli and G. Laverty, *ACS Omega*, 2019, **4**, 2584-2589.
37. G. Laverty, A. P. McCloskey, B. F. Gilmore, D. S. Jones, J. Zhou and B. Xu, *Biomacromolecules.*, 2014, **15**, 3429-3439.
38. C. Tang, A. M. Smith, R. F. Collins, R. V. Ulijn and A. Saiani, *Langmuir*, 2009, **25**, 9447-9453.
39. L. Chen, K. Morris, A. Laybourn, D. Elias, M. R. Hicks, A. Rodger, L. Serpell and D. J. Adams, *Langmuir*, 2010, **26**, 5232-5242.
40. K. McAulay, B. Dietrich, H. Su, M. T. Scott, S. Rogers, Y. K. Al-Hilaly, H. Cui, L. C. Serpell, A. M. Seddon, E. R. Draper and D. J. Adams, *Chem. Sci.*, 2019, **10**, 7801-7806.
41. G. F. Chimonides, A. A. Sohdi, M. R. Khaleghi, C. R. Hurley, D. J. Adams and P. D. Topham, *J. Polym. Sci Part A Polym. Chem.*, 2013, **51**, 4853-4859.
42. N. Tzokova, C. M. Fernyhouph, P. D. Topham, N. Sandon, D. J. Adams, M. F. Butler, S. P. Armes and A. J. Ryan, *Langmuir*, 2009, **25**, 2479-2485.
43. D. J. Adams, D. Atkins, A. I. Cooper, S. Furzeland, A. Trewin and I. Young, *Biomacromolecules*, 2008, **9**, 2997-3003.
44. R. P. Jain, B. K. Albrecht, D. E. DeMong and R. M. Williams, *Org. Lett.*, 2001, **3**, 4287-4289.
45. C. R. Woods, N. Faucher, B. Eschgfaller, K. W. Bair and D. L. Boger, *Bioorg. Med. Chem. Lett.*, 2002, **12**, 2647-2650.
46. K. Hattori, H. Sajiki and K. Hirota, *Tetrahedron*, 2000, **56**, 8433-8441.
47. A. Kulkarni, W. Zhou and B. Toeroek, *Org. Lett.*, 2011, **13**, 5124-5127.
48. P. R. Sultane, T. B. Mete and R. G. Bhat, *Tetrahedron Lett.*, 2015, **56**, 2067-2070.
49. V. R. Fernandes, A. M. F. R. Pinto and C. M. Rangel, *Int. J. Hydrog. Energy*, 2010, **35**, 9862-9868.
50. S. R. Angle and D. O. Arnaiz, *Tetrahedron Lett.*, 1989, **30**, 515-518.
51. G. S. Welmaker, J. A. Nelson, J. E. Sabalski, A. L. Sabb, J. R. Potoski, D. Graziano, M. Kagan, J. Coupet, J. Dunlop, H. Mazandarani, S. Rosenzweig-Lipson, S. Sukoff and Y. X. Zhang, *Bioorg. Med. Chem. Lett.*, 2000, **10**, 1991-1994.
52. J. Cluzeau and W. D. Lubell, *Biopolymers*, 2005, **80**, 98-150.

53. R. A. Perkins and R. A. Busch, *Zirconium in the Nuclear Industry: Ninth International Symposium*, 1991, **1132**, 595-611.
54. D. J. Adams and I. Young, *J. Polym. Sci. Part A: Polym. Chem.*, 2008, **46**, 6082-6090.
55. N. Tzokova, C. M. Fernyhough, M. F. Butler, S. P. Armes, A. J. Ryan, P. D. Topham and D. J. Adams, *Langmuir*, 2009, **25**, 11082-11089.
56. D. J. Adams, L. M. Mullen, M. Berta, L. Chen and W. J. Frith, *Soft Matter*, 2010, **6**, 1971-1980.
57. H. Rapaport, H. Grisaru and T. Silberstein, *Adv. Funct. Mater.*, 2008, **18**, 2889-2896.
58. S. Zarzhitsky, H. Edri, Z. Azoulay, I. Cohen, Y. Ventura, A. Gitelman and H. Rapaport, *Biopolymers*, 2013, **100**, 760-772.
59. A. Aggeli, M. Bell, L. M. Carrick, C. W. G. Fishwick, R. Harding, P. J. Mawer, S. E. Radford, A. E. Strong and N. Boden, *J. Am. Chem. Soc.*, 2003, **125**, 9619-9628.
60. M. J. Zhang and H. J. Vogel, *J. Bio. Chem.*, 1993, **268**, 22420-22428.
61. L. Y. Zhu, M. D. Kemple, P. Yuan and F. G. Prendergast, *Biochem.*, 1995, **34**, 13196-13202.
62. D. W. Urry, S. Q. Peng, D. C. Gowda, T. M. Parker and R. D. Harris, *Chem. Phys. Lett.*, 1994, **225**, 97-103.
63. C. Tang, R. V. Ulijn and A. Saiani, *Langmuir*, 2011, **27**, 14438-14449.
64. W. Helen, P. de Leonardis, R. V. Ulijn, J. Gough and N. Tirelli, *Soft Matter*, 2011, **7**, 1732-1740.
65. A. Z. Cardoso, L. E. Mears, B. N. Cattoz, P. C. Griffiths, R. Schweins and D. J. Adams, *Soft Matter*, 2016, **12**, 3612-3621.
66. Z. Chu and Y. Feng, *Chem. Comm.*, 2011, **47**, 7191-7193.
67. A. M. Smith, R. J. Williams, C. Tang, P. Coppo, R. F. Collins, M. L. Turner, A. Saiani and R. V. Ulijn, *Adv. Mater.*, 2008, **20**, 37-41.
68. A. M. Fuentes-Caparros, Z. Canales-Galarza, M. Barrow, B. Dietrich, J. Lauger, M. Nemeth, E. R. Draper and D. J. Adams, *Biomacromolecules*, 2021, **22**, 1625-1638.
69. M. M. Smith and D. K. Smith, *Soft Matter*, 2011, **7**, 4856-4860.
70. N. Reddy, Y. Tan, Y. Li and Y. Yang, *Macromol. Mater. Eng.*, 2008, **293**, 614-620.
71. M. Bertasa, A. Dodero, M. Alloisio, S. Vicini, C. Riedo, A. Sansonetti, D. Scalarone and M. Castellano, *Eur. Polym. J.*, 2020, **123**, 109442.

72. L. Chen, S. Revel, K. Morris, L. C. Serpell and D. J. Adams, *Langmuir*, 2010, **26**, 13466-13471.
73. S. Fleming, S. Debnath, P. W. J. M. Frederix, N. T. Hunt and R. V. Ulijn, *Biomacromolecules*, 2014, **15**, 1171-1184.
74. J. M. Poolman, J. Boekhoven, A. Besselink, A. G. L. Olive, J. H. van Esch and R. Eelkema, *Nat. Protoc.*, 2014, **9**, 977-988.
75. C. Yan and D. J. Pochan, *Chem. Soc. Rev.*, 2010, **39**, 3528-3540.
76. E. R. Draper and D. J. Adams, *Langmuir*, 2019, **35**, 6506-6521.
77. L. L. E. Mears, E. R. Draper, A. M. Castilla, H. Su, Zhuola, B. Dietrich, M. C. Nolan, G. N. Smith, J. Doutch, S. Rogers, R. Akhtar, H. Cui and D. J. Adams, *Biomacromolecules*, 2017, **18**, 3531-3540.
78. V. S. Raghuwanshi and G. Garnier, *Adv. Colloid Interface Sci.*, 2019, **274**, 102044.
79. B. Chu and T. Liu, *J. Nanopart. Res.*, 2000, **2**, 29-41.
80. T. Riley and F. A. Long, *J. Am. Chem. Soc.*, 1962, **84**, 522-526.
81. E. J. Howe, B. O. Okesola and D. K. Smith, *Chem. Comm.*, 2015, **51**, 7451-7454.
82. B. P. Nowak and B. J. Ravoo, *Soft Matter*, 2020, **16**, 7299-7304.
83. L. Chen, S. Revel, K. Morris, D. G. Spiller, L. C. Serpell and D. J. Adams, *Chem. Comm.*, 2010, **46**, 6738-6740.
84. L. Chen, T. O. McDonald and D. J. Adams, *RSC Adv.*, 2013, **3**, 8714-8720.

Chapter 5

Experimental Methods

5.1 Synthesis

Materials.

All chemicals were purchased from Sigma-Aldrich, ThermoFisher Scientific or Fluorochem and used as received. Deionised H_2O was used throughout.

Peptide Coupling.

The compound with a free carboxylic acid group (the acid) was dissolved in $CHCl_3$ (20 mL/1 g of solid) with the addition of N-methyl morpholine (NMM) until a transparent solution was obtained. Isobutyl chloroformate (IBCF, 1.2 equivalents) was added and the solution stirred on ice for 10 minutes. The compound with a free amine group (the amine, 1 molar equivalent) was dissolved separately in $CHCl_3$ (20 mL/1 g of solid) with the addition of NMM (aliquots of 5 equivalents until a transparent solution was obtained). Following activation of the acid, the amine solution was added, and the reaction mixture stirred on ice overnight. The following day, the reaction mixture was washed sequentially with HCl (1 M, 1.25 x the volume of the reaction mixture), H_2O (1.25 x the volume of the reaction mixture) and saturated brine (1.25 x the volume of the reaction mixture). The organic phase was dried with $MgSO_4$, filtered and the solvent removed in vacuo to give the product. Where required, the product was purified by column chromatography in a 2:8, 1:9 or 1:99 EtOAc:DCM solvent system, depending on separation from impurities on a think later chromatography (TLC) plate.

Boc Deprotection.

The Boc-protected peptide was dissolved in $CHCl_3$ (10 mL/1 g of solid) and trifluoroacetic acid (TFA) added such that the ratio of TFA:$CHCl_3$ was 1:2. The reaction was stirred overnight at room temperature before being poured into a large excess of Et_2O and stirred vigorously overnight. The resulting precipitate was filtered under vacuum to give the product as a solid. The product was dried further by azeotropic distillation with CH_3CN. Where required, the product was washed by trituration in Et_2O.

Methyl Ester Deprotection.

The methyl ester-protected peptide was dissolved in tetrahydrofuran (THF, 10 mL/1 g of solid). LiOH (5 molar equivalents) was dissolved separately in H_2O so that the ratio of THF:H_2O was 1:1. The LiOH solution was added to the peptide solution and the reaction

stirred at room temperature. The reaction was monitored by TLC using a suitable solvent system (generally 1:9 EtOAc:DCM). After the reaction had gone to completion, the reaction mixture was poured into a large excess of 1 M HCl and stirred vigorously overnight. The resulting precipitate was filtered under vacuum, washed with plentiful deionised H_2O and dried by azeotropic distillation with CH_3CN to give the product as a solid. Where required, the product was washed by trituration in Et_2O.

5.2 Sample preparation

Preparation of micellar suspensions.

Chapter 2: Micellar suspensions were prepared by suspending the individual components in H_2O with the addition of 1 molar equivalent of NaOH (0.1 M). The suspensions were stirred overnight to ensure complete dispersion of the molecules. Multicomponent suspensions were prepared by first preparing separate stock suspensions of the two components at twice the desired concentration before adjusting the pH to 10.5 by addition of 1 M NaOH and mixing the stock suspensions together at a 1:1 ratio. 2NapFF 2.5 mg/mL suspensions were prepared by first preparing a 2NapFF stock suspension at a concentration of 5 mg/mL and diluting the solution with deionised H_2O. The H_2O used for dilution was first adjusted to pH 10.5 using 1 M NaOH. Diluted and multicomponent suspensions were stirred for 2 hours before use to ensure homogenous mixing. All solutions were adjusted to pH 10.5 again immediately before use.

Chapter 3: A stock suspension (10 mg/mL) of each component was prepared in H_2O with the addition of 1 molar equivalent of NaOH (0.1 M). The suspensions were stirred overnight to ensure complete dispersion of the molecules. The pH of each suspension was adjusted to 10.5 before mixing components at the desired ratios. Multicomponent systems were stirred for 2 hours to ensure thorough mixing of components. The pH of all suspensions was adjusted to 10.5 again before analysis or gel formation. Where possible, the same stock solution of each component was used for all data that would be directly compared e.g., the same stock solutions were used for all viscosity measurements.

Chapter 4: Micellar suspensions (10 mg/mL and 5 mg/mL) were prepared by suspending the gelator in deionised H_2O and adding 2 molar equivalents of NaOH (0.1 M) to account for the amine group on the K residues. The solutions were stirred for a minimum of 24 hours

to ensure complete dissolution of the gelator. The pH of each solution was adjusted, if needed, to pH 11.7 ± 0.1 with either NaOH (1 M) or HCl (1 M).

NaOH (1 M) was used for pH adjustment to reduce the volume being added to the solutions and thereby minimise any changes to the concentrations of the solutions. Suspensions prepared in D_2O were prepared using the same methods with D_2O used in place of H_2O and NaOD of the appropriate concentration used in place of NaOH. The pH was adjusted using DCl (1 M) or NaOD (1 M).

Preparation of gels by reduction in pH using glucono-δ-lactone (GdL).

Micellar suspensions were prepared as previously described. Gel samples were prepared in 7 mL Sterilin vials by addition of 2 mL of the required suspension (pH 10.5 or pH 11.7 in Chapter 4) to 16 mg of solid GdL for 5 mg/mL solutions and 32 mg of solid GdL for 10 mg/mL solutions. The vials were swirled briefly by hand to ensure complete dissolution of GdL then left to stand overnight undisturbed.

Preparation of gels by addition of Ca^{2+} ions.

Micellar suspensions were prepared as previously described. 2 mL of the desired suspension (pH 10.5 or pH 11.7 in Chapter 4) was transferred to a 7 mL Sterilin vial. 2 molar equivalents (according to the total mass of peptide) of $CaCl_2$ (200 mg/mL aqueous solution) were pipetted on top of the centre of the suspension in the Sterilin vial. The samples were left to rest for 3 days at room temperature to allow formation of stable and reproducible gels before rheological measurements were performed.

Preparation of supramolecular noodles.

Noodles could be prepared by extrusion of the appropriate micellar suspension from a pipette directly into a static $CaCl_2$ solution (0.5 M). Longer, more homogenous noodles were formed using a combined syringe pump-spin coater method described in other work from our group:[1] an Alaris Carefusion syringe pump was used to control the flow rate of the peptide solutions. A 10 mL syringe was attached via a Luer lock fitting to 20 cm rubber tubing with a flat-headed needle (413 μm inner diameter) at the end. To load the syringe pump, the syringe was filled directly with gelator solution. The tubing (already connected to the needle) was attached to the syringe and the pre-gel solution pumped manually until the tubing was full. The tubing and needle were held vertically to prevent the formation of air bubbles. The syringe was then loaded into the syringe pump. The rubber tubing enabled movement of the

needle to allow positioning into the trigger medium ($CaCl_2$, 0.5 M aqueous solution). The flow rate on the syringe pump was set to 100 mL/hr. The spin-coater was set to spin at a rate of 100 rpm. A plastic Petri dish (900 mm diameter) containing $CaCl_2$ solution (0.5 M, 20 mL) was placed on the center of the spin coater plate. The needle connected to the syringe pump was held vertically into the petri dish. The length of the noodles could be altered by changing the length of time the needle was held in the $CaCl_2$ solution: longer time equates to longer noodles. Noodles prepared by this method were used for nanoindentation to increase homogeneity and thereby increase reproducibility of the mechanical properties along the length of the noodles.

Preparation of composite gel noodles.

Composite gel noodles were prepared by first preparing noodles from the multicomponent 2NapLG 2.5 mg/mL:2NapFF 5 mg/mL system as described above. The noodles were then transferred to a Petri dish of deionised H_2O and left for 3 days to allow sufficiently large and numerous crystals to form. pH 7-8 was sufficient to consistently observe formation of crystals without compromising the strength of the noodles. Faster and further reduction in pH using 0.1 M HCl or GdL solutions resulted in formation of lower quality crystals and caused the noodles to become too brittle to be transferred onto a glass surface for nanoindentation.

Cross-linking with glutaraldehyde (GTA).

For the post-gelation samples, the gels were prepared as previously described. After allowing gel formation overnight (~ 16 hours) GTA (1 molar equivalent, in the form of 50 % aqueous solution) was pipetted on top of the pre-formed gels. The 24-hour and 72-hours samples were left to sit undisturbed for 24 hours and 72 hours respectively before rheology measurements were performed. For the pre-gelation samples, the gelators were stirred with GTA (1 molar equivalent) at pH 11.7 for 24 hours before gelation was triggered. After sitting overnight (~16 hours), these sample were left to sit undisturbed for a further 24 hours to ensure the samples were the same age as the 24-hour post-gelation and 24-hour control samples.

Reduction with $NaBH_4$.

$NaBH_4$ (2 molar equivalents with respect to GTA) was added as a solid to the selected samples. The high pH sample was stirred for 16 hours while the gel samples were left to sit undisturbed while the reaction was monitored over 24 hours.

5.3 Instruments and procedures

pH measurements and pK_a titrations.

The pH of samples was measured using a FC200 pH probe from Hanna instruments. The pH meter was calibrated using pH 4.01, 7.01 and 10.01 buffer solutions. The probe was rinsed with deionised H_2O between measurements. The pK_a values of single and the multicomponent systems were determined by titration *via* addition of aliquots of 0.1 M HCl solution.

Viscosity measurements.

Viscosity measurements were performed using an Anton Paar Physica MCR 101 or 301 rheometer using a CP50 cone (cone angle: 0.995 °) and plate. ~1 mL of solution was transferred onto the plate by pouring. Viscosity values were collected at shear rates ranging from 1-100 or 1-1000 s^{-1}. Measurements were performed in each condition in duplicate or triplicate and the average calculated.

Chapter 2: The temperature of the plate was set to 25 °C for the 25 °C samples. For each of the 10 °C samples, the sample was loaded onto the plate at 25 °C. The plate was then cooled to 10 °C at a rate of 0.5 °C/s. The sample was allowed to equilibrate at 10 °C for 5 minutes before the viscosity measurement was carried out with temperature maintained at 10 °C. During the heat-cool cycles, the temperature of the plate was increased or decreased at a rate of 0.5 °C/s. The sample was then held at the temperature at which the next measurement was to be taken for 5 minutes to allow the sample to equilibrate to the new temperature before the viscosity measurement was carried out.

Chapters 3 and 4: All viscosity measurements were performed at a temperature of 25 °C.

Strain, Frequency and Time Sweeps.

All rheological measurements were carried out using an Anton Paar Physica MCR 101 or 301 rheometer at a defined temperature/series of temperatures. Strain, frequency and time sweeps were performed using cup and vane geometry (ST10-4V-8.8/97.5-SN18190) with a gap height of 1.8 mm. Strain sweeps were performed at a frequency of 10 rad/s from 0.01 % to 1000 % strain. Frequency sweeps were performed at 0.1 % strain from 1 rad/s to 100 rad/s frequency. Time sweeps were performed at 0.1 % strain and 10 rad/s frequency. All samples were prepared as previously described in a 2 mL volume in 7 mL Sterilin vials.

Quasi-static nanoindentation experiments.

All nanoindentation measurements were performed and analysed by G. Ciccone (CCM, UK). Nanoindentation measurements were carried out using a nanoindentation device (Chiaro, Optics11, Amsterdam, NL) mounted on top of an inverted microscope (Zeiss Axiovert 200M) equipped with two linear polariser films (Thorlabs, Newton, New Jersey, USA) in cross configuration. Measurements were performed following the standardised protocol described by Ciccone *et al*.[2] using a cantilever with stiffness (k) of 0.5 Nm^{-1} holding a spherical tip of radius (R) of 3 μm.

Each noodle was placed in a petri dish and aligned along the x direction of the microscope stage and stabilised using metal washers placed at either end on the sample. All measurements were carried out at room temperature (~ 23 ℃) in milliQ H_2O to maintain samples' hydration. For each experimental condition, at least 2 noodles were tested by performing a minimum of 2 matrix scans on each sample along its length. Each matrix scan consisted of ~ 20 indentations with spacing between subsequent indentations of 10 μm, or smaller when indentations were performed over a crystal due to its small size. For each indentation the probe moved at a speed of 2 μms^{-1} over a vertical range of 10 μm.

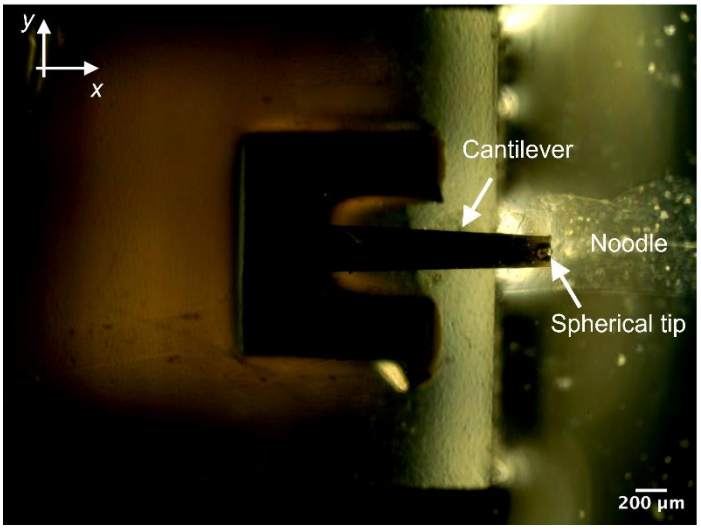

Figure 5.1. Photograph of gel noodle under cross-polarised light with indenter probe. Axes show direction of probe movement.

The forward segment of the collected force-displacement (*F-z*) curves was analysed using a custom open-source software.[2] Briefly, curves were first filtered using a Savitzky Golay filter from the SciPy computing stack[3] with window length of 25 nm and polynomial order of 3. After, the point where the probe came into contact with the sample (z_0, F_0) was identified with the ratio of variance (RoV) algorithm or a thresholding algorithm[4] to convert

(*F*-*z*) curves into force-indentation (*F*-δ) curves. To quantify the elastic properties of the gels, *F*-δ curves were fitted with the Hertz model (Equation 1) up to a maximum indentation of $\delta = 0.1\ R$. The Poisson's ratio (ν) was taken as 0.5 assuming material's incompressibility given the hydrated nature of the samples.

$$F = \frac{4}{3}\frac{E}{(1-\nu^2)}\delta^{\frac{3}{2}}R^{\frac{1}{2}} \quad (2).$$

Alternatively, the elasticity spectra of the data were computed:[2, 5]

$$E(\delta) = \frac{3}{8\sqrt{R}}\frac{1}{\delta}\frac{dF}{d\delta} \quad (3),$$

To quantify the difference between conditions, we extracted two values from each spectrum, E_{avg} and E_{max}, corresponding to the soft and hard component of the spectrum, respectively. The soft component E_{avg} was calculated as the average elasticity in a depth range between 2000 nm and 3000 nm of indentation, where crystals were never found. Instead, the hard component E_{max} was calculated as the average of the values of the elasticity spectrum lying above the 90th percentile.

Circular Dichroism (CD).

CD was measured using a Chirascan VX CD spectrometer (Applied Photophysics Limited, U.K.) using a quartz cell with a 0.01 mm path length and the following parameters: scanning mode, continuous; scanning speed, 120 nm/min and bandwidth, 1 nm. All CD data are presented as ellipticity and recorded in millidegree (mdeg). Absorbance and high tension (HT) spectra were recorded concomitantly with CD spectra. All spectra were recorded in triplicate and averaged with the exception of the temperature-variable CD experiments (Chapter 3). These were recorded as a single measurement on the same sample at each temperature. CD spectra were recorded at intervals of 5 ℃ at temperatures ranging from 25 ℃ to 95 ℃ (the upper limit of the CD spectrometer).

Powder X-ray diffraction (PXRD).

PXRD patterns were collected using a Rigaku MiniFlex 6G equipped with a D/teX Ultra detector, a 6-position (ASC-6) sample changer and Cu sealed tube (Kα1 and Kα2 wavelengths - 1.5406 and 1.5444 Å respectively). Patterns were measured as θ/2θ scans typically over a range of 3>2θ>60°. Data collection and analysis were carried out using Rigaku SmartLab Studio II software (Rigaku Corporation, 2014).

Single crystal X-ray diffraction.

X-ray diffraction patterns were collected on a Malvern Panalytical Empyrean with PIXcel3D-Medipix3 1x1 detector using Cu Kα radiation (wavelength 1.541874 (Å). $C_{20}H_{24}N_2O_5$ M = 372.41, orthorhombic, a = 9.0636 (4), b= 10.2968 (5) , c = 20.5621 (12) Å, U = 1918.98 (17) Å^3, T = 150 K, space group $P2_12_12_1$ (no.19), Z = 4. A colourless plate-like crystal 0.15 × 0.13 × 0.02 mm was used and 13073 reflections measured, 3630 unique (Rint = 0.076), which were used in all calculations. The final w$R(F^2)$ was 0.151 (all data), $R[F^2 > 2s(F^2)]$ = 0.053 (2960 reflections with $I > 2s(I)$).

UV-Vis Spectroscopy.

Solution UV-Vis absorption data were obtained with an Agilent Cary 60 UV-Vis spectrophotometer. The samples were prepared as described above and transferred into a 0.01 mm quartz cuvette.

Optical Microscopy.

Optical microscope images were taken of samples with and without magnetic field using a Nikon Eclipse LV100 microscope at 5x magnification. Images were collected under cross-polarised and non-polarised light. Scale bars were added to images using the software, ImageJ.[6]

Mass spectrometry.

Mass spectrometry was performed using a Bruker MicroTOF mass spectrometer using ESI.

Nuclear magnetic resonance (NMR) spectroscopy.

For characterisation following synthesis: NMR spectroscopy experiments were carried out on a Bruker DPX 400MHz spectrometer at 300 K. All compounds were dissolved in d_6-DMSO.

Chapter 2: NMR spectroscopy experiments were performed by M. Wallace (UEA, UK). Nuclear Overhauser effect (NOE) experiments and ^{1}H experiments were performed on a Bruker 500 MHz spectrometer equipped with a Neo console and Bruker 5 mm SmartProbe^{TM}. Solutions of the gelators were prepared in H_2O, as described above, and transferred to Wilmad 5 mm diameter 528-PP NMR tubes. A separate 2.0 mm outer diameter capillary (Bruker) containing 30 mM 3-(trimethylsilyl)propionic-2,2,3,3-d_4 acid sodium salt (TSP) in D_2O was inserted into the sample in the NMR tube to provide a chemical shift and integral reference (0 ppm). ^{1}H experiments were recorded using the perfect echo WATERGATE sequence of Adams *et al*.[7] incorporating the double echo W5 sequence of Liu *et al*.[8] The delay between successive pulses in the selective pulse train was set at 333 μs, corresponding to 3000 Hz between the null points. Spectra were acquired in 128 scans with a relaxation delay of 5 s and signal acquisition time of 4.2 s. one-dimensional selective NOE experiments were acquired using the Bruker library sequence, selnogp.[9] An 80 ms Gaussian pulse was used to selectively invert the methyl resonance of 2NapLG. Spectra were acquired in 128 scans with a relaxation delay of 2 s and signal acquisition time of 3.3 s. ^{1}H integrals were obtained relative to TSP internal reference.

Chapters 2 and 3: ^{1}H-NMR spectra for kinetics experiments were measured using a Bruker AVIII 500 MHz spectrometer. Samples were run in D_2O/NaOD using an internal capillary standard of 0.1% polydimethylsiloxane (PDMS) in tetrachloroethylene solution a reference. First, the standard was added to a 0.5 mL solution of the chosen system dissolved in d_6-DMSO and a proton spectrum collected to act as the 100 % free molecule to allow calculation of the % free molecule in each spectrum collected during the kinetics experiment as we assume the system is completely dissolved and therefore 100 % unassembled. A proton spectrum of the system in D_2O at pD 10.5 was also collected prior to the addition of the chosen trigger, in this case excess GdL. This spectrum was set as the time zero measurement (t = 0). Next, the trigger was added to the sample. An excess of trigger was added to ensure sufficient trigger could reach the entirety of the sample. The NMR tube was then inserted into the spectrometer. Due to experimental limitation, there was 5 minutes time delay between the addition of the sample to the instrument and the first measurement. Spectra were recorded every 5 minutes until the proton peaks were no longer detectable. This took ~3 hours for most systems. The PDMS reference proton environment was integrated and set to the same value in all the spectra. The protons selected for analysis were then integrated and compared to the integration value for the same proton peaks at t=0. When assembled, the

molecules become NMR invisible. Any remaining intensity accounts for the free molecules that remain unassembled in the sample at a given time. From this, the % free molecule was calculated at each time point using the d_6-DMSO spectrum and a trend plotted against time.

Small Angle Neutron Scattering (SANS).

Solutions were prepared as described above in D_2O using NaOD to adjust the pH. Scattering length density (SLD) values were calculated using the NIST neutron activation and scattering calculator,[10] assuming a density of 1.55 g/cm^3. SLD values used for all systems are shown in Table 5.1. For multicomponent systems, the SLD values were calculated based on the ratio of the two components.

System	SLD (x 10^{-6} Å^{-2})
2NapFF 2.5, 5, 10 mg/mL	2.730
2NapLG 2.5 mg/mL: 2NapFF 2.5 mg/mL	2.527
2NapLG 2.5 mg/mL: 2NapFF 5 mg/mL	2.594
PhOLL 2.5 mg/mL: 2NapFF 2.5 mg/mL	2.226
PhOLL 2.5 mg/mL: 2NapFF 5 mg/mL	2.394
2Nap-OH 2.5 mg/mL: 2NapFF 2.5 mg/mL	2.772
2Nap-OH 2.5 mg/mL: 2NapFF 5 mg/mL	2.758
7MeO2NapFV 10 mg/mL	2.357
7MeO2NapFV 5 mg/mL: 2NapFF 5 mg/mL	2.543
1NapVV 10 mg/mL	2.081
1NapVV 5 mg/mL: 2NapFF 5 mg/mL	2.406
CarbFV 10 mg/mL	2.553
CarbFV 5 mg/mL: 2NapFF 5 mg/mL	2.642
CarbIF 10 mg/mL	2.463
CarbIF 5 mg/mL: 2NapFF 5 mg/mL	2.597
2NapFFK/2NapFKF/2NapKFF	2.176
D_2O (solvent)	6.393

Table 5.1. SLD values used when fitting SANS data for all the systems studied.

Chapter 2: SANS data were collected by R. E. Ginesi (UofG, UK) and L. J. Marshall. Data were fitted by L. J. Marshall. Suspensions were prepared as described above in D_2O and NaOD (0.1 M). SANS measurements were performed using the Larmor instrument (ISIS, Rutherford Appleton Laboratory, Didcot, UK) under experiment RB2210011 using an Anton Paar Physica MCR 502 rheometer equipped with a bespoke titanium Couette geometry and a temperature controller (TC-30). The Couette cell has a gap of 0.5 mm and was set up for the neutron beam to shine in the radial direction. The incident neutron beam was 8 mm in diameter with a wavelength range of 1.75-16.5 Å and a sample-to-detector

distance of 4 m, resulting in an effective range of scattering wave vector, q, of 0.004-0.7 Å^{-1}:

$$q = \frac{4\pi}{\lambda} sin\left(\theta/_2\right) \text{ (4)},$$

where λ is the neutron wavelength and θ is the scattering angle. Raw scattering data are corrected for sample transmission, detector efficiency and solvent scattering[11] using the Mantid software,[12] and then converted to absolute scattering cross section (I(q)/cm^{-1}) using the scattering from a standard sample (a solid blend of hydrogenous and perdeuterated polystyrene) in line with established procedures.[13] Data modelling was performed using the SasView package.[14]

Due to shear alignment in the *y*-plane resulting from loading of the samples into the rheometer, certain samples underwent additional processing prior to fitting. This additional processing was only performed on samples that exhibited shear artefacts (see Figure 5.2 for example). The scattering from -45 to 45° was cut from the two-dimensional scattering pattern and only the scattering from 45 to 135° was used for data modelling. Such analysis has been previously referred to as bow-tie integration.[1]

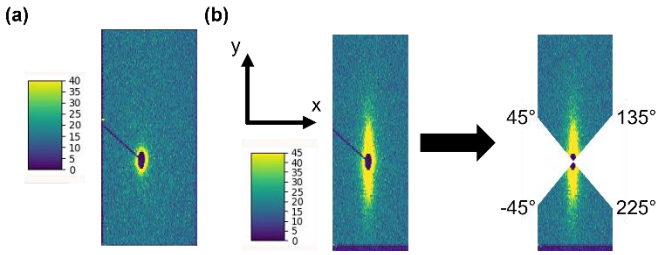

Figure 5.2. (a) Example of two-dimensional scattering pattern from d-2Nap-dd-FF which did not show any shear alignment and therefore was not processed using bowtie method. (b) Example of two-dimensional scattering data from 2NapFF showing alignment along the *y*-axis, resulting in low intensity scattering in the x-direction.

All data sets that exhibited shear alignment were subject to vertical bowtie integration where the weak scattering from between -45° and 45° (and between 135° and 225°) was cut from the two-dimensional scattering pattern (as shown in Figure 5.2) and only scattering from between 45° and 135° (and between 225° and -45°) was used in model fitting. This data was of better quality than the averaged data.

Chapter 3: SANS data were collected by R. E. Ginesi (UofG, UK), E. R. Draper (UofG, UK) and D. J. Adams (UofG, UK). Data were fit by S. Bianco (UofG, UK) and L. J.

Marshall. Suspensions were prepared as described above in D_2O and NaOD (0.1 M). SANS measurements were formed using the SANS2D and ZOOM instrument (ISIS, Rutherford Appleton Laboratory, Didcot, UK) under experiment numbers RB220189 for gels and RB2220215 for solutions, using a wavelength band of 0.9 to 13 Å to access a q range of 0.004 to 0.7 Å-1. Solutions and gels were measured in 2 mm path length UV spectrophotometer grade quartz cuvettes (Hellma). The samples were placed in a temperature-controlled sample rack during the measurements. All data was collected at 25 °C. Gels formed using GdL were prepared in a Sterilin vial and quickly transferred to the cuvettes, before being placed on the rack.

The data was reduced to one-dimensional scattering curves of intensity vs Q. using the facility provided software. The electronic background was subtracted, the full detector images for all data were normalised and scattering from the empty cell was subtracted. The scattering from D2O was also measured and subtracted from the data using the Mantid software package installed inside the ISIS virtual machines, IDAaaS.[12] The instrument-independent data were then fitted to the models discussed in the text using the SasView software package (version 5.0.3).[14] The scattering length density of each material was calculated using the National Institute of Standard and Technology's neutron activation and scattering calculator.[10]

Chapter 4: Due to COVID restrictions, R. Schweins and O. Matsarskaia (ILL, France) carried out the SANS experiments. SANS data were analysed by L. J. Marshall. SANS measurements were performed using the D11 instrument (Institut Laue Langevin, Grenoble, France). A neutron beam, with a fixed wavelength of 6 Å and divergence of $\Delta\lambda/\lambda = 9\%$, allowed measurements over a large range in Q [$Q = 4\pi\sin(\theta/2)/\lambda$] range of 0.002 to 0.3 $Å^{-1}$, by using three sample-detector distances of 1.5 m, 8 m, and 28 m. Solutions and gels were measured in 2 mm path length UV spectrophotometer grade, quartz cuvettes (Hellma). These were placed in a temperature-controlled sample rack during the measurements. Gels formed using GdL were prepared in the cuvettes and then transferred to the rack.

The data were then reduced to one-dimensional scattering curves of intensity vs. Q using the facility provided software. The electronic background was subtracted, the full detector images for all data were normalised and scattering from the empty cell was subtracted. The scattering from D_2O was also measured and subtracted from the data using the Mantid software package.[12] The instrument-independent data were then fitted to the models discussed in the text using the SasView software package version 5.0.3.[14]

5.4 Statistical analysis

Viscosity, rheology and CD spectroscopy data were collected in duplicate or triplicate, as stated in the experimental section. Origin 2020 graphing & analysis software was used to calculate the mean and standard deviation for each data set.

Statistical analysis was performed on data obtained from nanoindentation experiments. For each experimental condition, at least two separate noodles were indented, and successive indentations performed along the length of the sample (the specific number of indentations, n, is given in each figure caption; n> 20 for all experimental conditions). Data are reported as mean ± 95% CI. Normality was evaluated by a D'Agostino & Pearson test, and the appropriate statistical test was then performed to evaluate statistical significance (significance level set at 0.05) as described in each figure caption. No outliers were removed. All statistical analysis was performed in GraphPad Prism 9.

Two-sample T-tests assuming unequal variances were performed on data in Chapter 4 to determine the statistical significance of changes to the rheological properties of gels following chemical cross-linking with GTA under different conditions when compared to control samples that had not undergone chemical cross-linking.

5.5 References

1. D. McDowall, M. Walker, M. Vassalli, M. Cantini, N. Khunti, C. J. C. Edwards-Gayle, N. Cowieson and D. J. Adams, *Chem. Comm.*, 2021, **57**, 8782-8785.
2. G. Ciccone, M. A. G. Oliva, N. Antonovaite, I. Luchtefeld, M. Salmeron-Sanchez and M. Vassalli, *JoVE J. Vis. Exp.*, 2022, **179**, e63401.
3. P. Virtanen, R. Gommers, T. E. Oliphant, M. Haberland, T. Reddy, D. Cournapeau, E. Burovski, P. Peterson, W. Weckesser, J. Bright, S. J. van der Walt, M. Brett, J. Wilson, K. J. Millman, N. Mayorov, A. R. J. Nelson, E. Jones, R. Kern, E. Larson, C. J. Carey, I. Polat, Y. Feng, E. W. Moore, J. VanderPlas, D. Laxalde, J. Perktold, R. Cimrman, I. Henriksen, E. A. Quintero, C. R. Harris, A. M. Archibald, A. H. Ribeiro, F. Pedregosa, P. van Mulbregt and C. SciPy, *Nat. Methods*, 2020, **17**, 352-352.
4. N. Gavara, *Sci. Rep.*, 2016, **6**, 21267.

5. I. Luchtefeld, A. Bartolozzi, J. Mejia, O. Dobre, M. Basso, T. Zambelli and M. Vassalli, *J. Nanobiotechnol.*, 2020, **18**, 1-11.
6. https://imagej.nih.gov/ij/download.html.
7. R. W. Adams, C. M. Holroyd, J. A. Aguilar, M. Nilsson and G. A. Morris, *Chem. Comm.*, 2013, **49**, 358-360.
8. M. L. Liu, X. A. Mao, C. H. Ye, H. Huang, J. K. Nicholson and J. C. Lindon, *J. Magn. Reson.*, 1998, **132**, 125-129.
9. J. Stonehouse, P. Adell, J. Keeler and A. J. Shaka, *J. Am. Chem. Soc.*, 1994, **116**, 6037-6038.
10. https://www.ncnr.nist.gov/resources/sldcalc.html.
11. R. K. Heenan, J. Penfold and S. M. King, *J. Appl. Crystallogr.*, 1997, **30**, 1140-1147.
12. O. Arnold, J. C. Bilheux, J. M. Borreguero, A. Buts, S. I. Campbell, L. Chapon, M. Doucet, N. Draper, R. F. Leal, M. A. Gigg, V. E. Lynch, A. Markvardsen, D. J. Mikkelson, R. L. Mikkelson, R. Miller, K. Palmen, P. Parker, G. Passos, T. G. Perring, P. F. Peterson, S. Ren, M. A. Reuter, A. T. Savici, J. W. Taylor, R. J. Taylor, R. Tolchenoy, W. Zhou and J. Zikoysky, *Nuclear Instruments & Methods in Physics Research Section a-Accelerators Spectrometers Detectors and Associated Equipment*, 2014, **764**, 156-166.
13. G. D. Wignall and F. S. Bates, *J. Appl. Crystallogr.*, 1987, **20**, 28-40.
14. www.sasview.org

Conclusions

In this thesis, we have investigated possible methods of modulating the properties of hydrogels composed of at least one peptide-based LMWG *via* the preparation of multicomponent systems. Using a variety of systems, we have accessed new properties and behaviours that would not be feasible through the preparation of a single component system. Throughout this thesis we have probed the behaviour of these systems at multiple length scales, from interactions at the molecular level, the secondary self-assembled structures within the gel network and finally to the material properties of the systems. We have also investigated the systems throughout the gelation process, from their behaviour pre-gelation, during self-assembly and finally in the gel or crystal phase.

At the molecular level, we used CD spectroscopy to gain insight into the interactions between two structurally similar, peptide-based LMWGs and thereby provide evidence for either self-sorting or co-assembly between the two components. We also used CD spectroscopy to show that co-assembly of a peptide-based LMWG with a structurally similar, non-gelling component can amplify or disrupt the chirality of the secondary structures formed in the system, depending on the identity of the non-gelling component. Such co-assembly pre-gelation can be further tuned using temperature, with the non-gelling component imparting behaviour on the system that is usually observed at higher LMWG concentrations. These responses to temperature were probed using CD spectroscopy, NMR spectroscopy and viscosity measurements.

Using SANS, we have shown it is possible to change the morphology of the self-assembled structures formed by the peptide-based LMWG 2NapFF. Inclusion of a second, structurally similar, non-gelling component allowed us to achieve structures usually observed at higher 2NapFF concentrations. Varying the amino acid residues present in the non-gelling component allowed us to change the dimensions of the structures formed.

SANS data also showed that systems composed of two peptide-based LMWGs allow access to a wide variety of structures depending on the identities of the *N*-terminal capping group and amino acids in the peptide chain, the chirality of the components and the concentration ratio of the components. The self-assembled structures resulting from the co-assembly of two structurally similar LMWGs usually resemble one of the components. We hypothesise that the component that forms more stable structures directs self-assembly in such cases.

Self-sorting of two structurally similar LMWGs results in self-assembled structures that resemble those formed by each component alone at the concentration at which they are present in the system. Further investigation using scattering experiments at smaller angles as well as imaging the gel network would be required to investigate the effects of multicomponent assembly on the structures formed at longer length scales.

We used NMR spectroscopy, pH measurements and rheology experiments following changes to the systems with time to understand how the two components in our systems were assembling during the gelation process. This can provide strong evidence for self-sorting or indicate that the process is more complicated.

We measured the mechanical properties of the gels formed by these systems using rheology for bulk gels and nanoindentation for supramolecular noodles. The stiffness, elasticity and response to strain of supramolecular gels can be finely controlled by varying the identity, concentration ratio and chirality of the two components in multicomponent systems containing two structurally similar components. However, the outcome of such mixtures is hard to predict and requires trial of many different conditions. More predetermined outcomes can be achieved by preparing systems from a LMWG containing a cross-linkable group and an appropriate cross-linking agent. The effect of chemical cross-linking on the mechanical properties of the final gel can be carefully controlled using a multitude of factors. These factor include; the position of the cross-linkable group in the peptide chain, the concentration of the LMWG, the concentration ratio of LMWG to cross-linking agent, whether the cross-linking agent is added before or after gelation and the method used to trigger gelation.

Finally, systems composed of a LMWG and a structurally similar crystal-forming component allowed preparation of supramolecular noodles with enhanced mechanical strength compared to noodles composed of the LMWG alone. By careful choice of the external conditions of the noodles, we were able to prepare composite materials with both viscoelastic regions comprised of the gel and solid regions containing crystals.

Appendices

Contents of appendices

Appendix 1.1: Viscosity

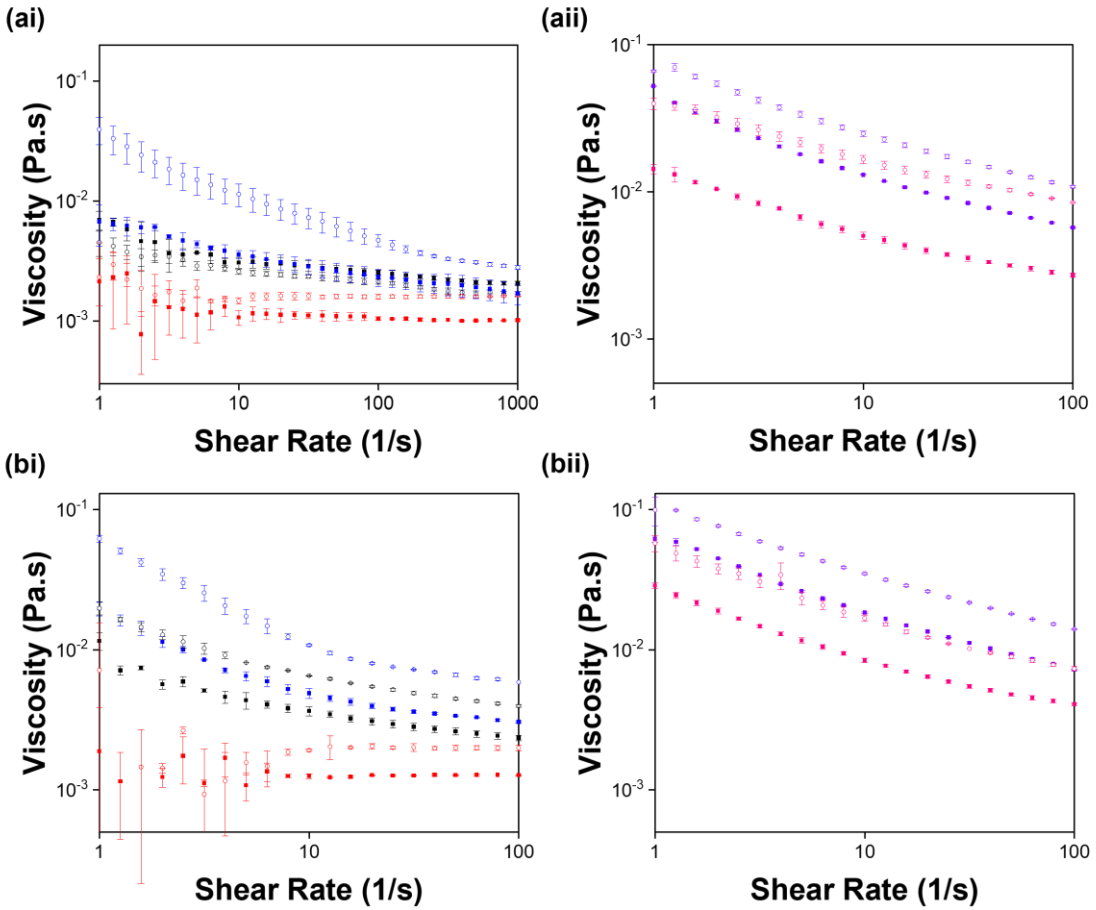

Figure A1.1.1. Full range viscosity data collected from the following systems: 2NapLG alone 2.5 mg/mL (red), 2NapFF alone 2.5 mg/mL (black), 2NapLG 2.5 mg/mL:2NapFF 2.5 mg/mL (blue), 2NapFF alone 5 mg/mL (pink) and 2NapLG 2.5 mg/mL:2NapFF 5 mg/mL (purple). Data was collected at 25 °C (filled squares) and 10 °C (empty circles) in (a) H_2O at pH 10.5 and (b) D_2O at pD 10.5. Data was collected in duplicate with a fresh sample for each repeat. The error bars show the standard deviation between the samples. The data in (a) and (b) is split into two separate graphs for clarity.

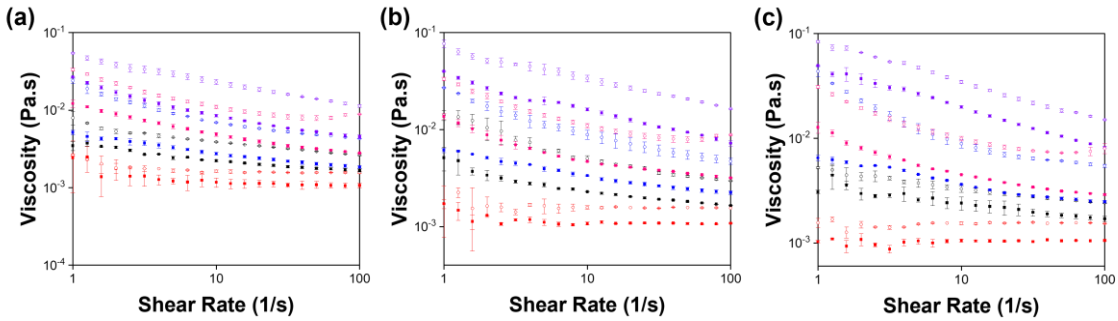

Figure A1.1.2. Full range viscosity data from the following systems (where X = (a) PhOLL, (b) 2NapVG and (c) 2Nap-OH): X alone 2.5 mg/mL (red), 2NapFF alone 2.5 mg/mL (black), X 2.5 mg/mL:2NapFF 2.5 mg/mL (blue), 2NapFF alone 5 mg/mL (pink) and X 2.5 mg/mL:2NapFF 5 mg/mL (purple). Data was collected at 25 °C (filled squares) and 10 °C (empty circles) in H_2O at pH 10.5.

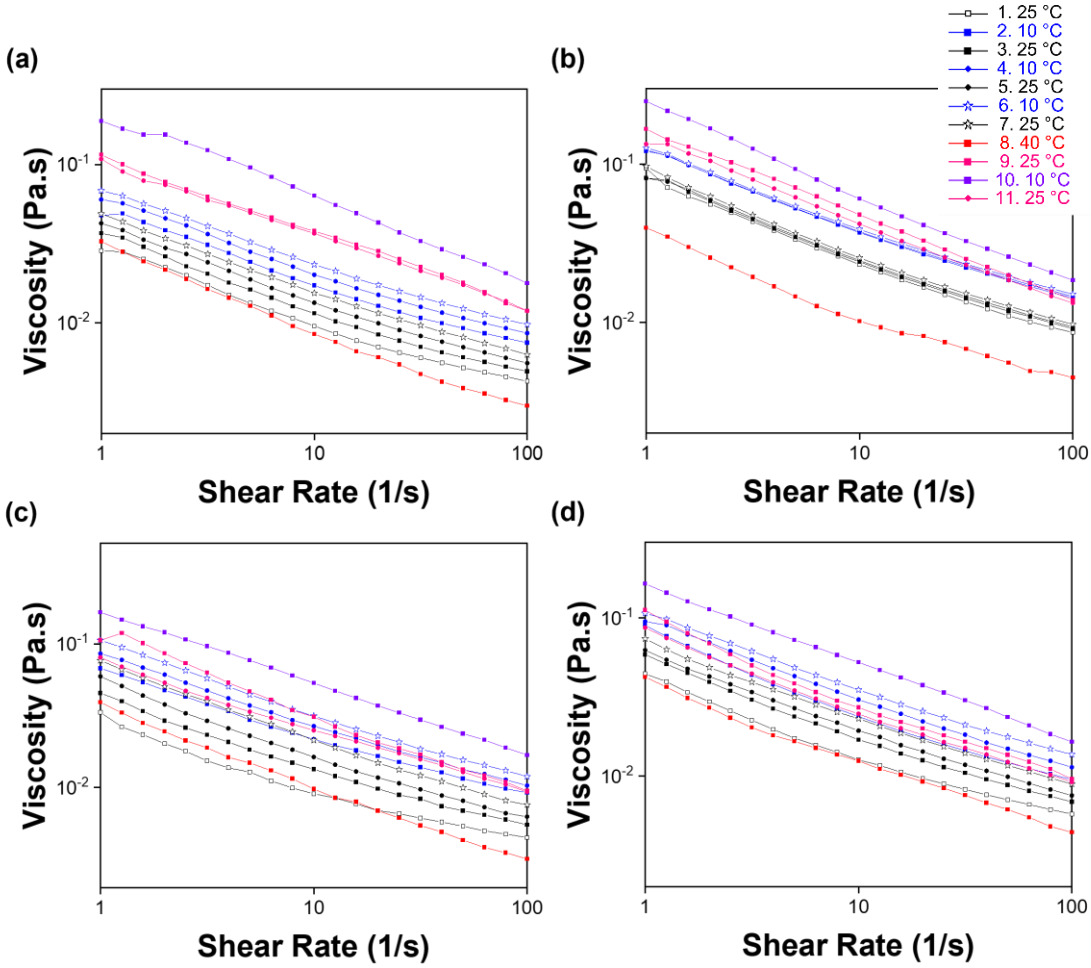

Figure A1.1.3. Full range of viscosity data collected to create heat-cool graphs for the following multicomponent systems: (a) 2NapLG 2.5 mg/mL:2NapFF 5 mg/mL, (b) PhOLL 2.5 mg/mL:2NapFF 5 mg/mL, (c) 2NapVG 2.5 mg/mL:2NapFF 5 mg/mL, (d) 2Nap-OH 2.5 mg/mL:2NapFF 5 mg/mL, (e) 2NapFF 5 mg/mL and (f) 2NapFF 10 mg/mL. The key on the right-hand side shows the temperature during each measurement in chronological order.

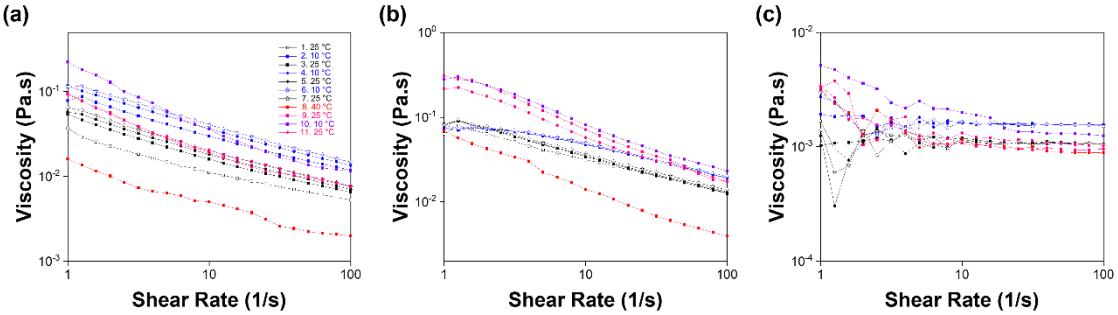

Figure A1.1.4. Full range of viscosity data collected to create heat-cool graphs for the following single component systems: (a) 2NapFF 5 mg/mL, (b) 2NapFF 10 mg/mL, (c) 2NapLG 2.5 mg/mL. The key on the right-hand side of (a) shows the temperature during each measurement in chronological order.

Appendix 1.2: CD, absorbance and HT data

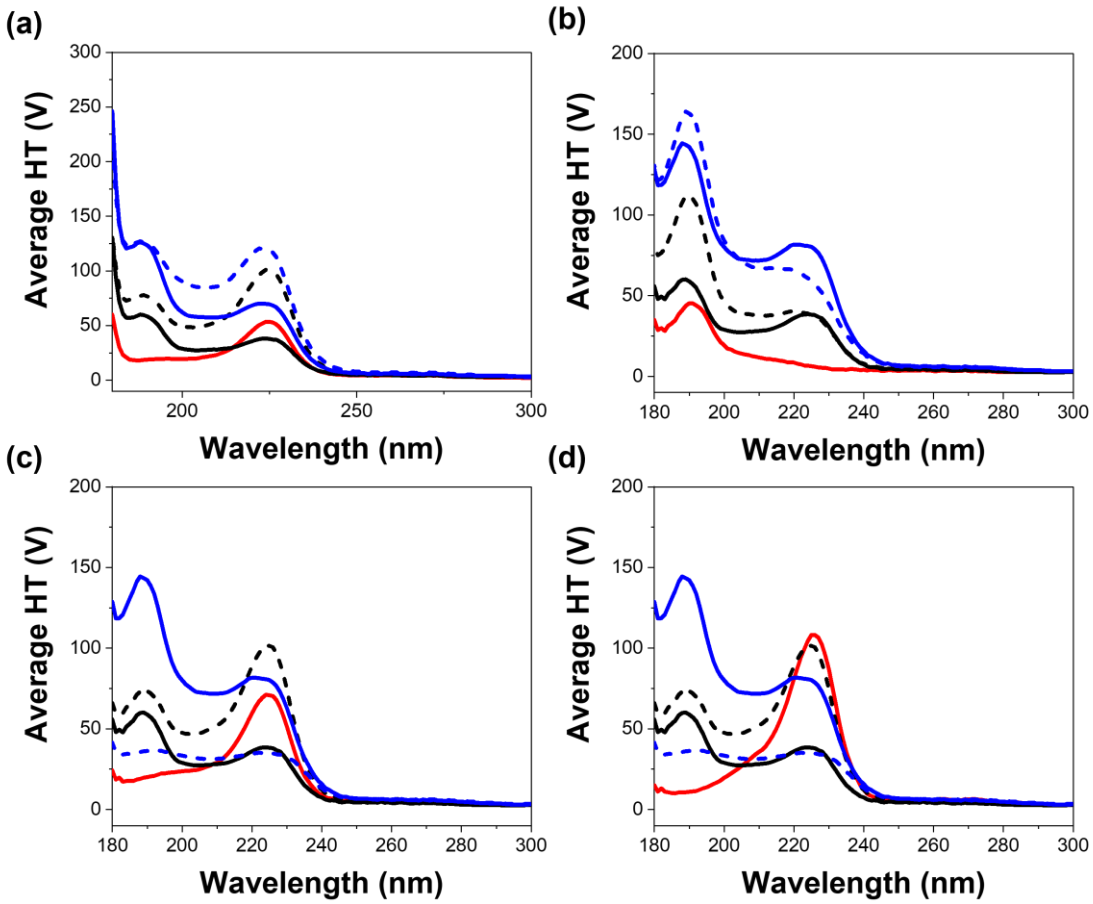

Figure A1.2.1. HT data collected from samples containing (a) 2NapLG, (b) PhOLL, (c) 2NapVG and (d) 2Nap-OH. HT spectra were recorded of each component alone at a concentration of 2.5 mg/mL (red), 2NapFF alone at concentrations of 2.5 mg/mL (black) and 5 mg/mL (blue), multicomponent systems at concentration ratios 2.5 mg/mL:2NapFF 2.5 mg/mL (black dashed), and 2.5 mg/mL:2NapFF 5 mg/mL (blue dashed) in H_2O at pH 10.5. All data was collected in triplicate and averaged. HT data were collected concurrently with CD data.

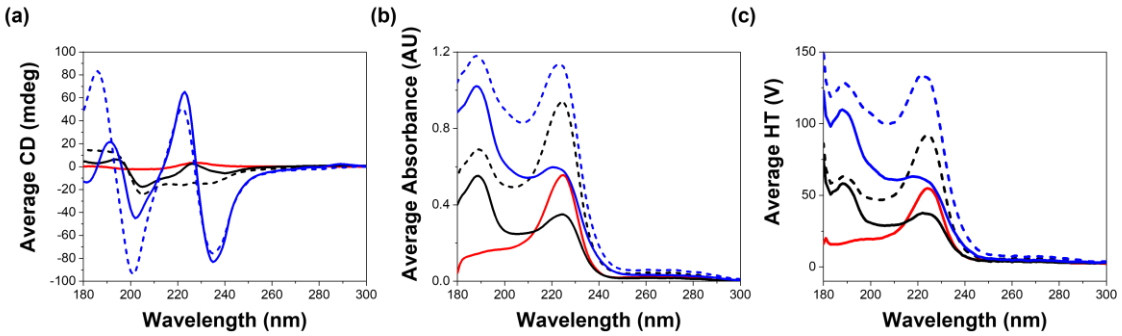

Figure A1.2.2. (a) CD, (b) absorbance and (c) HT data collected from samples containing 2NapLG 2.5 mg/mL (red), 2NapFF 2.5 mg/mL (black), 2NapLG 2.5 mg/mL:2NapFF 5 mg/mL (black dashed), 2NapFF 5 mg/mL (blue), and 2.5 mg/mL:2NapFF 5 mg/mL (blue dashed) in D2O at pD 10.5. All data was collected in triplicate and averaged. Absorbance and HT data were collected concurrently with CD data.

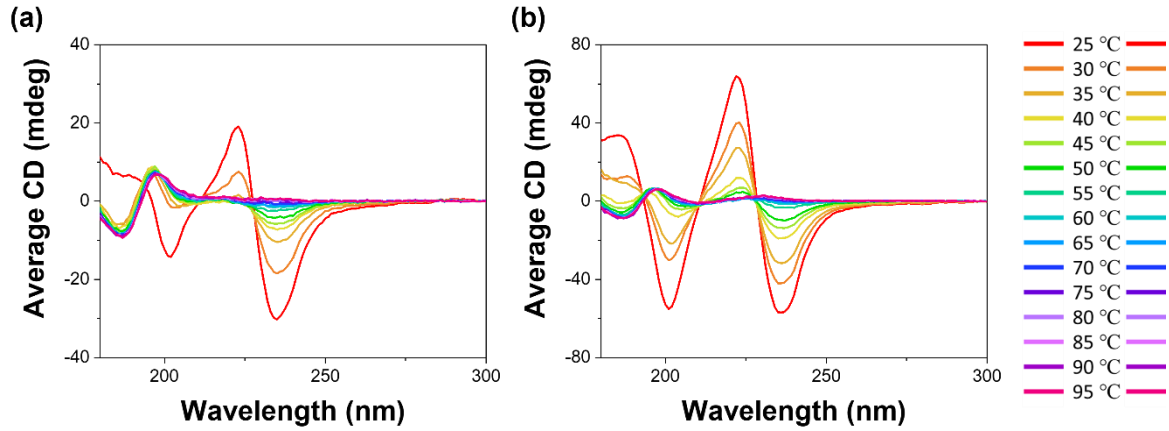

Figure A1.2.3. CD spectra recorded for (a) 2NapFF (5 mg/mL) and (b) 2NapLG (2.5 mg/mL):2NapFF (5 mg/mL). The temperature was increased in 5 ℃ increments between each recording, starting from 25 ℃ and ending at 95 ℃ (the upper limit of the CD spectrometer). The temperature at which each spectrum was recorded is shown in the key.

Appendix 1.3 Photographs and optical microscopy

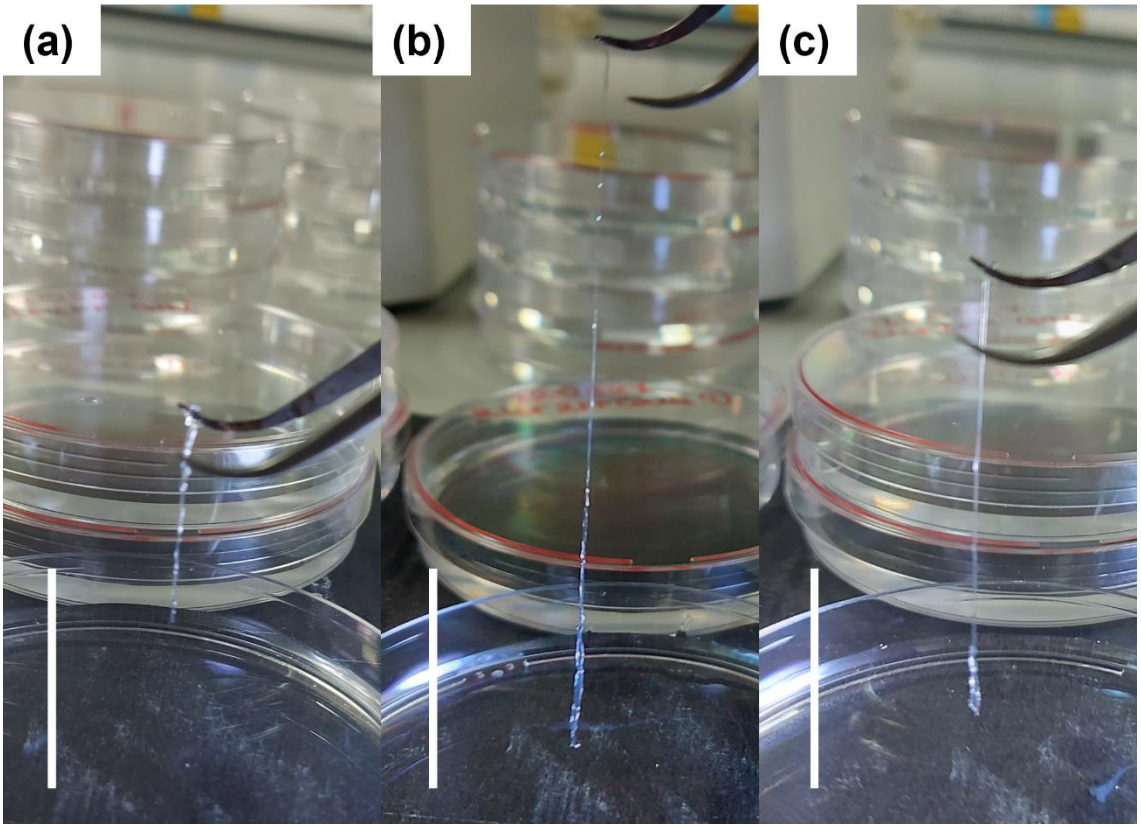

Figure 1.3.1. Photographs of supramolecular noodles prepared from solutions of (a) 2NapFF (5 mg/mL), (b) 2NapLG (2.5 mg/mL):2NapFF (5 mg/mL) and (c) PhOLL 2.5 mg/mL:2NapFF (5 mg/mL). Scale bars show 300 mm.

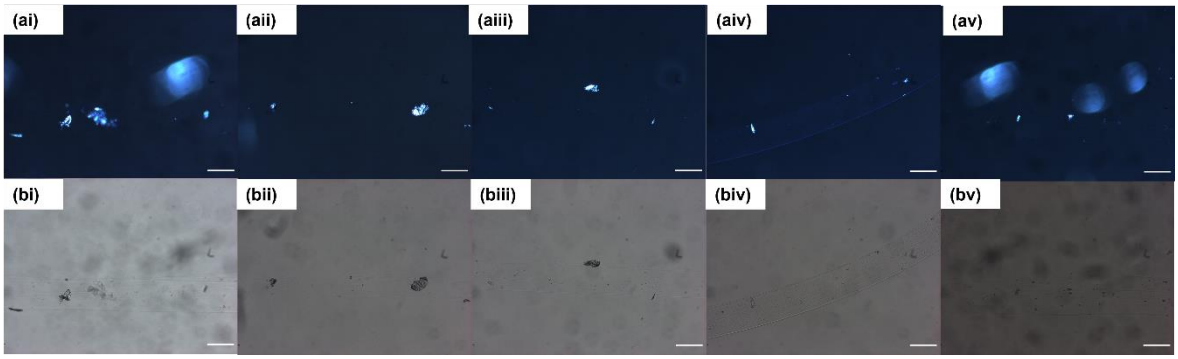

Figure A1.3.2. Images collected from optical microscopy of 2NapLG crystals within supramolecular gel noodles under (a) polarised and (b) non-polarised light. Scale bars represent 300 μm.

Appendix 1.4: Single crystal data

Single crystal data	**2NapLG**
Empirical formula	$C_{20}H_{24}N_2O_5$
Crystal colour	colourless
Molecular weight (g/mol)	372.41
Crystal size	0.15 × 0.13 × 0.02 mm
Space Group	Orthorhombic, P 2_1 2_1 2_1
Cell lengths (Å)	**a** 9.0636(4) **b** 10.2968(5) **c** 20.5621(12)
Cell angles (°)	**a** 90 **b** 90 **g** 90
Cell volume (Å^3)	1918.98
Z, Z'	**Z**: 4 **Z'**: 1
D_x (g/cm^3)	1.289
F(000)	792
θ (°)	4.3–70.1
μ CuKα (mm^{-1})	0.77
λ CuKα (Å)	1.54178
Temperature (K)	150
Reflections collected/observed [I>2σ(I)]	3630/2960
Data/restraints/parameters	3630/0/259
$R[F^2 > 2s(F^2)]$	0.053
$wR(F^2)$	0.151
S	1.06
R factor	5.29

Table A1.4.1. Summary of single crystal data and data collection. Crystallographic data for CCDC 2223449 are available free of charge from The Cambridge Crystallographic Data Centre (https://www.ccdc.cam.ac.uk).

Appendix 1.5 pH titrations

Molar equivalents HCl added	pH	Molar equivalents HCl added	pH
0.00	10.83	1.63	3.95
0.09	10.73	1.68	3.85
0.19	10.56	1.72	3.83
0.28	10.25	1.77	3.89
0.37	9.73	1.82	3.84
0.47	7.20	1.86	3.78
0.51	6.43	1.91	3.81
0.56	5.91	1.96	3.76
0.61	5.50	2.00	3.77
0.65	5.15	2.05	4.78
0.70	4.90	2.09	4.70
0.74	4.75	2.14	4.72
0.79	4.71	2.19	4.79
0.84	4.54	2.28	4.74
0.88	4.33	2.37	4.70
0.93	4.28	2.47	4.67
0.98	4.26	2.56	4.66
1.02	4.18	2.65	4.56
1.07	4.15	2.75	4.48
1.12	4.13	2.84	4.36
1.16	4.12	2.93	4.21
1.21	4.08	3.03	3.95
1.26	4.04	3.12	3.73
1.30	4.05	3.21	3.51
1.35	4.01	3.31	3.36
1.40	3.98	3.40	3.14
1.44	3.95	3.49	3.08
1.49	3.93	3.58	3.05
1.54	3.96	3.68	3.00
1.58	3.93	3.77	2.94

Table A1.5.1. Results from pK_a titration of 2NapLG (2.5 mg/mL).

Molar equivalents HCl added	pH	Molar equivalents HCl added	pH	Molar equivalents HCl added	pH
0.00	10.89	0.62	7.32	1.43	5.26
0.03	10.84	0.65	7.27	1.46	5.46
0.06	10.71	0.68	7.22	1.49	5.39
0.05	10.58	0.71	7.15	1.52	5.35
0.06	10.34	0.74	7.06	1.55	5.16
0.08	10.10	0.78	7.00	1.58	5.08
0.09	9.82	0.81	6.92	1.61	4.96
0.11	9.72	0.84	6.89	1.64	4.80
0.12	9.40	0.87	6.85	1.68	4.71
0.14	9.06	0.90	6.77	1.71	4.58
0.16	8.85	0.93	6.73	1.74	4.44
0.17	8.81	0.96	6.70	1.77	4.35
0.19	8.77	0.99	6.69	1.80	4.20
0.20	8.82	1.02	6.68	1.83	4.17
0.22	8.85	1.06	6.60	1.86	4.01
0.23	8.88	1.09	6.56	1.89	3.97
0.25	8.92	1.12	6.46	1.92	3.95
0.26	8.87	1.15	6.40	1.96	3.87
0.28	8.87	1.18	6.37	1.99	3.80
0.29	8.81	1.19	6.33	2.02	3.69
0.31	8.69	1.21	6.26	2.05	3.64
0.33	8.66	1.23	6.25	2.08	3.52
0.34	8.34	1.24	6.17	2.11	3.59
0.36	8.23	1.26	6.13	2.14	3.44
0.37	8.00	1.27	5.95	2.17	3.41
0.39	7.90	1.29	5.93	2.20	3.35
0.40	7.76	1.30	5.88	2.23	3.29
0.42	7.70	1.32	5.87	2.27	3.25
0.43	7.71	1.33	5.87	2.33	3.16
0.47	7.70	1.35	5.82	2.39	3.08
0.50	7.65	1.37	5.78	2.45	3.05
0.53	7.54	1.38	5.69	2.51	3.00
0.56	7.46	1.40	5.62	2.58	2.98
0.59	7.37	1.41	5.56		

Table A1.5.2. Results from pK_a titration of 2NapFF (5 mg/mL).

Molar equiv. HCl added	pH	Molar equiv. HCl added	pH	Molar equiv. HCl added	pH	Molar equiv. HCl added	pH
0.00	10.87	0.41	8.45	0.89	6.57	1.47	5.39
0.02	10.76	0.43	8.59	0.90	6.52	1.51	5.25
0.04	10.73	0.45	8.38	0.91	6.40	1.55	5.15
0.06	10.63	0.47	8.11	0.92	6.48	1.58	5.05
0.07	10.50	0.48	8.07	0.93	6.58	1.62	4.97
0.09	10.39	0.50	7.95	0.95	6.42	1.66	4.65
0.11	10.18	0.52	7.91	0.97	6.39	1.68	4.83
0.13	10.00	0.54	7.81	0.99	6.37	1.69	4.78
0.15	9.80	0.56	7.71	1.01	6.27	1.71	4.75
0.16	9.72	0.58	7.52	1.02	6.20	1.75	4.65
0.17	9.57	0.60	7.60	1.04	6.17	1.79	4.59
0.18	9.46	0.61	7.51	1.06	6.09	1.82	4.54
0.19	9.28	0.63	7.36	1.08	6.13	1.86	4.48
0.20	9.02	0.65	7.29	1.10	6.07	1.90	4.40
0.20	9.02	0.67	7.18	1.12	6.01	1.94	4.33
0.21	8.92	0.69	7.15	1.14	6.00	1.97	4.25
0.22	8.80	0.71	7.13	1.15	5.94	2.01	4.20
0.23	8.90	0.73	7.09	1.17	5.95	2.05	4.13
0.24	8.91	0.74	7.08	1.19	5.95	2.09	4.07
0.25	8.93	0.76	6.90	1.21	5.93	2.12	3.94
0.26	8.94	0.78	6.76	1.23	5.84	2.16	3.89
0.27	8.91	0.79	6.93	1.25	5.85	2.20	3.81
0.28	8.93	0.80	6.85	1.27	5.85	2.23	3.77
0.29	8.94	0.81	6.70	1.28	5.82	2.27	3.68
0.30	8.91	0.82	6.58	1.30	5.78	2.31	3.58
0.31	8.89	0.83	6.65	1.32	5.67	2.35	3.47
0.32	8.85	0.84	6.60	1.34	5.59	2.38	3.40
0.33	8.82	0.85	6.61	1.36	5.55	2.42	3.28
0.34	8.79	0.86	6.72	1.38	5.51	2.46	3.17
0.35	8.84	0.87	6.70	1.40	5.46	2.50	3.11
0.37	8.72	0.88	6.62	1.42	5.41	2.53	3.04
0.39	8.64	0.88	6.65	1.43	5.42	2.57	2.96

Table A1.5.3. Results from pK_a titration of 2NapLG (2.5 mg/mL):2NapFF (5 mg/mL).

Appendix 1.6 Kinetics of gelation and crystallisation

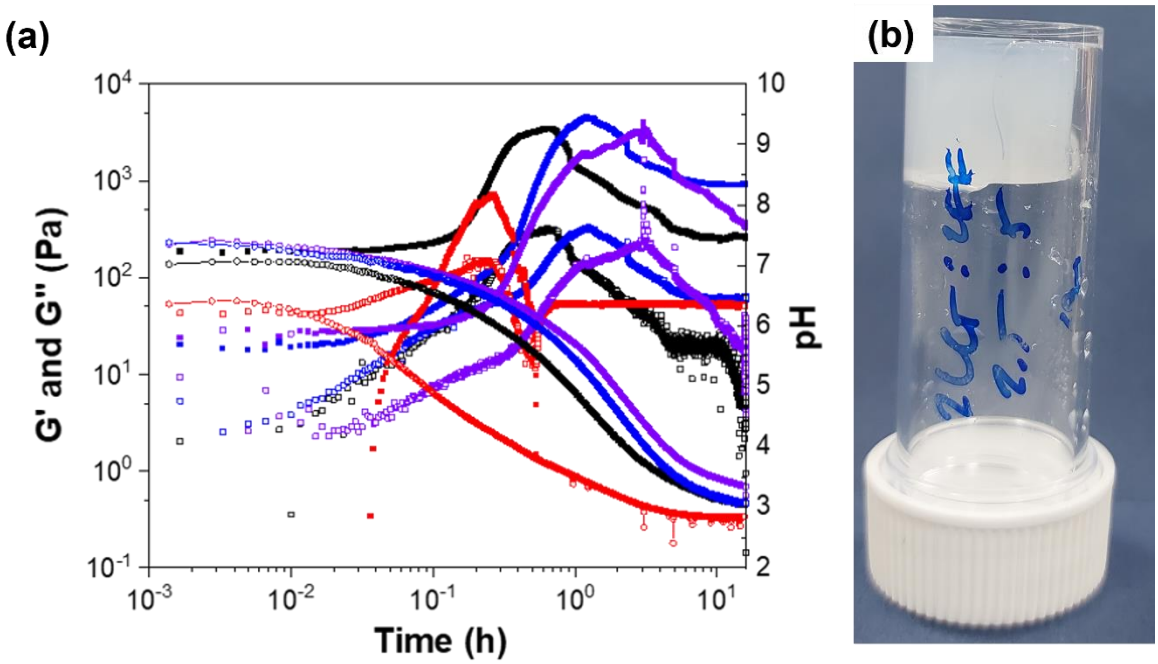

Figure A1.6.1. (a) Time sweeps (G′= filled squares, G″= empty squares) and pH logs (pH = empty circles) recorded from samples composed of 2NapLG 2.5 mg/mL:2NapFF 2.5 mg/mL. The samples were prepared in 7 mL Sterilin vials with a sample volume of 2 mL. Self-assembly was triggered using GdL (20 mg/mL). The experiments were performed at 25 °C (red), 15 °C (black), 10 °C (blue) and 5 °C (purple). Reducing the temperature reduces the rate of crystal formation and thereby the time taken for the gel to collapse. (b) Photograph showing the gel after undergoing syneresis with entrapped 2NapLG crystals.

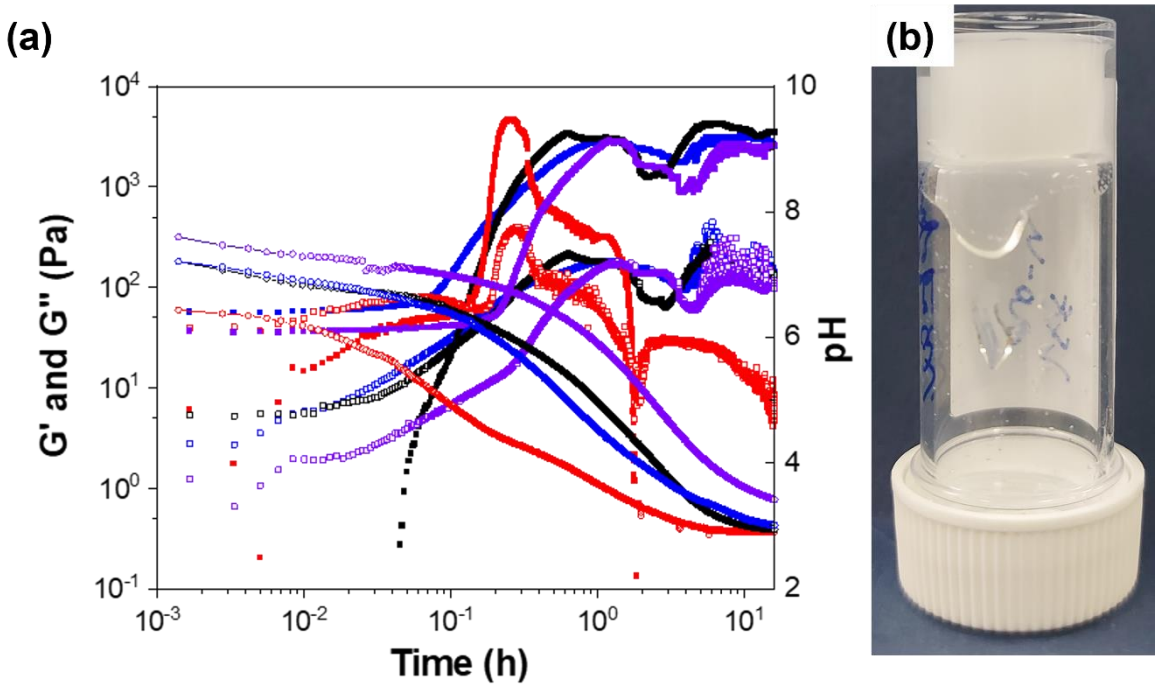

Figure A1.6.2. (a) Time sweeps (G′ = filled squares, G″ = empty squares) and pH logs (pH = empty circles). recorded from samples composed of PhOLL 2.5 mg/mL: 2NapFF 2.5 mg/mL. The samples were prepared in 7 mL Sterilin vials with a sample volume of 2mL. Self-assembly was triggered using GdL (20 mg/mL). The experiments were performed at 25 °C (red), 15 °C (black), 10 °C (blue) and 5 °C (purple). (b) Photograph showing the gel after undergoing syneresis with entrapped PhOLL crystals.

The experiments on the following pages were performed to try and replicate the conditions under 2NapLG forms crystals alone and transitions from co-assembly to self-sorting in the 2NapLG 2.5 mg/mL:2NapFF 5 mg/mL multicomponent system. The same experiment was performed on PhOLL 2.5 mg/mL:2NapFF 5 mg/mL.

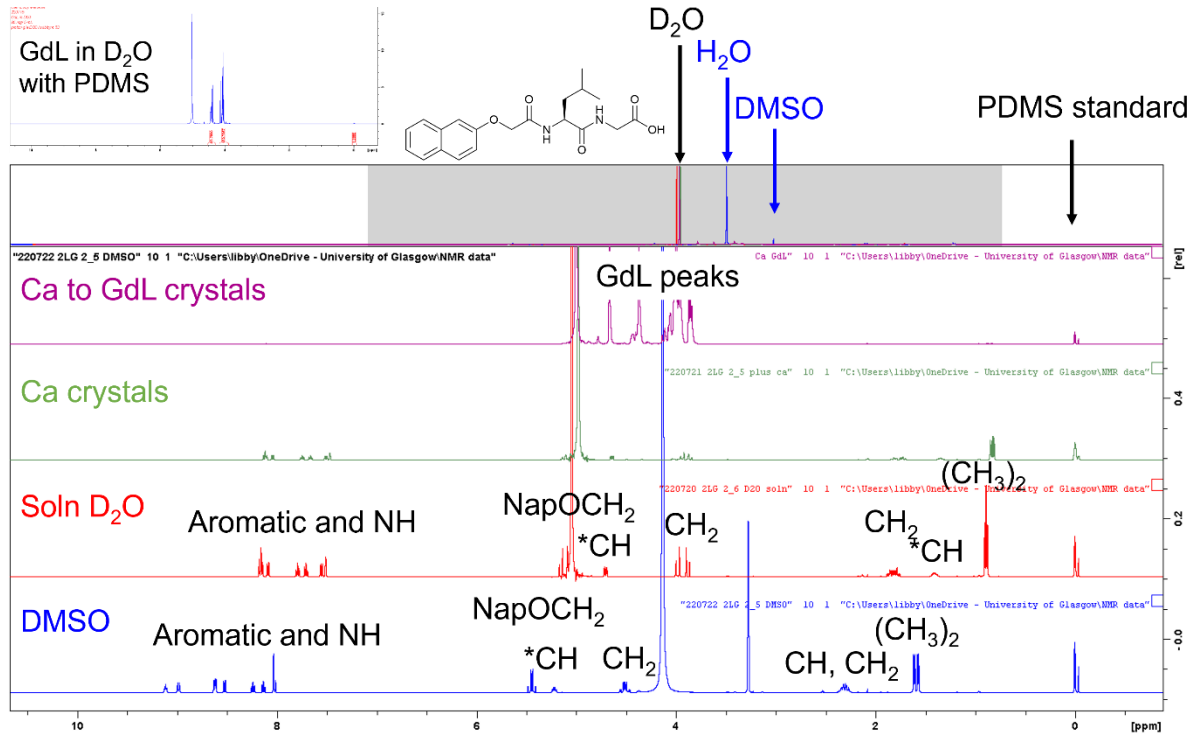

Figure A1.6.3. ^{1}H NMR spectra collected from samples of the 2NapLG 2.5 mg/mL single component system in d_6-DMSO (blue) where the system is completely dissolved and therefore 0 % assembled, in solution at high pD in D_2O (red), after addition of $CaCl_2$ (green) and after addition of GdL (purple). The spectrum on the top left shows a sample prepared from GdL alone in D_2O to verify that the peaks that appear in the GdL samples are from the hydrolysis of GdL.

2NapLG remains NMR visible in solution in D_2O, with peak intensities equivalent to those observed in d_6-DMSO, where we assume 0 % of the molecules are assembled. The presence of sharp peaks shows that the micelles formed by 2NapLG in D_2O have small correlation times allowing long enough transversal relaxation time, T_2, for sharp signals to be obtained.[1] This means the micelles are transient on an NMR timescale. On addition of $CaCl_2$, 2NapLG forms crystals. The spectrum shown was collected after only 24 hours. The presence of sharp peaks shows that not 100% of the 2NapLG molecules are involved in crystal formation. Calculations suggest 24 % of the molecules are in an assembled state, most likely as crystals. The molecules may require more Ca^{2+} ions or simply more time to allow 100 % of the molecules to be involved in crystallisation. 100 % crystallisation had not occurred 3.5 hours after addition of GdL. However, leaving the sample for a total of 24 hours after addition of GdL resulted in the complete disappearance of the 2NapLG peaks, showing that 100 % of the 2NapLG molecules were now trapped in the crystalline state.

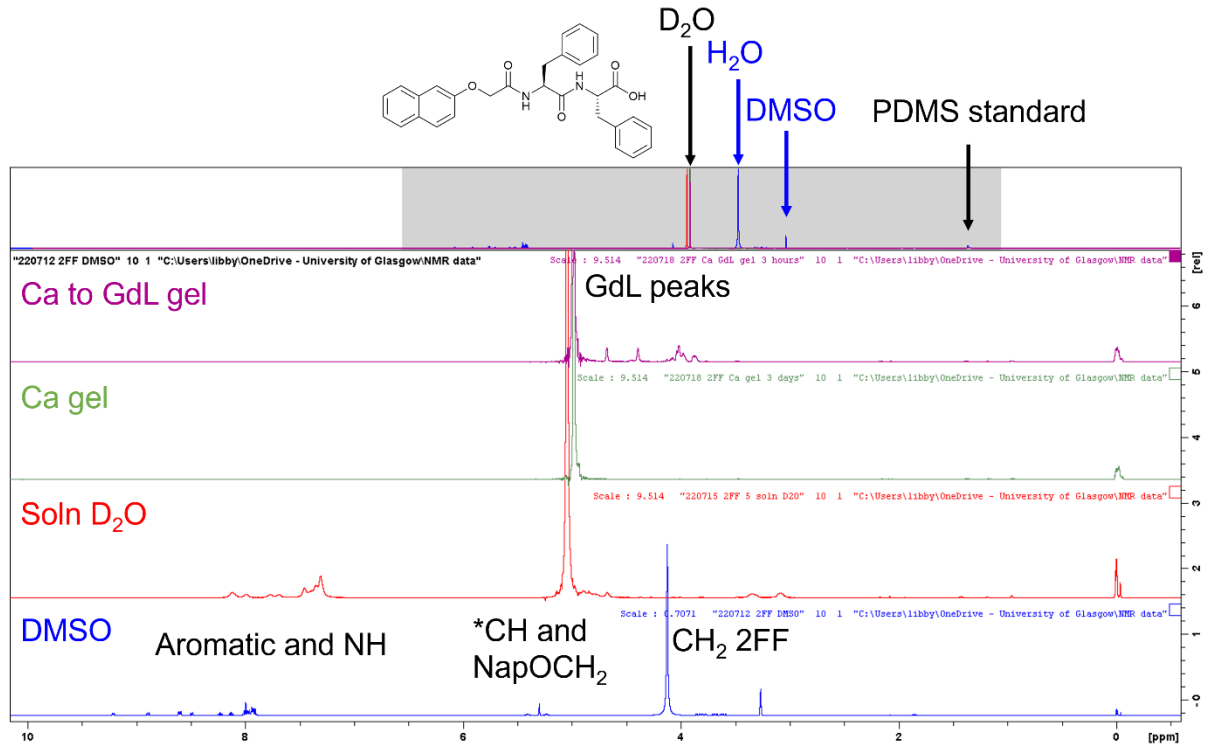

Figure A1.6.4. ^{1}H NMR spectra collected from samples of the 2NapFF 5 mg/mL single component system in d_6-DMSO (blue) where the system is completely dissolved and therefore 0 % assembled, in solution at high pD in D_2O (red), after addition of $CaCl_2$ (green) and after addition of GdL (purple).

2NapFF is soluble in d_6-DMSO, giving sharp peaks. In D_2O, 2NapFF forms worm-like micelles. These aggregates have large correlation times, resulting in short T_2 and broadening of the peaks in the NMR spectrum.[1] Using the integrals collected in d_6-DMSO as 0 % assembled (i.e., fully dissolved), ~50 % of the 2NapFF molecules are in an assembled state in D_2O at pD 10.5. This % assembly value was calculated using the ArH and C**H**$_2$Ph peaks. After addition of $CaCl_2$, all the 2NapFF peaks disappeared showing 100 % assembly. This is expected as the 2NapFF molecules are in a gel state. Subsequent addition of GdL shows 2NapFF remains 100 % assembled. No disassembly during the transition from a Ca gel to a GdL gel was observed.

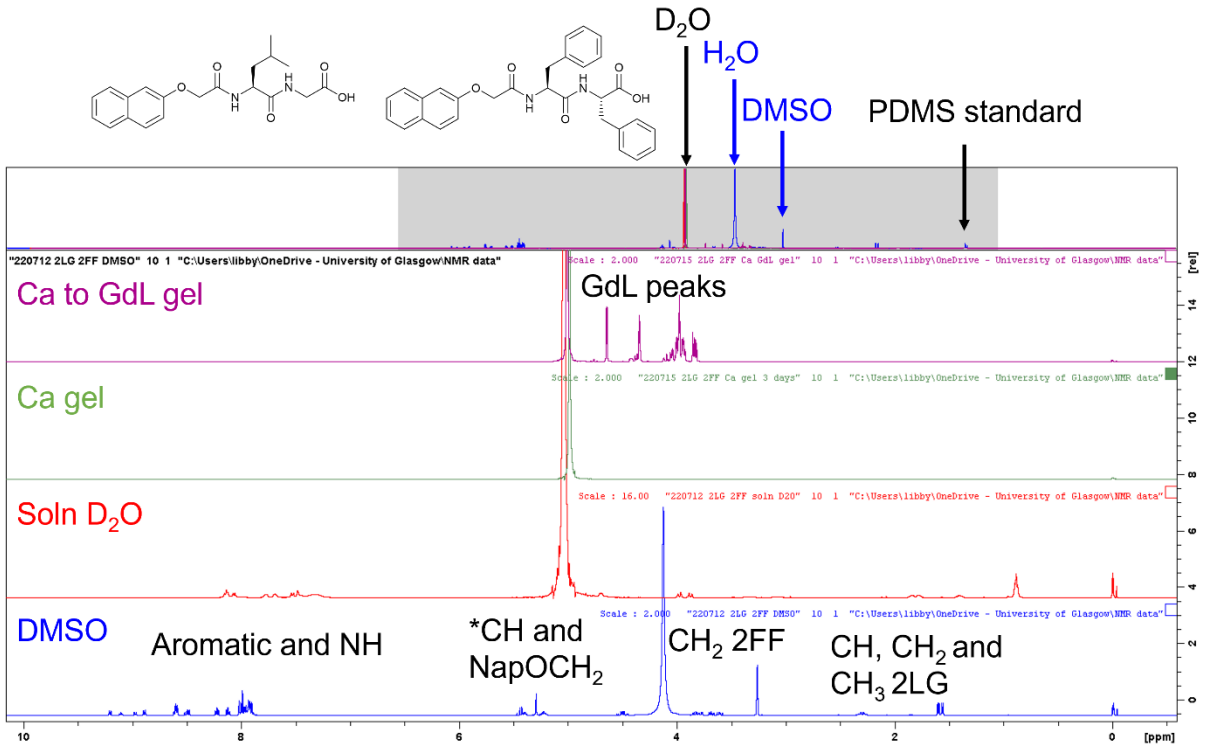

Figure A1.6.5. ^{1}H NMR spectra collected from samples of the 2NapLG 2.5 mg/mL:2NapFF 5 mg/mL multicomponent system in d_6-DMSO (blue) where the system is completely dissolved and therefore 0 % assembled, in solution at high pD in D_2O (red), after addition of $CaCl_2$ (green) and after addition of GdL (purple).

In the sol phase in D_2O, the peaks corresponding to 2NapLG remain sharp while the 2NapFF peaks broaden. This shows that while the 2NapLG molecules remain relatively mobile, the 2NapFF molecules are fixed within large aggregates. In agreement with our other NMR data, the % assembly of 2NapFF increases (from 50 % to 70 %) in the presence of 2NapLG. As in the 2NapFF single component system, the peaks completely disappear after addition of $CaCl_2$ and remain invisible after addition of GdL. This shows that 100 % of 2NapLG and 2NapFF molecules are assembled in these conditions.

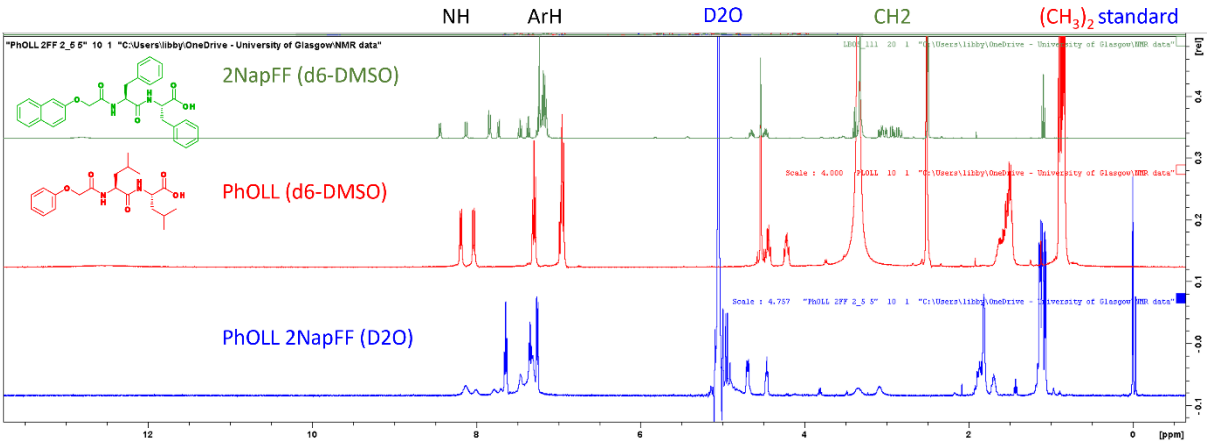

Figure A1.6.6. Example of NMR spectra used to calculate % assembly. The internal (capillary) standard 0.1% PDMS in tetrachloroethylene solution was used as a reference. This peak was calibrated to 1 in all the spectra. The CH_3 peak from PhOLL and the CH_2 peaks from 2NapFF were used to calculate the percent assembly by comparison with the reference peak.

The presence of the 2NapFF structures in solution at high pD increases the proportion of PhOLL molecules in the assembled state from 4 % in the PhOLL 2.5 mg/mL single component system to 15 % in the PhOLL 2.5 mg/mL:2NapFF 5 mg/mL multicomponent system. The presence of PhOLL increases the proportion of 2NapFF molecules in the assembled state from 52 % in the 2NapFF 5 mg/mL single component system to 80 % in the multicomponent system. This agrees with the viscosity and CD data which show that more aggregation is occurring in the co-assembled system.

Appendix 1.7 Characterisation of compounds under study

Bold highlights the assigned proton, * denotes a stereocentre.

<u>2NapLG</u> – previously synthesised.[2]

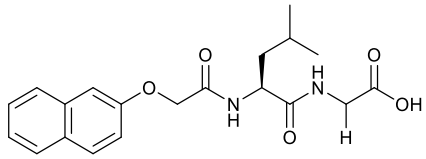

White solid.

δ_H(400 MHz, $DMSO_{d6}$**):** 12.53 (0.3H, broad s, COOH), 8.36 (1H, t, *J* = 5.7 Hz, N**H**CH_2), 8.25 (1H, d, *J* = 8.6 Hz, N**H***CH), 7.86-7.80 (2H, m, ArCH), 7.76-7.74 (1H, m, ArCH), 7.48-7.44 (1H, m, ArCH), 7.38-7.34 (1H, m, ArCH), 7.26-7.23 (2H, m, ArCH), 4.69 (1H, d, *J* = 14.6 Hz, Nap-OCH_2), 4.64 (1H, d, *J* = 14.6 Hz, Nap-OCH_2), 4.47-4.42 (1H, m, *CH), 3.73 (2H, ddd, *J* = 17.5, 6.4, 5.9 Hz, *CHC**H_2**), 3.30 (s, H_2O), 2.50 (q, d_6-DMSO), 1.62-1.45 (3H, m, NH**C**H_2, C**H**$(CH_3)_2$), 1.09 (t, Et_2O), 0.84 (3H, d, *J* = 6.2 Hz, CH(C**H_3**$)_2$), 0.80 (3H, d, *J* = 6.2 Hz, CH(C**H_3**$)_2$). Assignments were confirmed using COSY spectrum.

<u>PhOLL</u> – previously synthesised.[2]

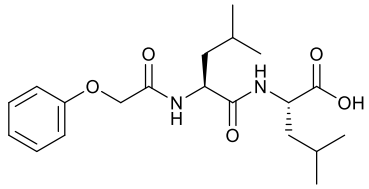

White solid.

δ_H(400 MHz, $DMSO_{d6}$**):** 12.52 (0.6H, broad s, COOH), 8.17 (1H, d, *J* = 7.9 Hz, NH), 8.02 (1H, d, *J* = 7.9 Hz, NH), 7.03-7.26 (2H, m, ArCH), 6.97-6.92 (3H, m, ArCH), 4.54 (1H, d, *J* = 14.8 Hz, Nap-OCH_2), 4.50 (1H, d, *J* = 14.8 Hz, Nap-OCH_2), 4.46-4.40 (1H, m, *CH), 4.23-4.18 (1H, m, *CH), 1.66-1.46 (6H, m, 2x *CHC**H_2**C**H**), 0.89-0.82 (12H, m, 4x$(CH_3)_2$).

<u>2NapVG</u> – previously synthesised.[3]

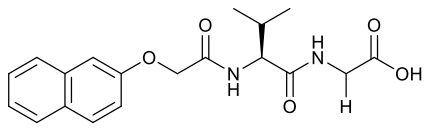

White solid.

δ_H(400 MHz, $DMSO_{d6}$**):** 12.54 (0.8H, broad s, COOH), 8.43 (1H, t, *J* = 5.8 Hz, N**H**CH_2), 8.01-7.98 (1H, d, *J* = 9.0 Hz, N**H***CH), 7.87-7.83 (2H, m, ArCH), 7.77-7.75 (1H, m, ArCH), 7.49-7.45 (1H, m, ArCH), 7.38-7.34 (1H, m, ArCH), 7.29-7.23 (2H, m, ArCH), 4.75 (1H, d, *J* = 14.6 Hz, 2Nap-$OCH_{2)}$, 4.70 (1H, d, *J* = 14.6 Hz, 2Nap-$OCH_{2)}$, 4.32 (1H, dd, *J* = 6.6, 8.9 Hz, *CH), 3.81 (1H, dd, *J* = 5.9, 17.5 Hz, CH_2), 3.73 (1H, dd, *J* = 5.8, 17.4 Hz, CH_2), 2.07-2.00 (1H, m, *CHC**H**), 0.88 (3H, d, *J* = 6.8 Hz, $(CH_3)_2$), 0.84 (3H, d, *J* = 6.8 Hz, $(CH_3)_2$).

<u>2Nap-OH</u> – commercially available.

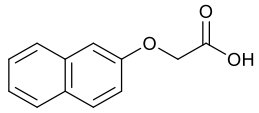

White solid.

δ_H(400 MHz, $DMSO_{d6}$**):** 13.07 (0.9H, broad s, COOH), 7.85-7.78 (3H, m, ArCH), 7.48-7.44 (1H, m, ArcH), 7.37-7.33 (1H, m, ArcH), 7.27-7.26 (1H, m, ArcH), 7.22-7.19 (1H, m, ArcH), 4.08 (2H, s, 2Nap-OCH_2).

Appendix 2.1: Synthesis of gelators

All *N*-functionalised dipeptides have been synthesised previously.[2, 5] Hence, only characterisation by ^{1}H NMR spectra are shown for each intermediate. Characterisation by ^{1}H and ^{13}C NMR spectra and mass spectrometry are shown for all final compounds. The same general synthesis as described in the Experimental Methods (Chapter 5) were used during the synthesis of each gelator. **Bold** highlights the assigned proton or carbon atom, * denotes a stereocentre.

7MeO2NapFV

7MeO2Nap-O^{t}Bu

7-methoxy-2-naphthol (8.71 g, 0.05 mol) was dissolved in acetone (100 mL). K_2CO_3 (20.7 g, 3 equiv., 0.15 mol) was added, followed by ^{t}butyl chloroacetate (8.28 g, 1.1 equiv., 0.055 mol) and the reaction stirred under reflux for 24 hours. After cooling, chloroform (200 mL) was added and the solution washed well with water, dried with $MgSO_4$ and the solvent removed *in vacuo*. The product was deemed sufficiently pure to be used in the next step.

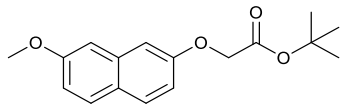

δ_H(400 MHz, DMSO$_{d6}$): 9.65 (0.08H, s, COOH), 8.30 (s, $CHCl_3$), 7.75-7.72 (2H, m, ArH), 7.18-7.15 (2H, m, ArH), 7.02-6.98 (2H, m, ArH), 4.73 (2H, s, 7MeO2Nap-O**C**$\mathbf{H_2}$), 3.84 (3H, s, **7Me**O2Nap), 1.44 (9H, s, O^{t}Bu).

7MeO2Nap-OH

The tButyl group was removed using the Boc protecting group removal method previously discussed in the Experimental Methods (Chapter 5). All subsequent steps follow the same methods as described in the Experimental Methods.

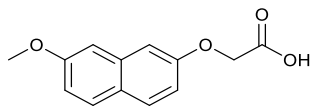

δ_H(400 MHz, DMSO$_{d6}$): 7.76-7.72 (2H, m, ArH), 7.22-7.21 (2H, m, ArH), 7.04-6.98 (2H, m, ArH), 4.77 (2H, s, 7MeO2Nap-O**C**$\mathbf{H_2}$), 3.85 (3H, s, **7Me**O2Nap).

Boc-FV-OMe

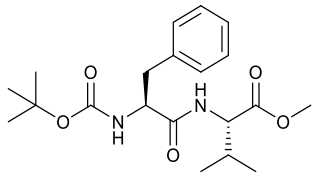

δ_H(400 MHz, DMSO$_{d6}$): 8.18 (0.2H, d, *J* = 8.3 Hz, NH), 8.08 (0.8H, d, *J* = 8.3 Hz, NH), 7.33-7.16 (5H, m, ArH), 6.92 (0.8H, d, *J* = 8.6 Hz, NH), 6.46 (0.2H, d, *J* = 8.6 Hz, NH), 4.29-4.23 (1H, m, * C**H**CH$_2$Ph), 4.21 (1H, dd, *J* = 6.3, 8.3 Hz, * C**H**CH(CH$_3$)$_2$), 3.63 (3H, s, COOCH$_3$), 2.94 (1H, dd, *J* = 4.2, 13.8 Hz, C**H$_2$**Ph), 2.72 (1H, dd, *J* = 10.5, 13.8 Hz, C**H$_2$**Ph), 2.09-1.99 (1H, m, C**H**(CH$_3$)$_2$), 1.29 (7H, s, COO(CH$_3$)$_3$), 1.24 (2H, s, COO(CH$_3$)$_3$), 0.91-0.87 (6H, m, CH(C**H$_3$)$_2$**).

TFA.FV-OMe

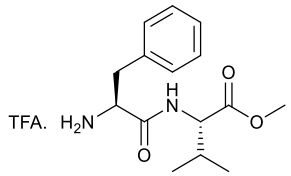

δ_H(400 MHz, DMSO$_{d6}$): 8.70 (1H, d, *J* = 8.2 Hz, NH), 8.17 (s, NH_3^+), 7.35-7.24 (5H, m, ArH), 4.21, (1H, dd, *J* = 6.3, 8.1 Hz, *C**H**CH(CH$_3$)$_2$), 4.13 (1H, dd, *J* = 6.2, 7.5 Hz, *C**H**CH$_2$Ph), 3.63 (3H, s, COOCH$_3$), 3.08 (1H, dd, *J* = 5.9, 14.0 Hz, *C**H**), 2.95 (1H, dd, *J* = 7.7, 14.0 Hz, *CHC**H$_2$**Ph), 2.08-2.00 (1H, m, C**H**(CH$_3$)$_2$), 0.90 (6H,dd, *J* = 6.9, 6.9 Hz, CH(C**H$_3$)$_2$**).

7MeO2NapFV-OMe

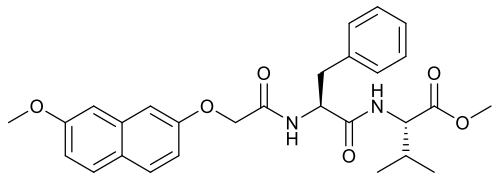

δ_H(400 MHz, DMSO$_{d6}$): 8.40 (1H, d, *J* = 8.1 Hz, NH), 8.17 (1H, d, *J* = 8.4 Hz, NH), 7.74-7.72 (2H, m, ArH), 7.25-7.10 (7H, m, ArH), 7.02-6.98 (2H, m, ArH), 4.77-4,74 (1H, m, *C**H**), 4.53 (2H, s, 7MeO2Nap-OC**H$_2$**), 4.18 (1H, dd, *J* = 6.5, 8.0 Hz, *CH), 3.85 (3H, s, OCH$_3$), 3.83 (3H, s, COOCH$_3$), 3.03 (1H, dd, *J* = 4.4, 13.9 Hz, C**H$_2$**Ph), 2.89 (1H, dd, *J* = 9.5, 13.8 Hz, C**H$_2$**Ph), 2.08-1.98 (1H, m, C**H**(CH$_3$)$_2$), 0.87 (3H, d, *J* = 6.8 Hz, CH(C**H$_3$)$_2$**), 0.84 (3H, d, *J* = 6.8 Hz, CH(C**H$_3$)$_2$**).

7MeO2NapFV –final compound, previously synthesised.[2]

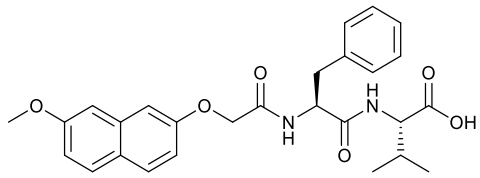

White solid, 75 % yield final step.

δ_H(400 MHz, DMSO$_{d6}$): 12.71 (0.8H, s, COOH), 8.24 (1H, d, *J* = 8.5 Hz, NH), 8.15 (1H, d, *J* = 8.5 Hz, NH), 7.74-7.72 (2H, m, ArH), 7.26-7.10 (7H, m, ArH), 7.02-6.97 (2H, m, ArH), 4.79-4,73 (1H, m, *C**H**), 4.54 (2H, s, 7MeO2Nap-OC**H$_2$**), 4.17 (1H, dd, *J* = 5.8, 8.4 Hz, *C**H**), 3.86 (3H, s, OCH_3), 3.05 (1H, dd, *J* = 4.0, 13.8 Hz, C**H$_2$**Ph), 2.90 (1H, dd, *J* = 9.6, 13.8 Hz, C**H$_2$**Ph), 2.12-2.00 (1H, m, C**H**$(CH_3)_2$), 0.88 (3H, d, *J* = 4.3 Hz, CH(C**H$_3$)$_2$**), 0.86 (3H, d, *J* = 4.3 Hz, CH(C**H$_3$)$_2$**).

δ_{13C}(100 MHz, DMSO$_{d6}$): 173.29 (C=O), 171.58 (C=O), 167.93 (C=O), 158.22 (ArC), 156.52 (ArC), 137.92 (ArC), 135.98 (ArC), 129.72 (ArC), 129.57 (ArCH), 129.49 (ArCH), 128.44 (ArCH), 126.75 (ArCH), 124.53 (ArC), 116.63 (ArC), 116.15 (ArCH), 107.28 (ArCH), 105.88 (ArCH), 67.13 (7MeO2NapO**C**H$_2$), 57.79 (*CH), 55.55 (OCH_3), 53.68 (*CH), 37.87 (**C**H_2Ph), 30.32 (**C**H$(CH_3)_2$), 19.52 (CH(**C**$H_3)_2$), 18.47 (CH(**C**$H_3)_2$).

HRMS (ESI) m/z: ([M+Na]+). Accurate Mass calculated for $C_{27}H_{30}N_2NaO_6$: 501.1996. Found: 501.1997.

<u>CarbFV</u>

CarbFV-OMe

The N-Carbazolyl-acetylchloride group was used pre-made and coupled to the already synthesised TFA.FV-OMe.

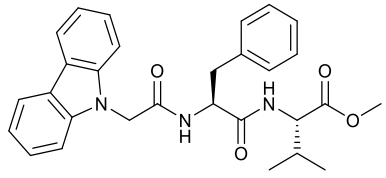

δ_H(400 MHz, DMSO$_{d6}$): 8.61 (1H, d, *J* = 8.6 Hz, NH), 8.39 (1H, d, *J* = 8.1 Hz, NH), 8.12-8.10 (2H, m, ArH), 7.38-7.16 (11H, m, ArH), 5.04 (1H, d, *J* = 16.8 Hz, Carb-**CH$_2$**), 4.93 (1H, d, *J* = 16.8 Hz, Carb-**CH$_2$**), 4.76-4.70 (1H, m, *C**H**CH_2Ph), 4.19 (1H, dd, *J* = 6.4, 8.0 Hz, *C**H**CH$(CH_3)_2$), 3.65 (3H, s, $COOCH_3$), 3.04 (1H, dd, *J* = 4.3, 13.7 Hz, C**H$_2$**Ph), 2.81

(1H, dd, *J* = 10.0, 13.9 Hz, C**H**$_2$Ph), 2.09-1.98 (1H, m, C**H**(CH_3)$_2$), 0.88-0.85 (6H, m, CH(C**H**$_3$)$_2$).

CarbFV – final compound, previously synthesised.[2]

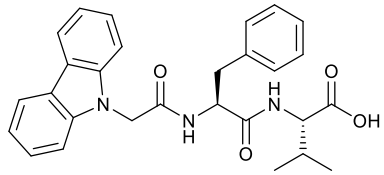

White solid, 99 % yield final step.

δ_H(400 MHz, DMSO$_{d6}$): 8.57 (1H, d, *J* = 8.6 Hz, NH), 8.22 (1H, d, *J* = 8.5 Hz, NH), 8.11-8.09 (2H, m, ArH), 7.37-7.15 (11H, m, ArH), 5.03 (1H, d, *J* = 16.8 Hz, Carb-**CH$_2$**), 4.92 (1H, d, *J* = 16.8 Hz, Carb-**CH$_2$**), 4.76-4.70 (1H, m, *CHC**H$_2$**Ph), 4.16 (1H, dd, *J* = 5.8, 8.4 Hz, *C**H**CH(CH_3)$_2$), 3.05 (1H, dd, *J* = 4.0, 13.9 Hz, C**H$_2$**Ph), 2.81 (1H, dd, *J* = 10.0, 13.7 Hz, C**H$_2$**Ph), 2.09-2.01 (1H, m, C**H**(CH_3)$_2$), 0.86 (6H, d, *J* = 6.8 Hz, CH(C**H$_3$)$_2$**).

δ_C(100 MHz, DMSO$_{d6}$): 173.29 (C=O), 171.79 (C=O), 167.58 (C=O), 140.93 (ArC), 138.05 (ArC), 129.85 (ArCH),128.51 (ArCH), 126.78 (ArCH), 126.04 (ArC), 122.55 (ArC),120.47 (ArCH), 119.35 (ArCH), 109.82 (ArCH), 57.77 (*CH), 53.94 (*CH), 45.68 (Carb-**CH$_2$**), 38.29 (**CH$_2$**Ph), 30.25 (**C**H(CH_3)$_2$, 19.57 (CH_3), 18.50 (CH_3). Assignments were confirmed using HSQC spectrum.

HRMS (ESI) m/z: ([M+Na]+). Accurate Mass calculated for $C_{28}H_{29}N_3NaO_4$: 494.2050. Found: 494.2056.

<u>CarbIF</u>

Boc-IF-OMe

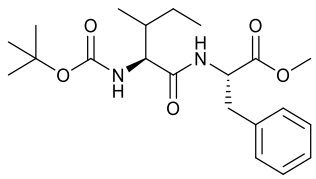

δ_H(400 MHz, DMSO$_{d6}$): 8.25 (1H, d, *J* = 7.6 Hz, NH), 7.29-7.18 (5H, m, ArH), 6.59 (1H, d, *J* = 9.1 Hz, NH), 4.51-4.46 (1H, m, *CH), 3.82-3.78 (1H, m, *CH), 3.56 (3H, s, $COOCH_3$), 3.02 (1H, dd, *J* = 5.6, 13.9 Hz, CH_2), 2.92 (1H, dd, *J* = 9.1, 13.8 Hz, CH_2), 1.61-1.56 (1H, m, C**H**CH_3), 1.37 (9H, s, $COOC(CH_3)_3$), 1.33-1.29 (1H, m, C**H$_2$**CH_3), 1.06-0.97 (1H, m,

C**H**$_2$CH$_3$), 0.76 (3H, t, *J* = 7.4 Hz, CHC**H**$_3$), 0.71 (3H, t, *J* = 6.8 Hz, CH$_2$C**H**$_3$). Assignments were confirmed using COSY spectrum.

TFA.IF-OMe

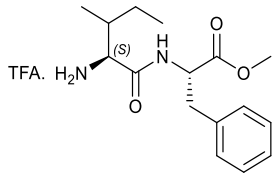

δ_H(400 MHz, DMSO$_{d6}$): 8.84 (1H, d, *J* = 7.2 Hz, NH), 8.05 (3H, s, NH_3^+), 7.32-7.21 (5H, m, ArH), 4.59-4.53 (1H, m, *CH), 3.64-3.63 (1H, m, *CH), 3.59 (3H, s, COOCH$_3$), 3.07 (1H, dd, *J* = 5.7, 14.1 Hz, CH$_2$), 2.98 (1H, dd, *J* = 8.6, 14.1 Hz, CH$_2$), 1.88-1.79 (1H, m, C**H**CH$_3$), 1.49-1.39 (1H, m, C**H**$_2$CH$_3$), 1.15-1.05 (1H, m, C**H**$_2$CH$_3$), 0.92 (3H, d, *J* = 6.9 Hz, CHC**H**$_3$), 0.85 (3H, t, *J* = 7.4 Hz, CH$_2$C**H**$_3$). Assignments were confirmed using COSY spectrum.

CarbIF-OMe

The N-Carbazolyl-acetylchloride group was used pre-made and coupled to the already synthesised TFA.IF-OMe.

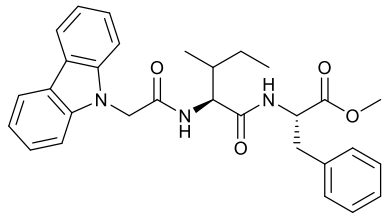

δ_H(400 MHz, DMSO$_{d6}$): 8.54 (1H, d, *J* = 7.3 Hz, NH), 8.33 (1N, d, *J* = 9.8 Hz, NH), 8.15-8.13 (2H, m, ArH), 7.52-7.50 (2H, m, ArH), 7.44-7.40 (2H, m, ArH), 7.26-7.18 (7H, m, ArH), 5.13 (1H, d, *J* = 16.7 Hz, Carb-C**H**$_2$), 5.05 (1H, d, *J* = 16.7 Hz, Carb-C**H**$_2$), 4.51-4.45 (1H, m, *C**H**CH$_2$Ph), 4.27 (1H, dd, *J* = 7.3 Hz, 9.0 Hz, *CH), 3.56 (3H, s, COOCH$_3$), 3.01 (1H, dd, *J* = 6.1, 14.0 Hz, C**H**$_2$Ph), 2.91 (1H, dd, *J* = 8.8, 13.9 Hz, C**H**$_2$Ph), 1.78-1.68 (1H, m, C**H**CH$_3$), 1.46-1.37 (1H, m, C**H**$_2$CH$_3$), 1.12-1.01 (1H, m, C**H**$_2$CH$_3$), 0.82-0.77 (6H, m, CH(C**H**$_3$)$_2$). Assignments were confirmed using COSY spectrum.

CarbIF – final compound, previously synthesised.[2]

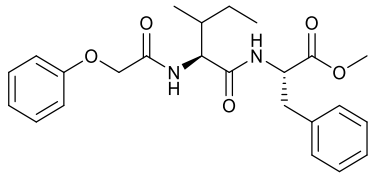

White solid, 99 % yield final step.

δ_H(400 MHz, DMSO$_{d6}$): 12.68 (0.81H, s, COOH), 8.36 (1H, d, *J* = 7.7 Hz, NH), 8.31 (1N, d, *J* = 9.2 Hz, NH), 8.15-8.13 (2H, m, ArH), 7.52-7.50 (2H, m, ArH), 7.43-7.39 (2H, m, ArH), 7.24-7.18 (7H, m, ArH), 5.13 (1H, d, *J* = 16.7 Hz, Carb-**C**$\mathbf{H_2}$), 5.04 (1H, d, *J* = 16.7 Hz, Carb-**C**$\mathbf{H_2}$), 4.47-4.41 (1H, m, *C**H**CH_2Ph), 4.27 (1H, dd, *J* = 7.1 Hz, 9.1 Hz, *CH), 3.04 (1H, dd, *J* = 5.4, 14.0 Hz, C$\mathbf{H_2}$Ph), 2.88 (1H, dd, *J* = 9.0, 14.0 Hz, C$\mathbf{H_2}$Ph), 1.79-1.69 (1H, m, C**H**CH_3), 1.47-1.37 (1H, m, C$\mathbf{H_2}CH_3$), 1.10-0.99 (1H, m, C$\mathbf{H_2}CH_3$), 0.82-0.76 (6H, m, CH(C$\mathbf{H_3}$)$_2$). Assignments were confirmed using COSY spectrum.

δ_{13}(100 MHz, DMSO$_{d6}$): 173.24 (C=O), 171.33 (C=O), 167.55 (C=O), 141.04 (ArC), 137.97 (ArC), 129.50 (ArCH), 128.62 (ArCH), 126.87 (ArCH), 126.05 (ArCH), 122.61 (ArC), 120.59 (ArCH), 119.40 (ArCH), 109.82 (ArCH), 56.88 (*CH), 53.97 (*CH), 45.69 (Carb-**C**CH_2), 37.75(**C**H_2Ph), 37.04 (**C**H_2Ph), 24.51 (**C**H_2CH_3), 15.73 (CH_3), 11.52 (CH_3). Assignments were confirmed using HSQC spectrum.

HRMS (ESI) m/z: ([M+Na]+). Accurate Mass calculated for $C_{29}H_{31}N_3NaO_4$: 471.2137. Found: 471.20116.

<u>1NapVV</u>

1NapV-OMe

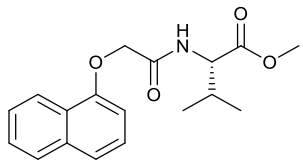

1NapVV was synthesised by addition of one V-OMe residue at a time to allow purification by precipitation in 1M HCl after each ester deprotection. The protocols used for peptide coupling and ester deprotection were the same as previously described.

δ_H(400 MHz, DMSO$_{d6}$): 8.41 (1H, d, *J* = 8.3 Hz, NH), 8.24-8.21 (1H, m, ArH), 7.89 -7.87 (1H, m, ArH), 7.56-7.49 (3H, m, ArH), 7.42-7.38 (1H, m, ArH), 6.89-6.87 (1H, m, ArH),

4.84 (1H, d, *J* = 14.6 Hz, 1Nap-O**CH$_2$**), 4.79 (1H, d, *J* = 14.4 Hz, 1Nap-OC**H$_2$**), 4.28 (1H, dd, *J* = 6.3, 8.3 Hz, *CH), 3.66 (3H, s, COOCH$_3$), 2.16-2.07 (1H, m, C**H**(CH$_3$)$_2$), 0.90-0.87 (6H, m, CH(C**H$_3$)$_2$**).

1NapV-OH

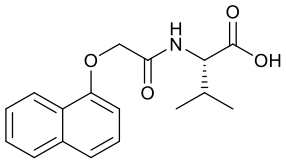

δ_H(400 MHz, DMSO$_{d6}$): 8.24-8.19 (2H, m, ArH, NH), 7.90 -7.88 (1H, m, ArH), 7.56-7.50 (3H, m, ArH), 7.42-7.38 (1H, m, ArH), 6.92-6.90 (1H, m, ArH), 4.84 (1H, d, *J* = 14.5 Hz, 1Nap-O**CH$_2$**), 4.80 (1H, d, *J* = 14.4 Hz, 1Nap-O**CH$_2$**), 4.26 (1H, dd, *J* = 5.6, 8.6 Hz, *CH), 2.18-2.09 (1H, m, C**H**(CH$_3$)$_2$), 0.91 (3H, d, *J* = 4.2 Hz, CH(C**H$_3$)$_2$**), 0.89 (3H, d, *J* = 4.2 Hz, CH(C**H$_3$)$_2$**).

1NapVV-OMe

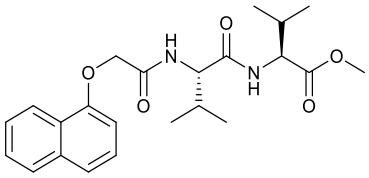

δ_H(400 MHz, DMSO$_{d6}$): 8.33 (1H, d, *J* = 7.7 Hz, NH), 8.23-8.21 (1H, m, ArH), 7.98 (1H, d, *J* = 9.0 Hz, NH), 7.91 -7.88 (1H, m, ArH), 7.57-7.50 (3H, m, ArH), 7.42-7.38 (1H, m, ArH), 6.92-6.90 (1H, m, ArH), 4.82 (1H, d, *J* = 14.5 Hz, 1Nap-O**CH$_2$**), 4.77 (1H, d, *J* = 14.4 Hz, 1Nap-O**CH$_2$**), 4.45 (1H, dd, *J* = 6.5, 9.0 Hz, *CH), 4.17 (1H, dd, *J* = 6.3, 7.6 Hz, *CH), 3.63 (3H, s, COOCH$_3$), 2.10-1.99 (2H, m, C**H**(CH$_3$)$_2$), 0.91-0.87 (9H, m, CH(C**H$_3$)$_2$**), 0.83 (3H, d, *J* = 6.8 Hz, CH(C**H$_3$)$_2$**).

1NapVV –final compound, previously synthesised.[5]

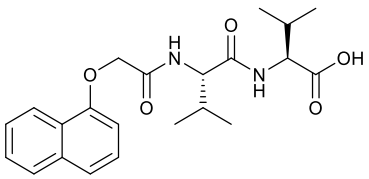

White solid, 96 % yield final step.

δ_H(400 MHz, DMSO$_{d6}$): 8.23-8.21 (1H, m, ArH), 8.16 (1H, d, *J* = 8.1 Hz, NH), 7.98 (1H, d, *J* = 9.0 Hz, NH), 7.91 -7.88 (1H, m, ArH), 7.57-7.50 (3H, m, ArH), 7.41-7.37 (1H, m, ArH), 6.92-6.90 (1H, m, ArH), 4.82 (1H, d, *J* = 14.5 Hz, 1Nap-O**C**$\mathbf{H_2}$), 4.77 (1H, d, *J* = 14.4 Hz, 1Nap-O**C**$\mathbf{H_2}$), 4.46 (1H, dd, *J* = 6.4, 8.9 Hz, *CH), 4.14 (1H, dd, *J* = 5.9, 8.1 Hz, *CH), 2.10-2.00 (2H, m, C**H**(CH_3)$_2$), 0.91-0.87 (9H, m, CH(C$\mathbf{H_3}$)$_2$), 0.83 (3H, d, *J* = 6.8 Hz, CH(C$\mathbf{H_3}$)$_2$).

δ_{13}(100 MHz, DMSO$_{d6}$): 173.18 (C=O), 167.73 (C=O), 153.56 (C=O), 134.53 (ArC), 128.00 (ArCH), 127.04 (ArCH), 126.50 (ArCH), 125.98 (ArCH), 125.21 (ArC), 121.88 (ArCH), 121.11 (ArCH), 106.15 (ArCH), 67.50 (1Nap-O**C**H_2), 58.15 (*CH), 57.32 (*CH), 31.50(**C**H(CH_3)$_2$), 30.30 (**C**H(CH_3)$_2$), 19.67 (CH(**C**H_3)$_2$), 18.58 (CH(**C**H_3)$_2$), 18.23 (CH(**C**H_3)$_2$). Assignments were confirmed using HSQC spectrum.

HRMS (ESI) m/z: ([M+Na]+). Accurate Mass calculated for $C_{22}H_{28}N_2NaO_5$: 423.1890. Found: 423.1901.

Appendix 2.2: Absorbance and HT data

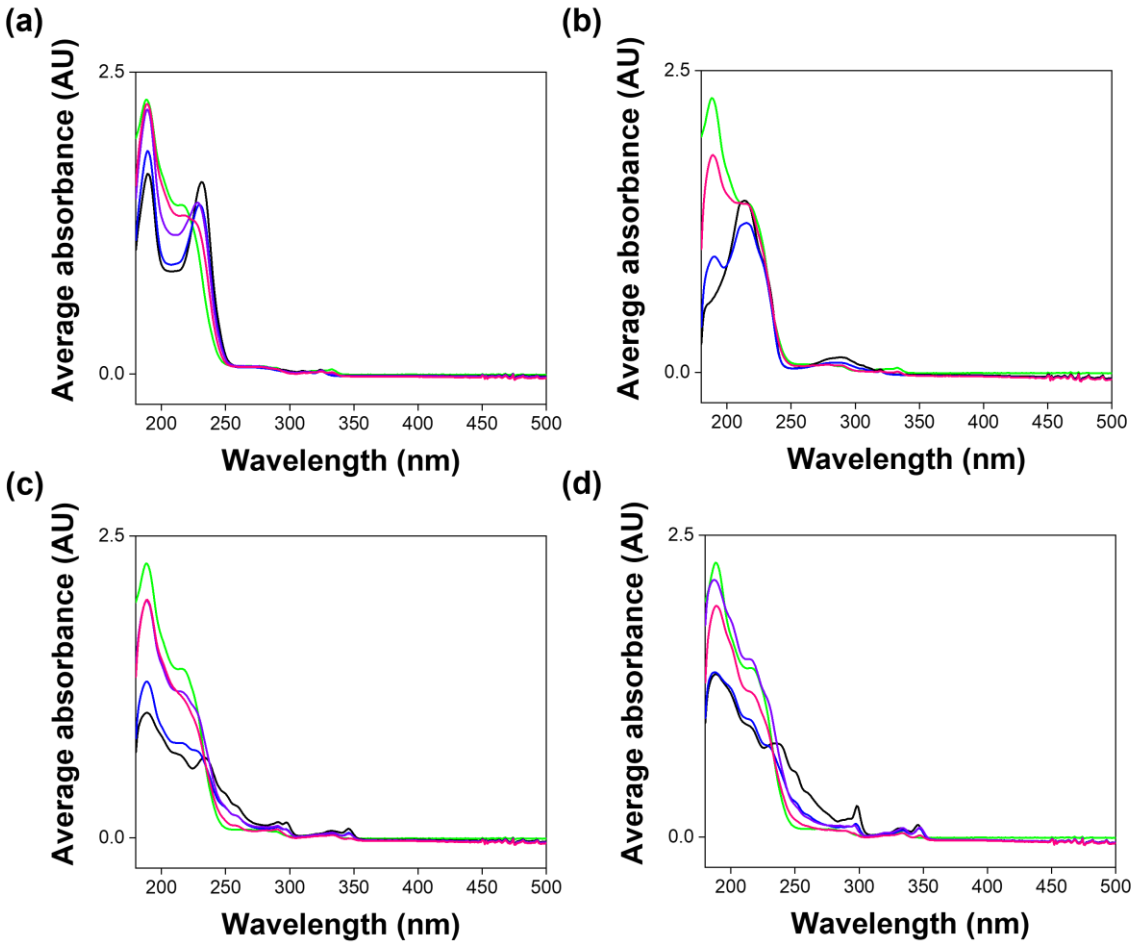

Figure A2.2.1. Absorbance spectra recorded concurrently with CD spectra of single and multicomponent systems of (a) 7MeO2NapFV, (b) 1NapVV, (c) CarbFV and (d) CarbIF at concentration ratios second component:2Nap-(*SS*)-FF of 10 mg/mL:0 mg/mL (black), 7.5 mg/mL:2.5 mg/mL (blue), 5 mg/mL:5 mg/mL (purple) and 2.5 mg/mL:7.5 mg/mL (pink) at pH 10.5. The spectrum recorded from 2Nap-(*SS*)-FF 10 mg/mL (green) is shown in each plot for easy comparison with the multicomponent systems. All data was collected in triplicate and averaged.

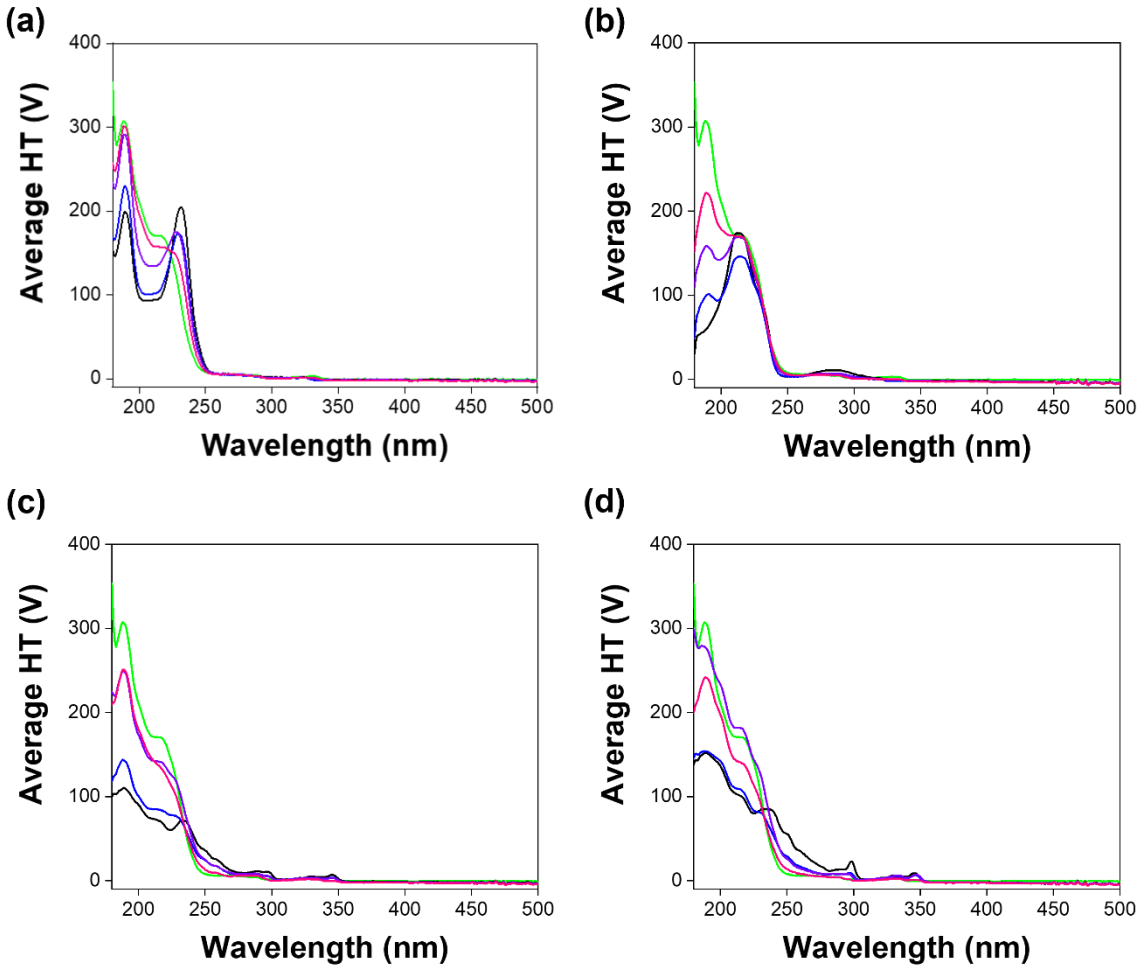

Figure A2.2.2. HT spectra recorded concurrently with CD spectra of single and multicomponent systems of (a) 7MeO2NapFV, (b) 1NapVV, (c) CarbFV and (d) CarbIF at concentration ratios second component:2Nap-(*SS*)-FF of 10 mg/mL:0 mg/mL (black), 7.5 mg/mL:2.5 mg/mL (blue), 5 mg/mL:5 mg/mL (purple) and 2.5 mg/mL:7.5 mg/mL (pink) at pH 10.5. The spectrum recorded from 2Nap-(*SS*)-FF 10 mg/mL (green) is shown in each plot for easy comparison with the multicomponent systems. All data was collected in triplicate and averaged.

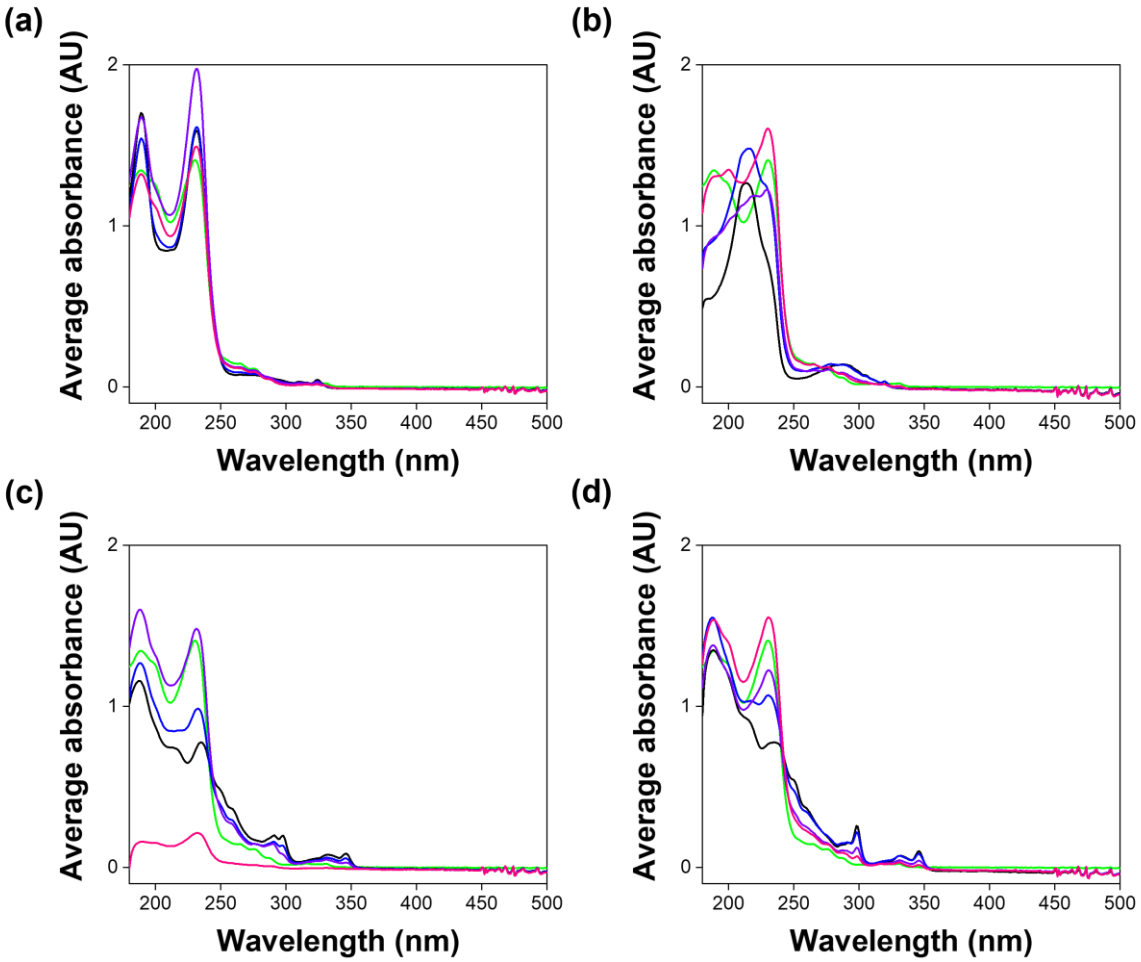

Figure A2.2.3. Absorbance spectra recorded concurrently with CD spectra of single and multicomponent systems of (a) 7MeO2NapFV, (b) 1NapVV, (c) CarbFV and (d) CarbIF at concentration ratios second component:2Nap-(*RS*)-FF of 10 mg/mL:0 mg/mL (black), 7.5 mg/mL:2.5 mg/mL (blue), 5 mg/mL:5 mg/mL (purple) and 2.5 mg/mL:7.5 mg/mL (pink) at pH 10.5. The spectrum recorded from 2Nap-(*RS*)-FF 10 mg/mL (green) is shown in each plot for easy comparison with the multicomponent systems. All data was collected in triplicate and averaged.

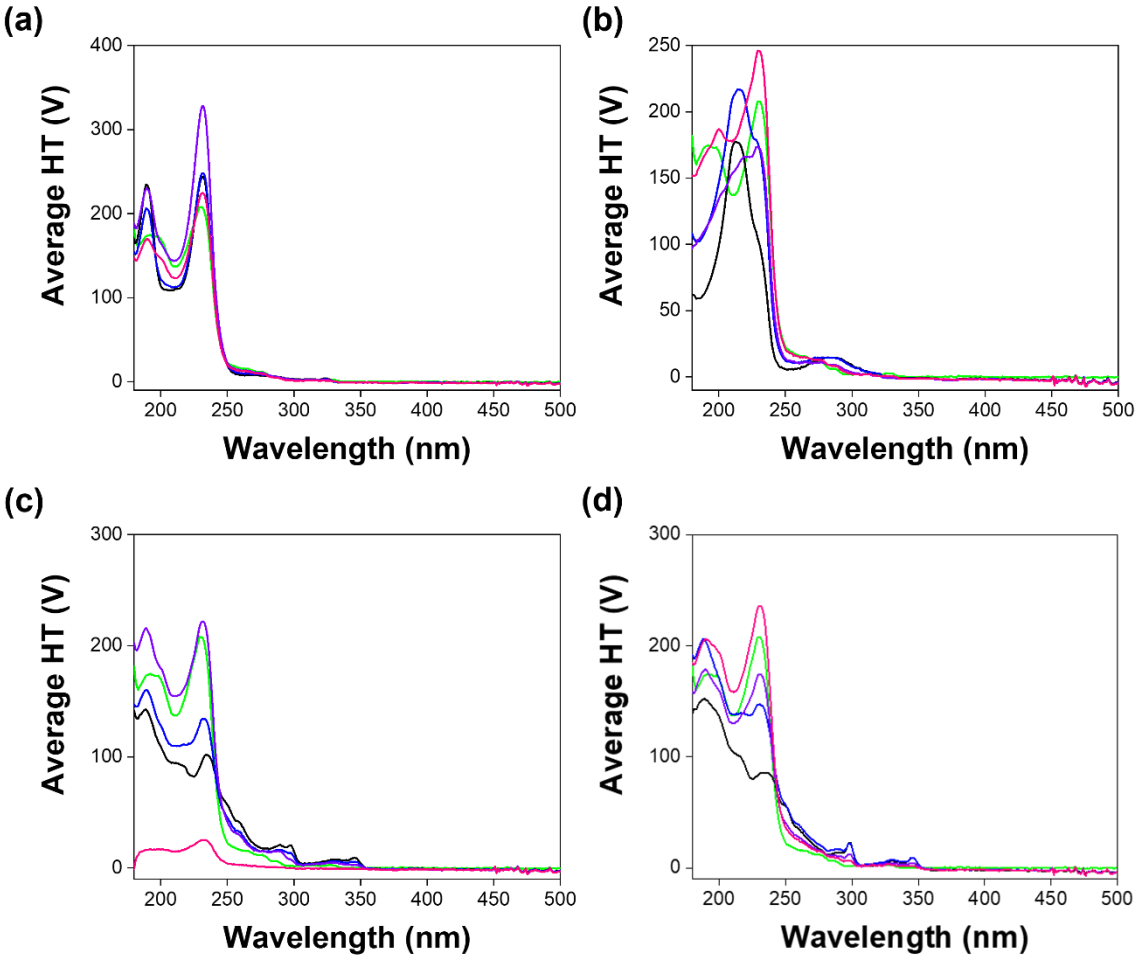

Figure A2.2.4. HT spectra recorded concurrently with CD spectra of single and multicomponent systems of (a) 7MeO2NapFV, (b) 1NapVV, (c) CarbFV and (d) CarbIF at concentration ratios second component:2Nap-(*RS*)-FF of 10 mg/mL:0 mg/mL (black), 7.5 mg/mL:2.5 mg/mL (blue), 5 mg/mL:5 mg/mL (purple) and 2.5 mg/mL:7.5 mg/mL (pink) at pH 10.5. The spectrum recorded from 2Nap-(*RS*)-FF 10 mg/mL (green) is shown in each plot for easy comparison with the multicomponent systems. All data was collected in triplicate and averaged.

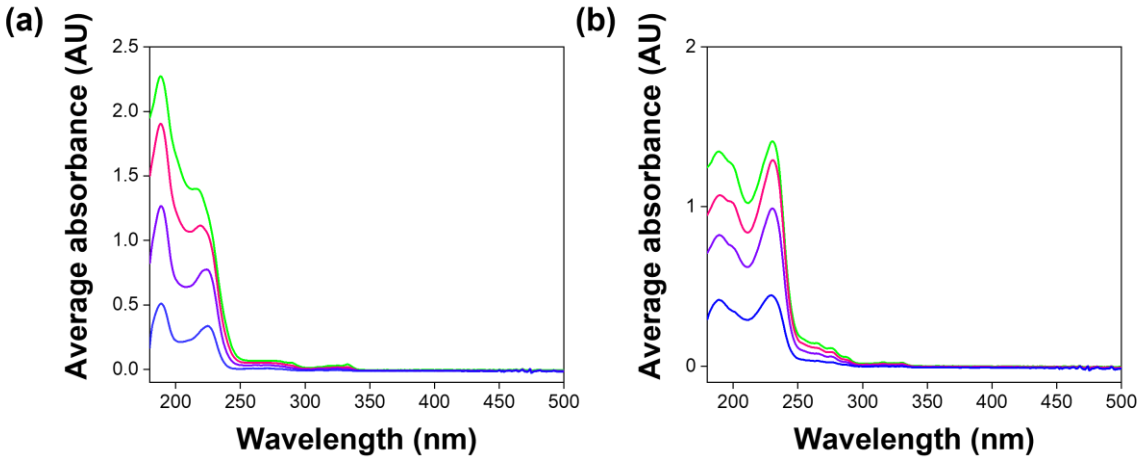

Figure A2.2.5. Absorbance spectra collected concurrently with CD spectra of (a) 2Nap-(*SS*)-FF and (b) 2Nap-(*RS*)-FF single component systems at concentrations of 10 mg/mL (green), mg/mL (pink), 5 mg/mL (purple) and 2.5 mg/mL (blue) at pH 10.5. All data was collected in triplicate and averaged.

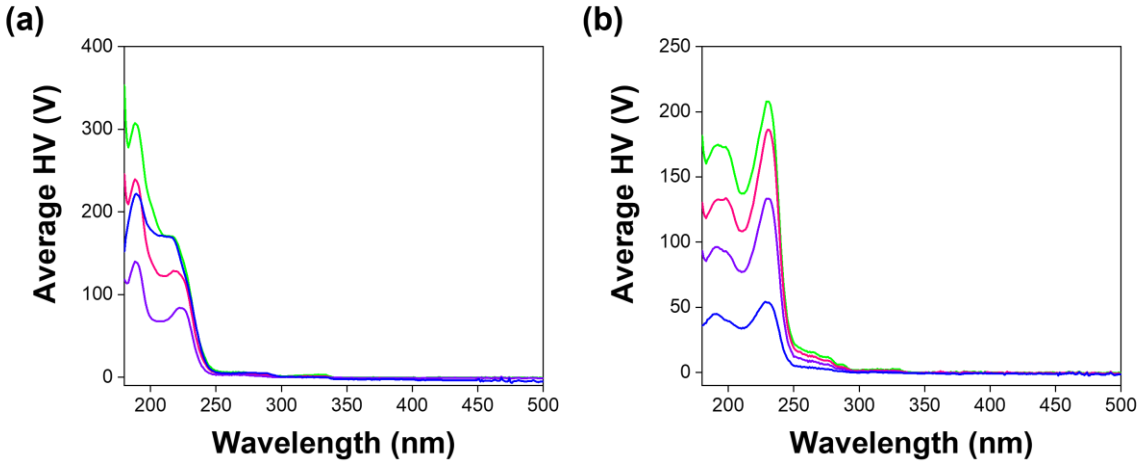

Figure A2.2.6. HT spectra collected concurrently with CD spectra of (a) 2Nap-(*SS*)-FF and (b) 2Nap-(*RS*)-FF single component systems at concentrations of 10 mg/mL (green), mg/mL (pink), 5 mg/mL (purple) and 2.5 mg/mL (blue) at pH 10.5. All data was collected in triplicate and averaged.

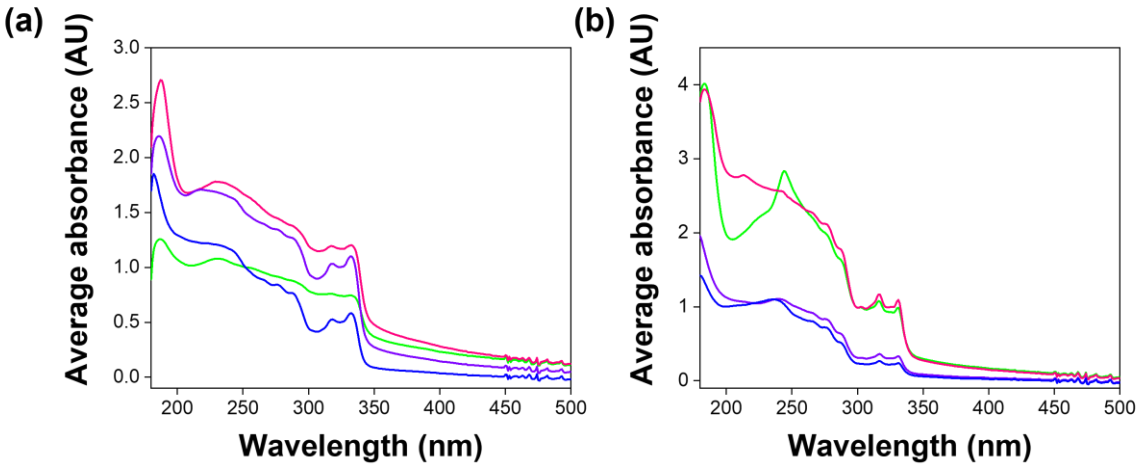

Figure A2.2.7. Absorbance spectra collected concurrently with CD spectra of (a) 2Nap-(*SS*)-FF and (b) 2Nap-(*RS*)-FF single component systems at concentrations of 10 mg/mL (green), mg/mL (pink), 5 mg/mL (purple) and 2.5 mg/mL (blue) in the gel state at low pH. All data was collected in triplicate and averaged.

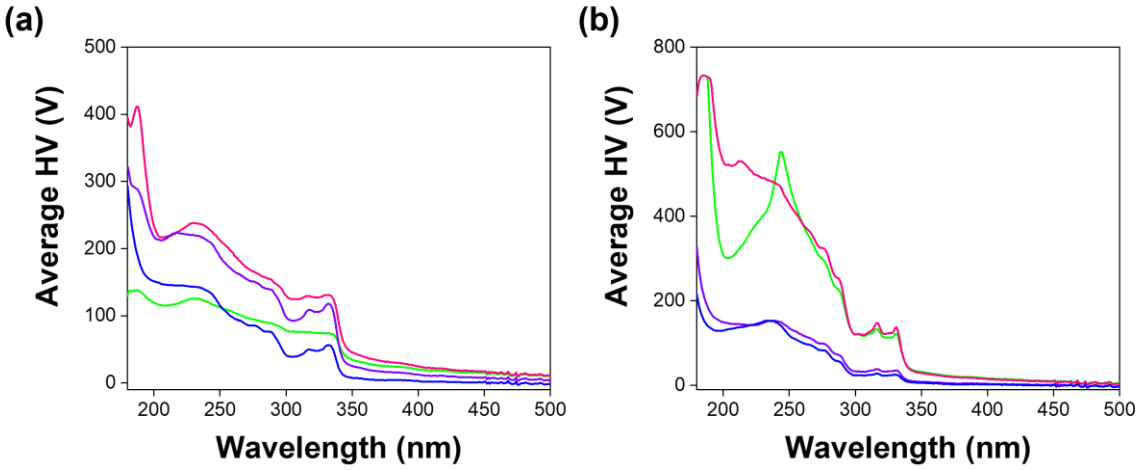

Figure A2.2.8. HT spectra collected concurrently with CD spectra of (a) 2Nap-(*SS*)-FF and (b) 2Nap-(*RS*)-FF single component systems at concentrations of 10 mg/mL (green), mg/mL (pink), 5 mg/mL (purple) and 2.5 mg/mL (blue) in the gel state at low pH. All data was collected in triplicate and averaged.

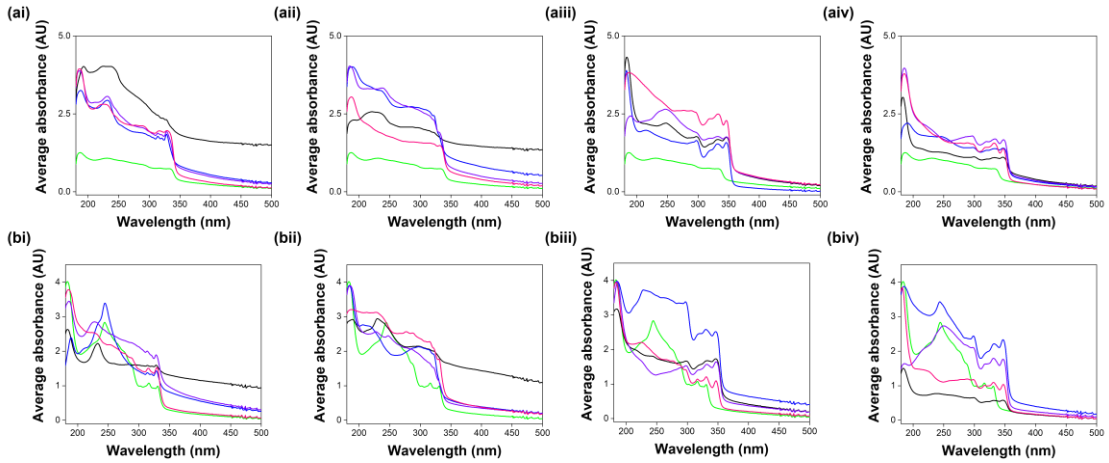

Figure A2.2.9. Absorbance spectra recorded concurrently with CD spectra of single and multicomponent systems of (i) 7MeO2NapFV, (ii) 1NapVV, (iii) CarbFV and (iv) CarbIF at concentration ratios second component: (a) 2Nap-(*SS*)-FF and (b) 2Nap-(*RS*)-FF of 10 mg/mL:0 mg/mL (black), 7.5 mg/mL:2.5 mg/mL (blue), 5 mg/mL:5 mg/mL (purple) and 2.5 mg/mL:7.5 mg/mL (pink) in the gel state at low pH. The spectra recorded from the corresponding diastereomer of 2NapFF 10 mg/mL (green) are shown in each plot for easy comparison with the multicomponent systems. All data was collected in triplicate and averaged.

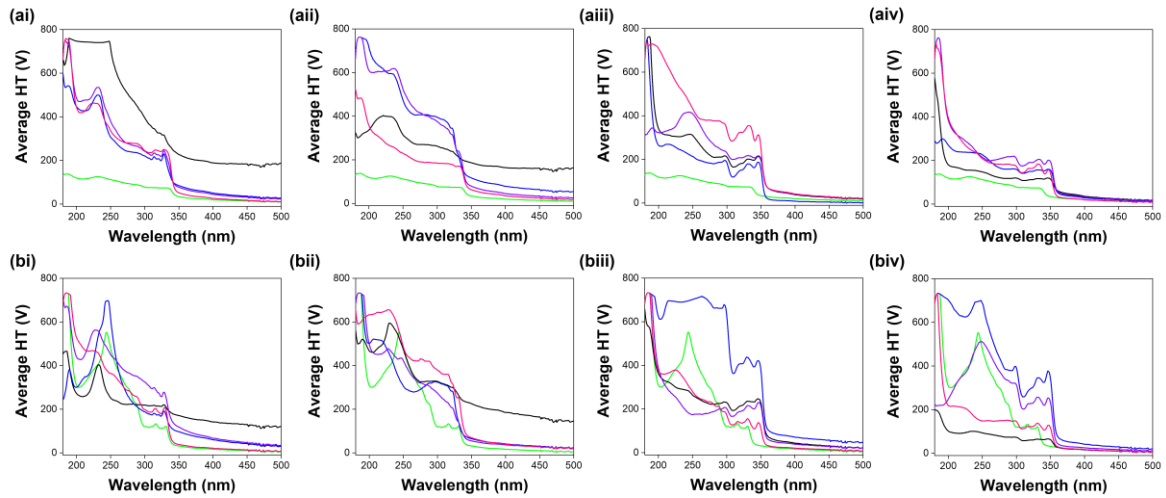

Figure A2.2.10. HT spectra recorded concurrently with CD spectra of single and multicomponent systems of (i) 7MeO2NapFV, (ii) 1NapVV, (iii) CarbFV and (iv) CarbIF at concentration ratios second component: (a)2Nap-(*SS*)-FF and (b) 2Nap-(*RS*)-FF of 10 mg/mL:0 mg/mL (black), 7.5 mg/mL:2.5 mg/mL (blue), 5 mg/mL:5 mg/mL (purple) and 2.5 mg/mL:7.5 mg/mL (pink) in the gel state at low pH. The spectra recorded from the corresponding diastereomer of 2NapFF 10 mg/mL (green) are shown in each spectrum for easy comparison with the multicomponent systems. All data was collected in triplicate and averaged.

Appendix 2.3: Rheology

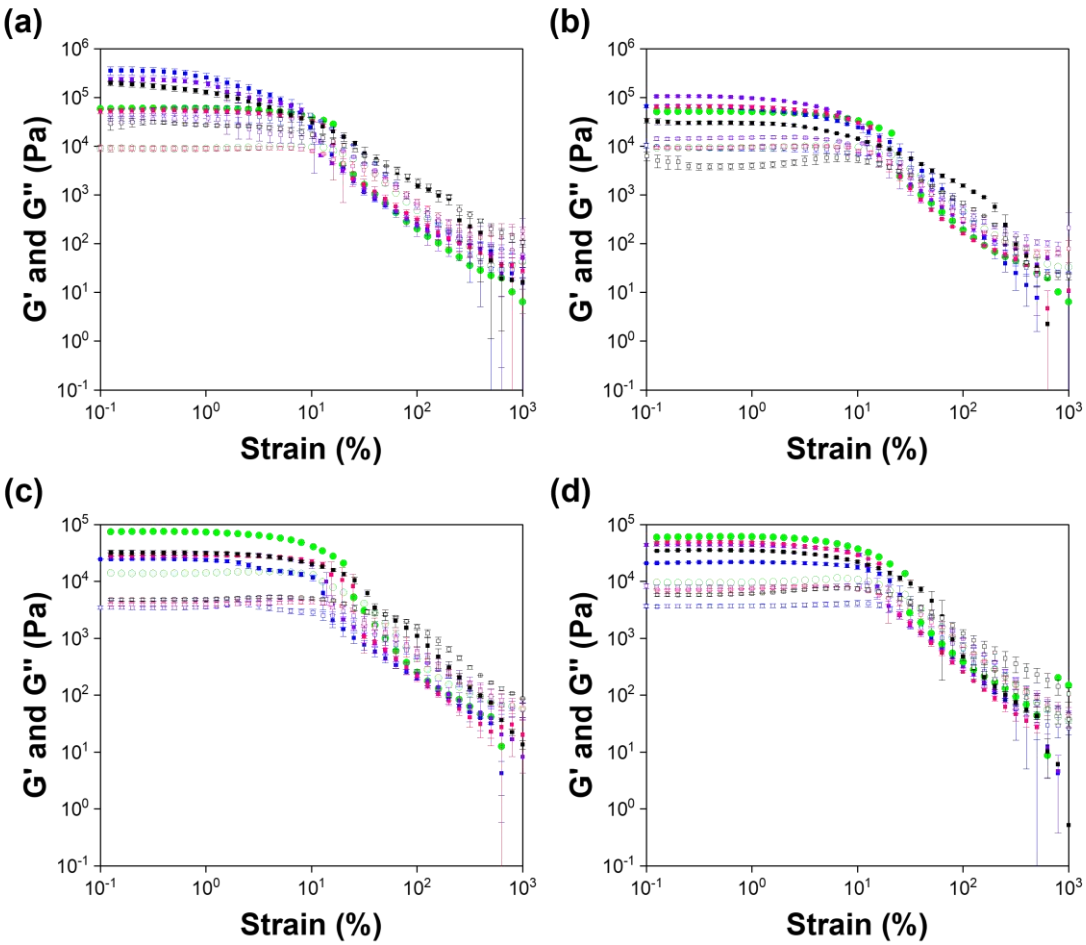

Figure A2.3.1. Strain sweeps collected from (a) 7MeO2NapFV, (b) 1NapVV, (c) CarbFV, (d) CarbIF alone at a concentration of 10 mg/mL (black) and in multicomponent systems with concentration ratios (second component:2Nap-(*SS*)-FF) 7.5 mg/mL:2.5 mg/mL (blue), 5 mg/mL:5 mg/mL (purple) and 2.5 mg/mL:7.5 mg/mL (pink). A single strain sweep from a 2Nap-(*SS*)-FF 10 mg/mL gel prepared form the same 2Nap-(*SS*)-FF stock solution as the corresponding multicomponent systems is shown in each plot for comparison.

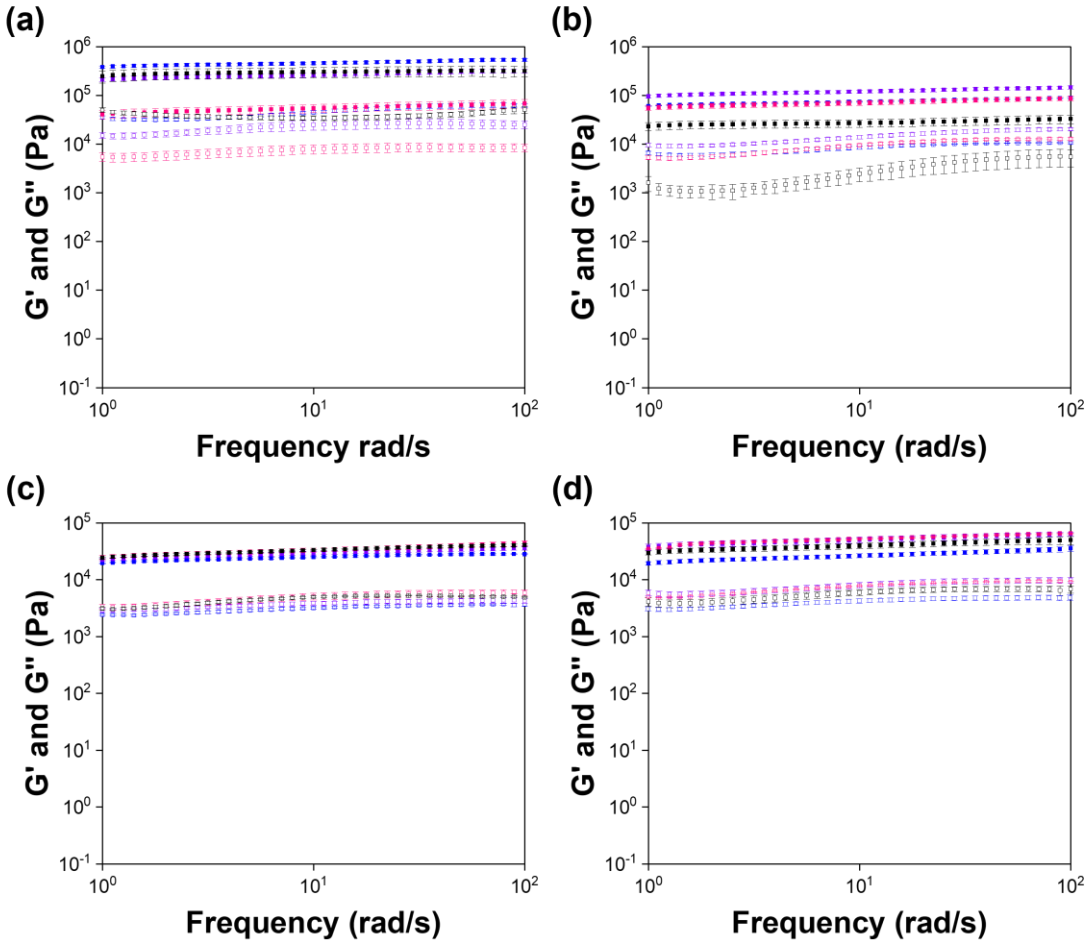

Figure A2.3.2. Frequency sweeps collected from (a) 7MeO2NapFV, (b) 1NapVV, (c) CarbFV, (d) CarbIF alone at a concentration of 10 mg/mL (black) and in multicomponent systems with concentration ratios (second component:2Nap-(*SS*)-FF) 7.5 mg/mL:2.5 mg/mL (blue), 5 mg/mL:5 mg/mL (purple) and 2.5 mg/mL:7.5 mg/mL (pink). The moduli values recorded during the frequency sweeps match those measured in the LVR of the strain sweeps.

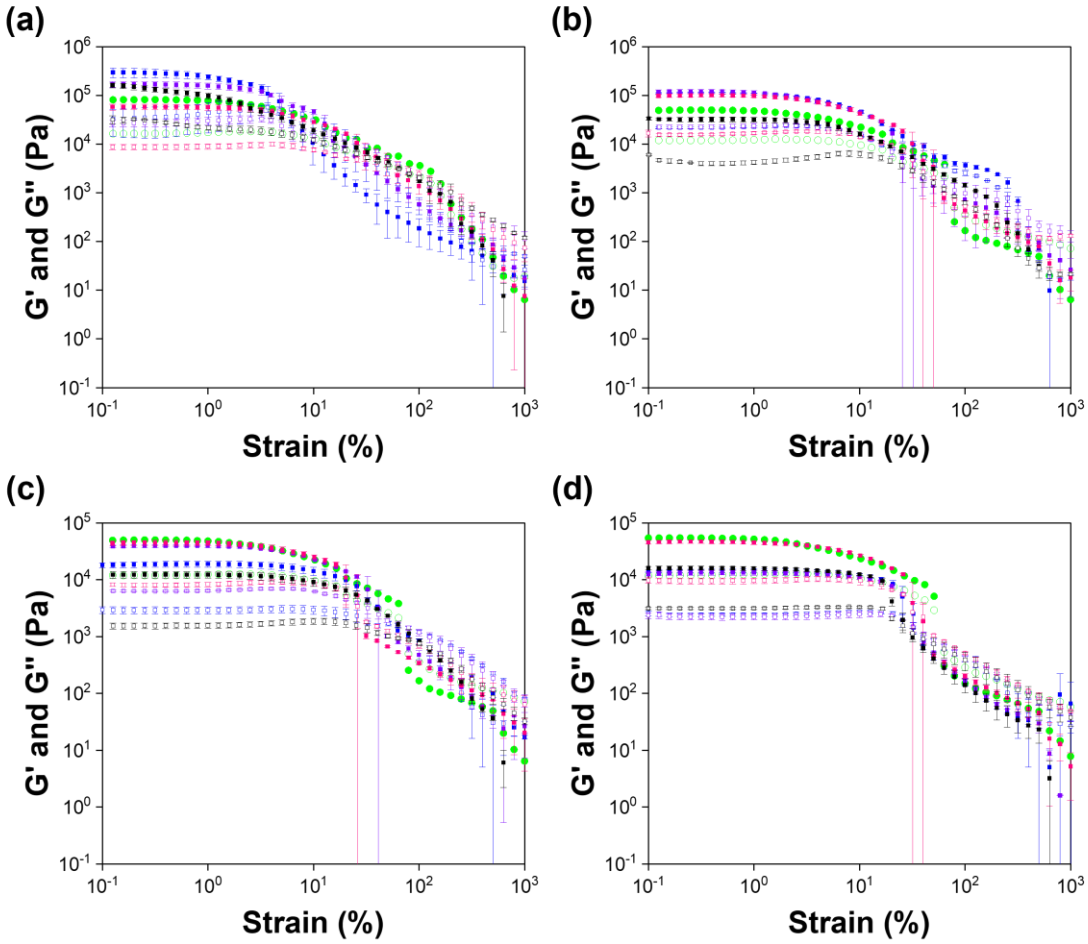

Figure A2.3.3. Strain sweeps collected from (a) 7MeO2NapFV, (b) 1NapVV, (c) CarbFV, (d) CarbIF alone at a concentration of 10 mg/mL (black) and in multicomponent systems with concentration ratios (second component:2Nap-(*RS*)-FF) 7.5 mg/mL:2.5 mg/mL (blue), 5 mg/mL:5 mg/mL (purple) and 2.5 mg/mL:7.5 mg/mL (pink). A single strain sweep from a 2Nap-(*RS*)-FF 10 mg/mL gel prepared form the same 2Nap-(*RS*)-FF stock solution as the corresponding multicomponent systems is shown in each plot for comparison.

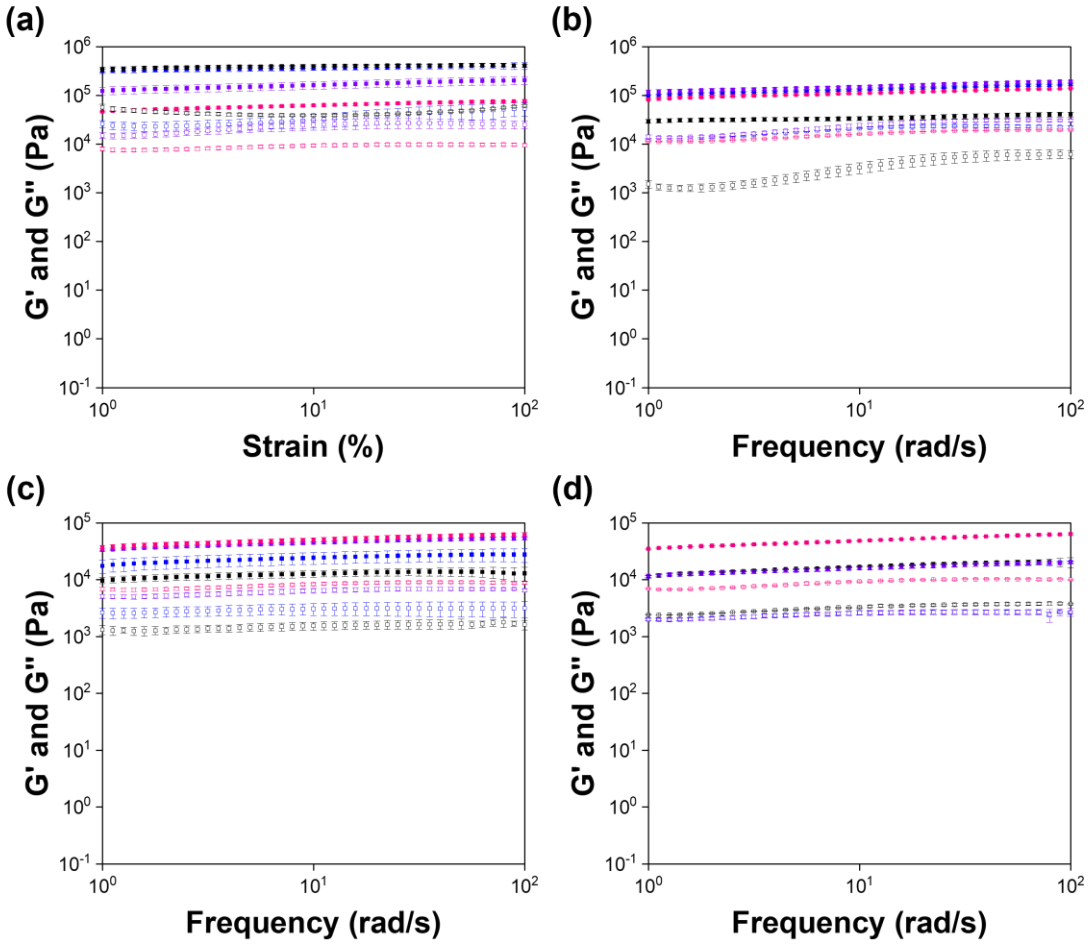

Figure A2.3.4. Frequency sweeps collected from (a) 7MeO2NapFV, (b) 1NapVV, (c) CarbFV, (d) CarbIF alone at a concentration of 10 mg/mL (black) and in multicomponent systems with concentration ratios (second component:2Nap-(*RS*)-FF) 7.5 mg/mL:2.5 mg/mL (blue), 5 mg/mL:5 mg/mL (purple) and 2.5 mg/mL:7.5 mg/mL (pink). The moduli values recorded during the frequency sweeps match those measured in the LVR of the strain sweep.

Appendix 3.1: Original synthetic scheme

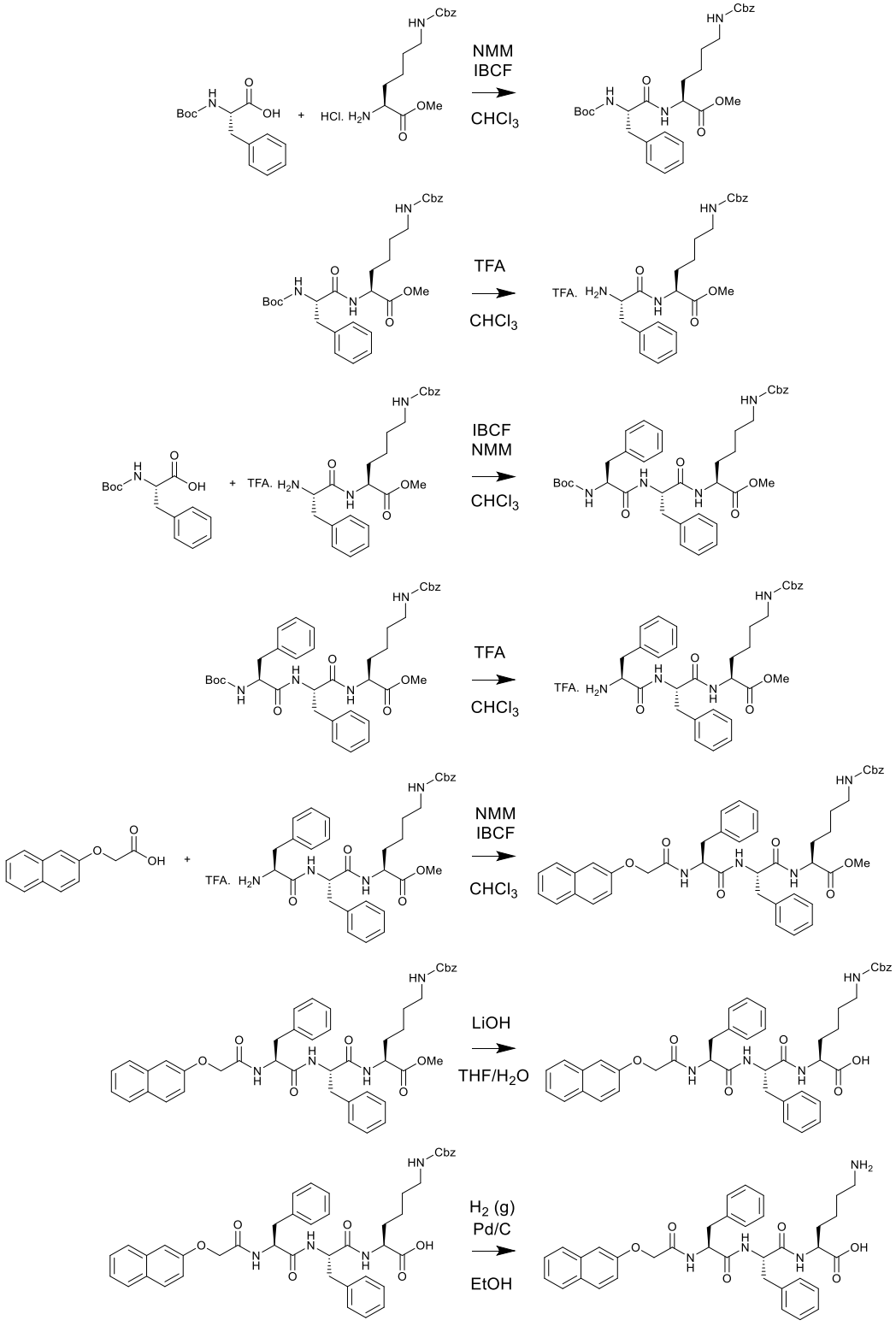

Figure A3.1. Synthetic scheme for the original synthetic method using 2NapFFK as an example.

Appendix 3.2: Characterisation from original synthesis

2NapFFK(Cbz)-OMe

Boc-FK(Cbz)-OMe:

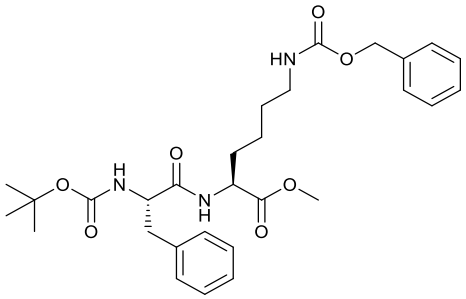

δ_H(400 MHz, $DMSO_{d6}$): 8.31-8.28 (0.2H, m, NH) 8.23 (0.8H, d, *J* 7.6, NH), 7.38-7.13 (12.5H, m, ArH, NH(Cbz), 6.86 (0.8H, d *J* 8.7, NH), 6.43-6.41 (0.2H, m, NH), 5.04 (0.25H, s, COOC**H**$_2$Ph), 5.00 (1.75H, s, COOC**H**$_2$Ph), 4.45-4.42 (0.1H, m, *CH), 4.27-4.17 (1.9H, m, *CH), 3.61 (3H, s, $COOCH_3$), 3.00-2.93 (3H, m, CH_2), 2.75-2.69 (1H, m, CH_2), 2.30 (s, toluene), 1.75-1.57 (2.2H, m, CH_2), 1.42-1.37 (2.2H, m, CH_2), 1.29 (9H, s, $(CH_3)_3$), 1.25-1.22 (1.6H, m, CH_2).

δ_{C13}(400 MHz, $DMSO_{d6}$): 172.46 (C=O), 171.95 (C=O), 156.08 (C=O), 155.18 (C=O), 138.07 (ArC), 137.26 (ArC), 129.19 (ArC), 128.86 (ArC), 128.30 (ArC), 128.16 (ArC), 127.95 (ArC), 127.69 (ArC), 126.13 (ArC), 125.27 (ArC), 77.98 (**C**$(CH_3)_3$), 65.10 (COO**C**H_2Ph), 55.42 (*CH), 51.86 (*CH), 51.77 (COO**C**H_3), 40.01 (CH_2, overlapping with DMSO peak), 37.34 (CH_2), 30.63 (CH_2), 28.95 (CH_2), 28.08 (C(**C**$H_3)_3$), 22.50 (CH_2).

HRMS (ESI) m/z: ([M+Na]+). Accurate Mass calculated for $C_{29}H_{39}N_3NaO_7$: 564.2680. Found: 564.2682.

TFA.FK(Cbz)-OMe:

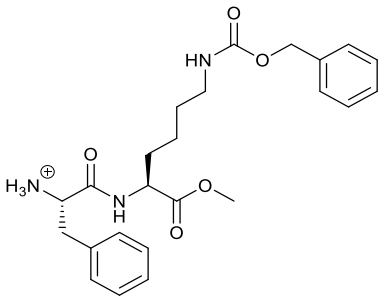

δ_H(400 MHz, DMSO$_{d6}$): 8.87 (1H, d, *J* 7.4, NH), 8.24 (3H, s, NH_3^+), 7.39-7.24 (11H, m, ArH, NH(Cbz)), 5.00 (2H, s, COOC**H$_2$**Ph), 4.31-4.25 (1H, m, *CH), 4.10-4.07 (1H, m, *CH), 3.83 (q, Et_2O), 3.62 (3H, m, $COOCH_3$), 3.12 (1H, dd, *J* 14.0, 5.8, CH_2), 3.01-2.94 (3H, m, CH_2), 1.77-1.68 (1H, m, CH_2), 1.66-1.57 (1H, m, CH_2), 1.44-1.37 (2H, m, CH_2), 1.36-1.23 (2H, m, CH_2), 1.09 (t, Et_2O).

δ_{13C}(400 MHz, DMSO$_{d6}$): 171.77 (C=O), 168.21 (C=O), 156.13 (C=O), 137.29 (ArC), 134.81 (ArC), 129.55 (ArC), 128.47 (ArC), 128.34 (ArC), 127.75 (ArC), 127.71 (ArC), 127.11 (ArC), 65.13 (COO**C**H$_2$Ph), 53.21 (*CH), 52.12 (*CH), 51.96 (COO**C**H$_3$), 40.00 (CH_2, overlapping with DMSO peak), 36.86 (CH_2), 30.61 (CH_2), 28.98 (CH_2), 22.45 (CH_2).

HRMS (ESI) m/z: ([M+Na]+). Accurate Mass calculated for $C_{24}H_{31}N_3NaO_5$: 464.2156. Found: 464.2152.

Boc-FFK(Cbz)-OMe:

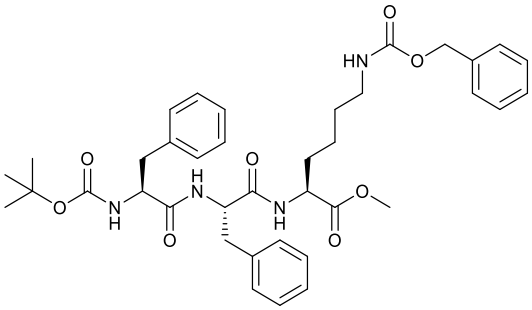

δ_H(400 MHz, DMSO$_{d6}$): 8.48-8.45 (0.2H, m, NH), 8.41 (1H, d, *J* 7.3, NH), 8.05-8.01 (0.2H, m, NH), 7.93 (0.8H, d, *J* 8.3, NH), 7.37-7.15 (16H, m, ArH, NH(Cbz)), 6.85 (0.87H, d, *J* 8.8, NH), 6.39-6.36 (0.13H, m, NH), 5.04-5.02 (0.25H, m, COOC**H$_2$**Ph), 4.99 (1.75H, s, COOC**H$_2$**Ph), 4.66-4.58 (1H, m, *CH), 4.24-4.19 (1H, m, *CH), 4.13-4.07 (0.88H, m, *CH), 4.04-4.00 (0.11H, m, *CH), 3.61 (3H, s, $COOCH_3$), 3.85 (q, Et_2O), 3.05-2.95 (3H, m, CH_2), 2.86-2.78 (2H, m, CH_2), 2.67-2.59 (1H, m, CH_2), 1.77-1.55 (2H, m, CH_2), 1.43-1.36 (2H, m, CH_2), 1.27 (9H, s, $(CH_3)_3$), 1.11-1.07 (2H, m, CH_2, overlapping with triplet from Et_2O).

δ_{13C}(400 MHz, DMSO$_{d6}$): 172.27 (C=O), 171.28 (C=O), 171.08 (C=O), 156.05 (C=O), 155.00 (C=O), 138.03 (ArC), 137.40 (ArC), 137.24 (ArC), 129.29 (ArC), 129.07 (ArC), 128.30 (ArC), 127.96 (ArC), 127.92 (ArC), 127.68 (ArC), 126.24 (ArC), 126.07 (ArC), 78.08 (**C**$(CH_3)_3$), 65.08 (COO**C**H$_2$Ph), 55.77 (*CH), 53.23 (*CH), 51.97 (*CH), 51.78 (COO**C**H$_3$), 39.96 (CH_2, overlapping with DMSO peak), 37.75 (CH_2), 37.50 (CH_2), 30.50 (CH_2), 28.93 (CH_2), 28.05 (C(**C**H$_3$)$_3$), 22.55 (CH_2).

HRMS (ESI) m/z: ([M+Na]+). Accurate Mass calculated for $C_{38}H_{48}N_4NaO_8$: 711.3364. Found: 711.3359.

TFA.FFK(Cbz)-OMe:

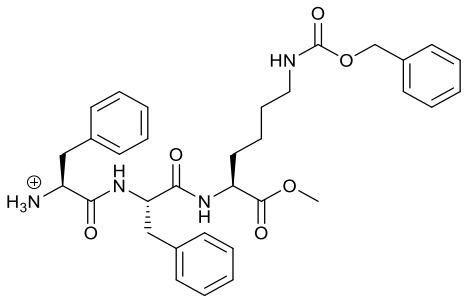

δ_H(400 MHz, DMSO$_{d6}$): 8.79 (0.3H, d, *J* 9.5, NH), 8.77 (0.7H, d, *J* 8.4, NH), 8.58 (0.3H, d, *J* 8.0, NH), 8.57 (0.7H, d, *J* 7.5, NH), 8.01 (2.6H, s, NH_3^+), 7.70 (0.4H, s, NH_3^+), 7.38-7.19 (15H, m, ArH, NH(Cbz)), 5.04-5.02 (0.15H, m, COOC**H$_2$**Ph), 4.99 (1.5H, s, COOC**H$_2$**Ph), 4.67-4.60 (1H, m, *CH), 4.30-4.21 (1H, m, *CH), 4.03-3.97 (1H, m, *CH), 3.62 (0.6H, s, $COOCH_3$), 3.61 (2.4H, s, $COOCH_3$), 3.11 (1H, dd, *J* 4.6, 14.4, CH_2), 3.05 (1H, dd, *J* 4.7, 13.8, CH_2), 2.98 (1.6H, dd, *J* 13.0, 6.7, CH_2), 2.91 (1H, dd, *J* 14.2, 8.2, CH_2), 2.83 (1H, dd, *J* 14.0, 9.1, CH_2), 2.78-2.73 (0.4H, m, CH_2), 1.78-1.67 (1H, m, CH_2), 1.65-1.51 (1.4H, m, CH_2), 1.45-1.38 (1.6H, m, CH_2), 1.35-1.24 (2H, m, CH_2).

δ_{C13}(400 MHz, DMSO$_{d6}$): 172.25 (C=O), 170.76 (C=O), 167.94 (C=O), 156.13 (C=O), 137.30 (ArC), 137.25 (ArC), 134.64 (ArC), 129.59 (ArC), 129.21 (ArC), 128.49 (ArC), 128.36 (ArC), 128.18 (ArC), 127.77 (ArC), 127.72 (ArC), 127.15 (ArC), 126.47 (ArC), 65.14 (COO**C**H$_2$Ph), 53.95 (*CH), 53.06 (*CH), 52.05 (*CH), 51.87 (COO**C**H$_3$), 39.96 (CH_2, overlapping with DMSO peak), 37.61 (CH_2), 36.93 (CH_2), 30.52 (CH_2), 28.97 (CH_2), 22.60 (CH_2).

HRMS (ESI) m/z: ([M+Na]+). Accurate Mass calculated for $C_{33}H_{40}N_4NaO_6$: 611.2840. Found: 611.2829.

2NapFFK(Cbz)-OMe:

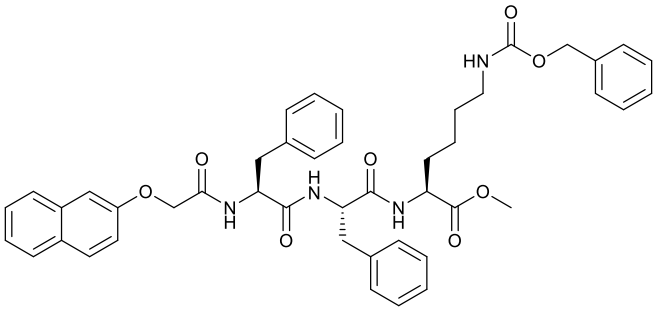

δ_H(400 MHz, DMSO$_{d6}$): 8.39 (1H, d, *J* 7.3, NH), 8.27 (1H, d, *J*, 8.3, NH), 8.06 (1H, d, *J* 8.3, NH), 7.84-7.82 (2H, m, ArH), 7.74-7.72 (1H, m, ArH), 7.48-7.44 (1H, m, ArH), 7.38-7.13 (17H, m, ArH, NH(Cbz)), 5.03-5.01 (0.2H, m, COOC**H$_2$**Ph), 4.99 (1.3H, s, COOC**H$_2$**Ph), 4.63-4.56 (2H, *CH), 4.53 (1.5H, s, Nap-OCH$_2$), 4.25-4.20 (1H, m, *CH), 3.61 (3H, s, COOCH$_3$), 3.06-2.96 (3.8H, m, CH$_2$), 2.85-2.78 (2.2H, m, CH$_2$), 1.72-1.54 (2H, m, CH$_2$), 1.46-1.37 (2H, m, CH$_2$), 1.33-1.24 (2H, m, CH$_2$).

δ_{C13}(400 MHz, DMSO$_{d6}$): 172.35 (C=O), 171.15 (C=O), 170.55 (C=O), 167.30 (C=O), 156.13 (ArC), 155.46 (C=O), 137.50 (ArC), 137.45 (ArC), 137.26 (ArC), 134.03 (ArC), 129.39 (ArC), 129.22 (ArC), 129.20 (ArC), 128.77 (ArC), 128.35 (ArC), 128.04 (ArC), 127.96 (ArC), 127.76 (ArC), 127.72 (ArC), 127.51 (ArC), 126.82 (ArC), 126.44 (ArC), 126.30 (ArC), 126.24 (ArC), 123.90 (ArC), 118.44 (ArC), 107.37 (ArC), 66.71 (Ar-OCH$_2$), 65.14 (Ar-OCH$_2$), 64.93 (Et$_2$O), 53.55 (*CH), 53.41 (*CH), 52.08 (*CH), 51.85 (COO**C**H$_3$), 37.55 (CH$_2$), 30.51 (CH$_2$), 37.39 (CH$_2$), 30.51 (CH$_2$), 28.98 (CH$_2$), 22.59 (CH$_2$), 15.17 (Et$_2$O).

HRMS (ESI) m/z: ([M+Na]+ Accurate Mass calculated for $C_{45}H_{48}N_4NaO_8$: 795.3364. Found: 795.3357.

2NapFK(Cbz)F-OBzl

Boc-K(Cbz)F-OBzl

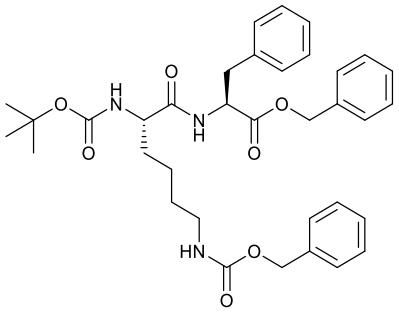

δ_H(400 MHz, $DMSO_{d6}$): 8.21 (1H, d, *J* 7.6, NH), 7.39-7.18 (m, 16H, ArH, NH), 6.74 (0.8H, d *J* 8.3, NH), 6.38-6.30 (0.2H, m, NH), 5.09-5.04 (2H, m, COOC**H_2**Ph), 5.00 (2H, s, COOC**H_2**Ph), 4.55-4.43 (1H, m, *CH), 3.91-3.74 (1H, m, *CH), 3.38 (q, Et_2O), 3.04 (1H, dd, *J* 13.8, 6.3, CH_2) 2.99-2.86 (3H, m, CH_2), 1.51-1.38 (2H, m, CH_2), 1.36 (9H, s, $(CH_3)_3$), 1.30-1.12 (4H, m, CH_2), 1.09 (t, Et_2O).

δ_{C13}(400 MHz, $DMSO_{d6}$): 172.30 (C=O), 171.22 (C=O), 156.05 (C=O), 155.17 (C=O), 137.26 (ArC), 136.91 (ArC), 135.63 (ArC), 129.09 (ArC), 128.31 (ArC), 128.19 (ArC), 127.99 (ArC), 127.86 (ArC), 127.69 (ArC), 126.49 (ArC), 77.95 (**C**$(CH_3)_3$), 66.01 (COO**C**H_2Ph), 65.09 (COO**C**H_2Ph), 54.08 (*CH), 53.46 (*CH), 40.07 (CH_2), 36.63 (CH_2), 31.70 (CH_2), 29.09 (CH_2), 28.15 (C(**C**$H_3)_3$), 22.68 (CH_2).

HRMS (ESI) m/z: ([M+Na]+). Accurate Mass calculated for $C_{35}H_{43}N_3NaO_7$: 640.2993. Found: 640.2978.

TFA.K(Cbz)F-OBzl

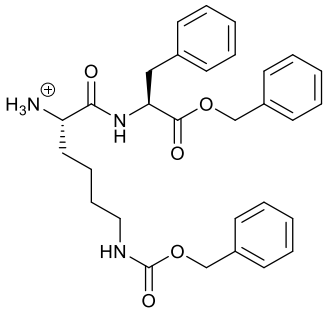

δ_H(400 MHz, $DMSO_{d6}$): 8.89 (1H, d, *J* 7.4, NH), 8.03 (3H, s, NH_3^+), 7.38-7.19 (17H, m, ArH, NH), 5.09 (2H, dd, *J* 16.1, 12.5, COOC**H_2**Ph), 5.01 (2H, s, COOC**H_2**Ph), 4.65-4.59 (1H, m, *CH), 3.74-3.71 (1H, m, *CH), 3.38 (q, Et_2O), 3.10 (1H, dd, *J* 14.0, 5.8, CH_2), 3.01-2.92 (3H, m, CH_2), 1.68-1.61 (2H, m, CH_2), 1.35-1.25 (4H, m, CH_2).

δ_{13C}(400 MHz, $DMSO_{d6}$): 170.82 (C=O), 169.04 (C=O), 156.10 (C=O), 137.25 (ArC), 136.73 (ArC), 135.54 (ArC), 129.08 (ArC), 128.40 (ArC), 128.39 (ArC), 128.36 (ArC), 128.15 (ArC), 127.98 (ArC), 127.77 (ArC), 127.74 (ArC), 126.74 (ArC), 66.30 (COO**C**H_2Ph), 65.18 (COO**C**H_2Ph), 53.99 (*CH), 51.95 (*CH), 40.04 (CH_2), 36.41 (CH_2), 30.88 (CH_2), 29.00 (CH_2), 21.32 (CH_2).

HRMS (ESI) m/z: ([M+Na]+). Accurate Mass calculated for $C_{30}H_{35}N_3NaO_5$: 540.2469. Found: 540.2467.

Boc-FK(Cbz)F-OBzl

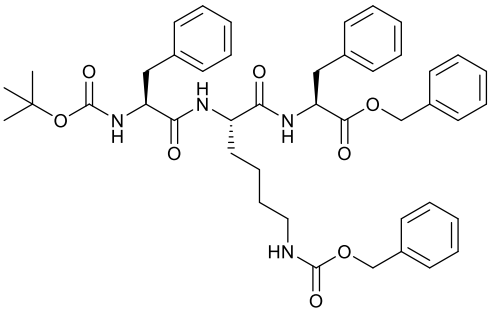

δ_H(400 MHz, DMSO$_{d6}$): 8.46 (1H, d, *J* 7.2, NH), 7.93-7.89 (0.2H, m, NH), 7.83 (0.8H, d, *J* 8.2, NH), 7.38-7.16 (21H, m, ArH, NH), 6.92 (0.9H, d, *J* 8.6, NH), 6.50 (0.2H, d, *J* 6.2, NH), 5.10-5.02 (2H, m, COOC**H$_2$**Ph), 5.01 (2H, s, COOC**H$_2$**Ph), 4.58-4.52 (1H, m, *CH), 4.36-4.30 (1H, m, *CH), 4.21-4.15 (0.9H, m, *CH), 4.01-3.97 (0.1H, m, *CH), 3.38 (q, Et_2O), 3.06 (1.2H, dd, *J* 13.8, 6.2, CH_2), 3.01-2.93 (3.8H, m, CH_2), 2.71 (1H, dd, *J* 13.5, 10.8, CH_2), 1.64-1.56 (1.3H, m, CH_2), 1.51-1.44 (1.3H, m, CH_2), 1.41-1.33 (2H, m, CH_2), 1.29 (9H, s, $(CH_3)_3$), 1.25-1.20 (1H, m, CH_2), 1.09 (t, Et_2O).

δ_{13C}(400 MHz, DMSO$_{d6}$): 171.66 (C=O), 171.36 (C=O), 171.14 (C=O), 171.14 (C=O), 156.04 (C=O), 155.20 (C=O), 138.18 (ArC), 137.26 (ArC), 136.90 (ArC), 135.63 (ArC), 129.15 (ArC), 129.01 (ArC), 128.32 (ArC), 128.30 (ArC), 128.25 (ArC), 128.01 (ArC), 127.94 (ArC), 127.87 (ArC), 127.70 (ArC), 126.53 (ArC), 126.09 (ArC), 78.06 (**C**$(CH_3)_3$), 66.02 (COO**C**H_2Ph), 65.11 (COO**C**H_2Ph), 55.67 (*CH), 53.64 (*CH), 51.94 (*CH), 40.22 (CH_2), 37.32 (CH_2), 36.52 (CH_2), 32.25 (CH_2), 29.17 (CH_2), 28.07 (C(**C**$H_3)_3$), 22.31 (CH_2).

HRMS (ESI) m/z: ([M+Na]+). Accurate Mass calculated for $C_{44}H_{52}N_4NaO_8$: 787.3677. Found:787.3684.

TFA.FK(Cbz)F-OBzl

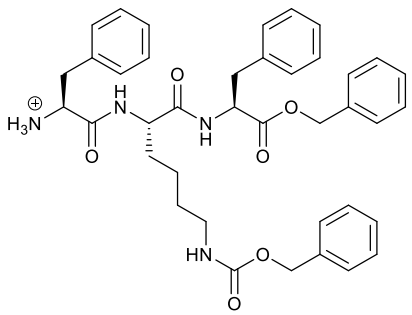

δ_H(400 MHz, DMSO$_{d6}$): 8.62 (0.2H, d, *J* 8.1, NH), 8.57 (1.8H, d, *J* 7.5, NH), 8.07 (2.8H, s, NH_3^+), 7.77 (0.2H, s, NH_3^+), 7.39-7.18 (20H, m, ArH, NH), 5.01-5.03 (2H, m, COOC**H$_2$**Ph), 5.01 (2H, s, COOC**H$_2$**Ph), 4.58-4.53 (1H, m, *CH), 4.36-4.31 (1H, m, *CH), 4.08-4.02 (1H, m, *CH), 3.10-3.03 (1.4H, m, CH_2), 3.00-2.91 (3.3H, m, CH_2), 2.88-2.82 (1H, m, CH_2), 2.73-2.65 (0.3H, m, CH_2), 1.61-1.54 (1H, m, CH_2), 1.51-1.45 (1H, m, CH_2), 1.42-1.32 (2H, m, CH_2), 1.29-1.20 (2H, m, CH_2, *overlapping with hexane multiplet at 1.25*), 0.86 (t, hexane).

δ_{13C}(400 MHz, DMSO$_{d6}$): 171.09 (C=O), 171.07 (C=O), 167.66 (C=O), 156.04 (C=O), 137.21 (ArC), 136.94 (ArC), 135.62 (ArC), 134.71 (ArC), 129.41 (ArC), 129.01 (ArC), 128.45 (ArC), 128.32 (ArC), 128.24 v, 128.02 (ArC), 127.86 (ArC), 127.82 (ArC), 127.74 (ArC), 127.71 (ArC), 127.06 (ArC), 126.54 (ArC), 66.05 (COO**C**H$_2$Ph), 65.11 (COO**C**H$_2$Ph), 53.65 (*CH), 53.14 (*CH), 52.22 (*CH), 40.18 (CH_2), 36.99 (CH_2), 36.46 (CH_2), 32.24 (CH_2), 29.21 (CH_2), 22.39 (CH_2).

HRMS (ESI) m/z: ([M+Na]+). Accurate Mass calculated for $C_{39}H_{44}N_4NaO_6$: 687.3153. Found: 687.3135.

2NapFK(Cbz)F-OBzl

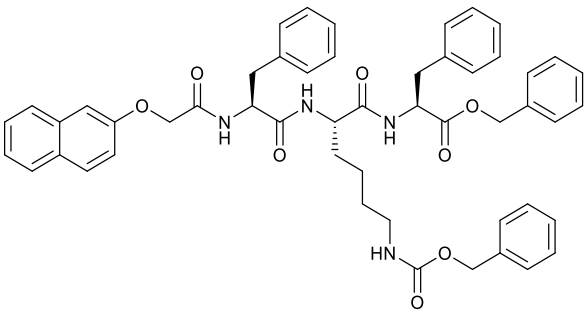

δ_H(400 MHz, DMSO$_{d6}$): 9.55 (0.1H, d, *J* 9.0, NH), 8.51 (0.1H, d, *J* 6.9, NH), 8.42 (0.9H, d, *J* 7.3, NH), 8.30 (0.2H, d, *J* 8.1, NH), 8.14 (1.8H, dd, *J* 7.3, 7.3, NH), 7.84-7.71 (3H, m, ArH), 7.47-7.12 (25H, m, ArH, NH), 5.05 (2H, dd, *J* 16.7, 12.8, COOC**H$_2$**Ph), 4.99 (2H, s, COOC**H$_2$**Ph), 4.67-4.61 (1H, m, *CH), 4.57-4.52 (3H, NapOCH_2, *CH), 4.32-4.27 (1H, m, *CH), 3.07-2.81 (6H, m, CH_2), 1.63-1.52 (1H, m, CH_2), 1.49-1.41 (1H, m, CH_2), 1.38-1.29 (2H, m, CH_2), 1.26-1.13 (2H, m, CH_2).

δ_{13C}(400 MHz, DMSO$_{d6}$): 171.65 (C=O), 171.16 (C=O), 170.55 (C=O), 167.34 (C=O), 156.04 (ArC), 155.46 (C=O), 137.54 (ArC), 137.25 (ArC), 136.91 (ArC), 135.63 (ArC), 134.00 (ArC), 129.34 (ArC), 129.17 (ArC), 129.04 (ArC), 128.73 (ArC), 128.32 (ArC), 128.26 (ArC), 128.02 (ArC), 127.94 (ArC), 127.88 (ArC), 127.70 (ArC), 127.47 (ArC),

126.77 (ArC), 126.55 (ArC), 126.40 (ArC), 126.20 (ArC), 123.84 (ArC), 118.41 (ArC), 107.33 (ArC), 66.71 (Nap-OCH_2), 66.03 (COO**C**H_2Ph), 65.10 (COO**C**H_2Ph), 53.68 (*CH), 53.41 (*CH), 52.22 (*CH), 40.18 (CH_2), 37.44 (CH_2), 36.52 (CH_2), 29.15 (CH_2), 22.52 (CH_2).

HRMS (ESI) m/z: ([M+Na]+). Accurate Mass calculated for $C_{51}H_{52}N_4NaO_8$: 871.3677. Found: 871.3669.

2NapK(Cbz)FF-OBzl

Boc-FF-OBzl

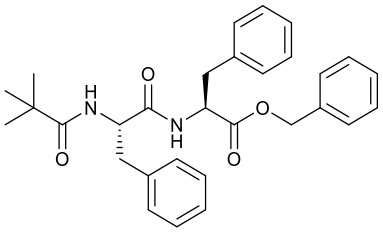

δ_H(400 MHz, $DMSO_{d6}$): 8.46-8.43 (0.2H, m, NH), 8.40 (0.8H, d, *J* 7.5, NH), 7.36-7.17 (15H, m, ArH), 6.85 (0.8H, d, *J* 8.9, NH), 6.40 (0.2H, d, *J* 7.2, NH), 5.11-5.03 (2H, m, COOC**H₂**Ph), 4.60-4.54 (1H, m, *CH), 4.22-4.17 (0.8H, m, *CH), 4.12-4.05 (0.2H, m, *CH), 3.09-2.98 (2H, m, *CHC**H₂**), 2.87-2.84 (1H, m, *CHC**H₂**), 2.67-2.64 (1H, m, *CHC**H₂**), 1.32 (0.2H, s, $C(CH_3)_3$), 1.28 (7.4H, s, $C(CH_3)_3$), 1.12 (1.4H, s, $C(CH_3)_3$).

δ_{13C}(400 MHz, $DMSO_{d6}$): 171.95 (C=O), 171.23 (C=O), 155.13 (C=O), 138.04 (ArC), 136.92 (ArC), 135.68 (ArC), 129.16 (ArC), 129.13 (ArC), 128.38 (ArC), 128.31 (ArC), 128.06 (ArC), 127.98 (ArC), 127.90 (ArC), 126.61 (ArC), 126.17 (ArC), 78.04 (**C**$(CH_3)_3$), 66.08 (COO**C**H_2Ph), 55.43 (*CH), 53.66 (*CH), 37.48 (CH_2), 36.70 (CH_2), 28.12 ($C(\mathbf{C}H_3)_3$).

HRMS (ESI) m/z: ([M+Na]+). Accurate Mass calculated for $C_{30}H_{34}N_2NaO_5$: 525.2360. Found: 525.2353.

TFA.FF-OBzl

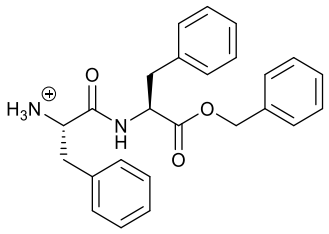

δ_H(400 MHz, DMSO$_{d6}$): 9.01 (1H, d, *J* 7.6, NH), 8.06 (3H, s, NH_3^+), 7.38-7.21 (15H, m, ArH), 5.13 (1H, d, *J* 12.5, COOC**H$_2$**Ph), 5.08 (1H, d, *J* 12.5, COOC**H$_2$**Ph), 4.65 (1H, dd, *J* 7.2, 14.5, *CH), 4.03-4.00 (1H, m, *CH), 3.38 (q, Et_2O), 3.13-2.97 (3H, m, *CHC**H$_2$**), 2.88-2.82 (1H, dd, *J* 14.2, 8.6, *CHC**H$_2$**), 1.09 (t, Et_2O).

COSY: 9.01-4.66 (NH-*CH), 4.66-3.11 (*CH-CH_2), 4.66-3.00 (*CH-CH_2), 4.03-3.07 (*CH-CH_2), 4.03-2.85 (*CH-CH_2), 3.13-2.99 (CH_2-CH_2), 3.09-2.86 (CH_2-CH_2), 2.89-2.84 (CH_2-CH_2).

δ_{13C}(400 MHz, DMSO$_{d6}$): 170.61 (C=O), 168.34 (C=O), 136.53 (ArC), 135.49 (ArC), 134.67 (ArC), 129.47 (ArC), 129.08 (ArC), 128.48 (ArC), 128.37 (ArC), 128.13 (ArC), 128.00 (ArC), 127.14 (ArC), 126.74 (ArC), 66.29 (COO**C**H_2Ph), 53.89 (*CH), 53.10 (*CH), 36.89 (CH_2), 36.69 (CH_2).

HRMS (ESI) m/z: ([M+Na]+). Accurate Mass calculated for $C_{25}H_{26}N_2NaO_3$: 435.1836. Found: 425.1825.

Boc-K(Cbz)FF-OBzl

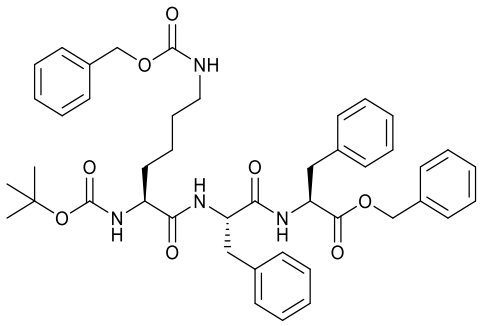

δ_H(400 MHz, DMSO$_{d6}$): 8.58 (1H, d, *J* 7.1, NH), 7.75 (1H, d *J* 8.3, NH), 7.38-7.16 (21H, m, ArH, NH), 6.80 (1H, d *J* 8.2, NH), 5.07 (2H, dd, *J* 19.6, 12.6, COOC**H$_2$**Ph), 5.01 (2H, s, COOC**H$_2$**Ph), 4.60-4.55 (2H, m, *CH), 3.84-3.79 (0.8H, m, *CH), 3.72-3.64 (0.2H, m, *CH), 3.09-2.93 (5H, m, CH_2), 2.73 (1H, dd, *J* 13.7, 9.5, CH_2), 1.36 (9H, s, $(CH_3)_3$), 1.31-1.10 (6H, m, CH_2).

δ_{13}(400 MHz, DMSO$_{d6}$): 171.67 (C=O), 171.15 (C=O), 171.06 (C=O), 156.04 (C=O), 155.15 (C=O), 137.38 (ArC), 137.26 (ArC), 136.77 (ArC), 135.64 (ArC), 129.22 (ArC), 129.00 (ArC), 128.32 (ArC), 128.30 (ArC), 128.26 (ArC), 128.00 (ArC), 127.87 (ArC), 127.69 (ArC), 126.56 (ArC), 126.16 (ArC), 78.07 (**C**$(CH_3)_3$), 66.03 (COO**C**H_2Ph), 65.08 (COO**C**H_2Ph), 54.55 (*CH), 53.64 (*CH), 52.94 (*CH), 40.07 (CH_2), 37.82 (CH_2), 36.67 (CH_2), 31.77 (CH_2), 29.07 (CH_2), 28.14 (C(**C**$H_3)_3$), 22.66 (CH_2).

HRMS (ESI) m/z: ([M+Na]+). Accurate Mass calculated for $C_{44}H_{52}N_4NaO_8$: 787.3677. Found: 787.3672.

TFA.K(Cbz)FF-OBzl

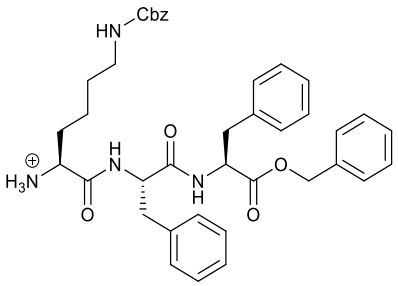

δ_H(400 MHz, DMSO$_{d6}$): 8.72 (0.7H, d, *J* 7.6, NH), 8.61 (0.85H, d, *J* 8.2, NH), 8.04 (3H, s, NH_3^+), 7.74 (0.2H, d, *J* 8.7, NH), 7.37-7.05 (21H, m, ArH, NH), 6.79 (0.3H, d, *J* 8.3, NH), 5.10-5.03 (2H, m, COOC**H$_2$**Ph), 5.00 (2H, s, COOC**H$_2$**Ph), 4.64-4.52 (2H, m, *CH), 3.81-3.76 (0.3H, m, *CH), 3.69-3.67 (0.7H, m, *CH), 3.06 (1H, dd, *J* 13.9, 6.0, CH_2), 3.00-2.89 (4H, m, CH_2), 2.73 (1H, dd, *J* 14.0. 9.9, CH_2), 1.65-1.62 (1H, m, CH_2), 1.40-1.32 (3H, m, CH_2), 1.30-1.19 (2H, m, *CHCH$_2$C**H$_2$**CH$_2$CH$_z$NH).

δ_{13}(400 MHz, DMSO$_{d6}$): 171.04 (C=O), 170.93 (C=O), 168.57 (C=O), 156.05 (C=O), 137.41 (ArC), 137.24 (ArC), 136.85 (ArC), 135.66 (ArC), 129.83 (ArC), 129.22 (ArC), 129.09 (ArC), 129.02 (ArC), 128.35 (ArC), 128.33 (ArC), 128.27 (ArC), 128.24 (ArC), 128.19 (ArC), 128.11 (ArC), 128.04 (ArC), 128.02 (ArC), 127.89 (ArC), 127.73 (ArC), 127.71 (ArC), 126.54 (ArC), 126.38 (ArC), 126.17 (ArC), 66.09 (COO**C**H$_2$Ph), 65.14 (COO**C**H$_2$Ph), 53.88 (*CH), 53.59 (*CH), 51.97 (*CH), 37.43 (CH_2), 36.61 (CH_2), 30.91 (CH_2), 28.94 (CH_2), 28.15 (CH_2), 21.29 (CH_2).

HRMS (ESI) m/z: ([M+Na]+). Accurate Mass calculated for $C_{39}H_{44}N_4NaO_6$: 687.3153. Found: 687.3142.

2Nap-K(Cbz)FF-OBzl

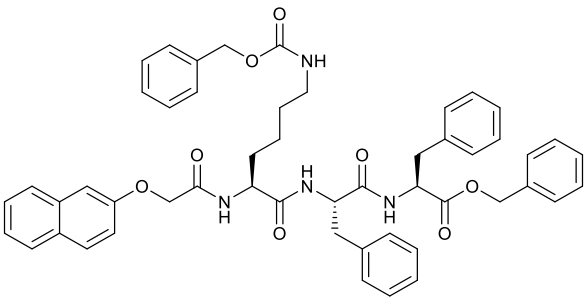

δ_H(400 MHz, DMSO$_{d6}$): 8.57 (0.1H, d, *J* 7.9, NH), 8.51 (0.9H, d, *J* 7.4, NH), 8.08 (1H, d, *J* 8.4, NH), 8.00 (1H, d, *J* 8.2, NH), 7.85-7.82 (2H, m, ArH), 7.78-7.76 (1H, m, ArH), 7.46-7.10 (26H, m, ArH, NH), 5.76 (s, DCM), 5.05 (2H, m, COOC**H$_2$**Ph), 4.99 (2H, s, COOC**H$_2$**Ph), 4.66-4.59 (2H, m, Nap-OCH$_2$), 4.59-4.52 (2H, m, *CH), 4.48-4.10 (0.1H, m, *CH), 4.29-4.24 (0.9H, m, *CH), 3.38 (q, Et$_2$O), 3.06-2.84 (5H, m, CH$_2$), 2.73-2.68 (1H, m, CH$_2$), 1.56-1.41 (2H, m, CH$_2$), 1.35-1.24 (2H, m, CH$_2$, *Boc still present*), 1.14-1.08 (2H, m, CH$_2$), 1.09 (t, Et$_2$O).

δ_{13C}(400 MHz, DMSO$_{d6}$): 171.17 (C=O), 171.11 (C=O), 171.03 (C=O), 167.32 (C=O), 156.04 (ArC), 155.5, (C=O), 137.53 (ArC), 137.27 (ArC), 136.82 (ArC), 135.66 (ArC), 134.04 (ArC), 129.38 (ArC), 129.11 (ArC), 129.05 (ArC), 128.74 (ArC), 128.34 (ArC), 128.32 (ArC), 128.27 (ArC), 128.02 (ArC), 127.95 (ArC), 127.95 (ArC), 127.87 (ArC), 127.69 (ArC), 127.50 (ArC), 126.74 (ArC), 126.57 (ArC), 126.47 (ArC), 126.21 (ArC) (ArC), 123.86 (ArC), 118.49 (ArC), 107.36 (ArC), 66.79 (Nap-OCH$_2$), 66.03 (COO**C**H$_2$Ph), 65.10 (COO**C**H$_2$Ph), 53.74 (*CH), 53.33 (*CH), 52.23 (*CH), 37.47 (CH$_2$), 36.63 (CH$_2$), 31.81 (CH$_2$), 29.11 (CH$_2$), 22.40 (CH$_2$), (*missing CH$_2$ peak may be obscured by DMSO peak or not resolved from another CH$_2$ peak).*

HRMS (ESI) m/z: ([M+Na]+). Accurate Mass calculated for $C_{51}H_{52}N_4NaO_8$: 871.3677. Found: 871.3681.

Appendix 3.3: Synthetic scheme

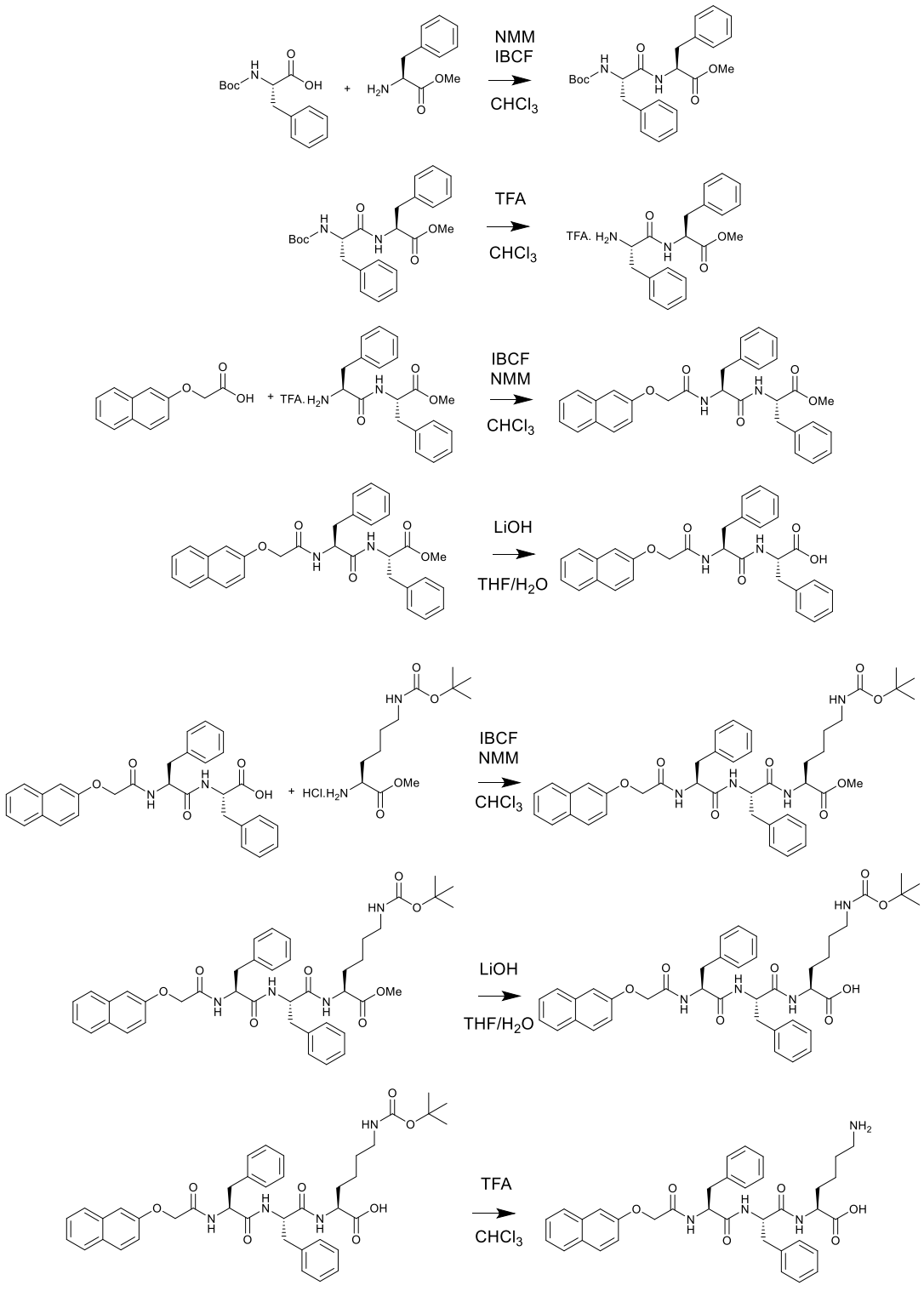

Figure A3.3. Synthetic scheme used to synthesise each K-containing tripeptide, using 2NapFFK as an example. For 2NapFFK and 2NapKFF, TFA.FF-OMe was first prepared in bulk. 2NapFKF had to be prepared one amino acid at a time, building from the *N*- to the *C*-terminus, but sill used the same coupling and deprotection methods.

Appendix 3.4: Synthetic characterisation

Bold highlights the assigned proton or carbon atom, * denotes a stereocentre.

TFA.FF-OMe

Boc-FF-OMe

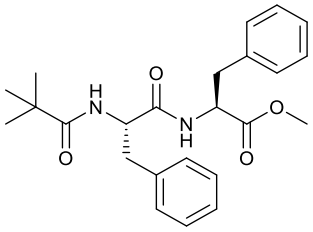

δ_H(400 MHz, DMSO$_{d6}$): 8.38 (0.2H, d, *J* 7.8, NH), 8.31 (0.8H, d, *J* NH), 7.30-7.16 (10H, m, ArH), 6.83 (0.8H, d, *J* 8.9, NH), 6.39 (0.2H, d, *J* 8.5, NH), 4.53-4.48 (1H, m, *CH), 4.20-4.15 (0.8H, m, *CH), 4.10-4.04 (0.2H, m, *CH), 3.58 (3H, s, $COOCH_3$), 3.05 (1H, dd, *J* 13.8, 5.7, CH_2), 2.96 (1H, dd, *J* 13.8, 8.6, CH_2), 2.88 (1H, dd, *J* 13.7, 4.0, CH_2), 2.67 (1H, dd, *J* 13.1, 10.8, CH_2), 1.28 (7H, s, $(CH_3)_3$), 1.14 (2H, s, $(CH_3)_3$).

δ_{13C}(400 MHz, DMSO$_{d6}$): 171.81 (C=O), 171.78 (C=O), 155.08 (C=O), 137.99 (ArC), 136.98 (ArC), 129.14 (ArC), 129.10 (ArC), 128.25 (ArC), 127.96 (ArC), 126.56 (ArC), 126.15 (ArC), 78.02 (**C**(CH_3), 55.50 (*CH), 53.49 (*CH), 51.83 (COO**C**H_3), 37.43 (**C**H_2Ph), 36.72 (**C**H_2Ph)), 28.09 (C(**C**$H_3)_3$.

HRMS (ESI) m/z: ([M+Na]+). Accurate Mass calculated for $C_{24}H_{30}N_2NaO_5$: 449.2047. Found: 449.2048.

TFA.FF-OMe

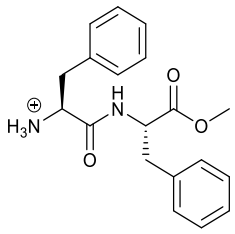

δ_H(400 MHz, DMSO$_{d6}$): 8.99 (1H, d, *J* 7.2, NH), 8.14 (3H, s, NH_3^+), 7.35-7.22 (10H, m, ArH), 4.60-4.55 (1H, m, *CH), 4.06-4.03 (1H, m, *CH), 3.61 (3H, s, $COOCH_3$), 3.13-3.05 (2H, m, C**H$_2$**Ph), 3.00-2.91 (2H, m, C**H$_2$**Ph).

δ_{13C}(400 MHz, DMSO$_{d6}$): 171.13 (C=O), 168.23 (C=O), 136.64 (ArC), 134.64 (ArC), 129.50 (ArC), 129.05 (ArC), 128.52 (ArC), 128.39 (ArC), 127.18 (ArC), 126.75 (ArC), 53.81 (*CH), 53.13 (*CH), 52.03 (COO**C**H$_3$), 36.87 (C**H$_2$**Ph), 36.65 (C**H$_2$**Ph).

HRMS (ESI) m/z: ([M+Na]+). Accurate Mass calculated for $C_{19}H_{22}N_2NaO_3$: 349.1523. Found: 349.1511.

2NapFFK

2NapFF-OMe

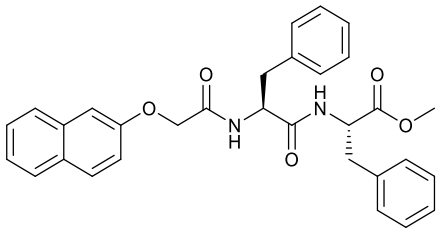

δ_H(400 MHz, DMSO$_{d6}$): 8.60 (1H, d, *J* 7.6, NH), 8.13 (1H, d, *J* 8.5, NH), 7.85-7.82 (2H, m, ArH), 7.74-7.72 (1H, m, ArH), 7.47-7.44 (1H, m, ArH), 7.38-7.34 (1H, m, ArH), 7.27-7.12 (12H, m, ArH), 4.68-4.62 (1H, m, *CH), 4.54 (2H, s, 2Nap-OC**H$_2$**), 4.52-4.49 (1H, m, *CH), 3.36 (3H, s, COOCH$_3$), 3.07-2.92 (3H, m, *CHC**H$_2$**), 2.85 (1H, dd, *J* 13.8, 9.5, *CHC**H$_2$**).

δ_{13C}(400 MHz, DMSO$_{d6}$): 171.70 (C=O), 170.95 (C=O), 167.26 (C=O), 155.49 (ArC), 137.41 (ArC), 136.94 (ArC), 134.03 (ArC), 129.36 (ArC), 129.20 (ArC), 129.05 (ArC), 128.75 (ArC), 128.26 (ArC), 128.00 (ArC), 127.50 (ArC), 126.78 (ArC), 126.58 (ArC), 126.43 (ArC), 126.29 (ArC), 123.87 (ArC), 118.45 (ArC), 107.34 (ArC), 66.68 (2Nap-O**C**H$_2$), 53.65 (*CH), 53.19 (*CH), 51.86 (COO**C**H$_3$), 37.43 (CH$_2$), 36.63 (CH$_2$).

HRMS (ESI) m/z: ([M+Na]+). Accurate Mass calculated for $C_{31}H_{30}N_2NaO_5$: 533.2047. Found: 533.2054.

2NapFF-OH – final and intermediate compound, previously synthesised.[6]

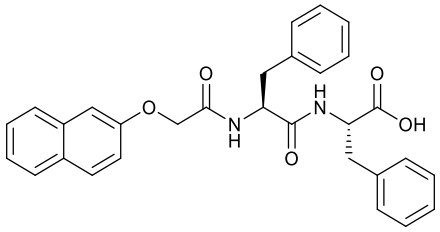

White solid, 90 % yield final step.

δ_H(400 MHz, DMSO$_{d6}$): 12.82 (1H, s, COOH), 8.42 (1H, d, *J* 7.8, NH), 8.11 (1H, d, *J* 8.5, NH), 7.85-7.82 (2H, m, ArH), 7.74-7.72 (1H, m, ArH), 7.48-7.44 (1H, m, ArH), 7.38-7.34 (1H, m, ArH), 7.27-7.13 (12H, m, ArH), 4.68-4.62 (1H, m, *CH), 4.54 (2H, s, 2Nap-OC**H$_2$**), 4.50-4.45 (1H, m, *CH), 3.10-3.00 (2H, m, *CHC**H$_2$**), 2.95-2.82 (2H, m, *CHC**H$_2$**), 2.07 (0.7864, s, CH_3CN).

δ_{13C}(400 MHz, DMSO$_{d6}$): 172.64 (C=O), 170.74 (C=O), 167.15 (C=O), 155.45 (ArC), 137.46 (ArC), 137.34 (ArC), 133.98 (ArC), 129.30 (ArC), 129.19 (ArC), 129.08 (ArC), 128.70 (ArC), 128.12 (ArC), 127.92 (ArC), 127.45 (ArC), 126.74 (ArC), 126.38 (ArC), 126.19 (ArC), 123.81 (ArC), 118.39 (ArC), 107.31 (ArC), 66.65 (2Nap-O**C**H_2), 53.47 (*CH), 53.18 (*CH), 37.37 (*CH**C**H_2), 36.65 (*CH**C**H_2).

HRMS (ESI) m/z: ([M+Na]+). Accurate Mass calculated for $C_{30}H_{28}N_2NaO_5$: 519.1890. Found: 519.1882.

2NapFFK(Boc)-OMe

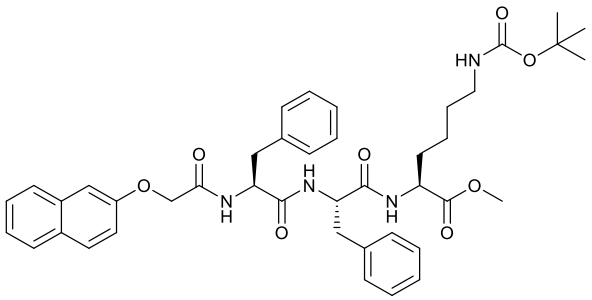

δ_H(400 MHz, DMSO$_{d6}$): 8.56 (0.5H, d, *J* 8.6, NH), 8.44 (0.5H, d, *J* 7.9, NH), 8.39 (0.5H, d, *J* 7.2, NH), 8.31 (s, $CHCl_3$), 8.28 (0.5H, d, *J* 8.1, NH), 8.11 (0.3H, d, *J* 8.6, NH), 8.06-8.03 (0.9H, m, NH), 7.84-7.82 (2H, m, ArH), 7.74-7.72 (1H, m, ArH), 7.48-7.44 (1H, m, ArH), 7.38-7.34 (1H, m, ArH), 7.30-7.08 (12H, m, ArH), 6.98-6.96 (1H, m, ArH), 6.78-6.72 (1H, m, NH-Boc), 5.75 (s, DCM), 4.69-4.56 (2H, m, *CH), 4.53 (2H, s, 2Nap-O**CH$_2$**), 4.49-4.30 (0.3H, m, *CH), 4.26-4.19 (0.9H, m, *CH), 3.62-3.61 (3H, m, $COOCH_3$), 3.10-2.96 (2H, m, CH_2), 2.93-2.77 (3H, m, CH_2), 2.75-2.67 (1H, m, CH_2), 1.75-1.50 (2.5H, m, CH_2), 1.36-1.35 (9H, m, $C(CH_3)_3$), 1.32-1.23 (1.8H, m, CH_2), 1.21-1.11 (1H, m, CH_2).

δ_{13C}(400 MHz, DMSO$_{d6}$): 172.43 (C=O), 172.30 (C=O), 171.07 (C=O), 171.02 (C=O), 170.42 (C=O), 167.18 (C=O), 155.53 (C=O), 155.44 (ArC), 137.60 (ArC), 137.48 (ArC), 137.42 (ArC), 137.34 (ArC), 133.99 (ArC), 129.32 (ArC), 129.19 (ArC), 129.16 (ArC), 129.11 (ArC), 128.73 (ArC), 128.71 (ArC), 128.11 (ArC), 127.98 (ArC), 127.93 (ArC), 127.90 (ArC), 127.83 (ArC), 127.46 (ArC), 126.76 (ArC), 126.38 (ArC), 123.82 (ArC),

118.39 (ArC), 107.33 (ArC), 107.30 (ArC), 77.31 (**C**(CH_3)$_3$), 77.29 (**C**(CH_3)$_3$), 66.65 (2Nap-O**C**H_2), 66.62 (Nap-OCH_2), 53.69 (*CH), 53.56 (*CH), 53.49 (*CH), 53.42 (*CH), 53.34 (*CH), 53.23 (*CH), 51.80 (COO**C**H_3), 51.70 (COO**C**H_3), 37.61 (CH_2), 37.36 (CH_2), 30.76 (CH_2), 30.52 (CH_2), 29.06 (CH_2), 28.91 (CH_2), 28.22 (C(**C**H_3)$_3$), 22.60 (CH_2), 22.43 (CH_2).

HRMS (ESI) m/z: ([M+Na]+). Accurate Mass calculated for $C_{42}H_{50}N_4NaO_8$: 761.3521. Found: 761.3507

2NapFFK(Boc)

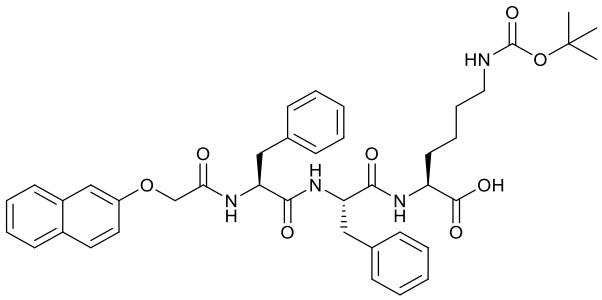

δ_H(400 MHz, DMSO$_{d6}$): 12.66 (1H, s, COOH), 8.54 (0.3H, d, *J* 8.5, NH), 8.42 (0.3H, d, *J* 7.6, NH), 8.32 (0.3H, d, *J* 7.9, NH), 8.26 (0.5H, d, *J* 8.0, NH), 8.24 (0.5H, d, *J* 7.3, NH), 8.11 (0.3H, d, *J* 8.6, NH), 8.06 (0.5H, d, *J* 8.3, NH), 8.02 (0.3H, d, *J* 8.4, NH), 7.84-7.82 (2H, m, ArH), 7.75-7.72 (1H, m, ArH), 7.48-7.44 (1H, m, ArH), 7.38-7.34 (1H, m, ArH), 7.31-7.05 (11.4H, m, ArH), 6.97-6.95 (0.6H, m, ArH), 6.78-6.72 (1H, m, NH-Boc), 5.75 (s, DCM), 4.70-4.56 (1.7H, m, *CH), 4.53 (2H, s, 2Nap-OC**H$_2$**), 4.50-4.44 (0.3H, m, *CH), 4.21-4.14 (1H, m, *CH), 3.10-2.95 (2H, m, CH_2), 2.93-2.80 (3H, m, CH_2), 2.78-2.67 (0.6H, m, CH_2), 2.58 (0.4H, dd, *J* 13.5, 9.4, CH_2), 2.07 (s, CH_3CN), 1.77-1.49 (3H, m, CH_2), 1.42-1.27 (11H, m, CH_2, C(CH_3)$_3$), 1.23-1.13 (1H, m, CH_2).

δ_{13C}(400 MHz, DMSO$_{d6}$): 173.39 (C=O), 172.66 (C=O), 170.94 (C=O), 170.86 (C=O), 170.49 (C=O), 170.39 (C=O), 167.19 (C=O), 167.16 (C=O), 155.54 (C=O), 155.43 (ArC), 137.68 (ArC), 137.56 (ArC), 137.44 (ArC), 137.35 (ArC), 134.00 (ArC), 129.34 (ArC), 129.23 (ArC), 129.17 (ArC), 129.09 (ArC), 128.73 (ArC), 128.72 (ArC), 128.14 (ArC), 127.97 (ArC), 127.90 (ArC), 127.83 (ArC), 127.47 (ArC), 126.79 (ArC), 126.76 (ArC), 126.39 (ArC), 126.33 (ArC), 126.22 (ArC), 126.18 (ArC), 123.84 (ArC), 118.40 (ArC), 107.33 (ArC), 107.32 (ArC), 77.33 (**C**(CH_3)$_3$), 66.67 (2Nap-O**C**H_2), 53.76 (*CH), 53.54 (*CH), 53.49 (*CH), 53.41 (*CH), 53.34 (*CH), 53.21 (*CH), 51.97 (*CH), 51.95 (*CH), *38.43 (CH_2), 37.64 (CH_2), 37.52 (CH_2), 37.36 (CH_2) (not visible in HSQC),* 30.96 (CH_2), 30.78 (CH_2), 29.12 (CH_2), 28.97 (CH_2), 28.24 (C(**C**H_3)$_3$), 22.72 (CH_2), 22.50 (CH_2).

HRMS (ESI) m/z: ([M+Na]+). Accurate Mass calculated for $C_{41}H_{48}N_4NaO_8$: 747.3364. Found: 747.3363

2NapFFK – final compound, not previously synthesised to our knowledge.

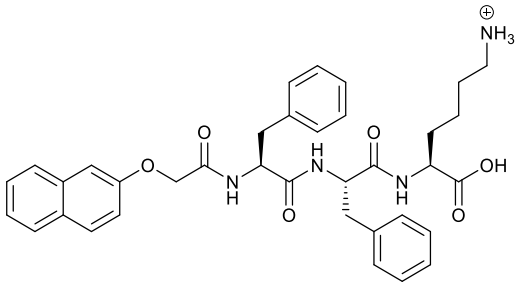

White solid, 95 % yield final step.

δ_H(400 MHz, DMSO$_{d6}$): 12.71 (1H, s, COOH), 8.56 (0.3H, d, *J* 8.5, NH), 8.33-8.28 (0.9H, m, NH), 8.24 (0.7H, d, *J* 8.2, NH), 8.09 (0.6H, d, *J* 8.3, NH), 8.05 (0.4H, d, *J* 8.4, NH), 7.85-7.83 (1.9, m, ArH), 7.75-7.70 (3.5H, m, ArH, NH_3^+), 7.48-7.45 (1H, m, ArH), 7.39-7.34 (1H, m, ArH), 7.31-7.08 (10H, m, ArH), 6.98-6.96 (0.6H, m, ArH), 4.69-4.57 (2H, m, *CH), 4.54 (2H, s, 2Nap-OC**H$_2$**), 4.24-4.16 (1H, m, *CH), 3.10-2.95 (2H, m, CH_2), 2.95-2.67 (4H, m, CH_2), 2.62-2.56 (0.6H, m, CH_2), 2.08 (s, CH_3CN), 1.80-1.70 (0.7H, m, CH_2), 1.69-1.45 (3.2H, m, CH_2), 1.43-1.33 (1.4H, m, CH_2), 1.26-1.19 (0.7H, m, CH_2).

δ_{13C}(400 MHz, DMSO$_{d6}$): 173.30 (C=O), 173.28 (C=O), 171.01 (C=O), 170.94 (C=O), 170.56 (C=O), 170.48 (C=O), 167.33 (C=O), 167.25 (C=O), 155.45 (ArC), 155.43 (ArC), 137.69 (ArC), 137.53 (ArC), 137.48 (ArC), 137.34 (ArC), 136.34 (ArC), 134.01 (ArC), 129.38 (ArC), 129.35 (ArC), 129.25 (ArC), 129.16 (ArC), 128.76 (ArC), 128.74 (ArC), 128.01 (ArC), 127.96 (ArC), 127.87 (ArC), 127.49 (ArC),126.81 (ArC), 126.77 (ArC), 126.44 (ArC), 126.27 (ArC), 126.22 (ArC), 123.90 (ArC), 123.87 (ArC), 118.40 (ArC), 107.37 (ArC), 107.34 (ArC), 66.71 (Nap-O**C**H_2), 66.66 (2Nap-O**C**H_2), 53.59 (*CH), 53.53 (*CH), 53.49 (*CH), 53.47 (*CH), 51.71 (*CH), 51.46 (*CH), 38.64 (CH_2), 38.61 (CH_2), 30.67 (CH_2), 30.46 (CH_2), 26.56 (CH_2), 26.50 (CH_2), 22.33 (CH_2), 22.10 (CH_2).

HRMS (ESI) m/z: ([M+Na]+). Accurate Mass calculated for $C_{36}H_{40}N_4NaO_6$: 647.2840. Found: 647.2830

2NapKFF

2NapK(Boc)-OMe

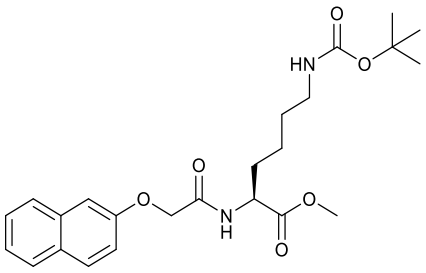

δ_H(400 MHz, DMSO$_{d6}$): 8.50 (1H, d, *J* 7.8, NH), 7.85 (2H, dd, *J* 8.3, 4.9, ArH), 7.77 (1H, d, *J* 8.2, ArH), 7.47 (1H, m, ArH), 7.36 (1H, m, ArH), 7.27 (1.5H, s, ArH), 7.25-7.24 (0.5H, m, ArH), 6.75 (1H, t, *J* 5.3, NH-Boc), 4.69 (1H, d, *J*= 14.7 Hz, 2Nap-OC**H$_2$**), 4.65 (1H, d, *J*= 14.7 Hz, 2Nap-OC**H$_2$**), 4.35-4.30 (1H, m, *CH), 3.62 (3H, s, COOCH_3), 2.86 (2H, dd, *J* 12.8, 6.4, CH_2-Boc), 1.80-1.64 (2H, m, CH_2), 1.36 (9H, s, $(CH_3)_3$), 1.33-1.20 (4H, m, CH_2).

δ_{13C}(400 MHz, DMSO$_{d6}$): 172.30 (C=O), 167.81 (C=O), 155.60 (C=O), 155.53 (ArC), 133.99 (ArC), 129.26 (ArC), 128.71 (ArC), 127.49 (ArC), 126.66 (ArC), 126.45 (ArC), 123.82 (ArC), 118.59 (ArC), 107.31 (ArC), 77.31 (**C**$(CH_3)_3$), 66.68 (2Nap-O**C**H_2), 51.86 (COO**C**H_3), 51.63 (*CH), 39.27 (*CH**C**H_2, overlapping with DMSO peak, visible in HSQC) 30.31 (CH_2), 28.99 (CH_2), 28.23 (C(**C**$H_3)_3$, 22.67 (CH_2).

HRMS (ESI) m/z: ([M+Na]+). Accurate Mass calculated for $C_{24}H_{32}N_2NaO_6$: 467.2153. Found: 467.2152.

2NapK(Boc)

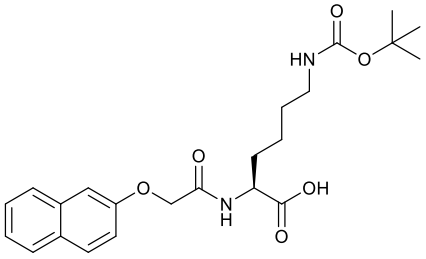

δ_H(400 MHz, DMSO$_{d6}$): 12.68 (1H, s, COOH), 8.33 (1H, d, *J* 8.0, NH), 7.86-7.83 (2H, m, ArH), 7.78-7.76 (1H, m, ArH), 7.48-7.44 (1H, m, ArH), 7.38-7.34 (1H, m, ArH), 7.29-7.24 (2H, m, ArH), 6.74 (1H, t, *J* 5.9, NH-Boc), 4.69 (1H, d, *J*= 14.7 Hz, 2Nap-OC**H$_2$**), 4.64 (1H, d, *J*= 14.7 Hz, 2Nap-OC**H$_2$**), 4.29-4.23 (1H, m, *CH), 2.88-2.84 (2H, m, CH_2), 1.80-1.62 (2H, m, CH_2), 1.36 (9H, s, $(CH_3)_3$), 1.34-1.30 (2H, m, CH_2), 1.31-1.22 (2H, m, CH_2).

δ_{13C}(400 MHz, DMSO$_{d6}$): 173.34 (C=O), 167.61 (C=O), 155.60 (C=O), 155.54 (ArC), 134.01 (ArC), 129.26 (ArC), 128.70 (ArC), 127.48 (ArC), 126.70 (ArC), 126.42 (ArC), 123.81 (ArC), 118.60 (ArC), 107.33 (ArC), 77.31 (C(CH_3)$_3$), 66.73 (2Nap-O**C**H_2), 51.57 (*CH), 39.23 (CH_2, overlapping with DMSO peak, visible in HSQC), 30.51 (CH_2), 29.04 (CH_2), 28.24 (C(**C**H_3)$_3$, 22.75 (CH_2).

HRMS (ESI) m/z: ([M+Na]+). Accurate Mass calculated for $C_{23}H_{30}N_2NaO_6$: 453.1996. Found: 453.1995.

2NapK(Boc)FF-OMe

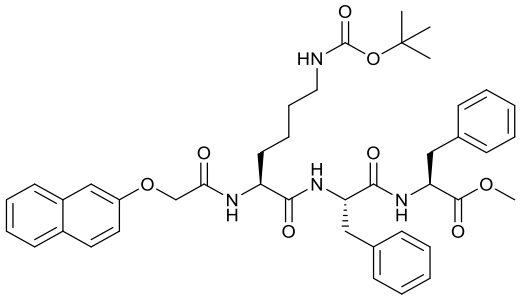

δ_H(400 MHz, DMSO$_{d6}$): 8.42 (1H, d, *J* 7.4, NH), 8.07 (1H, d, *J* 8.3, NH), 8.01 (1H, d, *J* 8.1, NH), 7.86-7.83 (2H, m, ArH), 7.78-7.76 (1H, m, ArH), 7.47-7.43 (1H, m, ArH), 7.38-7.34 (1H, m, ArH), 7.27-7.12 (11H, m, ArH), 6.69 (1H, t, *J* 5.5, NH-Boc), 5.74 (s, DCM), 4.65 (1H, d, *J*= 14.7 Hz, 2Nap-OC**H$_2$**), 4.60 (1H, d, *J*= 14.7 Hz, 2Nap-OC**H$_2$**), 4.57-4.52 (1H, m, *CH), 4.50-4.45 (1H, m, *CH), 4.30-4.24 (1H, m, *CH), 3.56 (3H, s, COOCH_3), 3.04-2.91 (3H, m, CH_2), 2.82-2.71 (3H, m, CH_2), 1.56-1.43 (2H, m, CH_2), 1.36 (9H, s, C(CH_3)$_3$), 1.30-1.22 (2H, m, CH_2), 1.15-1.05 (2H, m, CH_2).

δ_{13C}(400 MHz, DMSO$_{d6}$): 171.65 (C=O), 171.63 (C=O), 171.03 (C=O), 167.32 (C=O), 155.53 (C=O, *overlapping ArC peak not resolved*), 137.49 (ArC), 136.93 (ArC), 134.04 (ArC), 129.38 (ArC), 129.15 (ArC), 129.00 (ArC), 128.75 (ArC), 128.25 (ArC), 127.98 (ArC), 127.51 (ArC), 126.75 (ArC), 126.56 (ArC), 126.48 (ArC), 126.23 (ArC), 123.88 (ArC), 118.50 (ArC), 107.36 (ArC), 77.34 (**C**(CH_3)$_3$), 66.78 (Nap-O**C**H_2), 54.89, 53.63 (*CH), 53.42 (*CH), 52.23 (*CH), 51.81 (*CH), 39.0 (CH_2, visible in HSQC), 37.43 (CH_2), 36.60 (CH_2), 31.83 (CH_2), 29.21 (CH_2) 28.26 (C(**C**H_3)$_3$), 22.47 (CH_2).

HRMS (ESI) m/z: ([M+Na]+). Accurate Mass calculated for $C_{42}H_{50}N_4NaO_8$: 761.3521. Found: 761.3531.

2NapK(Boc)FF

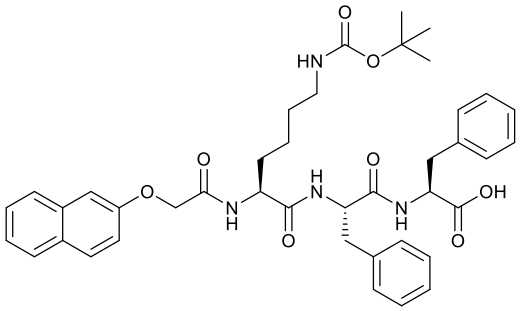

δ_H(400 MHz, DMSO$_{d6}$): 12.74 (1H, s, COOH), 8.25 (1H, d, *J* 7.8, NH), 8.05 (1H, d, *J* 8.5, NH), 8.00 (1H, d, *J* 8.3, NH), 7.86-7.83 (2H, m, ArH), 7.78-7.76 (1H, m, ArH), 7.58-7.44 (1H, m, ArH), 7.48-7.34 (1H, m, ArH), 7.28-7.17 (12H, m, ArH), 6.69 (1H, t, *J* 7.8, NH-Boc), 4.64 (1H, d, *J*= 14.7 Hz, 2Nap-OC**H$_2$**), 4.60 (1H, d, *J*= 14.7 Hz, 2Nap-OC**H$_2$**), 4.57-4.53 (1H, m, *CH), 4.48-4.43 (1H, m, *CH), 4.30-4.25 (1H, m, *CH), 3.08-2.90 (3H, m, CH_2), 2.84-2.71 (3H, m, CH_2), 1.58-1.41 (2H, m, CH_2), 1.36 (9H, s, $C(CH_3)_3$), 1.31-1.23 (2H, m, CH_2), 1.20-1.03 (2H, m, CH_2).

δ_{13C}(400 MHz, DMSO$_{d6}$): 172.63 (C=O), 170.98 (C=O), 170.90 (C=O), 167.21 (C=O), 155.51 (C=O, *overlapping ArC peak not resolved*), 137.56 (ArC), 137.30 (ArC), 134.02 (ArC), 129.34 (ArC), 129.16 (ArC), 129.06 (ArC), 128.72 (ArC), 128.15 (ArC), 127.91 (ArC), 127.48 (ArC), 126.72 (ArC), 126.44 (ArC), 126.40 (ArC), 126.16 (ArC), 123.83 (ArC), 118.48 (ArC), 107.35 (ArC), 77.28 (**C**$(CH_3)_3$), 66.78 (2Nap-O**C**H_2), 53.45 (*CH), 53.41 (*CH), 52.17 (*CH), 37.42 (CH_2), 36.66(CH_2), 31.84 (CH_2), 30.40 (CH_2), 29.21 (CH_2), 28.24 $C(CH_3)_3$, 22.46 (CH_2).

HRMS (ESI) m/z: ([M+Na]+). Accurate Mass calculated for $C_{41}H_{48}N_4NaO_8$: 747.3364. Found: 747.3351.

2NapKFF – final compound, not previously synthesised to our knowledge.

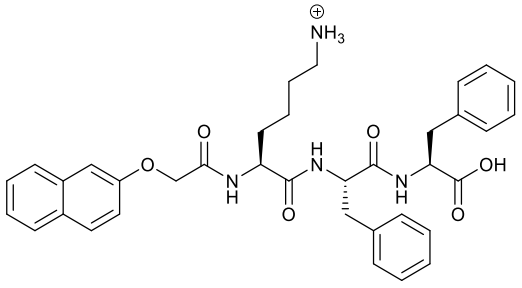

White solid, 76 % yield final step.

δ_H(400 MHz, DMSO$_{d6}$): 12.78 (1H, s, COOH), 8.34 (1H, d, *J* 7.8, NH), 8.07 (1H, d, *J* 8.5, NH), 8.04 (1H, d, *J* 8.3, NH), 7.87-7.84 (2H, m, ArH), 7.79-7.77 (1H, m, ArH), 7.64 (3H, s, NH_3^+), 7.49-7.45 (1H, s, ArH), 7.39-7.35 (1H, m, ArH), 7.28-7.10 (12H, m, ArH), 4.67-4.60 (2H, m, 2Nap-OC**H$_2$**), 4.59-4.55 (1H, m, *CH), 4.47-4.42 (1H, m, *CH), 4.34-4.28 (1H, m, *CH), 3.09-2.99 (2H, m, *CHC**H$_2$**), 2.93 (1H, dd, *J* 14.0, 8.6, *CHC**H$_2$**), 2.75 (1H, dd, *J* 13.9, 9.8, *CHC**H$_2$**), 2.67-2.58 (2H, m, C**H$_2$**-NHBoc), 1.61-1.38 (4H, m, CH_2), 1.20-1.12 (2H, m, CH_2).

δ_{13C}(400 MHz, DMSO$_{d6}$): 172.64 (C=O), 170.98 (C=O), 170.80 (C=O), 167.28 (C=O), 155.57 (ArC), 137.53 (ArC), 137.36 (ArC), 134.00 (ArC), 129.38 (ArC), 129.17 (ArC), 129.08 (ArC), 128.73 (ArC), 128.17 (ArC), 127.92 (ArC), 127.51 (ArC), 126.70 (ArC), 126.49 (ArC), 126.42 (ArC), 126.18 (ArC), 123.89 (ArC), 118.49 (ArC), 107.32 (ArC), 66.77 (2Nap-O**C**H$_2$), 53.51 (*CH), 53.39 (*CH), 51.82 (*CH), 38.62 (CH_2), 37.42 (CH_2), 36.64 (CH_2), 31.50 (CH_2), 26.58 (CH_2), 21.95 (CH_2).

HRMS (ESI) m/z: ([M+Na]+). Accurate Mass calculated for $C_{36}H_{40}N_4NaO_6$: 647.2840. Found: 647.2818.

2NapFKF

2NapF-OMe

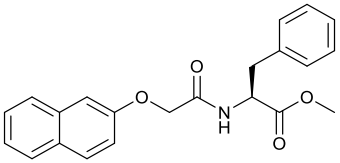

δ_H(400 MHz, DMSO$_{d6}$): 8.53 (1H, d, *J* 7.9, NH), 7.86-7.84 (2H, m, ArH), 7.75-7.73 (1H, m, ArH), 7.49-7.45 (1H, m, ArH), 7.39-7.35 (1H, m, ArH), 7.23-7.15 (7H, m, ArH), 4.65-4.57 (3H, m, *CH, 2Nap-OC**H$_2$**), 3.62 (3H, s, COOCH_3), 3.12 (1H, dd, *J* 13.8, 5.3, C**H$_2$**Ph), 3.03 (1H, dd, *J* 13.8, 9.3, C**H$_2$**Ph).

δ_{13C}(400 MHz, DMSO$_{d6}$): 171.68 (C=O), 167.78 (C=O), 155.51 (ArC), 137.14 (ArC), 133.99 (ArC), 129.32 (ArC), 129.04 (ArC), 128.76 (ArC), 128.23 (ArC), 127.51 (ArC), 126.74 (ArC), 126.52 (ArC), 126.45 (ArC), 123.87 (ArC), 118.53 (ArC), 107.35 (ArC), 66.64 (2Nap-O**C**H$_2$), 56.03 (EtOH), 53.22 (*CH), 51.99 (COO**C**H$_3$), 36.32 (**C**H$_2$Ph), 18.53 (EtOH).

HRMS (ESI) m/z: ([M+Na]+). Accurate Mass calculated for $C_{22}H_{21}NNaO_4$: 386.1363. Found: 386.1361.

2NapF

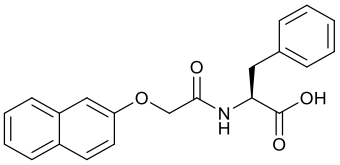

δ_H(400 MHz, DMSO$_{d6}$): 12.89 (1H, s, COOH), 8.34 (1H, d, *J* 8.2, NH), 7.85-7.83 (1H, m, ArH), 7.75-7.72 (1H, m, ArH), 7.49-7.45 (1H, m, ArH), 7.39-7.43 (1H, m, ArH), 7.22-7.14 (7H, m, ArH), 4.64-4.57 (2H, m, 2Nap-OC**H$_2$**), 4.56-4.51 (1H, m, *CH), 3.13 (1H, dd, *J* 13.8, 4.7, C**H$_2$**Ph), 3.00 (1H, dd, *J* 13.8, 9.3, *C**H$_2$**Ph).

δ_{13C}(400 MHz, DMSO$_{d6}$): 172.68 (C=O), 167.63 (C=O), 155.52 (ArC), 137.49 (ArC), 134.02 (ArC), 129.33 (ArC), 129.08 (ArC), 128.76 (ArC), 128.18 (ArC), 127.50 (ArC), 126.78 (ArC), 126.43 (ArC), 123.87 (ArC), 118.53 (ArC), 107.37 (ArC), 66.70 (2Nap-O**C**H$_2$), 53.13 (*CH), 36.40 (**C**H$_2$Ph).

HRMS (ESI) m/z: ([M+Na]+). Accurate Mass calculated for $C_{21}H_{29}NNaO_4$: 372.1206. Found: 372.13201.

2NapFK(Boc)-OMe

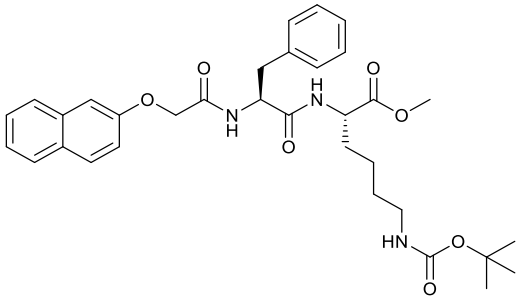

δ_H(400 MHz, DMSO$_{d6}$): 8.50 (1H, d, *J* 7.4, NH), 8.17 (1H, d, *J* 8.4, NH), 7.84-7.82 (2H, m, ArH), 7.74-7.72 (1H, m, ArH), 7.48-7.44 (1H, m, ArH), 7.38-7.34 (1H, m, ArH), 7.27-7.12 (7H, m, ArH), 6.74 (1H, t, *J* 6.0, NH-Boc), 4.72-4.66 (1H, m, *CH), 4.60 (2H, s, 2Nap-OC**H$_2$**), 4.26-4.20 (1H, m, *CH), 3.63 (3H, s, COOCH$_3$), 3.06 (1H, dd, *J* 13.8, 4.3, *CHC**H$_2$**), 2.92-2.85 (3H, m, *CHC**H$_2$**, C**H$_2$**-NHBoc), 2.30 (0.9, s, toluene), 1.74-1.64 (1.2H, m, CH$_2$), 1.62-1.55 (1.2H, m, CH$_2$), 1.36 (9H, s, C(CH$_3$)$_3$), 1.33-1.20 (2.5H, m, CH$_2$).

δ_{13C}(400 MHz, DMSO$_{d6}$): 172.39 (C=O), 171.07 (C=O), 167.33 (C=O), 155.57 (ArC), 155.50 (C=O), 137.46 (ArC), 134.02 (ArC), 129.34 (ArC), 129.22 (ArC), 128.89 (ArC), 128.74 (ArC), 128.20 (ArC), 127.99 (ArC), 127.49 (ArC), 126.76 (ArC), 126.41 (ArC), 126.29 (ArC), 125.31 (ArC), 123.85 (ArC), 118.45 (ArC), 107.31 (ArC), 77.35 (**C**$(CH_3)_3$, 66.69 (2Nap-O**C**H_2), 53.19 (*CH), 52.09 (*CH), 51.82 (COO**C**H_3), 39.04 (in DMSO peak, CH_2, visible in HSQC) 37.48 (CH_2), 30.53 (CH_2), 29.05 (CH_2), 28.25 (C(**C**$H_3)_3$), 22.66 (CH_2).

HRMS (ESI) m/z: ([M+Na]+). Accurate Mass calculated for $C_{33}H_{41}N_3NaO_7$: 614.2837. Found: 614.2834.

2Nap-FK(Boc)

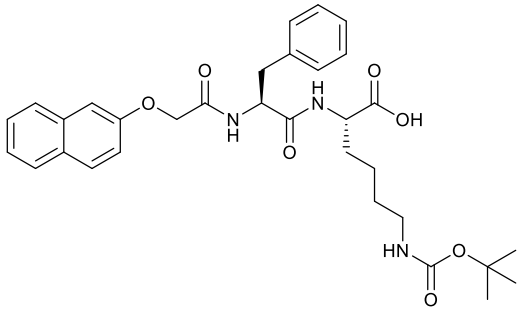

δ_H(400 MHz, DMSO$_{d6}$): 12.62 (1H, s, COOH), 8.35 (1H, d *J* 7.7, NH), 8.14 (1H, d, *J* 8.5, NH), 7.85-7.82 (2H, m, ArH), 7.74-7.72 (1H, m, ArH), 7.48-7.44 (1H, m, ArH), 7.38-7.34 (1H, m, ArH), 7.25-7.12 (7H, m, ArH), 6.74 (1H, t, *J* 5.4, NH-Boc), 4.71-4.66 (1H, m, *CH), 4.57 (2H, s, 2Nap-OC**H**$_2$), 4.20-4.15 (1H, m, *CH), 3.07 (1H, dd, *J* 13.8, 3.9, CH_2), 2.92-2.85 (3H, m, CH_2), 1.76-1.67 (1.1H, m, CH_2), 1.63-1.52 (1.3H, m, CH_2), 1.36 (9H, s, C(CH_3)), 1.34-1.20 (3.6H, m, CH_2).

δ_{13C}(400 MHz, DMSO$_{d6}$): 173.39 (C=O), 170.84 (C=O), 167.23 (C=O), 155.51 (ArC), 155.47 (C=O), 137.49 (ArC), 133.98 (ArC), 129.30 (ArC), 129.22 (ArC), 128.70 (ArC), 127.92 (ArC), 127.45 (ArC), 126.73 (ArC), 126.37 (ArC), 126.20 (ArC), 123.80 (ArC), 118.40 (ArC), 107.30 (ArC), 77.29 (**C**$(CH_3)_3$), 66.68 (2Nap-O**C**H_2), 53.18 (*CH), 51.95 (*CH), 37.46 (CH_2), 30.71 (CH_2), 29.08 (CH_2), 28.23 (CH_2, C$(CH_3)_3$, visible from HSQC), 22.74 (CH_2).

HRMS (ESI) m/z: ([M+Na]+). Accurate Mass calculated for $C_{32}H_{39}N_3NaO_7$: 600.2680. Found: 600.2690.

2Nap-FK(Boc)F-OMe

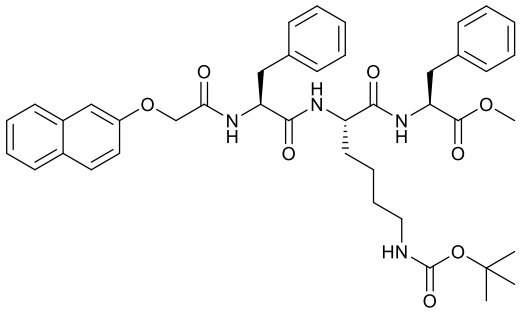

δ_H(400 MHz, DMSO$_{d6}$): 8.36 (1H, d, *J* 7.3, NH), 8.25 (0.15H, d, *J* 8.2, NH), 8.21 (0.15H, d, *J* 8.5, NH), 8.15-8.13 (1.7H, m, NH), 7.84-7.82 (2H, m, ArH), 7.74-7.72 (1H, m, ArH), 7.48-7.44 (1H, m, ArH), 7.38-7.34 (1H, m, ArH), 7.29-7.12 (12H, m, ArH), 6.71 (1H, t, *J* 5.3, NH-Boc), 5.75 (s, DCM), 4.67-4.61 (1H, m, *CH), 4.56 (2H, s, 2Nap-OC**H$_2$**), 4.52-4.46 (1H, m, *CH), 4.31-4.26 (1H, m, *CH), 4.03 (q, EtOAc),3.58 (3H, s, COOCH_3), 3.06-2.92 (3H, m, CH_2), 2.87-2.81 (3H, m, CH_2), 1.99 (s, EtOAc), 1.64-1.55 (1H, m, CH_2), 1.51-1.42 (1H, m, CH_2), 1.36 (9H, s, C(CH_3), 1.32-1.29 (1.5H, m, CH_2), 1.24-1.15 (2.5H, m, CH_2).

δ_{13C}(400 MHz, DMSO$_{d6}$): 171.73 (C=O), 171.56 (C=O), 170.51 (C=O), 167.32 (C=O), 155.51 (ArC), 155.47 (C=O), 137.53 (ArC), 137.01 (ArC), 134.00 (ArC), 129.33 (ArC), 129.17 (ArC), 128.99 (ArC), 128.72 (ArC), 128.23 (ArC), 127.94 (ArC), 127.47 (ArC), 126.78 (ArC), 126.53 (ArC), 126.39 (ArC), 126.20 (ArC), 123.84 (ArC), 118.41 (ArC), 107.33 (ArC), 77.32 (**C**(CH_3)$_3$), 66.71 (2Nap-O**C**H$_2$), 53.53 (*CH), 53.38 (*CH), 52.27 (*CH), 51.78 (*CH), 39.45 (CH_2, masked by DMSO peak, visible in HSQC), 37.45 (CH_2), 36.51 (CH_2), 31.97 (CH_2), 29.26 (CH_2), 28.25 (C(**C**H$_3$)$_3$, 22.49 (CH_2).

HRMS (ESI) m/z: ([M+Na]+). Accurate Mass calculated for $C_{42}H_{50}N_4NaO_8$: 761.3521. Found: 761.3508.

2NapFK(Boc)F

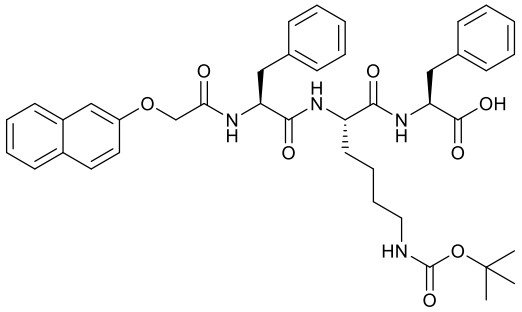

δ_H(400 MHz, DMSO$_{d6}$): 12.74 (1H, s, COOH), 8.28-8.13 (3H, m, NH), 7.84-7.82 (2H, m, ArH), 7.74-7.72 (1.1H, m, ArH), 7.48-7.44 (1.2H, m, ArH), 7.38-7.34 (1.2H, m, ArH), 7.28-7.12 (11.3H, m, ArH), 6.71 (1H, t, *J* 5.4, NH-Boc), 4.66-4.61 (1H, m, *CH), 4.56 (2H, s, 2Nap-OC**H$_2$**), 4.47-4.42 (1H, m, *CH), 4.34-4.24 (1H, m, *CH), 3.10-2.81 (5H, m, CH_2), 2.69-2.65 (0.3H, m, CH_2), 2.07 (s, CH_3CN), 1.65-1.56 (1.1H, m, CH_2), 1.51-1.42 (1.6H, m, CH_2), 1.36 (9H, s, $C(CH_3)_3$), 1.32-1.27 (1.5H, m, CH_2), 1.25-1.11 (1.8H, m, CH_2).

δ_{13C}(400 MHz, DMSO$_{d6}$): 172.68 (C=O), 171.42 (C=O), 170.51 (C=O), 167.29 (C=O), 155.50 (ArC), 155.56 (C=O), 137.55 (ArC), 137.39 (ArC), 134.00 (ArC), 129.32 (ArC), 129.17 (ArC), 129.07 (ArC), 128.72 (ArC), 128.14 (ArC), 127.92 (ArC), 127.46 (ArC), 126.76 (ArC), 126.38 (ArC), 126.17 (ArC), 123.82 (ArC), 118.41 (ArC), 107.32 (ArC), 77.30 (**C**$(CH_3)_3$), 66.71 (2Nap-O**C**H_2), 53.35 (2x *CH, visible in HSQC), 52.41 (*CH), 39.45 (CH_2, overlapping with DMSO peak, visible in HSQC), 37.43 (CH_2), 36.58 (CH_2), 31.97 (CH_2), 29.26 (CH_2), 28.24 ($C(\mathbf{C}H_3)_3$, 22.54 (CH_2).

HRMS (ESI) m/z: ([M+Na]+). Accurate Mass calculated for $C_{36}H_{41}N_4NaO_6$: 625.3021. Found: 625.3035.

2NapFKF –final compound, not previously synthesised to our knowledge.

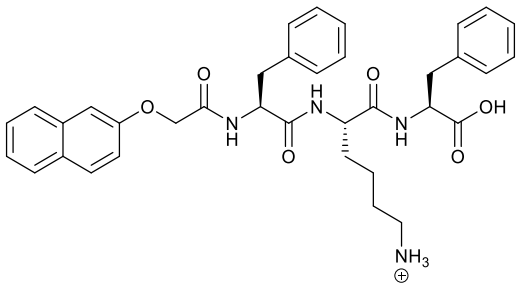

White solid, 65 % yield final step.

δ_H(400 MHz, DMSO$_{d6}$): 12.79 (1H, s, COOH), 8.25 (1H, d, *J* 8.3, NH), 8.19 (1H, d, *J* 8.3, NH), 8.16 (1H, d, *J* 7.8, NH), 7.85-7.82 (1.9H, m, ArH), 7.74-7.72 (1.1H, m, ArH), 7.66 (2.6H, s, NH_3^+), 7.49-7.45 (1H, m, ArH), 7.39-7.35 (1.1H, m, ArH), 7.28-7.13 (11.7H, m, ArH), 4.65-4.60 (1H, m, *CH), 4.56 (2H, s, 2Nap-OC**H$_2$**), 4.50-4.44 (1H, m, *CH), 4.34-4.28 (1H, m, *CH), 3.08 (1H, dd, *J* 14.1, 5.3, *CHC**H$_2$**), 3.01 (1H, dd, *J* 13.9, 3.9, *CHC**H$_2$**), 2.93 (1H, dd, *J* 14.0, 8.7, *CHC**H$_2$**), 2.85 (1H, dd, *J* 14.0, 9.6, *CHC**H$_2$**), 2.71-2.63 (2H, m, C**H$_2$**-NH_3^+), 2.07 (s, CH_3CN), 1.67-1.58 (1H, m, CH_2), 1.54-1.43 (2.8H, m, CH_2), 1.35-1.19 (2.2H, m, CH_2).

δ_{13C}(400 MHz, DMSO$_{d6}$): 172.68 (C=O), 171.31 (C=O), 170.66 (C=O), 167.44 (C=O), 155.45 (ArC), 137.53 (ArC), 137.36 (ArC), 133.99 (ArC), 129.35 (ArC), 129.15 (ArC), 129.08 (ArC), 128.72 (ArC), 128.16 (ArC), 127.97 (ArC), 127.48 (ArC), 126.75 (ArC), 126.42 (ArC), 126.23 (ArC), 123.86 (ArC), 118.41 (ArC), 107.30 (ArC), 66.66 (2Nap-O**C**H$_2$), 53.50 (*CH), 53.31 (*CH), 52.12 (*CH), 38.68 (CH$_2$), 37.36 (CH$_2$), 36.56 (CH$_2$), 31.58 (CH$_2$), 26.60 (CH$_2$), 22.05 (CH$_2$).

HRMS (ESI) m/z: ([M+Na]+). Accurate Mass calculated for $C_{36}H_{40}N_4NaO_6$: 647.2840. Found: 647.2840.

Appendix 3.5: Rheology

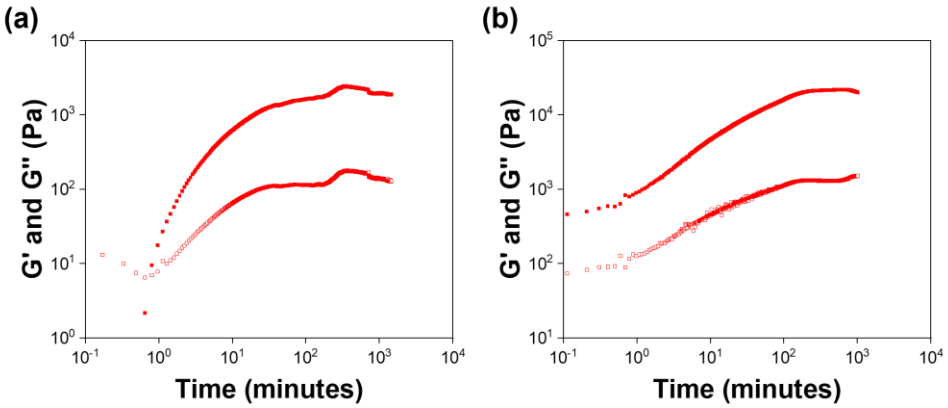

Figure A3.5.1. Time sweeps of (a) 2NapFFK and (b) 2NapKFF at concentrations of 5 mg/mL. G′ is represented by filled squares and G″ is represented by empty squares.

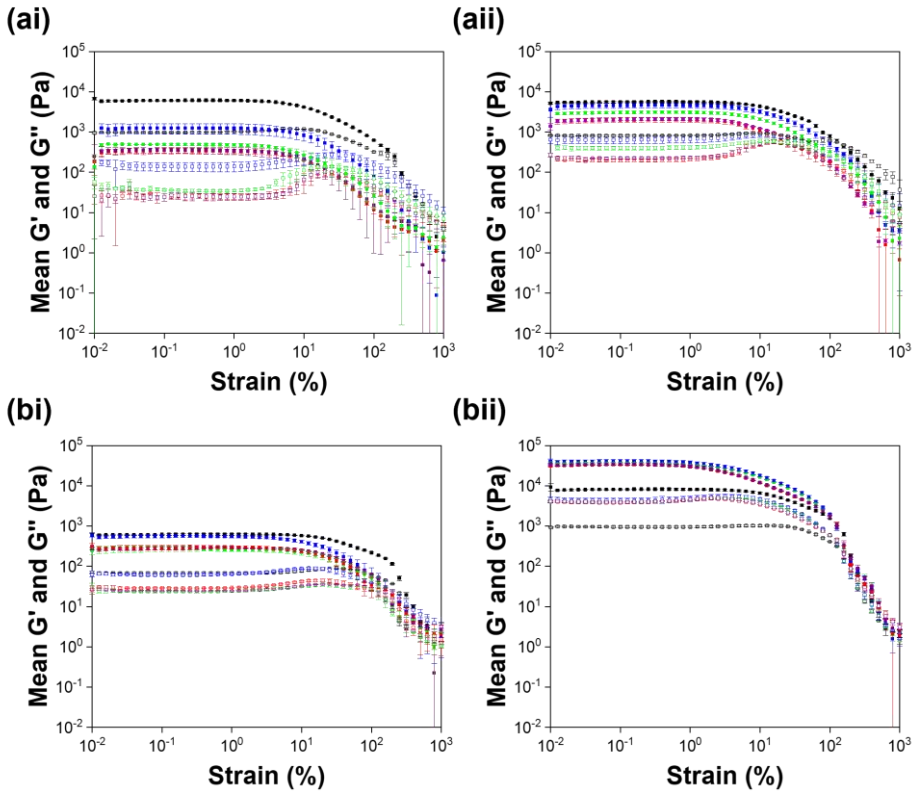

Figure A3.5.2. Strain sweeps from gels formed from (a) 2NapFFK and (b) 2NapKFF at concentrations of (i) 5 mg/mL and (ii) 10 mg/mL with GTA added pre-gelation (black), GTA added post-gelation and left to react for 24 hours (green), GTA added post-gelation and left to react for 72 hours (blue), 24-hour controls without GTA (red) and 72-hour controls without GTA (purple). G′ (filled squares) and G″ (empty squares) were calculated from the average of three samples. Error bars show the standard deviation between the three samples.

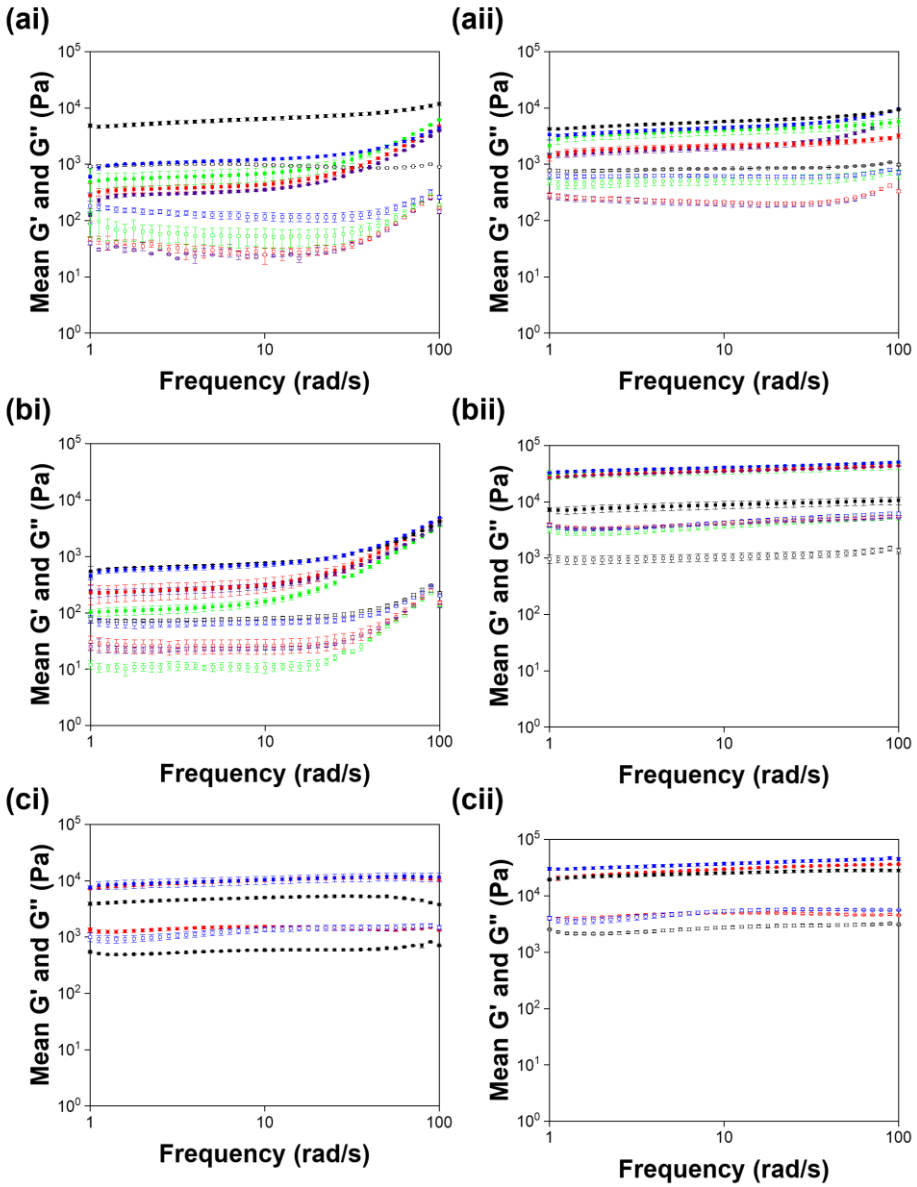

Figure A3.5.3. Frequency sweeps from gels formed from (a) 2NapFFK, (b) 2NapKFF and (c) 2NapFKF at concentrations of (i) 5 mg/mL and (ii) 10 mg/mL with GTA added pre-gelation (black), GTA added post-gelation and left to react for 24 hours (green), GTA added post-gelation and left to react for 72 hours (blue), 24-hour controls without GTA (red) and 72-hour controls without GTA (purple). G′ (filled squares) and G″ (empty squares) were calculated from the average of three samples. Error bars show the standard deviation between the three samples. The G′ and G″ values measured during the frequency sweeps are in agreement with those observed in the strain sweeps.

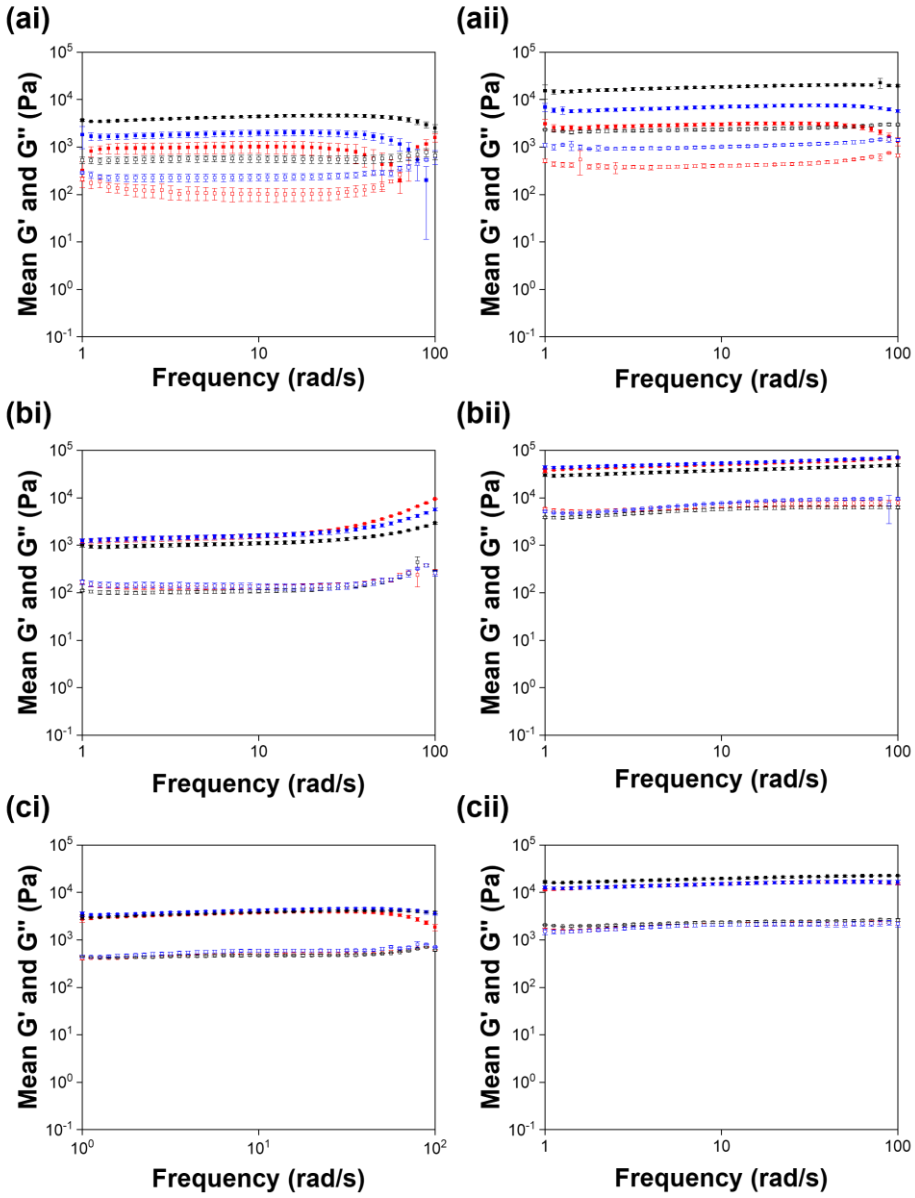

Figure A3.5.4. Frequency sweeps from gels formed from (a) 2NapFFK, (b) 2NapKFF and (c) 2NapFKF in D_2O at concentrations of (i) 5 mg/mL and (ii) 10 mg/mL with GTA added pre-gelation (black), GTA added post-gelation and left to react for 24 hours (green), GTA added post-gelation and left to react for 72 hours (blue), 24-hour controls without GTA (red) and 72-hour controls without GTA (purple). G′ (filled squares) and G″ (empty squares) were calculated from the average of three samples. Error bars show the standard deviation between the three samples. The G′ and G″ values measured during the frequency sweeps are in agreement with those observed in the strain sweeps.

Appendix 3.6: pH titrations

Molar equivalents of HCl added	pH	Molar equivalents of HCl added	pH	Molar equivalents of HCl added	pH
0.00	11.94	0.45	9.96	0.91	6.75
0.02	11.80	0.47	9.90	0.92	6.74
0.03	11.70	0.48	9.83	0.94	6.65
0.05	11.63	0.50	9.76	0.95	6.61
0.06	11.50	0.52	9.66	0.97	6.55
0.08	11.40	0.53	9.56	0.98	6.50
0.09	11.33	0.55	9.46	1.00	6.34
0.11	11.22	0.56	9.35	1.02	6.28
0.12	11.22	0.58	9.42	1.03	6.21
0.14	11.12	0.59	9.40	1.05	6.00
0.16	11.05	0.61	9.38	1.06	6.00
0.17	10.99	0.62	9.26	1.08	5.91
0.19	10.95	0.64	9.22	1.09	5.73
0.20	10.95	0.66	9.08	1.11	5.37
0.22	10.95	0.67	8.96	1.12	5.04
0.23	10.88	0.69	8.71	1.14	4.80
0.25	10.82	0.70	8.56	1.16	4.47
0.27	10.68	0.72	8.46	1.17	4.34
0.28	10.65	0.73	8.33	1.19	4.09
0.30	10.57	0.75	7.84	1.20	3.88
0.31	10.50	0.77	7.80	1.22	3.59
0.33	10.44	0.78	7.70	1.23	3.46
0.34	10.40	0.80	7.60	1.25	3.36
0.36	10.30	0.81	7.39	1.27	3.36
0.37	10.25	0.83	7.21	1.28	3.30
0.39	10.20	0.84	7.10	1.30	3.13
0.41	10.10	0.86	7.00	1.31	2.95
0.42	10.02	0.87	6.92		
0.44	10.01	0.89	6.75		

Table A3.6.1. Results from pK_a titration of 2NapFFK.

Molar equivalents of HCl added	pH	Molar equivalents of HCl added	pH	Molar equivalents of HCl added	pH
0.00	12.00	0.44	11.15	0.87	7.72
0.02	12.00	0.45	11.10	0.89	7.47
0.03	11.98	0.47	11.05	0.91	7.23
0.05	11.92	0.48	11.02	0.92	6.99
0.06	11.90	0.50	10.99	0.94	6.80
0.08	11.86	0.52	10.64	0.95	6.75
0.09	11.82	0.53	10.63	0.97	6.60
0.11	11.88	0.55	10.53	0.98	6.52
0.12	11.80	0.56	10.52	1.00	6.35
0.14	11.82	0.58	10.50	1.02	6.21
0.16	11.78	0.59	10.47	1.03	6.09
0.17	11.68	0.61	10.38	1.05	5.88
0.19	11.63	0.62	10.35	1.06	5.62
0.20	11.61	0.64	10.30	1.08	5.14
0.22	11.62	0.66	10.25	1.09	4.68
0.23	11.61	0.67	10.13	1.11	4.29
0.25	11.60	0.69	10.00	1.12	4.03
0.27	11.50	0.70	9.94	1.14	3.83
0.28	11.56	0.72	9.73	1.16	3.68
0.30	11.49	0.73	9.66	1.17	3.53
0.31	11.48	0.75	9.50	1.19	3.44
0.33	11.47	0.77	9.47	1.20	3.26
0.34	11.34	0.78	9.42	1.22	3.19
0.36	11.36	0.80	9.22	1.23	3.12
0.37	11.29	0.81	9.06	1.25	3.05
0.39	11.24	0.83	8.94	1.27	2.99
0.41	11.23	0.84	8.65	1.28	2.92
0.42	11.19	0.86	8.41		

Table A3.6.2. Results from pK_a titration of 2NapKFF.

Molar equivalents HCl added	pH	Molar equivalents HCl added	pH	Molar equivalents HCl added	pH
0.00	11.99	0.41	11.18	0.81	7.73
0.02	12.00	0.42	11.14	0.83	7.51
0.03	11.90	0.44	11.13	0.84	7.30
0.05	11.95	0.45	11.08	0.86	7.08
0.06	11.90	0.47	11.00	0.87	6.91
0.08	11.90	0.48	10.93	0.89	6.69
0.09	11.90	0.50	10.87	0.91	6.57
0.11	11.86	0.52	10.84	0.92	6.42
0.12	11.84	0.53	10.84	0.94	6.36
0.14	11.82	0.55	10.68	0.95	6.21
0.16	11.79	0.56	10.63	0.97	6.11
0.17	11.78	0.58	10.47	0.98	5.99
0.19	11.77	0.59	10.42	1.00	5.74
0.20	11.71	0.61	10.30	1.02	5.41
0.22	11.68	0.62	10.21	1.03	5.01
0.23	11.65	0.64	10.12	1.05	4.44
0.25	11.61	0.66	10.03	1.06	4.05
0.27	11.57	0.67	9.93	1.08	3.75
0.28	11.55	0.69	9.93	1.09	3.53
0.30	11.51	0.70	9.82	1.11	3.37
0.31	11.42	0.72	9.68	1.12	3.27
0.33	11.46	0.73	9.57	1.14	3.15
0.34	11.41	0.75	9.40	1.16	3.05
0.36	11.37	0.77	9.21	1.17	3.05
0.37	11.27	0.78	8.93	1.19	2.95
0.39	11.23	0.80	8.54		

Table A3.6.3. Results from pK_a titration of 2NapFKF.

References

1. B. Escuder, M. Llusar and J. F. Miravet, *Journal of Organic Chemistry*, 2006, **71**, 7747-7752.
2. J. K. Gupta, D. J. Adams and N. G. Berry, *Chemical Science*, 2016, **7**, 4713-4719.
3. E. R. Draper, B. Dietrich, K. McAulay, C. Brasnett, H. Abdizadeh, I. Patmanidis, S. J. Marrink, H. Su, H. Cui, R. Schweins, A. Seddon and D. J. Adams, *Matter*, 2020, **2**, 764-778.
4. K. McAulay, H. Wang, A. M. Fuentes-Caparros, L. Thomson, N. Khunti, N. Cowieson, H. Cui, A. Seddon and D. J. Adams, *Langmuir*, 2020, **36**, 8626-8631.
5. K. A. Houton, K. L. Morris, L. Chen, M. Schmidtmann, J. T. A. Jones, L. C. Serpell, G. O. Lloyd and D. J. Adams, *Langmuir*, 2012, **28**, 9797-9806.
6. L. Chen, S. Revel, K. Morris, L. C. Serpell and D. J. Adams, *Langmuir*, 2010, **26**, 13466-13471.